

AD723348

Bulletin 41
(Part 3 of 7 Parts)

THE SHOCK AND VIBRATION BULLETIN

Part 3
Instrumentation, Data Analysis, Test Facilities

DECEMBER 1970

A Publication of
THE SHOCK AND VIBRATION
INFORMATION CENTER
Naval Research Laboratory, Washington, D.C.



Reproduced by
NATIONAL TECHNICAL
INFORMATION SERVICE
Springfield, Va. 22151

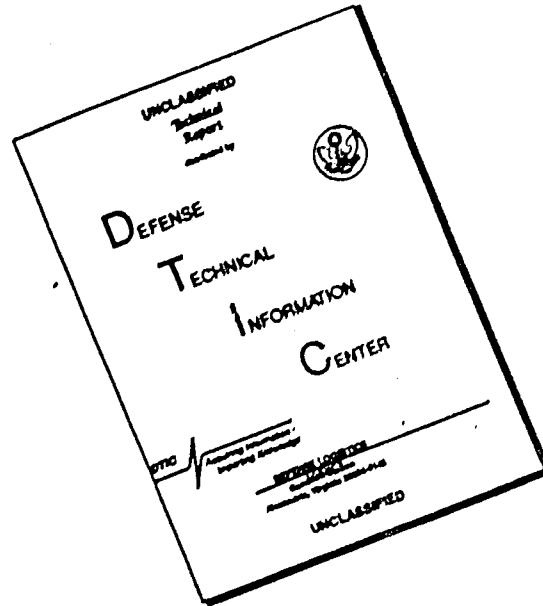
Office of
The Director of Defense
Research and Engineering



This document has been approved for public release and sale; its distribution is unlimited.

138

DISCLAIMER NOTICE



THIS DOCUMENT IS BEST QUALITY AVAILABLE. THE COPY FURNISHED TO DTIC CONTAINED A SIGNIFICANT NUMBER OF PAGES WHICH DO NOT REPRODUCE LEGIBLY.

ACCESSION BY	
CPST	WRITE SECTION <input checked="" type="checkbox"/>
DDC	DIFF SECTION <input type="checkbox"/>
UNANNOUNCED	<input type="checkbox"/>
JUSTIFICATION	
BY	
DISTRIBUTION/AVAILABILITY CODES	
DIST.	AVAIL. and/or SPECIAL
A	21

SYMPOSIUM MANAGEMENT

THE SHOCK AND VIBRATION INFORMATION CENTER

William W. Mutch, Director
 Henry C. Pusey, Coordinator
 Rudolph H. Volin, Coordinator
 Edward H. Schell, Coordinator
 Katherine G. Jahnel, Clerk Typist

Bulletin Production

Graphic Arts Branch, Technical Information Division,
 Naval Research Laboratory

Bulletin 41
(Part 3 of 7 Parts)

THE SHOCK AND VIBRATION BULLETIN

DECEMBER 1970

**A Publication of
THE SHOCK AND VIBRATION
INFORMATION CENTER
Naval Research Laboratory, Washington, D.C.**

The 41st Symposium on Shock and Vibration was held at the Air Force Academy, Air Force Academy, Colorado, on 27-29 October 1970. The U.S. Air Force was host.

**Office of
The Director of Defense
Research and Engineering**

CONTENTS

PAPERS APPEARING IN PART 3

Instrumentation

A PRACTICAL APPLICATION OF ACCELEROMETER CALIBRATIONS	1
R. R. Bouche, Endeavor. Dynamic Instrument Division, Pasadena, California	
DESIGNING AN INSTRUMENTED TEST EGG FOR DETECTING IMPACT BREAKAGE	11
William L. Shupe, USDA, Agricultural Research Service, Transportation and Facilities Research Div., University of California, Davis, California and Robert M. Lake, Mayo Clinic, Rochester, Minnesota	
AN ACCELEROMETER DESIGN USING FERROFLUID ULTRASONIC INTERFEROMETRY. . .	17
Jack G. Parks, U.S. Army Tank-Automotive Command, Warren, Michigan	
HYBRID TECHNIQUES FOR MODAL SURVEY CONTROL AND DATA APPRAISAL	25
Robert A. Salyer, TRW Systems, Inc., Redondo Beach, California	
OBJECTIVE CRITERIA FOR COMPARISON OF RANDOM VIBRATION ENVIRONMENTS. . . .	43
F. F. Kazmierczak, Lockheed Missiles and Space Company, Sunnyvale, California	
THE APPLICATION OF ANALOG TECHNIQUES TO REAL TIME ANALYSIS AND SCREENING OF DYNAMIC DATA.	55
Roger C. Crites, McDonnell Aircraft Co., St. Louis, Mo.	
SHOCK LOADING AND HOLOGRAPHIC INTERFEROMETRY IN NDT	63
R. L. Johnson, R. Aprahamian and P. G. Bhuta, TRW Systems Group, Redondo Beach, California	

Data Analysis

A NEW SYNTHESIS TECHNIQUE FOR SHOCK SPECTRUM ANALYSIS	75
William G. Pollard, Spectral Dynamics Corporation of San Diego, San Diego, California	
THE ROLE OF LATENT INFORMATION IN INFORMATION PROCESSING IN MEASURING SYSTEMS.	81
Peter K. Stein, Arizona State University, Tempe, Arizona	

Test Facilities

USBR VIBRATION TEST SYSTEM.	109
R. M. McCafferty, U.S. Bureau of Reclamation, Denver, Colorado	
MULTI-DEGREE OF FREEDOM MOTION SIMULATOR SYSTEMS FOR TRANSPORTATION ENVIRONMENTS.	119
T. K. DeClue, R. A. Arone and C. E. Deckard, Wyle Laboratories, Huntsville, Alabama	
DESIGN AND FABRICATION OF AN AIRCRAFT SEAT CRASH SIMULATOR	133
Nelson M. Isada, State University of New York at Buffalo, Buffalo, New York	
DESCRIPTION OF A SHOCK AND VIBRATION DISPLACEMENT AMPLIFIER	149
D. Cerasuolo and J. Chin, Raytheon Company, Sudbury, Massachusetts	

ARTILLERY SIMULATOR FOR FUZE EVALUATION.	155
H. D. Curchack, Harry Diamond Laboratories, Washington, D.C.	
GAS SPRING FIRING AND THE SOFT RECOVERY OF A HARD-WIRE INSTRUMENTED 155 MM PROJECTILE.	175
S. L. Fluent, Heat, Plasma, Climatic, Towers Division, Sandia Laboratories, Albuquerque, New Mexico	
FULL-SCALE RECOIL MECHANISM SIMULATOR (FORCED FLUID FLOW THROUGH A CONCENTRIC ORIFICE).	187
W. J. Courtney, IIT Research Institute, Chicago, Illinois and R. Rossmiller and R. Reade, U.S. Army Weapons Command, Rock Island, Illinois	
ISOTOPE FUEL IMPACT FACILITY	195
Larry O. Seamons, Sandia Laboratories, Albuquerque, New Mexico	
A REVERBERATION CHAMBER FOR USE AT REDUCED PRESSURES	207
M. H. Hieken, J. N. Olson, and G. W. Olmsted, McDonnell Aircraft Company, St. Louis, Missouri	
DESIGN OF AN OFF-ROAD VEHICLE MOTION SIMULATOR	215
Nelson M. Isada, Cornell Aeronautical Laboratory, Inc., and State University of New York at Buffalo, Buffalo, New York and Robert C. Sugarman, and E. Donald Sussman, Cornell Aeronautical Laboratory, Inc., Buffalo, New York	
AN AERIAL CABLE TEST FACILITY USING ROCKET POWER	223
C. G. Coalson, Sandia Laboratories, Albuquerque, New Mexico	

PAPERS APPEARING IN PART 1
Part 1 - Classified
(Unclassified Titles)

CASC (CAPTIVE AIR SPACE CRAFT) — A POSSIBLE CONCEPT FOR RIVERINE BOAT DESIGN
V. H. Van Bibber, Naval Ship Research and Development Laboratory, Panama City, Florida, and N. Elmore, Naval Ship Research and Development Center, Portsmouth, Va.
PROBLEMS OF DAMPING THE WINDOW AREAS OF SONAR DOMES
Howard N. Phelps, Jr., Naval Underwater Systems Center, New London, Connecticut
APPLICATION OF THE FINITE ELEMENT METHOD TO THE SHOCK ANALYSIS OF SONAR TRANSDUCERS
Vincent D. Godino and George A. Ziegler, General Dynamics/Electric Boat Division, Groton, Connecticut
DYNAMIC RESPONSE OF ABOVE-GROUND TARGETS TO A BLAST WAVE
P. N. Mathur, D. M. Rogers, R. H. Lee, and J. W. Murdock, The Aerospace Corporation, San Bernardino, California

PAPERS APPEARING IN PART 2
Keynote Talk

THE DYNAMIC CENTURY
D. Zonars, Air Force Dynamics Laboratory, Wright-Patterson Air Force Base, Ohio

Physiological Effects

TESTING AND MODELING STANDING MAN'S RESPONSE TO IMPACT

Joseph Gesswein and Paul Corrao, Naval Ship Research and Development Center, Washington, D.C.

EQUAL ANNOYANCE CONTOURS FOR THE EFFECT OF SINUSOIDAL VIBRATION ON MAN

C. Ashley, Mechanical Engineering Department, University of Birmingham, England

Isolation

ISOLATION FROM MECHANICAL SHOCK WITH A MOUNTING SYSTEM HAVING NONLINEAR DUAL-PHASE DAMPING

J. C. Snowdon, Ordnance Research Laboratory, The Pennsylvania State University, University Park, Pennsylvania

INTERACTIVE OPTIMAL DESIGN OF SHOCK ISOLATION SYSTEMS

W. D. Pilkey, University of Virginia, Charlottesville, Virginia

DESIGN OF HIGH-PERFORMANCE SHOCK ISOLATION SYSTEMS

Ronald L. Eshleman, IIT Research Institute, Chicago, Illinois

ELASTIC WAVE PROPAGATION IN A HELICAL COIL WITH VARYING CURVATURE AND ITS APPLICATION AS AN IMPACT LOAD DISPERSER

Nam P. Suh, Department of Mechanical Engineering, Massachusetts Institute of Technology, Cambridge, Massachusetts

ANALYSIS OF THE INVERTING TUBE ENERGY ABSORBER

J. M. Alcone, Sandia Laboratories, Livermore, California

THE EFFECTS OF PAYLOAD PENETRATION AND VARIOUS ANALYTICAL MODELS ON THE DESIGN OF A SPHERICAL CRUSHABLE CASING FOR LANDING ENERGY ABSORPTION

Robert W. Warner and Margaret Covert, NASA Ames Research Center

Damping

EFFECT OF FREE LAYER DAMPING ON RESPONSE OF STIFFENED PLATE STRUCTURES

David I. G. Jones, Air Force Materials Laboratory, Wright-Patterson AFB, Ohio

VIBRATION CONTROL BY A MULTIPLE-LAYERED DAMPING TREATMENT

A. D. Nashif, University of Dayton Research Institute, Dayton, Ohio and T. Nicholas, Air Force Materials Laboratory, Wright-Patterson Air Force Base, Ohio

DETERMINATION OF DAMPING PROPERTIES OF SOFT VISCOELASTIC MATERIALS

Fakhruddin Abdulhadi, IBM General Systems Division, Rochester, Minnesota

IMPROVING RELIABILITY AND ELIMINATING MAINTENANCE WITH ELASTOMERIC DAMPERS FOR ROTOR SYSTEMS

J. L. Potter, Lord Manufacturing Company, Erie, Pennsylvania

EFFECT OF HIGH POLYMER ADDITIVES ON DIFFUSER FLOW NOISE

B. M. Ishino, California State College, Fullerton, California and R. C. Binder, University of Southern California, Los Angeles, California

HAWK SUSPENSION SYSTEM PERFORMANCE ON M754 TRACKED VEHICLE

Paul V. Roberts, Raytheon Company, Missile Systems Division, Bedford, Massachusetts

PAPERS APPEARING IN PART 4

Vibration

- SURVEY OF SPACE VEHICLE VIBRATION ANALYSIS AND TEST TECHNIQUES**
W. Henricks, R. J. Herzberg, B. G. Wrenn, Lockheed Missiles and Space Company,
Sunnyvale, California
- METHODS USED TO REALISTICALLY SIMULATE VIBRATION ENVIRONMENTS**
J. V. Otts, Centrifuge, Vibration, and Acoustics Division, Sandia Laboratories,
Albuquerque, New Mexico
- SIMULATION OF COMPLEX-WAVE PERIODIC VIBRATION**
A. J. Curtis, H. T. Absteir, Jr., and N. G. Tinling, Hughes Aircraft Company,
Culver City, California
- RATIONALES APPLYING TO VIBRATION FOR MAINTENANCE**
A. H. Grundy, Canadian Forces Headquarters, Ottawa, Canada
- SPECIFICATION OF SINE VIBRATION TEST LEVELS USING A FORCE-ACCELERATION
PRODUCT TECHNIQUE**
A. F. Witte, Vibration and Acoustics Test Division, Sandia Laboratories,
Albuquerque, New Mexico
- SOME EFFECTS OF EQUALIZATION WITH A SINGLE MASS VS AN ELASTIC
SYSTEM ON ACCELERATIONS AND STRESSES**
R. M. Mains, Washington University
- A METHOD FOR PREDICTING STRUCTURAL RESPONSES FROM LOWER LEVEL
ACOUSTIC TESTS**
D. O. Smallwood, Centrifuge, Vibration, Acoustics Division, Sandia Laboratories,
Albuquerque, New Mexico
- SWEEP SPEED EFFECTS IN RESONANT SYSTEMS**
Ronald V. Trull, USAF, 4750th Test Squadron, Tyndall AFB, Florida
- THE DYNAMIC RESPONSE OF A STEEL EYEBAR CHAIN SUSPENSION BRIDGE
OVER THE OHIO RIVER TO VARIOUS EXCITATIONS**
R. F. Varney, J. G. Viner, Federal Highway Administration, Department of
Transportation, Washington, D.C.
- DUAL SPECIFICATIONS IN RANDOM VIBRATION TESTING, AN APPLICATION
OF MECHANICAL IMPEDANCE**
A. F. Witte, Vibration and Acoustics Test Division, Sandia Laboratories, Albuquerque,
New Mexico and R. Rodeman, Applied Mechanics Division, Sandia Laboratories,
Albuquerque, New Mexico
- VIBRATION - A DIAGNOSTIC TOOL FOR SHOCK DESIGN**
Culver J. Floyd, Raytheon Company, Submarine Signal Division, Portsmouth,
Rhode Island
- THE RESONANT RESPONSE OF A MECHANICAL SYSTEM SUBJECTED TO
LOGARITHMICALLY SWEPT AND NOTCHED BASE EXCITATION, USING
ASYMPTOTIC EXPANSION**
B. N. Agrawal, COMSAT Laboratories, Clarksburg, Maryland
- EFFECTS OF FLIGHT CONDITIONS UPON GUNFIRE INDUCED VIBRATION
ENVIRONMENT**
J. A. Hutchinson and B. G. Musson, LTV Aerospace Corporation, Vought Aeronautics
Division, Dallas, Texas

THE BOX CAR DYNAMIC ENVIRONMENT

Robert W. Luebke, C and O/B and O Railroad Companies, Baltimore, Maryland

THE NOISE ENVIRONMENT OF A DEFLECTED-JET VTOL AIRCRAFT

S. L. McFarland and D. L. Smith, Air Force Flight Dynamics Laboratory, Wright-Patterson Air Force Base, Ohio

VIBRATION SIGNATURE ANALYSIS OF BEARINGS AND ELECTRONIC PACKAGES

Charles H. Roos, General Electric Company, Aerospace Electronic Systems, Utica, New York

OUTER LOOP CONTROL FOR VIBRATION TESTING

Gordon Lester, Perkin-Elmer Corporation, Danbury, Connecticut and James Gay Helmuth, Chadwick-Helmuth Company, Inc., Monrovia, California

EMPIRICAL PREDICTION OF MISSILE FLIGHT RANDOM VIBRATION

A. E. Kartman, The Bendix Corporation, Mishawaka, Indiana

STRUCTURAL VIBRATIONS IN THE BELL AH-1G HELICOPTER DURING WEAPON FIRING

R. Holland, Kinetic Systems, Inc., Boston, Massachusetts and D. Marcus and J. Wiland, U.S. Army Frankford Arsenal, Philadelphia, Pennsylvania

CHARACTERISTICS OF GUNFIRE INDUCED VIBRATION IN HELICOPTERS

C. E. Thomas and V. C. McIntosh, Air Force Flight Dynamics Laboratory, Wright-Patterson Air Force Base, Ohio

INFLIGHT VIBRATION AND NOISE STUDY OF THREE HELICOPTERS

Phyllis G. Bolds and John T. Ach, Air Force Flight Dynamics Laboratory, Wright-Patterson Air Force Base, Ohio

PAPERS APPEARING IN PART 5

Shock

A DISCUSSION OF PYROTECHNIC SHOCK CRITERIA

M. B. McGrath, Martin Marietta Corporation, Denver, Colorado

A SUMMARY OF PYROTECHNIC SHOCK IN THE AEROSPACE INDUSTRY

W. P. Rader, Martin Marietta Corporation, Denver, Colorado and William F. Bangs, Goddard Space Flight Center, Greenbelt, Maryland

MEASURES OF BLAST WAVE DAMAGE POTENTIAL

C. T. Morrow, LTV Research Center, Western Division, Anaheim, California

SHOCK RESPONSE OF A BILINEAR, HYSTERETIC BEAM AND SUPPORT SYSTEM

Bruce E. Burton, Ohio Northern University and Robert S. Ayre, University of Colorado, Boulder, Colorado

DIGITAL FOURIER ANALYSIS OF MECHANICAL SHOCK DATA

H. A. Gaberson, and D. Pal, Naval Civil Engineering Laboratory, Port Hueneme, California

THE COMPUTER DETERMINATION OF MECHANICAL IMPEDANCE FOR SMALL ARMS FROM THE RESPONSE TO RECOIL

L. B. Gardner, R. K. Young, and D. E. Frericks, U.S. Army Weapons Command, Rock Island, Illinois

SHOCK PULSE SHAPING USING DROP TEST TECHNIQUES

R. E. Keefe and E. A. Bathke, Kaman Sciences Corporation, Colorado Springs, Colorado

ANALYSIS OF PROJECTILE IMPACT ON COMPOSITE ARMOR

Richard A. Fine, IBM Corporation, Rochester, Minnesota and Raymond R. Hagglund, Worcester Polytechnic Institute, Worcester, Massachusetts

A SYSTEMATIC APPROACH TO SHOCK HARDENING

J. L. Lipeles, Littleton Research and Engineering Corporation, Littleton, Massachusetts and D. Hoffman, Naval Ammunition Depot, Crane, Indiana

THE DEVELOPMENT OF SHOCK TEST CRITERIA FOR AIRCRAFT DISPENSER WEAPON EJECTION MECHANISMS

K. D. Denton, K. A. Herzing, and S. N. Schwantes, Honeywell, Inc., Ordnance Division, Hopkins, Minnesota

SHOCK LOAD RESPONSE OF AN ELASTIC ANNULAR PLATE ON A DISTRIBUTED FOUNDATION

John R. Mays, Department of Civil and Environmental Engineering, University of Colorado, Denver, Colorado and James E. Nelson, Space Systems Dynamics, Martin Marietta Corporation, Denver, Colorado

Fragility

METHODOLOGY AND STANDARDIZATION FOR FRAGILITY EVALUATION

R. C. Rountree, Logicon, San Pedro, California and F. B. Safford, TRW Systems Group, Redondo Beach, California

CONTROLLING PARAMETERS FOR THE STRUCTURAL FRAGILITY OF LARGE SHOCK ISOLATION SYSTEMS

Robert J. Port, Air Force Weapons Laboratory, Kirtland Air Force Base, New Mexico

HARDNESS EVALUATION

W. H. Rowan, TRW Systems Group, Redondo Beach, California

INITIAL DESIGN CONSIDERING STATISTICAL FRAGILITY ASSESSMENT

R. L. Grant, the Boeing Company, Seattle, Washington

TRANSIENT PULSE DEVELOPMENT

J. Crum and R. L. Grant, The Boeing Company, Seattle, Washington

FRAGILITY TESTING FOR HYDRAULIC SURGE EFFECTS

D. M. Eckblad, The Boeing Company, Seattle, Washington and W. L. Hedrick, TRW Systems Group, Redondo Beach, California

PAPERS APPEARING IN PART 6

Dynamics

PARAMETRIC RESPONSE OF MONOSYMMETRIC IMPERFECT THIN-WALLED COLUMNS UNDER SINUSOIDAL LOADING

Stanley G. Ebner, USAF Academy, Colorado and Martin L. Moody, University of Colorado, Denver, Colorado

PREDICTION OF UPSTAGE RANDOM VIBRATION ENVIRONMENT USING A STATISTICAL ENERGY APPROACH

D. E. Hines, G. R. Parker, and R. D. Hellweg, McDonnell Douglas Astronautics Company-West, Santa Monica, California

- ON THE REDUCTION AND PREVENTION OF THE FLUID-INDUCED VIBRATIONS OF CIRCULAR CYLINDERS OF FINITE LENGTH**
Dirse W. Sallet, Department of Mechanical Engineering, University of Maryland, College Park, Maryland and U.S. Naval Ordnance Laboratory, White Oak, Silver Spring, Maryland
- EFFECTS OF LOOSENESS ON DYNAMIC BEHAVIOR**
R. E. Beckett, K. C. Pan, U.S. Army Weapons Command, Rock Island, Illinois and D. D. Penrod, The University of Iowa, Iowa City, Iowa
- DYNAMIC DEFLECTIONS OF MULTIPLE-SPAN GUIDEWAYS UNDER HIGH SPEED, AIR CUSHION VEHICLES**
James F. Wilson, Duke University, Durham, North Carolina
- ANALYSIS OF THE MOTION OF A LONG WIRE TOWED FROM AN ORBITING AIRCRAFT**
S. A. Crist, Department of Engineering Mechanics, USAF Academy, Colorado
- A POSTSHOT STUDY OF THE DYNAMIC RESPONSE OF THE LASL MOBILE TOWER DURING THE PLIERS EVENT**
R. E. Bachman, E. F. Smith, Holmes and Narver, Inc., Las Vegas, Nevada and R. P. Kennedy, Holmes and Narver, Inc., Los Angeles, California
- BOUNDS FOR THE RESPONSE OF A CONSERVATIVE SYSTEM UNDER DYNAMIC LOADING**
H. Brauchli, The University of Alabama in Huntsville, Huntsville, Alabama
- THREE DEGREE OF FREEDOM SPRING MASS EJECTION SYSTEM**
R. Muskat, Aerospace Corporation, San Bernardino, California
- STRUCTURAL DYNAMICS OF A PARABOLOIDAL ANTENNA**
Myron L. Gossard and William B. Haile, Jr., Lockheed Missiles and Space Company, Sunnyvale, California
- AN APPLICATION OF COMPONENT MODE SYNTHESIS TO ROCKET MOTOR VIBRATION ANALYSIS**
F. R. Jensen, Hercules Inc., and H. N. Christiansen, Brigham Young University
- COMPARISON OF CONSISTENT AND LUMPED MASS MATRIX SOLUTIONS WITH THE EXACT SOLUTION FOR A SIMPLY-SUPPORTED TIMOSHENKO BEAM**
C. Baum, J. T. Higney, Gibbs and Cox, Inc., New York, New York and A. Jenks, Esso International Inc., New York, New York
- APPLICATION OF APPROXIMATE TRANSMISSION MATRICES TO DESCRIBE TRANSVERSE BEAM VIBRATIONS**
R. D. Rocke and Ranjit Roy, University of Missouri-Rolla, Rolla, Missouri
- MEASUREMENT OF MOMENT-CURVATURE RELATIONSHIP FOR STEEL BEAMS**
V. H. Neubert and W. Vogel, The Pennsylvania State University, University Park, Pennsylvania
- SELF-SYNCHRONIZATION OF TWO ECCENTRIC ROTORS ON A BODY IN PLANE MOTION**
Mario Paz, Associate Professor, University of Louisville, Louisville, Kentucky
- PROPAGATION OF THE ERROR IN COMPUTED FREQUENCIES AND MODE SHAPES RESULTING FROM A DISCRETE MASS REPRESENTATION OF UNIFORM, SLENDER BEAMS WITH VARYING HEIGHT-TO-LENGTH RATIOS**
Francis M. Henderson, Naval Ship Research and Development Center, Washington, D. C.

Dynamic Stress Analysis

A DISCUSSION ON THE ANALYTICAL DYNAMICS, STRESS, AND DESIGN INTERFACES

Irvin P. Vatz, Teledyne Brown Engineering, Huntsville, Alabama

DYNAMIC STRESS ANALYSIS IN A STRATIFIED MEDIUM

Jackson C.S. Yang, Ames Research Center, NASA, Moffett Field, California

COMPARISON OF STRUCTURAL LOADS: STATIC VERSUS DYNAMIC

Paul J. Jones and William J. Kacena, III, Martin Marietta Corporation,
Denver, Colorado

EGGSHELLING AND VIBRATIONS OF A HIGH SPEED SHAFT WITH NASTRAN ANALYSIS

Dennis J. Martin and William C. Walton, Jr., NASA Langley Research Center,
Hampton, Virginia

PARAMETRIC STUDY OF A BEAM WITH A COMPOUND SIDE-BRANCH RESONATOR AS A DEVICE TO EVALUATE PRELIMINARY DESIGN LOADS

J. Roger Ravenscraft, Teledyne Brown Engineering, Huntsville, Alabama

RAIL LAUNCHING DYNAMICS OF THE SAM-D SURFACE-TO-AIR MISSILE

Martin Wohltmann, Leonard A. Van Gulick, H. Carlton Sutphin, Martin Marietta
Corporation, Orlando, Florida

PAPERS APPEARING IN PART 7

Mathematical Analysis

ROCKET-SLED MODEL STUDY OF PREDICTION TECHNIQUES FOR FLUCTUATING PRESSURES AND PANEL RESPONSE

Eric E. Ungar, Bolt Beranek and Newman Inc., Cambridge, Massachusetts

DETERMINATION OF STRUCTURAL PROPERTIES FROM TEST DATA

A. E. Galef and D. L. Cronin, TRW Systems Group, Redondo Beach, California

VALIDITY OF MATHEMATICAL MODELS OF DYNAMIC RESPONSE OF STRUCTURES TO TRANSIENT LOADS

Wilfred E. Baker, Southwest Research Institute, San Antonio, Texas

DYNAMIC RESPONSE OF PLATES WITH CUT-OUTS

Nicholas L. Basdekas, Office of Naval Research, Arlington, Virginia and
Michael Chi, Catholic University of America, Washington, D. C.

NATURAL FREQUENCIES AND MODE SHAPES OF PLATES WITH INTERIOR CUT-OUTS

Jon Monahan, P. J. Nemergut, USAF Air Force Institute of Technology,
G.E. Maddux, Air Force Flight Dynamics Laboratory Wright-Patterson AFB, Ohio

FINITE BEAM ELEMENTS FOR DYNAMIC ANALYSIS

V. H. Neubert, The Pennsylvania State University, State College, Pennsylvania and
H. Lee, Westinghouse Research Laboratory, Pittsburgh, Pennsylvania

EVALUATION OF MODELS FOR ONE-DIMENSIONAL VIBRATION SYSTEMS

R. D. Rocke, University of Missouri-Rolla, Rolla, Missouri

**DYNAMIC ELASTOPLASTIC RESPONSE OF GEOMETRICALLY NONLINEAR
ARBITRARY SHELLS OF REVOLUTION UNDER IMPULSIVE AND
THERMAL LOADINGS**

T. J. Chung, J. T. Oden, R. L. Eldson, J. F. Jenkins, and A. E. Masters,
Research Institute, The University of Alabama in Huntsville, Huntsville, Alabama

**RIGID BODY MOTIONS OF ELASTICALLY RESTRAINED UNDERWATER STRUCTURES
FROM DETONATION-INDUCED SHOCK**

H. S. Zwibel and J. G. Hammer, Naval Civil Engineering Laboratory,
Port Hueneme, California

EXTENSION OF CLASSICAL BINARY FLUTTER MODEL USING ROOT LOCUS

J. C. Hornbuckle, and R. L. Sierakowski, University of Florida, Gainesville, Florida

STIFFNESS AND MASS MATRICES FOR A TRIANGULAR ELEMENT

Mario Paz, Associate Professor, Civil Engineering Department, University of
Louisville, Louisville, Kentucky and Earl Perry, Jr., Graduate Student,
University of Louisville, Louisville, Kentucky

**HELICOPTER FUSELAGE VIBRATION RESPONSE ANALYSIS USING THE
HYBRID COMPUTER**

James D. Cronkhite, Bell Helicopter Company, Fort Worth, Texas

**VIBRATION OF A CLASS OF NONCONSERVATIVE SYSTEMS WITH TIME-DEPENDENT
BOUNDARY CONDITIONS**

Shoel-sheng Chen, Argonne National Laboratory, Argonne, Illinois

Fluid-Structure Interactions

**A VARIATIONAL APPROACH TO THE FLUID-SHELL DYNAMIC
INTERACTION PROBLEM**

A. S. Benson, Lockheed Missiles and Space Company, Sunnyvale, California

**EQUIVALENT MECHANICAL MODEL OF PROPELLANT FREE-SURFACE
VIBRATIONS IN THE SATURN S-IVB WORKSHOP CONFIGURATION**

Franklin T. Dodge and Luis R. Garza, Southwest Research Institute,
San Antonio, Texas

**THE EFFECT OF LIQUID OSCILLATIONS ON THE LM PROPELLANT QUANTITY
GAUGE SYSTEM**

M. Rimer, Grumman Aerospace Corporation, Bethpage, New York and
D. G. Stephens, NASA Langley Research Center, Hampton Virginia

**DERIVATION OF SKYLAB PROPELLANT STORAGE MODULE RANDOM VIBRATION
ENVIRONMENT**

A. E. Chirby, R. A. Stevens, H.C. Allen and W.R. Wood, Jr., North American
Rockwell Corporation, Space Division, Downey, California

THE FLUTTER OF A HYDROFOIL

Thomas M. Ward, California Institute of Technology, Pasadena, California and
Raymond C. Binder, University of Southern California, Los Angeles, California

SUPPLEMENT

AN AIR PULSER FOR VIBRATION TESTING

J. R. Peoples, Naval Ship Research and Development Center, Washington, D.C.
and J. G. Viner, Federal Highway Administration, Washington, D. C.,

STATISTICAL APPROACH TO OPTIMIZE RANDOM VIBRATION TEST SPECTRA
David L. Earls and John F. Dreher, Air Force Flight Dynamics Laboratory,
Wright-Patterson AFB, Ohio

**THE EFFECT OF TAILFINS ON THE VIBRACOUSTIC ENVIRONMENT OF
EXTERNALLY CARRIED AIRCRAFT STORES**
John F. Dreher, Air Force Flight Dynamics Laboratory, Wright-Patterson
Air Force Base, Ohio

**THE EFFECTS OF VISCOUS DAMPING ON DYNAMIC LOAD FACTORS FOR
SINGLE DEGREE-OF-FREEDOM SYSTEMS**
Harry Price Gray, Naval Ship Research and Development Center, Washington, D.C.

**THE EFFECT OF CAVITATION ON THE FLAT PLATE HULL UNDERWATER
SHOCK MODEL**
R. J. Scavuzzo, Rensselaer Polytechnic Institute, Hartford Graduate Center,
East Windsor Hill, Connecticut, and D. D. Raftopoulos, The University of Toledo,
Toledo, Ohio

INSTRUMENTATION

A PRACTICAL APPLICATION OF ACCELEROMETER CALIBRATIONS

R. R. Bouche
Endevco
Dynamic Instrument Division
Pasadena, California

Recent advances in calibration techniques and instrumentation now make it possible to perform complete calibrations on accelerometers. High frequency shakers which are virtually free of distortion and transverse motion are used to perform calibrations depicting the true performance of accelerometers. A recently published standard is most useful as a guideline in performing calibrations. This standard describes which calibrations need to be performed and how to use the results. The sensitivity, frequency response, and resonance frequency are the most important calibrations.

The sensitivity calibration is performed at 100 Hz on accelerometers intended for ordinary use in shock and vibration measurements. However, it is also important to obtain a continuous plot of frequency response and resonance frequencies to detect any undesirable characteristics and unwanted resonances in the accelerometer. Good performance is indicated by a calibration which demonstrates that the accelerometer operates as a single-degree-of-freedom mechanical system. Some accelerometers have irregular frequency response characteristics and possess several resonances. By performing these calibrations the accelerometers with marginal performance are detected and judgments can be made regarding possible effects when making shock and vibration measurements.

Another use of resonance frequency calibrations is to detect damaged accelerometers. It is practical to cull out these accelerometers before any serious problems are encountered in their use.

INTRODUCTION

The recently published American National Standard for the Selection of Calibrations and Tests for Electrical Transducers Used for Measuring Shock and Vibration, S2.11-1969 [1], is useful for determining which calibrations to perform and how to put calibration results to practical use. Many of the calibrations and tests specified in S2.11-1969 are used to verify the performance characteristics of accelerometers. Some of these calibrations and tests are performed at the time of design and manufacture and need not be repeated thereafter. Other calibrations should be performed at time intervals ranging from three months to one year, depending upon usage. These important calibrations include sensitivity, frequency response, and resonance frequency. The sensitivity calibration must be performed in order to use the accelerometer accurately. The frequency response calibration is useful for detecting unusual performance characteristics and the resonance frequency calibration is the most accurate means for determining the operating condition of accelerometers.

SENSITIVITY AND FREQUENCY RESPONSE

Primary accelerometer standards previously calibrated by the reciprocity method and recently developed shakers are required for performing accurate sensitivity and frequency response calibrations routinely. With these instruments it is practical to detect unusual performance characteristics. The use of inferior accelerometer standards and shakers makes it difficult to determine whether unusual results are a characteristic of the accelerometer or are errors caused by the instruments on which the calibration is being performed.

Accelerometer Standard

In order to establish the performance characteristics of accelerometer standards, it is necessary to perform the calibrations and tests listed in S2.11-1969. These calibrations and tests determine that the standard will perform accurately under all conditions of use. The performance characteristics of an accelerometer standard now in use in many laboratories are listed in Table I. This standard is used

TABLE 1
SHOCK AND VIBRATION STANDARD ENOEVC0® MODEL 2270

Performance Characteristic	Specification
Sensitivity Error	±0.5 per cent
Sensitivity Stability at 100 Hz	±0.5 per cent/year
Mass Effect on Sensitivity at 100 Hz	±0.2 per cent/100 grams
Frequency Response and Relative Motion	
Sensitivity Change, 5 Hz - 5000 Hz with up to 100 grams attached mass	-2 per cent*
Sensitivity Change, 5 Hz - 10,000 Hz with up to 50 grams attached mass	±4 per cent*
Amplitude Linearity Sensitivity Change	+0.1 per cent/1000 g
Transverse Sensitivity Ratio	±3 per cent
Temperature Response Change Sensitivity	±0.5 per cent/10° C
Strain Sensitivity	0.001 g/μ In/in

*Estimated maximum error of correction made from curves showing nominal response is ±1 per cent.

for both shock motion and vibration calibrations. It is necessary for an accelerometer standard to have low strain sensitivity and certain other characteristics in order to perform accurate calibrations on the standard and demonstrate that the sensitivity of the standard remains unchanged for long periods of time [2]. These high quality standards are calibrated by the reciprocity method. This absolute calibration method has a unique advantage in establishing the sensitivity of the standard with an error not exceeding ±0.5 per cent. First of all the standard must possess good performance characteristics to make small errors achievable and the reciprocity method must be used to obtain small errors. Consequently, the use of the reciprocity method helps to establish that the standard possesses good performance characteristics and, therefore, can be used to accurately calibrate other accelerometers.

Sensitivity Calibrations

The sensitivity calibration of most accelerometers is usually performed at 100 Hz. This calibration is very important because it is impossible to use an accelerometer accurately without it. The sensitivity calibration is performed routinely at periodic intervals as specified in S2.11-1969. The calibration result is used to determine the required gain setting on accessory amplifiers and to compute the accelerations being measured during test applications. The sensitivity calibration basically serves this sole purpose. It is not very useful for determining other characteristics or the operating condition of accelerometers.

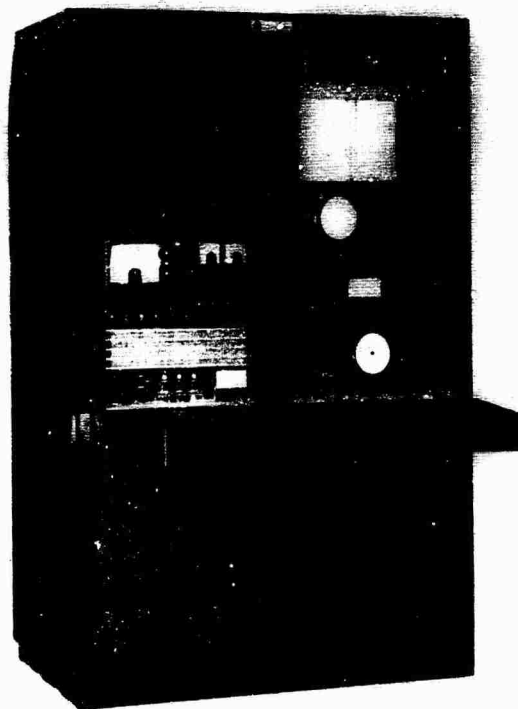


Fig. 1 - High frequency shaker and instrumentation used for automatically plotting the frequency response and resonance frequencies of accelerometers

Shaker Requirements

Almost any shaker can be used to perform accurate sensitivity calibrations on most accelerometers at a single frequency. However, it is important to perform a frequency response calibration throughout the range of intended use. Accurate frequency response calibrations can only be performed on shakers having low acceleration distortion, and little transverse motion, Fig. 1. If the shaker used does not have these characteristics, it is necessary to previously determine the frequencies of excessive distortion and transverse motions and avoid these frequencies during the calibration. Since improved shakers have been developed [3, 4], it is good practice to avoid the use of other shakers. The use of good shakers is necessary to determine the true performance of accelerometers such as detecting abnormalities in frequency response.

Frequency Response Calibrations

Frequency response calibrations serve two useful purposes. One is to establish the operating frequency range. The second and perhaps more important practical use of frequency response calibration is to determine that the accelerometer is free from abnormal response. Does the accelerometer have erratic response at any frequency within the operating range? This question is answered through the use of calibration shakers having the above mentioned characteristics. Normally, the frequency response of accelerometers is as shown in Fig. 2. Most of the accelerometers calibrated have the characteristic of no minor resonances and increasing sensitivity at the high frequencies. However, there are a number of accelerometers which have responses similar to those given in Fig. 3. The irregular response in Fig. 3(a) is due to the performance characteristics of this particular accelerometer. The minor resonance at 7300 Hz may be due to a resonance in the accelerometer case. Another accelerometer, Fig. 3(b), has a minor resonance with unusually high sensitivity between 8000 Hz and 9400 Hz. Fig. 3(c) shows an erratic frequency response which sometimes occurs in accelerometers having very small size. The frequency response of an accelerometer having damaged mounting threads is shown in Fig. 3(d). These results are extreme examples of certain accelerometers.

It is important to know that the frequency response is normal throughout most, if not all, of the operating frequency range. The presence of large sensitivity changes in narrow frequency bands might be overlooked or mistakenly attributed to shaker characteristics if the calibration is performed on shakers having excessive transverse motion or acceleration distortion. It is also important to use standards having low relative motion [5] in order to be sure that unusual response at the higher frequencies is due to the accelerometer rather than being caused by excessive calibration error. In some test applications it may be important to avoid

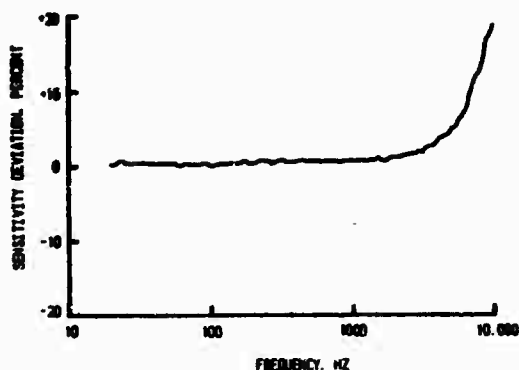


Fig. 2 - Frequency response calibration performed on an accelerometer having the characteristics of a single-degree-of-freedom mechanical system with no minor resonances

the use of accelerometers having poor frequency response such as those given in Fig. 3. It is easy to cull out these accelerometers when performing routine frequency response calibrations. Abnormal frequency response in accelerometers may be due to internal damage, internal lead wire resonances, connector resonances, accelerometer case resonances, cable effects, etc.

RESONANCE FREQUENCY CALIBRATIONS

Although sensitivity and frequency response calibrations are required for the accurate use of accelerometers, the plot of resonance frequencies is a very important and definitive calibration. The resonance frequency calibration is the only method for evaluating the basic performance characteristic of accelerometers and their operating condition. The resonance frequency calibration determines whether or not the accelerometer operates as a single-degree-of-freedom mechanical system. Perhaps even more important is its use for detecting internal damage. In order to perform resonance frequency calibrations it is necessary to use a high frequency shaker, Fig. 1, in which the resonance frequencies [1, 3] of the shaker moving element exceeds the resonance frequencies of the accelerometers being calibrated. The resonance frequency of most accelerometers is less than 50,000 Hz. However, some accelerometers used for shock measurements have their resonance frequency above 100,000 Hz. Even with these accelerometers it is useful to perform resonance frequency calibrations up to 50,000 Hz to detect any unusual performance characteristics at lower frequencies.

Ideal Accelerometers

Many accelerometers now being used operate as the ideal accelerometer shown in Fig. 4. It has a single resonance and few, if any, minor resonances. This ideal response is very similar to the theoretical response given in ANSI Standard S2-2-1959 [6]. It is good practice for the

user to perform resonance frequency calibrations on accelerometers to establish their performance characteristics and to detect any changes in future years. This practice should be followed on accelerometers used for important and accurate measurements. The resonance frequency calibration should be repeated when there is evidence that the accelerometer was subjected to severe environments or rough handling. Although there may be no external indications, internal damage may occur.

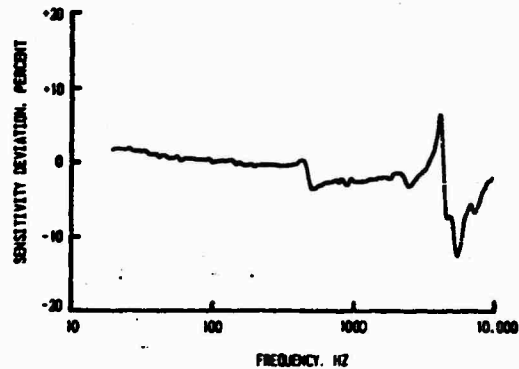
Another reason for performing resonance frequency calibration is to determine if the response is like the ideal accelerometer. The use of accelerometers having a single resonance, Fig. 4, may be preferred for some applications where high accuracy and reliability are required. On the other hand accelerometers having multiple resonances, Fig. 5, are quite suitable for most applications and are used because of other desirable characteristics such as special size and shape.

Damaged Accelerometer

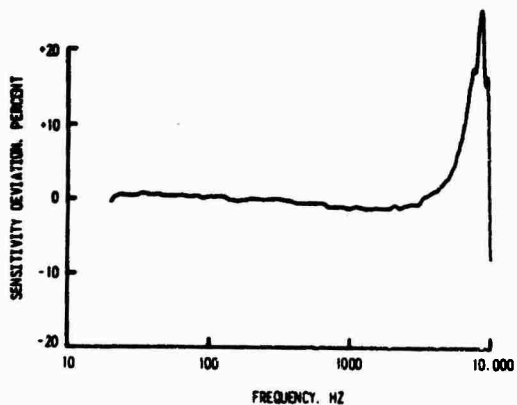
Although it is difficult to damage many piezoelectric accelerometers, the design of some accelerometers makes them vulnerable to extremely high shock motions. It is possible to apply high shock motions above the rated environmental limit by rough handling. Resonance frequency calibration is the most accurate method for determining accelerometer damage. Fig. 6(a) and 6(b) show the resonance frequency calibrations before and after an accelerometer was subjected to excessive shock motion. The resonance frequency of the accelerometer is decreased from 32,000 Hz to 29,500 Hz and a minor resonance is present at 9000 Hz, Fig. 6(b). The decrease in resonance frequency is a definite indication of internal damage. It is interesting to note that this is the same accelerometer used during the frequency response calibration in Fig. 3(b). On the basis of the frequency response calibration alone the minor resonance at 9000 Hz may have been overlooked



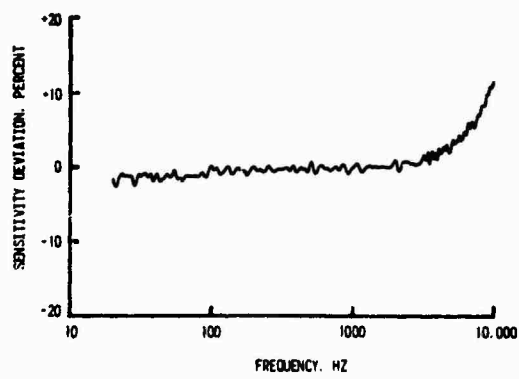
(a)



(c)

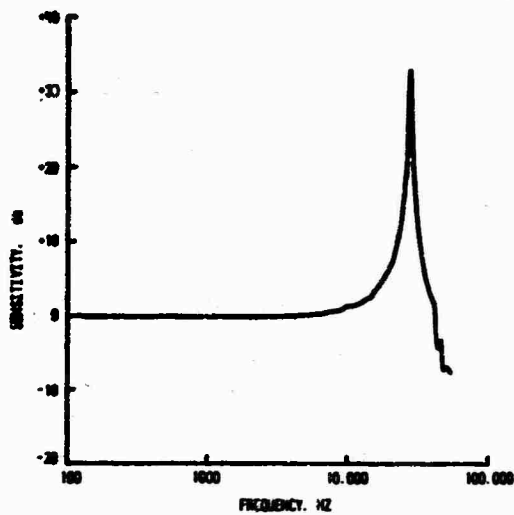


(b)

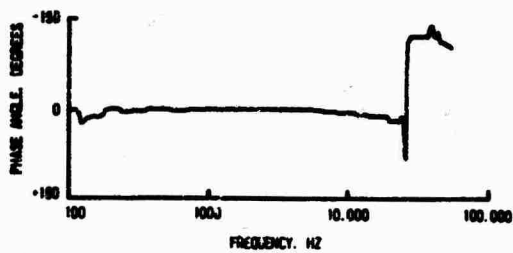


(d)

Fig. 3 - Frequency response calibrations performed on accelerometers having unusual characteristics



(a)



(b)

Fig. 4 - Typical resonance frequency calibration indicates performance characteristics of an ideal accelerometer. Phase angle calibration provides supplemental data at resonance

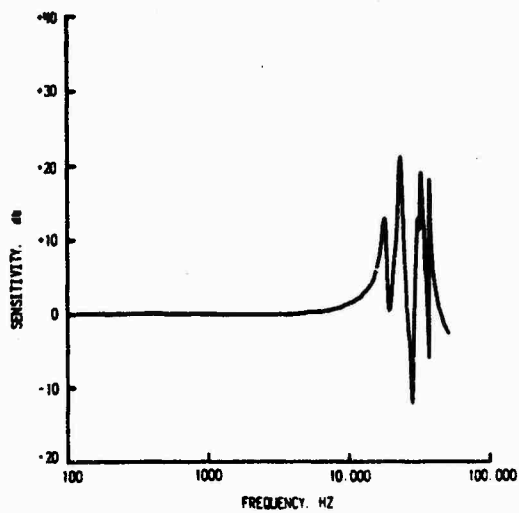
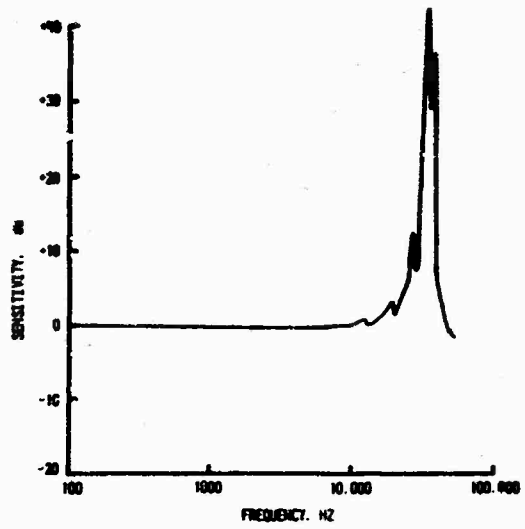
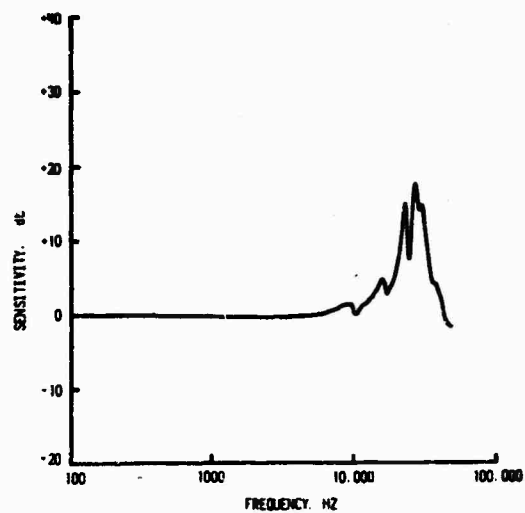


Fig. 5 - Calibration of an accelerometer having several resonances



(a)



(b)

Fig. 6 - Calibrations performed on an accelerometer show a resonance frequency of (a) 32,000 Hz before damage and (b) 29,500 Hz after damage

because the response is acceptable at lower frequencies. However, the resonance frequency calibration in Fig. 6(b) establishes the fact that the accelerometer is damaged and probably should not be used in important tests.

It is becoming routine to perform resonance frequency calibrations as supplemental information during shock motion calibrations to detect any changes in the operating characteristics of the accelerometers. In most accelerometers no malfunction is detected. An exception to this is the accelerometer shown in Fig. 7. The result of the shock motion

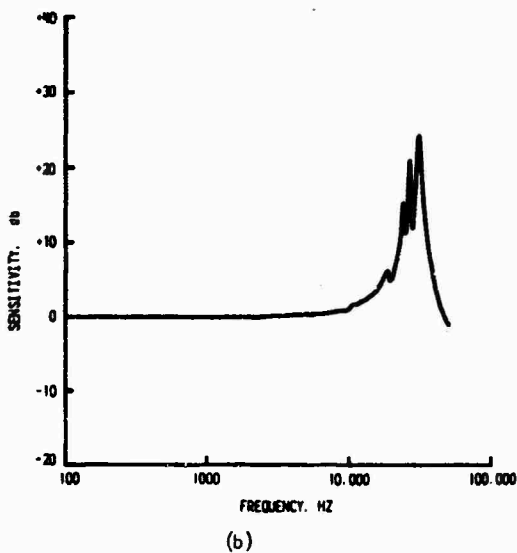
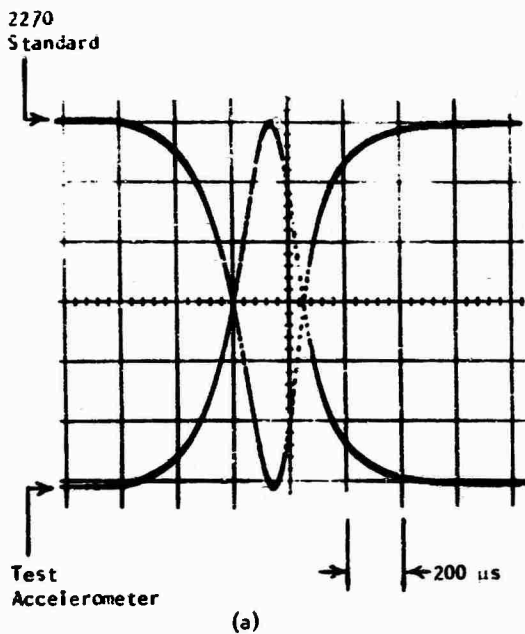


Fig. 7 - Calibrations performed on a damaged accelerometer show (a) normal response during 1000 g shock motion calibration and (b) unusually low resonance frequency which indicates the accelerometer has internal damage

calibration, Fig. 7(a), is perfectly normal. No unusual response is present in the oscillogram and the shock motion sensitivity agreed precisely with the sinusoidal calibration. However, the routine resonance frequency calibration, Fig. 7(b), shows multiple resonances and a resonance frequency of 28,500 Hz. The nominal resonance frequency of this accelerometer is 35,000 Hz. The low resonance frequency

again is a definite indication of internal damage.

Failures in damaged accelerometers include such things as cracked piezoelectric elements and epoxy joints, plastic deformation in screws, defaced accelerometer mounting surface, deformed accelerometer case, etc.

Minor Resonances

Minor resonances detected during the frequency response calibration are the result of resonances in lead wires, accelerometer cases, etc. These resonances in some accelerometers occur at frequencies above 10,000 Hz which is the upper limit of most frequency response calibrations. The accelerometer in Fig. 8(a) has a minor resonance at 37,000 Hz. It is known that this is a minor resonance because the phase angle changes abruptly to 100 degrees at the resonance and returns to zero degrees above the resonance, and because the sensitivity changes only 20 db. Although this accelerometer is usually used for shock motion measurements, the presence of the minor resonance should have little effect in many test applications. However, it is desirable to be aware of the local resonance during the selection of accelerometers particularly in those instances where very high frequency characteristics are measured [7]. The calibration in Fig. 9 shows the response of a shock accelerometer having no minor resonances up to 50,000 Hz.

Accelerometer Effects on Structures

It is desirable to have resonance frequency data on accelerometers when considering the possible effects of the accelerometer on the motion of the structure. Neglecting the effects of rotary inertia, the motion of the structure with the accelerometer attached is given by the following equation: [1]

$$A = \frac{A_0 M_s}{M_s + M_t}$$

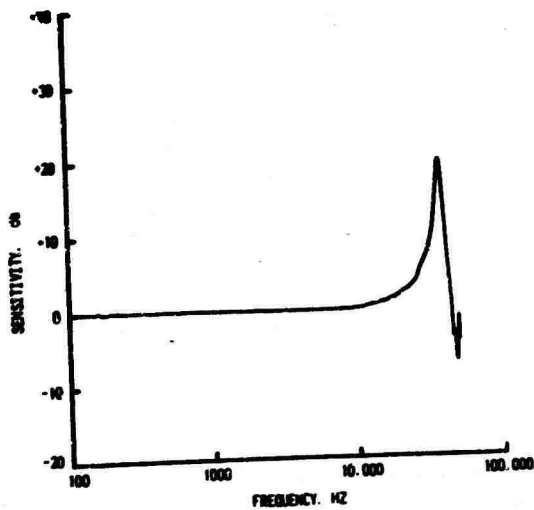
where: A = amplitude of motion of the structure with accelerometer attached

A_0 = amplitude of motion without accelerometer attached

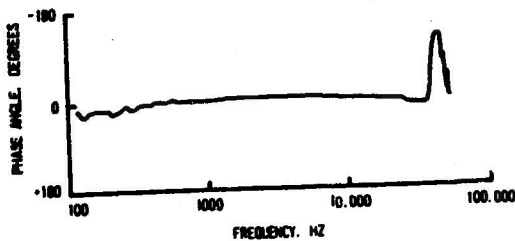
M_s = point dynamic mass of the structure at the accelerometer mounting location in the sensitive direction of the accelerometer

M_t = dynamic mass of the accelerometer in its sensitive direction

The dynamic mass of the accelerometer at all frequencies below the lowest resonance is equal to the total mass of the accelerometer measured statically. However, it should be expected that the dynamic mass of the accel-



(a)



(b)

Fig. 8 - Calibration of shock motion accelerometer having a minor resonance below 50,000 Hz

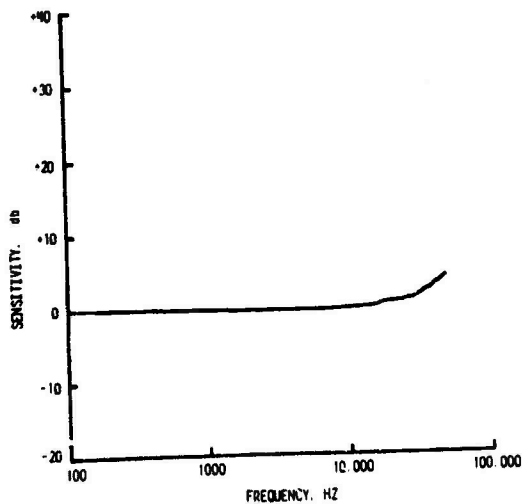
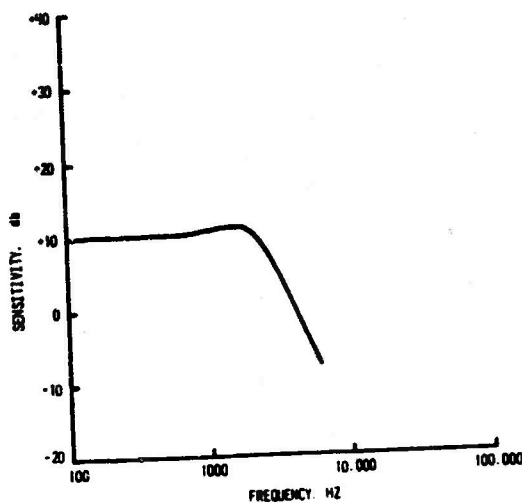


Fig. 9 - Calibration of shock motion accelerometer having no resonances below 50,000 Hz

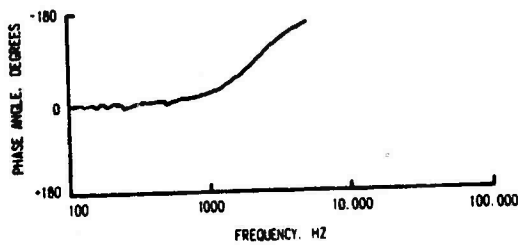
erometer changes significantly at minor resonances particularly if the response has a rather large sensitivity change at the resonance [8]. The largest changes in dynamic mass should occur at the accelerometer resonance frequency. It is usually difficult to compute the change in response of the structure as a result of resonances in the accelerometer. However, a reasonable prediction of the effect can be obtained through the use of the above equation by knowing the resonance frequency of the accelerometer and the characteristics of the structure being tested.

Accelerometers With Damping

A resonance frequency calibration on a piezoresistive accelerometer with oil damping is shown in Fig. 10. During manufacture the damping is adjusted to approximately 0.7 of critical damping in order to assure that complex vibration and shock motions are measured



(a)



(b)

Fig. 10 - Frequency response calibration on a piezoresistive accelerometer using internal damping to produce proportionate phase response

accurately. In order to avoid distortion in the accelerometer output it is necessary for the phase angle to vary linearly with frequency which is indicated in Fig. 10 by taking into account the use of the logarithmic frequency scale. The waveform of the accelerometer output is identical to the waveform of the measured acceleration only when the phase angle response has this characteristic or is zero degrees as in the case of undamped accelerometers. The accelerometer is selected so that proportionate phase response is maintained at all significant frequency components of the motion to be measured. This usually requires that the proportionate phase response be maintained at frequencies up to about two-thirds of the natural frequency for damped accelerometers. Damped accelerometers are preferred in applications where it is desirable to filter out frequencies present near and above the natural frequency or resonance frequency of the accelerometer. However, if the damping changes significantly for any reason, the output will be distorted when the damping exceeds the range of about 0.5 to 0.85 of critical damping. Large changes in damping can occur at temperature extremes due to viscosity changes in oil damped accelerometers. It is important that no large changes in damping occur for unknown reasons, such as might be caused by damage or air leaks. Resonance frequency calibrations performed periodically should be useful for detecting changes in damping by comparing the response to that of an ideal accelerometer [6].

SUMMARY

With the introduction of new testing procedures using primary accelerometer standards and high frequency shakers, routine resonance frequency calibrations are performed in addition to sensitivity and frequency response calibrations. The sensitivity is obtained merely to determine the calibration factor for using the accelerometer in making shock and vibration measurements. The frequency response calibration determines the operating frequency range, and is useful for evaluating certain performance characteristics.

The resonance frequency calibration is used to determine how closely the accelerometer operates as a single-degree-of-freedom system. It also identifies minor resonances which may affect the accuracy while making shock and vibration measurements at high frequencies. A very important use of the resonance frequency calibration is to detect changes in the accelerometer's operating condition and determine whether or not the accelerometer has suffered any internal damage. Resonance frequency calibrations should be used in laboratories responsible for verifying the operating condition of measuring instruments.

REFERENCES

1. Anon, "American National Standard for the Selection of Calibrations and Tests for Electrical Transducers Used for Measuring Shock and Vibration," S2.11-1969, American National Standards Institute, Inc., New York, 19 pp., 1969
2. R. R. Bouche and L. C. Ensor, "Accelerometer Calibration With Reciprocity Vibration Standards," *Measurements and Data*, Vol. 4, No. 4, pp. 84-89, July/August 1970
3. R. R. Bouche, "High Frequency Shaker for Accurate Accelerometer Calibrations," *The Journal of Environmental Sciences*, Vol. 13, No. 3, pp. 10-15, July/August 1970
4. T. Dimoff, "Electrodynamic Vibration Standard With a Ceramic Moving Element," *Journal of Acoustical Society of America*, Vol. 40, No. 3, pp. 671-676, 1966
5. R. R. Bouche, "Vibration Standards for Performing Comparison Calibrations," *Instrument Society of America Preprint No. M18-3-MESTIND-67*, 7 pp., 1967 (TP241)
6. Anon, "American Standard Methods for the Calibration of Shock and Vibration Pick-ups," S2.2-1959, American National Standards Institute, Inc., New York, 39 pp., 1959
7. G. K. Rasanen and B. M. Wigle, "Accelerometer Mounting and Data Integrity," *Sound and Vibration*, pp. 8-15, November 1967
8. E. T. Pierce, O. W. Price, S. Edelman and E. Jones, "Accelerometer Resonances Affect Vibration Measurements," *The Journal of Environmental Sciences*, pp. 17-21, December 1967

DISCUSSION

Mr. Schell (Shock and Vibration Information Center): I noticed on a curve that the resonant frequency had shifted from about 35 down to 28 KHz., yet the calibration curve still looked pretty good. Is this still a useful accelerometer or is it damaged beyond use?

Mr. Bouche: It is still a very useful accelerometer. However, it is desirable to be aware of this situation since once an accelerometer is damaged, it can be further damaged more easily. It might have, for example, cracked ceramics inside the accelerometer. If you are aware that you have a damaged accelerometer, for important tests you might set that one aside. However, as long as it is

not damaged further it will operate just as indicated by that response curve.

Mr. Peete (Naval Undersea R and D Center): After first determining the resonant frequency response of a given accelerometer dynamically under shock, does the effect of the sweep rate when applying a vibratory input signal cause any variation on the sensitivity when determining the resonant frequency under vibration?

Mr. Bouche: I think that you are asking whether the magnification factor might be affected by the rate of sweep when measuring the resonant frequency. It is. Frequently, when going up to 10 or 15 KHz, we slow down the sweep speed as we approach resonance.

DESIGNING AN INSTRUMENTED TEST EGG FOR DETECTING IMPACT BREAKAGE

William L. Shupe
USDA, Agricultural Research Service, Transportation & Facilities Research Div.
University of California, Davis, California

and
Robert M. Lake
formerly with
USDA, Agricultural Research Service, Transportation & Facilities Research Div.
University of California, Davis, California
present address
Mayo Clinic, Rochester, Minnesota

An electronic shock sensing device for detecting areas of egg breakage occurring in commercial grading and packing equipment was designed, constructed, and laboratory tested. A small accelerometer and transmitter system was built into a plastic egg-shaped container. The signal generated by the accelerometer caused by any sudden impact encountered was recorded on the screen of an oscilloscope. The image was a sharp spike that was readily measured, as to severity, on the screen's grid. The height from which a normal egg can be dropped onto a hard surface without cracking was measured. Then the "spike" that appeared on the oscilloscope screen, when the test egg was submitted to the same treatment, was measured and identified as the peak, at or beyond which a normal egg will crack. The test egg was then run through a component of a mechanized egg grading system and the image of the impact signal on the oscilloscope screen was identified and photographed. Although difficulty was encountered in precise replication of the image signals, the location of points where various degrees of shock occurred could be readily identified. The laboratory tests indicate that this method is a feasible one for detecting impacts involving egg-against-egg or egg-against-equipment collisions that cause egg breakage in commercial egg grading and packing operations that employ high-speed mechanized equipment.

SUMMARY

A miniaturized accelerometer and radio transmitter system that senses shock (impact) forces and transmits the information as an electric signal to an oscilloscope screen was constructed and sealed into a plastic container having the shape and size of a hen egg. The force range necessary to crack an average egg was determined by tests and replicated with the instrumented plastic egg. The intensity of the electric signal, pictured as a spike-like image on the oscilloscope, was equated to the impact force necessary to cause egg breakage. The test egg was then run several times through a component of a commercial egg grading and packing line. During each pass through the machine, shock peaks appearing on the oscilloscope screen occurred at identical intervals, validating previous signals and identifying areas of mistreatment by the machine to the egg. Test results indicate that the miniature sensing device will be useful in pinpointing machine design features that cause egg breakage.

BACKGROUND

During 1968, the United States poultry industry produced approximately 5.8 billion dozen hen eggs (1). Various mechanized systems were used to grade and pack most of these eggs and, in the process, a considerable number of eggs were cracked or smashed. Breakage was estimated to range from 3 percent to 10 percent. Assuming that the breakage between the time of gathering the eggs and packaging averaged 5 percent, the loss to the poultry industry amounted to approximately \$34 million during 1968. The \$34 million loss is based on a complete loss of 28 million dozen smashed eggs valued at 30¢ per dozen and 260 million dozen checked eggs decreased in value by 10¢ per dozen. Although an undetermined amount of this loss was caused by poor shell quality, preliminary studies show that much of the breakage was caused by machine handling, regardless of shell condition.

Based on these findings, research was initiated to develop sensing equipment designed to measure the shocks (impact forces of egg-against-egg and egg-against-equipment) to which an egg is subjected during mechanized grading and packing.

MATERIALS AND METHODS

A search of literature on the subject of the telemetry systems found that Deboo and Fryer had developed a small biopotential transmission system (2) and Harrison had developed a triaxial accelerometer and transmitter system (3), which, although too large to fit in an egg-size package, appeared to be similar to the needs of this study. A miniature impact (acceleration) sensing and transmitting device was then developed that could accurately measure shocks to which an egg was subjected as it moved through mechanized egg grading and packing equipment. An acrylic plastic material was machined to simulate the surface shape of a hen egg with a cavity machined inside within which to mount the accelerometer and transmitter system.

During the development phases several methods of assembly were tried. First, the accelerometer was mounted in wax (inside a polyvinylchloride (PVC) egg) (4) and wired directly to an oscilloscope for indication of voltage output from impact. Several initial measurements were made with this type of assembly. The next assembly and packaging arrangement included a reed magnetic switch (single pole, double-throw switch hermetically sealed in glass) to permit turning off the transmitter without disassembly. The wiring arrangement was so designed that the switch, upon reaching the proximity of a permanent magnet, would open the circuit. The switch, although moderately successful, proved to be too expensive and fragile. Next, plaster of Paris was molded inside the egg-shaped package, then a space was hollowed out and the accelerometer glued in place. All of these types of assemblies were discarded because of the difficulty in disassembly for maintenance.

In the final effort, an acrylic rod was machined into the shape of an egg, shown in Fig. 1. The top or large end of the acrylic egg was cut off and threaded for easy removal. The transmitters were mounted (glued) on a 1/16 inch circular piece of sheet acrylic. The accelerometer was glued into the lower cavity with its leads coiled loosely. The removable top permitted ready access to the cavity within for installation of the transmitter, removal of the battery, or adjustment of components. After all of the parts were in place, the cap was screwed on and the instrumented, waterproof, egg-shaped shock sensor package was ready for testing, shown in Fig. 2.



Fig. 1 - Egg-shaped container with threaded cap removed to permit access to miniaturized components



Fig. 2 - Instrumented egg-shaped package next to a normal hen egg (extra large size)

The shock measurement device used in the instrumented egg was a miniaturized single axis accelerometer. The technique selected to measure impulsive shock was a piezoelectric voltage generated when a crystal such as quartz or barium titanate was distorted by application of an external force. The accelerometer contains a crystal and an inert mass mounted on the crystal. Any motion of the accelerometer causes the crystal to oppose the inertia of the mass. Thus, the crystal distorts or bends, producing an electrical signal. The signal can be related directly to the distortion of the crystal and the movement of the container in which it is mounted. The accelerometer, though small, proved extremely sensitive.

TRANSMITTER DESIGN

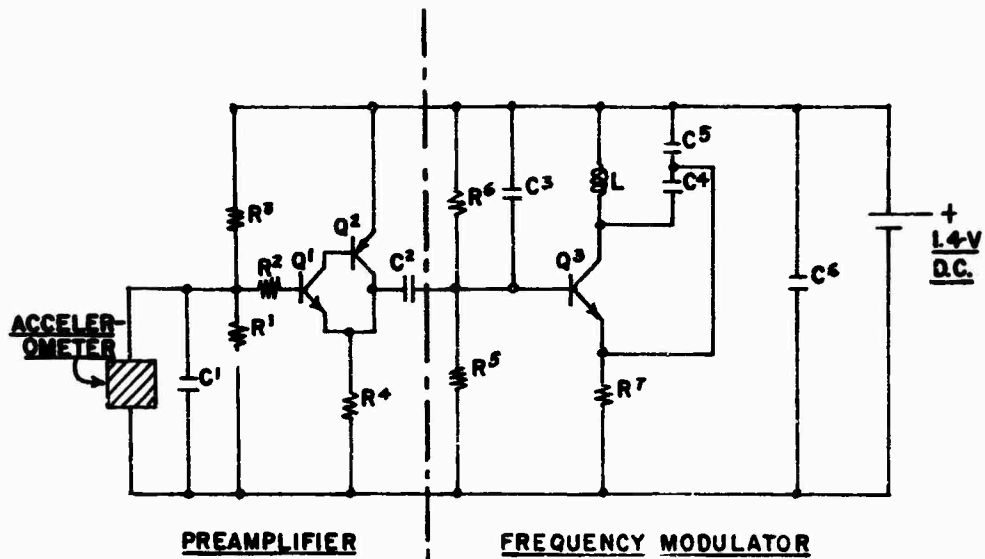
The characteristics of a piezoelectric accelerometer that made the design of a reliable transmitter difficult were the extremely high output impedance and the very low power output. These characteristics made a conventional amplifier circuit useless.

The design of the transmitter was limited by the size of the package enclosing it and by the available power supply. The size limitation in turn limited the number of components that could be used and the power supply (the battery) limited the maximum peak-to-peak input voltage.

The transmitter, shown in Fig. 3, was designed basically as an emitter-follower preamplifier and a voltage-controlled frequency modulator.

The transistors Q1 and Q2 made up the preamplifier and Q3 made up the modulator stage. The power supply was a mercury-cell battery. The source of the signal was the piezoelectric accelerometer, described above, with a sensitivity of 3 millivolts per g (where 1 g is the acceleration of gravity = 32 ft./sec.²). The number and the availability of micro-miniature components allowed the transmitter, including the battery, to be packaged in a plastic matrix 0.5 in. x 0.5 in. x 0.3 in.

The particular arrangement of transistors Q1 and Q2 in the preamplifier was in a super alpha NPN/PNP pair (5) where advantages of high input impedance and power amplification were used.



LEGEND

<u>CAPACITORS</u>	<u>RESISTORS</u>	<u>TRANSISTORS</u>
C1 - 680 pf	R1 - 5.6 M	Q1 - D-26E5GE
C2 - 2.2 μf	R2 - 18 M	Q2 - NSC-6201
C3 - 68 pf	R3 - 4.7 M	Q3 - D-26G1GE
C4 - 10 pf	R4 - 10 K	
C5 - 47 pf	R5 - 5.6 M	L - THREE TURNS
C6 - .068 μf	R6 - 27 K	NO-28 WIRE
	R7 - 390 Ω	

Fig. 3 - Diagram of transmitter circuit

The frequency modulating (FM) stage of transmitter was a Colpitts oscillator tuned to a carrier frequency in the standard FM broadcast band. This carrier frequency was modulated by applying a signal at the base of transistor Q3. The maximum power output of the unit was 5.4 milliwatts under ideal conditions for a transmission distance of 25 to 30 feet.

BREAKAGE TESTS

Upon completing the construction of the instrumented egg-shaped package, drop tests (impulsive shock) were conducted to determine a range of values within which the shell of a normal egg (weighing approximately as much as the instrumented package) would fracture. A pendulum, with a cradle attached to the free end for the support of an egg (or the instrumented package), was suspended in front of a scale graduated in 2° intervals of arc to the left of a vertical line as shown in Fig. 4.

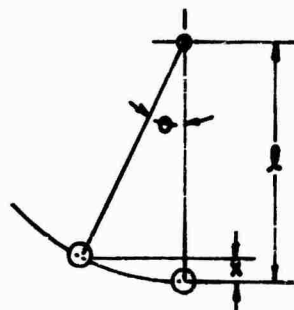


Fig. 4 - Drop test equipment showing egg in pendulum cradle touching impact block (A)

A steel impact block (in Fig. 4) was fixed in place at the point where the shell of a test egg would make contact when reaching the bottom of the pendulum arc. Thus, when an egg was placed in the cradle,

drawn back and released, the angle at which breakage occurred could be determined. Breakage (cracked shell) was determined by the sound produced at impact and confirmed by examination before a candle light. When a clear bell-like sound was noted, the shell was assumed to be unbroken. When the impact resulted in a dull "clack" sound, the egg was assumed to be cracked.

An accurate measurement of the pendulum length, shown in Fig. 5, and angle of drop was used to determine the height of vertical drop.



$$x = l(1 - \cos \theta)$$

Fig. 5 - Relationship of pendulum length (l), angle (θ), and vertical drop (x)

The first part of the test involved the use of eggs (extra large size, grade A) that had been carefully candled to exclude checks and shell abnormalities.

A test of 90 eggs showed that variations in the shell caused eggs to crack at various levels of impact force. The range at which breakage occurred was within a range of 8° (equivalent to a drop of 0.2 inch) and 12° (equivalent to a drop of 0.5 inch).

The second part of the pendulum drop test involved the use of the instrumented egg in lieu of hen eggs. The signal produced by the instrumented egg at time of impact was transmitted to a receiver. The radio frequency of 98 mega-Hertz (MHz) was modulated by the receiver to a wave form which was recorded directly on an oscilloscope screen and photographed, shown in Fig. 6.

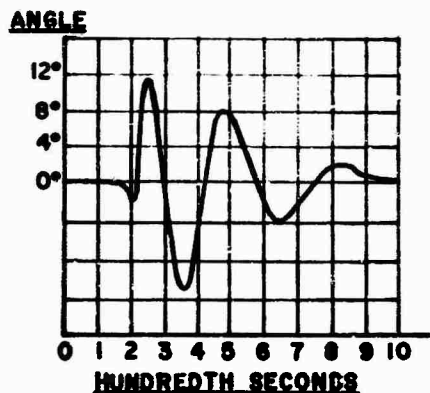


Fig. 6 - Typical shock curve from oscilloscope calibration tests

From the oscilloscope record, the maximum amplitude of the signal was assumed to correspond to the point at which eggs break. However, precise replication of the wave form was difficult, probably because of variations in the point of impact as related to the angle of the accelerometer axis.

A practical application of the test involved the use of a mechanized egg conveyor, as shown in Fig. 7, with a motor driven belt with arms to move the egg over a path which had some drops in it large enough to break an egg.

The machine was started and the instrumented egg placed on the conveyor belt. As the egg was moved along, a sharp spike similar to that shown in Fig. 8 was noted on the oscilloscope screen.



Fig. 7 - Laboratory mechanical egg conveyor

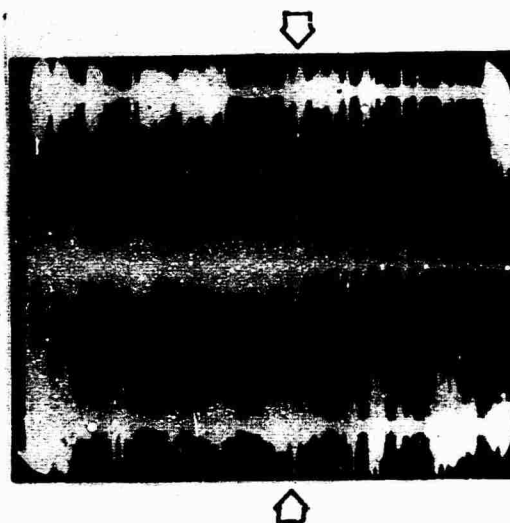


Fig. 8 - Photograph of three oscilloscope traces (recording from the same starting point in the equipment) show replication of critical shock peaks

By observing the position of the egg and when the impact signal was greatest (peak on spike-like images), the critical impact areas were easily detected. Replication showed similar traces with vertical peaks coinciding with locations in equipment where a vertical drop of 1/2 inch occurred.

CONCLUSION

Placing a miniaturized accelerometer and radio transmitter system into an egg-size package to detect breakage-causing situations in mechanized egg handling systems and receiving and recording the shock information (the wave form) on a remote oscilloscope was proven to be feasible. However, there are equipment factors, such as, transmitter design and consistency in signal replication that require further study. It should also be noted that detection was limited to impact-type shock in one direction. Further, this study limited test situations to shock equivalents experienced by an egg striking against nonresilient surfaces at a point on its small diameter. With this impact detecting device, only limited breakage-causing situations can be observed during handling and use of processing equipment. Experimentation with and modification of the test equipment is necessary to detect impact shocks caused by glancing blows, impact shocks involving resilient surfaces, and impact shocks on the long diameter of the shell. Other techniques will have to be developed for detecting breakage caused by compression (crushing) or expansion (through

heating) that also contribute significantly to egg breakage in mechanized egg handling systems.

REFERENCES

- (1) USDA, Agricultural Statistics, pp. 424-425, U.S. Government Printing Office, 1969.
- (2) Deboo, G. J. and Fryer, T. B., "Miniature Biopotential Telemetry System," The American Journal of Medical Electronics, Vol. 4, No. 3, July-September, 1965.
- (3) Harrison, D. R., "FM/AM Telemetry To Measure Impact Accelerations," Ames Research Center, NASA, Moffett Field, California.
- (4) Nanceau, J. R., "Physical Properties and Stress Analysis Of Egg Shell," M.S. thesis, University of California Library, Davis, California, 1968.
- (5) Watson, J., "Semi-Conductor Circuit Design," Van Nostrand, Princeton, N.J., 92098, 1967.

DISCUSSION

Mr. Renius (Army Tank-Automotive Command): Were you able to locate any areas in your machine handling that you were able to improve as a result of this test?

Mr. Shupe: We have not yet. We have not gotten to that point. We have found three particular areas that are problems.

Mr. Renius: You are still working on that?

Mr. Shupe: Most of the problems that we encounter are in the areas where the egg is moved.

Those are the points where they get the most rough handling.

Mr. Luebke (C and O Railroad): Could you use similar techniques to develop vibration and shock data on other food stuff being moved either in trucks or railroad cars?

Mr. Shupe: I would think this technique would be applicable to transportation and handling of any commodities. The problem is the transmission of the signal. I am sure it can be developed if we used integrated components and get parts that are small enough. It would be well within the range of possibility.

AN ACCELEROMETER DESIGN USING FERROFLUID ULTRASONIC INTERFEROMETRY

Jack G. Parks
U. S. Army Tank-Automotive Command
Warren, Michigan

An accelerometer design is described which incorporates the principles of ultrasonic interferometry and ferrofluid dynamics. The chamber of a two transducer ultrasonic interferometer contains two immiscible liquids; one of the liquids being a fluid which responds to a magnetic field gradient (i.e., a ferrofluid). The interferometer is operated at a constant frequency which is slightly different than the resonant frequency caused by reflections from the liquid-liquid interface. Motion of the chamber disturbs the interface and the consequent variation in acoustical path length provides an output signal variation. Damping is accomplished using a magnetic field to modify the motion of the ferrofluid. System variations due to liquid selection, magnetic field intensities, and operating parameters are discussed.

INTRODUCTION

For several years research has been conducted at the U. S. Army Tank-Automotive Command Laboratories on liquids using ultrasonic techniques. In addition to this effort, the application of ferromagnetic fluids to automotive purposes has recently been initiated. These programs have contributed to the design of a sensitive accelerometer which may have engineering applications.

The present paper describes an ultrasonic interferometer which contains a ferrofluid and a secondary immiscible liquid as the intra-transducer medium. The response of the system to mechanical vibration is described as a function of physical parameters and electronic conditions.

ULTRASONIC INTERFEROMETER

The standard ultrasonic interferometer consists of a source of longitudinal sound waves (normally a piezoelectric crystal) mounted at one

end of a fluid column and a flat metallic reflector at the other end. By suitable use of electronic circuits, one may observe the variation of circuit parameters as the standing wave pattern within the chamber is altered. This pattern is created by the interaction of the sound wave produced by the transducer and the wave reflected by the flat plate. Pattern changes can be affected by either moving the reflector along the principle axis of the chamber or by varying the frequency at which the transducer oscillates; in both cases the ratio of path length to wave length in the fluid is changed.

The movable plate, single crystal interferometer was first constructed and analyzed by Pierce [1]. It was used for the determination of velocity and attenuation of sound waves in gases. The application of this device to liquids was accomplished by McMillan and Iagemann [2]. Increased sensitivity, especially in the presence of fluids with large absorption coefficients, can be obtained by replacing the reflecting plate by a second

crystal, identical to the transmitting crystal. Changes are then detected in the circuit associated with the second transducer. The two-crystal interferometer was first analyzed by Fry [3].

FERROFLUIDS

A ferromagnetic fluid (or ferrofluid) is a colloidal suspension of submicron-sized ferrite particles in a carrier fluid such as kerosene, with a dispersing agent added to prevent flocculation. When a magnetic field is applied to such a fluid, a body force is developed within it which is sufficient to change radically its gross behavior without altering its fluid characteristics. It is thus utterly unlike a magnetic clutch fluid, whose particles chain together and solidify under applied fields.

By carefully arranging the conditions under which a ferrofluid is exposed to a magnetic field, such a fluid can have its internal pressure augmented, its velocity increased, or its free surface elevated. These phenomena, and others lead to a variety of novel application, one of which is presented in this paper.

Experience with ordinary colloids teaches that particles that are sufficiently fine can be suspended indefinitely in a liquid even though the particles specific gravity differs greatly from that of the liquid. The mechanism that makes this possible is Brownian motion. Should the particles be magnetic; however, there is an energy of attraction to be overcome if they are not to flocculate and then settle. Although calculations made on colloidal phenomena often suffer from considerable uncertainty, it is none the less worth while to try to sketch a rough picture.

To begin with, the magnetic energy of uniformly magnetized, tangent spheres is proportional to the square of the magnetization and to the cube of the particle radius. Thus, by making the particles very small the magnetic flocculating effect can be reduced. At some size, then, thermal agitation alone should prevent flocculation provided that the magnetic energy is less than the thermal energy kT (where k is

the Boltzmann constant, and T is the absolute temperature). Computation indicates that particles 25-100 angstroms in diameter should be stable on this basis, for the range of magnetic materials available. Calculations of the sedimentation equilibrium for particles of this size show also that even a magnetic force field cannot separate the particles from the fluid. Such a field can, however, create a particle density gradient.

However, we have to face another factor that looms in the realm of particles as small as those in ferrofluids. This is the attractive van der Waals force, whose origin is the attraction of a flocculating electric dipole for a neighboring induced dipole. According to theory, the energy for two distant particles is proportional to the inverse sixth power of distance. For equal-sized spheres, this attractive energy equals the thermal energy kT when the two surfaces are about one sphere radius apart - a result which is valid for any size sphere. As the spheres approach each other closer than this, the attractive energy increases rapidly. Hence, to avoid flocculation, it becomes essential to prevent such close approach of the particles.

It turns out that the necessary separation can be achieved by coating each particle, during its manufacture, with a dispersing agent (such as oleic acid) which provides an elastic sheath around each particle. The size of the typical particle made in this manner is 100 Å and is somewhat less than the dimensions of a single magnetic domain. The dispersing agent can be visualized as a monomolecular layer absorbed on the surface of each particle. When two particles approach each other, compression of the coating (which is about 20 Å in the case of oleic acid) provides an elastic repulsion to oppose the attractive force that would otherwise cause flocculation.

The resulting colloidal mixtures are found to behave, when they flow, like true homogeneous fluids. But they have the extra characteristic of a high susceptibility to magnetic fields. The magnetic force on these fluids originates within the particles whose particle number concentration is on

the order of 10^{17} per cm³. Since these particles are sub-domain in size, each is an individual permanent magnet. Under the influence of a uniform magnetic field, the particles experience a torque and line up with the field. But when there is, in addition, a gradient of the magnetic field, the particles experience a force and attempt to slip through the fluid. This, in turn, transmits drag to the fluid, causing the dispersion to move as a whole.

EXPERIMENTAL DEVICE

A schematic of the bifluid ultrasonic interferometer is shown in Figure 1. In operation a high frequency signal is applied to an ultrasonic transducer (1) that is an integral part of a chamber containing two immiscible fluids. The first fluid (2) is any liquid which is chemically pure, does not react with liquid (3) or the walls of the chamber, and possesses low attenuation for the ultrasonic waves being generated by transducer (1). Liquid (3) is a ferrofluid which is in contact with the top of the chamber. The sound wave generated by transducer (1) propagates through liquids (2) and (3) and is received by transducer (4). The rectified output of this last transducer may be considered as the output signal of the device.

The ferrofluid used in this experiment employed kerosene as a carrier liquid and possessed a measured permeability of 3.59×10^{-6} newtons amp⁻². This value corresponds to a magnetic susceptibility of 1.85. A limited number of liquids were tested for use as a second fluid in the accelerometer and were judged on the basis of compatibility with kerosene and low acoustical attenuation. Liquids acceptable on this basis include distilled water, glycerol, and ethylene glycol.

Sound waves originating from transducer (1) establish standing wave patterns in the chamber that are caused by the interference between the transmitted sound wave and waves reflected from the liquid-liquid interface. This phenomenon requires proper selection of liquid volumes.

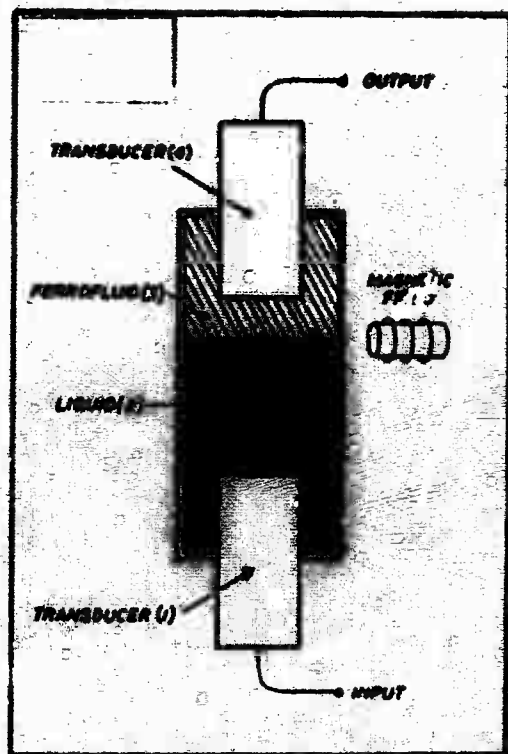


Figure 1
Schematic of Device

The frequency response of the device is a series of peaks or "nodal resonances" (Figure 2). The frequencies where these resonances occur may be determined by the first order expression

$$f_n = nV/2L ; n = \text{integer} \quad (1)$$

where V is the velocity of sound propagation in liquid (2), and L is the distance from transducer (1) to the liquid-liquid interface.

A typical single nodal resonance is shown in Figure 3. When the interferometer is operated at an off-resonance frequency, f_c , ($f_c \neq f_n$) a signal amplitude will be produced at the output of the device which is completely determined by the shape of the associated resonance. The application of an acceleration to the device will distort the liquid-liquid interface and thereby alter the value of L . The

modification of L has the effect of moving the nodal resonance curve along the frequency axis (see dotted curve in Figure 3). The mechanical displacement of the liquid-liquid interface is recorded as a change in the amplitude of the output signal of the device. A source of magnetic field gradient is used to control the damping constant of the device by altering the rigidity of the ferrofluid.

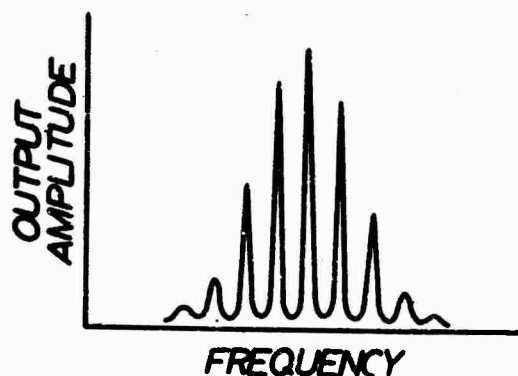


Figure 2
Frequency Spectrum of Device

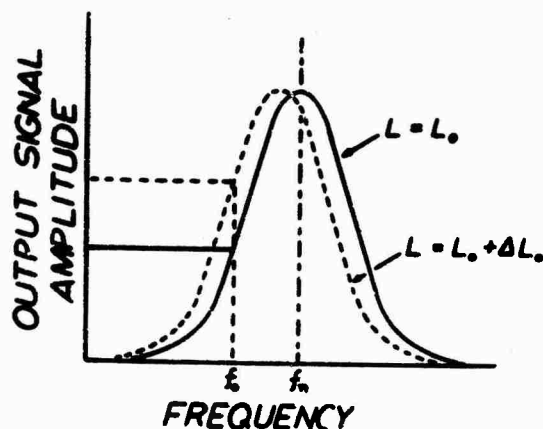


Figure 3
Typical Nodal Resonance

The shape of a typical resonance shows some distortion near resonance and anti-resonance frequencies. However, linear operation between these extremes was demonstrated to be practical for accelerations up to 50g. Irregularities observed in the frequency spectrum are caused by sound reflections from the chamber walls and the receiving transducer and should be

avoided as they distort the linear response of the device. Movement of the nodal resonance due to temperature variations give rise to changes in static output and do not significantly alter the shape of the nodal resonance curve.

Figure 4 is a photograph of a pilot model of the device. The chamber is one inch diameter pyrex tubing. Transducers were encapsulated barium titanate crystals cut for a basic resonance near one megacycle. The black liquid in the upper portion of the chamber is a ferrofluid and the secondary fluid in the lower half is ethylene glycol.



Figure 4
Pilot Model of Device

TEST RESULTS

An electromagnetic shaker system was used to analyze the vibration response of the device. By means of a servomechanism control the shaker was operated at constant acceleration from 10 to 100 Hertz. Piezoelectric accelerometers were mounted to the device for the purposes of calibration. The magnetic field required for damping was a

permanent magnet mounted on the fixture holding the device and positioned near the liquid-liquid interface. Output of the device was rectified, amplified, ac-dc converted and recorded on an X-Y plotter as a function of shaker excitation frequency.

The combination of water and ferrofluid showed a response exemplified by Figure 5.

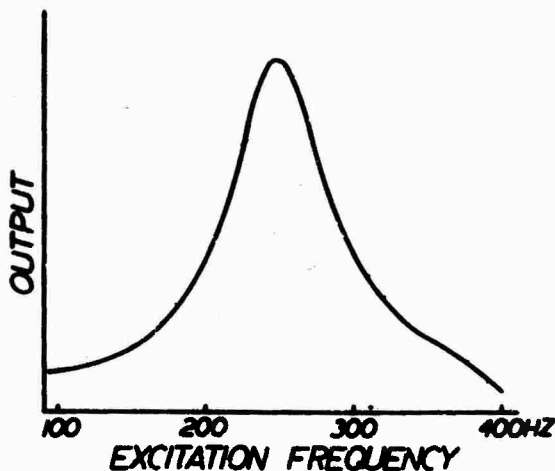


Figure 5
Typical Vibration Response

Table 1 lists the operating parameters used in testing this liquid combination.

The quantity f_c is the operating frequency of the transducers, gain is the slope of nodal resonance at f_c measured in volts per kilohertz, and the entries under the column labeled f_n indicate the order of the nodal resonance (n) and whether f_c is less or greater than f_n .

The remaining values tabulated in Table 1 were based on analysis of a mechanical analog composed of a resistance (R), spring (k) and inertial mass (m), elements arranged in parallel. This model leads to a mechanical impedance of the form.

$$Z^2 = R^2 + \left[m\omega - \frac{k}{\omega} \right]^2 \quad (2)$$

where $\omega/2\pi$ is the excitation frequency. The resonance which results from such a model may be characterized by the following parameters.

$$Q = \sqrt{km}/R \quad (3)$$

$$T = Q/\omega_0 \quad (4)$$

$$R = R_c/2Q \quad (5)$$

where Q is the quality factor of the resonance, T is the relaxation time of the system, $\omega_0/2\pi$ the resonant frequency, and R_c is the value for

TABLE 1 FERROFLUID-WATER TEST RESULTS $f_0 = 250$ Hz						
RUN	f_c (kHz)	GAIN (v/kHz)	B (GAUSS)	f_n	Q	T (MSEC)
1	760.40	0.61	0	< f_8	6.42	4.09
2	767.15	0.86	0	> f_8	5.51	3.51
3	823.19	1.13	0	< f_{10}	5.53	3.52
4	827.22	2.30	0	> f_{10}	4.15	2.64
5	903.91	1.26	0	< f_{12}	4.59	2.92
6	906.65	2.81	0	> f_{12}	2.80	1.78
7	760.79	0.61	43	< f_8	5.40	3.44
8	907.16	2.81	43	> f_{12}	2.35	1.50

critical damping.

The effect of the magnetic field is shown in Table 1 by runs numbered (7) and (8). Some distortion of the nodal resonance was observed when the magnet was positioned next to the device. The operating frequency, f_c , was therefore adjusted to provide the same gain values as observed in entries (1) and (6).

Results for tests conducted using glycerol as the secondary liquid are shown in Table 2.

RUN	f_c (kHz)	B (GAUSS)	Q	T (MSEC)
1	869.44	0	6.05	5.07
2	895.82	0	5.87	4.91
3	963.59	0	5.06	4.24
4	870.23	43	5.08	4.26
5	896.14	43	4.94	4.14
6	964.06	43	4.25	3.56

The lower value of f_0 (natural resonance observed from vibration testing) is primarily due to the greater specific density and lower surface tension of glycerol compared to water.

The use of ethylene glycol as a secondary liquid provides the following test results.

RUN	f_c (kHz)	B (GAUSS)	Q	T (MSEC)
1	804.61	0	8.57	3.59
2	962.12	0	4.48	1.88
3	803.50	43	7.05	2.95
4	961.56	43	3.84	1.61
5	803.16	105	4.52	1.89
6	960.89	105	2.46	1.03

Low frequency resonances were observed for the liquid combinations described above. These resonances were detected from phase angle variations evident during vibration testing and through the application of sinusoidal magnetic fields applied to the interface region. Typical findings are presented in Table 4.

Fluid	f_r (Hz)	Velocity (CM/SEC)
Water	0.75	8.27
Glycerol	1.22	13.20
Ethylene Glycol	0.99	10.90

The presence of these widely separated resonances are a direct consequence of the hydrodynamical theory of superimposed liquids as presented by Milne-Thomson [4]. When surface tension and the thickness of the liquid layers are considered the velocity of wave propagation is given by

$$c^2 = \frac{g(\rho - \rho')}{\rho + \rho'} \left[\frac{\lambda}{2} + \frac{2\pi T}{\lambda g(\rho - \rho')} \right] \frac{2\pi h}{\lambda} \quad (6)$$

where g is the acceleration due to gravity, $\rho(\rho')$ the density of the lower (upper) liquid, λ the wavelength of the disturbance, T the surface tension at the interface, and h is the depth of the liquids (here considered to be equal). At low frequencies and large wavelengths, the first term of equation (6) predominates and the velocity is given by

$$c^2 = \frac{g(\rho - \rho')}{\rho + \rho'} h \quad (7)$$

At higher frequencies, wave motions termed "ripples" predominate and have a velocity

$$c^2 = \left[\frac{2\pi}{\lambda} \right]^2 \frac{Th}{\rho_1 \rho'} \quad (8)$$

It is to be noticed that wavelengths deduced from Table 4 are consistent with those derived from a boundary condition analysis of oscillation modes as given by Lamb [5].

The amplitude of disturbances arising from the low frequency resonances were negligible compared to high frequency displacements. Typical ratios of 100 to 1 were observed for high frequency amplitudes compared to low frequency displacements.

All tests showed a marked dependency between gain, operating frequency (f_c), and Q values. This relationship has its origin in the following analysis; Assume that displacements of the path length, L, are given by the standard relaxation equation

$$\frac{dL}{L} = - \frac{dt}{T_L} \quad (9)$$

where T_L is the relaxation time for the motion of L. Now from equation (1) we have, upon differentiation

$$df_n = - f_n \frac{dL}{L} = + f_n \frac{dt}{T_L} \quad (10)$$

where use has been made of equation (9). If one further assumes that the response of the device is linear with respect to changes in f_n , then

$$dA = - \beta df_n \quad (11)$$

where β is the slope of the nodal resonance at the operating frequency, f_c . Equations (10) and (11) may be combined to yield

$$dA = - \beta f_n \frac{dt}{T_L} \quad (12)$$

The typical response of A for small excursions in terms of a relaxation time, T_A , is given by

$$dA/A_0 = - dt/T_A \quad (13)$$

where A_0 is equilibrium value of A. Coupling equations (12) and (13) gives

$$\beta f_n = \frac{\omega_0}{Q} A_0 T_L \quad (14)$$

where use has been made of equation (4). It is therefore evident from this simple calculation that the product of βf_n is inversely proportional to the observed Q value. The quantities ω_0 , A_0 , and T_L are constants as a result of fixed values of the physical parameters and positioning of f_c .

CONCLUSIONS

The device described in this paper was found to be extremely sensitive to small amplitude displacements of the liquid-liquid interface. The limit of detection of interface displacements for the observed gain values was on the order of fifty microns. This limit was largely independent of liquid selection. It is possible to reduce this limit further by increasing the value of the operating frequency, f_c , and by decreasing the acoustical path length, L; both alterations result in an increase in dA/dL where A is the output signal amplitude of the device.

The principle disadvantage of the present device is the relatively low frequency of the natural resonance. In accelerometer design it is desirable to have a natural frequency at least twice as high as the highest frequency of the accelerations to be recorded [6]. The liquid combinations tested have a useful frequency range of 0 to 190 Hertz. At this value, the device, with damping, has only seismic applications. This situation can be improved to some extent by choosing a liquid combination with high surface tension, such as water and mercury. Further research on this aspect is planned.

The observation of the dependency of measured Q values on the selection of operating conditions (β and f_c) indicate to this author that the inherent Q resulting from the interface motion can be significantly altered by tuning the electronic components associated with the interferometer. This means that the ferrofluid primarily serves to reduce the low frequency

oscillations (near 1 Hz) but that the high frequency resonance can be easily modified by proper selection of liquids, liquid thicknesses and operating frequencies (f_c). The true resonance shape of the interface motion is theoretically observable by examining the device response at f_c values selected for zero gain (i.e. at node or anti-node conditions). Experimental attempts at these frequencies were not conclusive, however, due to the rapid change of β with frequency at these frequencies.

The device may be operated in a manner opposite to that depicted in Figure 1. The transducer in contact with the ferrofluid may serve as the transmitting element or, equivalently, the roles played by the transducers shown may be preserved and a secondary liquid used which has a density less than the density of the ferrofluid (i.e., the ferrofluid is at the bottom of the chamber). The response of the device in these circumstances differs, from the normal configuration, in terms of received amplitude and nodal resonance frequency spacing. However, the basic operation of the device remains unchanged.

Mr. Stein (Arizona State University): You said that the low frequency mechanical resonance was eliminated by the magnetic field. Could that be interpreted as matching the impedance across the interface of the two liquids, and that one might be able to infer the dynamic mechanical impedance of an unknown lower liquid by the magnetic field that was necessary to control this phenomenon?

Mr. Parks: I think that is a correct statement. There were many aspects observed during the experimentation that seemed to indicate that a system such as this could have other applications than as an accelerometer. One thought that occurred to me was that it might be an excellent way to measure the surface tension between two liquids: which is normally a very difficult thing to do. However, there are some aspects of this device that can be used to arrive at that.

Mr. Bort (Naval Research Laboratory): In which direction did you shake this device?

Mr. Parks: It was primarily shaken in a vertical mode. We observed that when the accelerometer was canted at 1 or 5 degrees off the vertical the presence of the magnetic field maintained a level of the interface perpendicular to the axis of the instrument. So it could be used off axis but within certain limitations.

REFERENCES

1. F. W. Pierce, "Piezoelectric Crystal Oscillations Applied to the Precision Measurement of the Velocity of Sound in Air and CO₂ at High Frequencies", American Academy of Arts and Science, Vol 37, 1925
2. D. R. McMillan Jr. and R. T. Lageman, "Application of Ultrasonic Interferometry to the Measurement of Sound Velocities in Liquids", Journal of the Acoustical Society of America, Vol 21, 1947.
3. W. J. Fry, "The Two Crystal-Ultrasonic Interferometer", Journal of the Acoustical Society of America, Vol 21, 1949
4. L. M. Milne-Thomson, Theoretical Hydrodynamics, pp 404-411, The MacMillan Company, New York 1960
5. Sir Horace Lamb, Hydrodynamics, pp 283-290, Dover Publications, New York, 1945
6. J. P. Den Hartog, Mechanical Vibrations, pp 57-62, McGraw-Hill Book Company, New York, 1956

DISCUSSION

Mr. Bert: Is the mechanism of this device the change in shape of the interface because of the change in curvature of your meniscus?

Mr. Parks: Yes, it is actually the movement of the interface which brings about the actual analog output of the device.

Mr. Rymer: In regard to the previous question, that seemed to touch on cross axis sensitivity, the normal off-the-shelf type accelerometers that are used in aircraft testing cross-axis sensitivity can be a problem. If this device were further developed into a practical useable unit for sale, would you expect high values of cross-axis sensitivity, or do you think it could be developed to overcome that problem?

Mr. Parks: We are not in the business of selling this device, however we have examined the transverse sensitivity of the device and we feel that it can be controlled, both by using higher magnetic fields, maybe two or three hundred gauss, and also by changing the diameter of the vessel containing the liquid. We feel that there is quite an influence due to surface tension on the aspects of transverse oscillations. However, we did not have available a shaker that would give us any indication of transverse motion.

HYBRID TECHNIQUES FOR MODAL
SURVEY CONTROL AND DATA APPRAISAL

Robert A. Salyer
TRW Systems, Inc.
Redondo Beach, California

The subject is introduced by briefly reviewing the objectives of a Modal Survey and examining the problems generally encountered during the preparation for and performance of a modal survey. A logical growth path to eliminate these problems has culminated in a Computer-Oriented Modal Control and Appraisal System (COMCAS) which utilizes both analog and digital techniques for reduction of modal response data.

The hybrid techniques employed in COMCAS are discussed. COMCAS provides amplitude control of the total force distribution, frequency slewing to maintain resonance, conditioning and filtering of the control force gages and accelerometers, A/D conversion and multiplexing of control parameters to provide computer intervention if the forcing distribution is disturbed, resolution of response data into vector components that are in- and-out-of-phase with the applied force, A/D conversion and multiplexing of the resolved response data and real-time displays of raw, engineering unit and generalized coordinate data. Orthographic and stereographic plots are generated immediately after all response data have been acquired.

The performance of COMCAS during a recent modal survey is reviewed and the results of the modal survey are discussed. A final upgrading of the system is proposed to utilize sweep techniques in which the computer plays the major role of providing foreground interactive control of excitation, data acquisition and reduction, and data appraisal with mode documentation being performed concurrently on a background basis. Incorporating these features into the present system will result in a "hands-off" capability which will significantly reduce the cost of performing a modal survey.

INTRODUCTION

The dynamic behavior of a structure resulting from transient loading events is an extremely important design consideration, especially for one whose size and design is such that its modal response is significant at or near any transient fundamental frequency. Severe loading will result, for instance, if a first axial mode of a satellite is excited by the boost vehicle staging event; similarly, root structure overstressing can occur on large aircraft during taxi if the first wing bending mode is excited.

During the initial design phase, the dynamic behavior of a structure is predicted by constructing a math model and performing parameter studies. The validity of the results obtained during these studies is, at best, questionable due to the gross assumptions that must be made in order to construct this model. Obviously, this method is the only choice for obtaining characteristic response data until a

structural model is available, at which time a modal survey can be performed to allow an experimental assessment of the analytical results obtained with the math model. Additionally, these experimental results provide a basis for updating the math model so that future analytical studies will yield accurate and valid data.

A modal survey is conducted over a frequency range in which all significant modes reside and in which all notable transient inputs are included. Orbital loads, i.e., those induced by deployment of on-board devices or orbital maneuvers, are not usually considered significant; hence, the modal survey of a satellite is customarily performed to define its behavior due to ascent transients which fall generally between 5 and 50 cps. If the rigid body modes are desired, however, the frequency range of interest will begin at approximately 1 cps.

A typical time history of a payload input transient due to Stage 1 shutdown is shown in

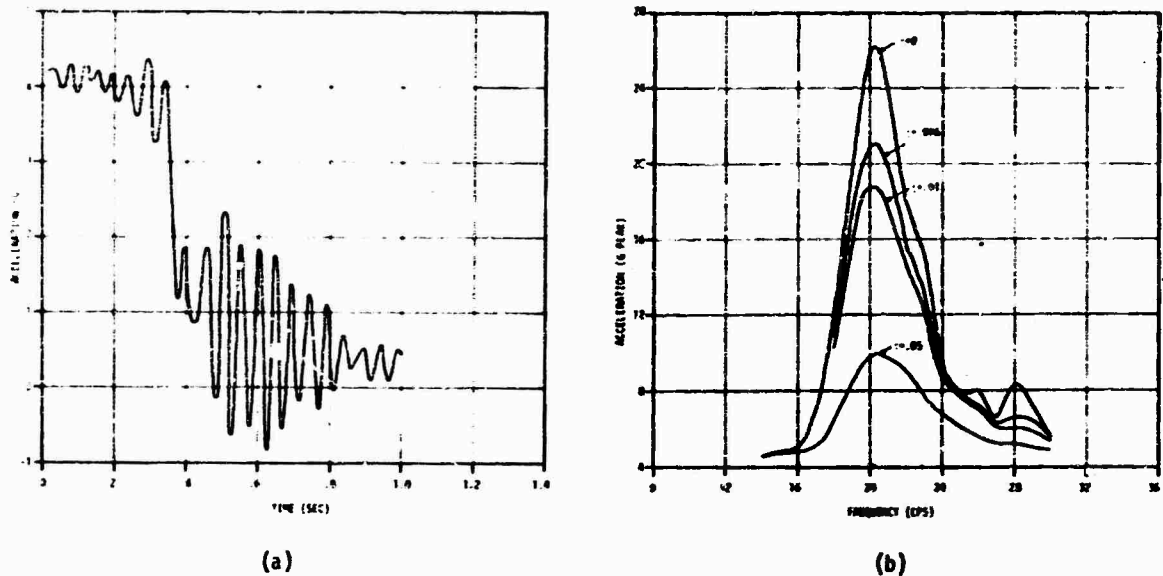


Fig. 1 - Typical Stage 1 Shutdown Transient

Figure 1(a). Figure 1 (b) is a family of shut-down transient response spectra for the cases of structural damping noted on the curves. As can be seen in Figure 1(b), the damping factor should be high to avoid structural damage as a result of transient inputs. This gives rise to an interesting and unavoidable paradox since the theory of modal testing to determine the normal modes of a structure is predicated on zero structural damping; the frequency shift, however, due to the damping is considered insignificant.

Objectives of a typical modal survey of a satellite are to determine the frequency, damping and shape of all modes of the structure configured to meet the desired end conditions, e.g., rigid base, free-free, from 5 to 50 cps which are significant in the determination of ascent loads. The participation of the higher frequency modes is slight compared to those which are closer in frequency to transient fundamental frequencies; consequently, the importance of modes to the loads analysis decreases as the frequency increases.

The usual approach to performing a modal survey is divided into three phases: the pre-survey analysis of the structure, the survey to acquire and record the data and the post-survey data reduction. Generally, the pre-survey analysis is accomplished by a group not involved with the actual survey and after the survey is complete this same group receives the data for appraisal of validity and subsequent use in the loads analysis. Several major problems are eliminated when the performing group participates in the pre-survey analysis. In this manner the intimate knowledge of the structure and its predicted behavior which is required to efficiently perform the survey is acquired,

limitations of the modal facility, e.g., number of exciters or of transducers, can be considered when constructing the mass model or transformation equations and software required for data reduction can be used for pre-survey analysis.

There should be no post-survey appraisal or reduction of data. Too often this is accomplished after the structure has been removed and the setup is disassembled and there is no chance to repeat the survey when serious anomalies are found. Fragmentary or questionable modal survey data is worse than no data at all. Rarely will it correlate exactly with the analytical data above the first bending modes and it must be completely accurate if it is to be used to correct the math model and to perform a loads analysis of the structure. For this reason, the complete appraisal of modal data must be accomplished as data for each mode are acquired. This results in an extremely high confidence factor for all data as soon as data from the last mode is obtained and appraised.

The foregoing considerations have led to the development of a Computer-Oriented Modal Control and Appraisal System (COMCAS) which utilizes both analog and digital techniques to acquire, reduce and document modal survey data on a real-time basis.

A GENERAL MODAL SURVEY OVERVIEW

It is appropriate at this point to briefly discuss the various tasks associated with performing a modal survey. Although the treatment of each task is condensed, it will provide the reader having limited modal survey experience with some understanding of the purpose of each task.

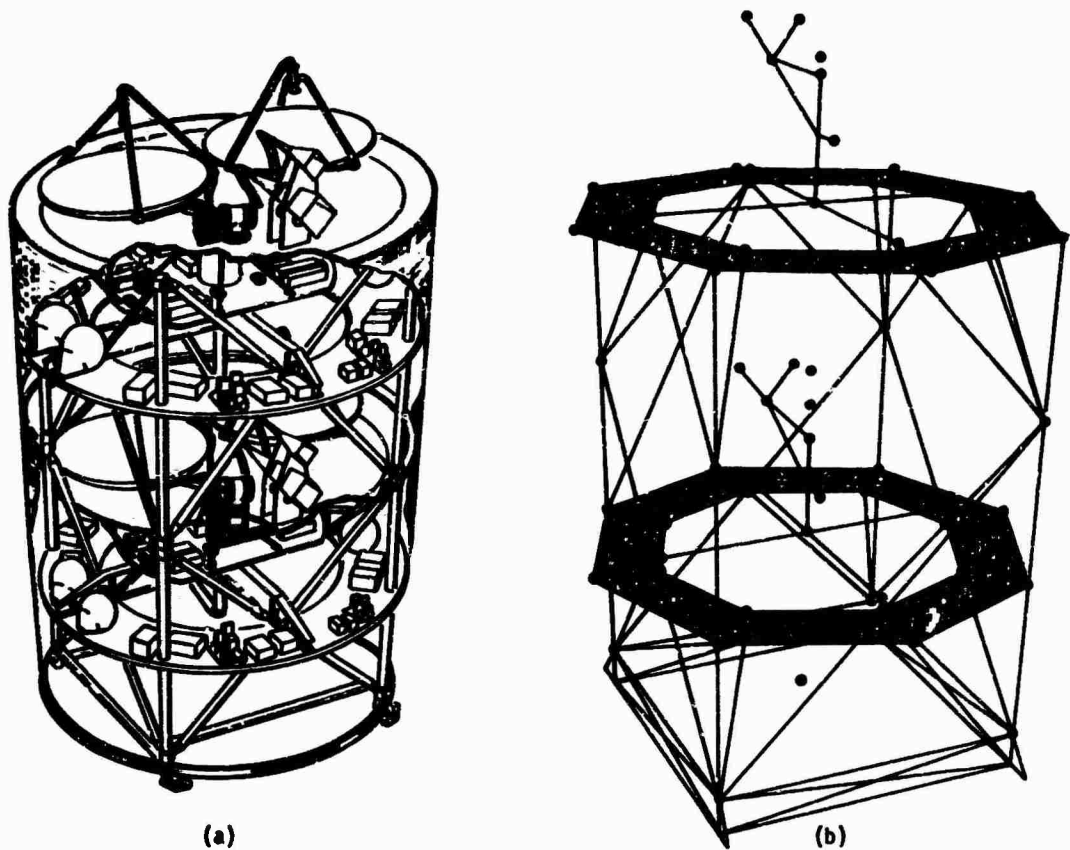


Fig. 2 - Satellite Structure and Mass Model

Pre-survey tasks consist of the preparation of the mass model and the generation of the plots of all modes which are predicted by math model analysis.

Briefly, the steps required in constructing a mass model are: determine properties of all components of the structure; judiciously combine the component masses and assign the lumped masses to appropriate coordinates; determine the mass and inertia values for each lumped mass; and, assign degrees-of-freedom to each mass point. Gross checks of the mass model so constructed are: about each axis the sum of the moments-of-inertia of the individual lumped masses must equal the moment-of-inertia of the total structure and along each axis the sum of the masses associated with each node must equal the mass of the total structure. A typical satellite structure is shown in Figure 2(a) and the mass model of the structure is depicted in Figure 2(b). Each node of the mass model, represented in Figure 2(b) by the darkened circles, has associated with it the degrees-of-freedom required to define its behavior. A sample of the mass model tabular data is given in Table 1, in which the inertial property of each degree-of-freedom is listed. Each node of the mass model in Figure 2(b) is, of course, numbered; these were deleted from the figure for clarity.

Care must be taken in preparing the mass model since errors due to poor techniques in construction can easily overshadow errors attributable to instrumentation. Possible causes for error in constructing a mass model are: important secondary structure may be lumped into nodes containing many other small masses; inaccuracies may exist in the calculated moments, masses and coordinate locations for each node; and the model may contain an insufficient number of degrees-of-freedom to properly describe the behavior of the structure. Use of the mass model in performing orthogonality checks is discussed in the latter part of this section.

Analytical mode plots are generated from data obtained from math model studies of the structure. These plots represent the best data available until the modal survey is performed and are used for analysis until the experimental data is obtained and plotted. Although the analytical plots are not entirely accurate, they generally are correct in representing the gross motion of the structure and are useful in predicting optimum exciter locations for each mode.

Tasks associated with the actual performance of the modal survey are excitation of the structure, acquisition of the response data, analog and digital reduction of the data, listing of data and appraisal of the results.

TABLE 1
Sample Mass Model Tabular Data

Node	Station (Inches)			Inertia Value (LB or LB- IN^2)						Degree-of-Freedom
	X	Y	Z	M _x	M _y	M _z	I _x	I _y	I _z	
59	0	0	60	11.15	10.26	-	-	-	15,000	139,140,141
60	0	0	87.3	11.15	10.26	-	-	-	15,000	142,143,144
61	34.0	34.0	67.8	24.66	13.22	0	-	-	-	145,145,147
62	-34.0	34.0	67.8	15.83	15.83	0	-	-	-	148,149,150
63	-10.5	15.2	38.1	100.00	100.00	100.00	94,700	100,000	100,600	151-156
64	-10.5	15.2	104.85	100.00	100.00	100.00	94,100	98,010	100,600	157-162
65	0	0	0	13.75	13.75	13.75	94,100	98,000	190,000	163-168

Perhaps the most important aspect of modal survey performance is the proper excitation of the structure. Budd's Procedure [1] is generally followed in performing a modal search. The forcing distribution, i.e., the application of in-phase or out-of-phase forces of varying amplitudes, must be such that energy is applied throughout the structure at the proper phase, amplitude and frequency to excite a desired mode. Although various and sundry tuning techniques are available to excite a given mode while another mode is simultaneously being suppressed, these are usually a matter of experience and no attempt will be made to list or explain these here. A prime consideration is that the amount of energy supplied to the structure must be sufficient only to excite the mode; any additional energy will tend to distort the structure and give erroneous results. Co/quad analysis [2], i.e., resolution of acceleration signals into coincident and quadrature vector components which are in- and out-of-phase, respectively, with a reference force signal, of the structural response data is generally the method used to determine if resonance is achieved. The purity of the mode is checked by performing a modal decay. This consists of observing the signals from selected accelerometers and simultaneously removing all excitation from the structure. The lack of beating in the response signals indicates only the mode of interest is excited.

After the mode is deemed acceptable, excitation is reinstated and the data is acquired. Data acquisition and analog reduction consists of conditioning and filtering the acceleration signals and resolving them into coincident (Co) and quadrature (Quad) components.

At this point a myriad of mathematical operations must be performed. The data must be translated from accelerometer coordinates to mass coordinates. The generalized mass and the sum of the mass-phi products, which provide a general definition of the predominant structural

behavior, e.g., torsional about the longitudinal axis, must be computed. Normalized deflections for each mass point are required to perform orthogonality checks between the mode being investigated and all other modes for which data has been acquired. These orthogonality results, along with modal decay data and modal plots, are used to appraise the quality and validity of the acquired data.

Modal plots are generated to completely define the character of the mode. These plots also provide a fast and sure method of assessing the effectiveness of the exciters located about the structure in exciting the mode under investigation.

COMCAS - A HYBRID SYSTEM

COMCAS was conceived as an extension of a previous system which utilized a time-share terminal to process data. As this earlier system was used, it became obvious that the survey was outpacing the data appraisal and mode plotting capability. An evaluation of the system performance [3] indicated that the excitation control and the analog acquisition and reduction subsystems were adequately designed but that the system should include a computer with sophisticated I/O capabilities, supported by a software package capable of real-time performance of all analytical tasks associated with a modal survey.

A simplified block diagram of a typical channel of the excitation control sub-system is shown in Figure 3. This sub-system features amplitude servo control of the total forcing distribution, frequency slewing to maintain resonance conditions, computer cognizance of control parameters to prevent data acquisition if the forcing distribution is perturbed and the display of control parameters and any out-of-tolerance messages on a CRT display unit. The CRT display unit includes a keyboard which is used for assigning limits on the force levels for a given forcing distribution and for

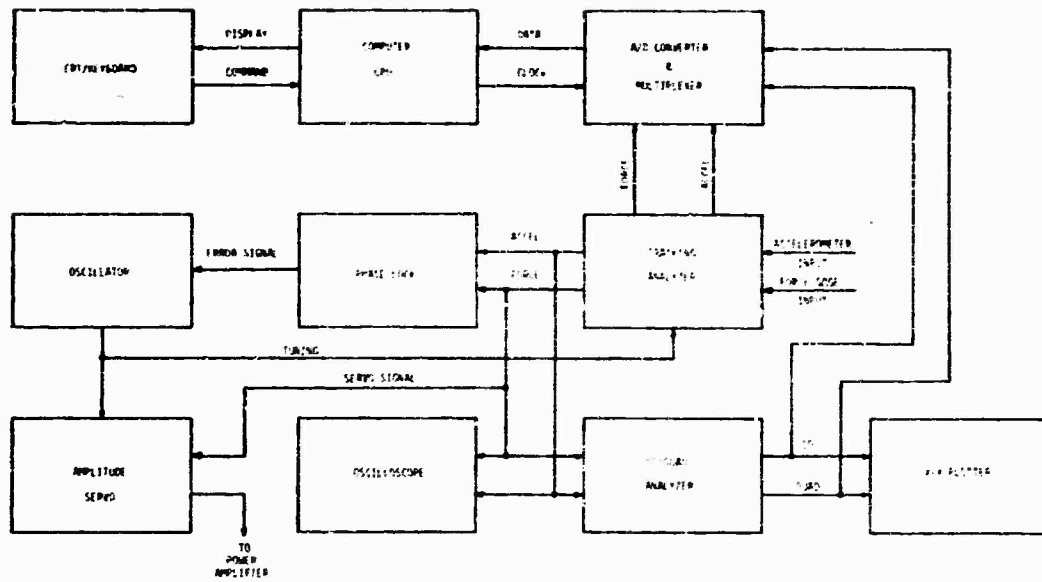


Fig. 3 - Block Diagram of Typical Control Channel

entering bookkeeping data such as date, time, mode number, exciter locations, and so forth, in core memory.

A force gage/accelerometer pair is located at each force input. A selected pair provides signals to each of their associated tracking filters. The filtered signals are applied to the co/quad analyzer which operates on the force and acceleration signals to provide co and quad components of acceleration. Proper tuning of a mode is evidenced by a peaking of the quadrature signal as shown in Figure 4. As can be seen in the co/quad plot, mode 11 is suppressed; the adequacy of suppression is confirmed by performing a modal decay. This consists of observing the unfiltered signals from selected accel-

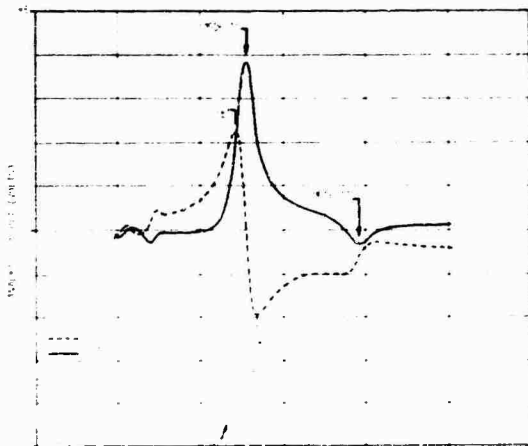


Fig. 4 - Co/Quad Components of Acceleration

erometers as excitation is removed. A clean decay, i.e., no beating, indicates that proper tuning techniques have been employed to effectively eliminate adjacent mode response. Typical decay curves are shown in Figure 5. After the decay curves are obtained and the modal purity seems satisfactory, the excitation is reinstated in preparation for acquiring modal data.

The output of the filters are also fed simultaneously to the phase-lock system, an oscilloscope used to monitor the force/acceleration lissajous pattern and to the A/D converter, which interfaces the control and acquisition console with the computer. If the frequency of resonance should change the phase-lock

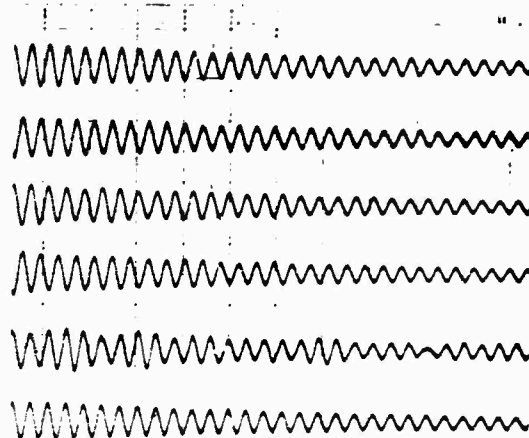


Fig. 5 - Modal Decay Curves

system causes the oscillator to change frequency to maintain a resonance condition. The A/D converter, which includes multiplexing, is programmed to constantly update control parameter data. If, after the forcing distribution is established, any force level exceeds pre-established limits the acquisition of data is terminated, an error message appears on the keyboard and the out-of-limit parameter is continuously scanned until the proper correction is made. These limits may be changed or removed at will by a manual entry on the keyboard.

The data acquisition and analog reduction sub-system resolves the response accelerometer signals into co and quad components and provides this data, along with range data from the various units which operate on the reference force gage and the response accelerometer signals, to the A/D converter and multiplexer. A block diagram of a typical response channel is given in Figure 6. The symbols are defined in Appendix A.

After a given accelerometer signal is selected as an input to the co/quad analyzer, all range switches are optimized and an entry on the CRT keyboard initiates a data scan on the multiplexer. The computer receives the data, stores it in core memory and displays the value read at each data point on a monitor CRT.

Although absolute amplitude is not a property of a normal mode, it is convenient to cancel out the force contribution to the co and quad components, thereby obtaining values in units of acceleration only. In other words, if

the quantities

$$Co = |F| |A| \cos \theta \quad 1)$$

and

$$Quad = |F| |A| \sin \theta \quad 2)$$

were converted from voltage to engineering units, dimensionally they would have units of lbs force-G. In Appendix B, the conversion equations are derived so as to cancel out the force to give

$$Co = |A| \cos \theta \quad 3)$$

and

$$Quad = |A| \sin \theta \quad 4)$$

with dimensional units of G. The equations, derived in Appendix B, used to convert the data from voltage to engineering units and corresponding to equations (3) and (4), respectively, are, using symbols defined in Appendix A,

$$Co = \frac{C_v \times S_a \times Z}{5 \times F_v} \quad B-13)$$

and

$$Quad = \frac{Q_v \times S_a \times Z}{5 \times F_v} \quad B-14)$$

where

$$Z = \frac{1}{10 \exp(A_r/20) \times 10 \exp(G_s/20) \times 10 \exp(A_a/20)}$$

The engineering data are then translated from accelerometer coordinates to mass point coordinates for each degree-of-freedom. This

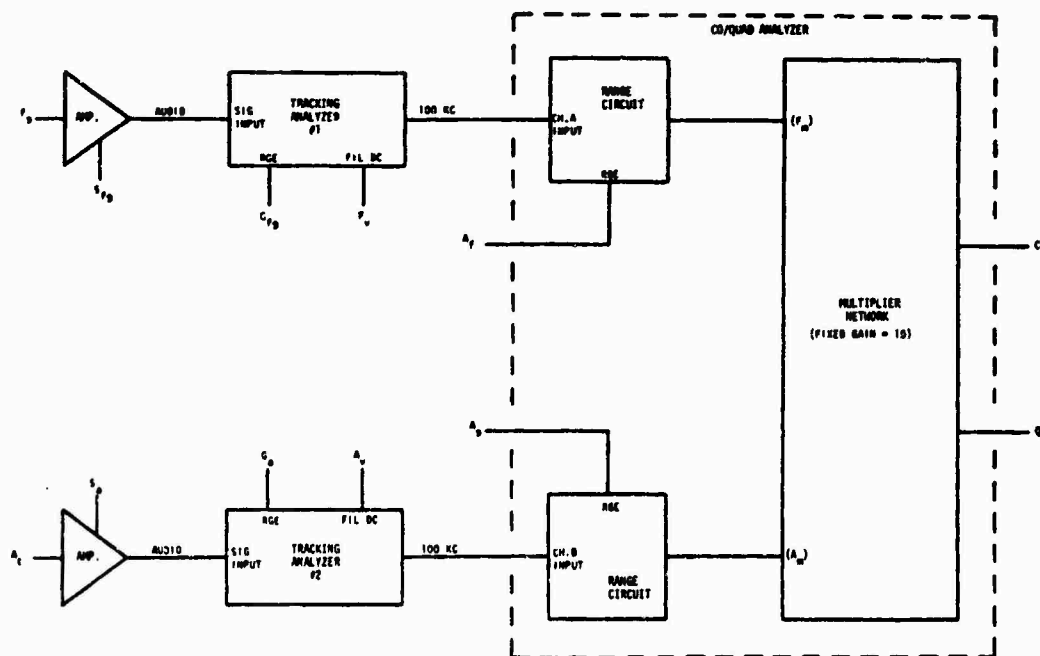


Fig. 6 - Typical Response Channel

technique, which takes advantage of any rigid body motion which the various components may tend to exhibit in given coordinates, eliminates the need for an inordinate number of transducers to adequately define the behavior of the structure.

A brief treatment of a simplified method of computing the orthogonality between modes is given in Appendix C to complement the following discussion. This serves the purpose of limiting any extraneous discussion in the development of the relationships as well as allowing only the useful results to be used here.

The generalized mass, G_r , for the r th measured mode of a system with n degrees of freedom is calculated easily by performing the summation

$$G_r = \sum_{i=1}^n m_i \theta_{i,r}^2 \quad (C-2)$$

where m_i denotes the mass or inertia property of the i th degree-of-freedom of the mass model and θ_i is the acceleration which has been translated to the i th coordinate. Acceleration may be used

here instead of displacement since acceleration is equal to displacement multiplied by a constant, and, as mentioned earlier, amplitude is not a defining property of a normal mode.

The generalized mass is used to normalize the translated accelerations so that the generalized mass of the normalized data is equal to unity. As shown in Appendix C, this allows the determination of orthogonality to be performed in a simple and straightforward manner. The normalized acceleration value, $\theta_{i,r}$, for the i th degree-of-freedom of the r th measured mode is obtained by dividing the translated acceleration value $\theta_{i,r}$ by the root of the r th generalized mass, G_r

$$\theta_{i,r} = \frac{\theta_{i,r}}{(G_r)^{1/2}} \quad (C-10)$$

Utilizing the normalized deflection values, the orthogonality, or mass coupling, $\delta_{r,s}$, is calculated by performing the summation

$$\delta_{r,s} = \sum_{i=1}^n m_i \theta_{i,r} \theta_{i,s} \quad (C-11)$$

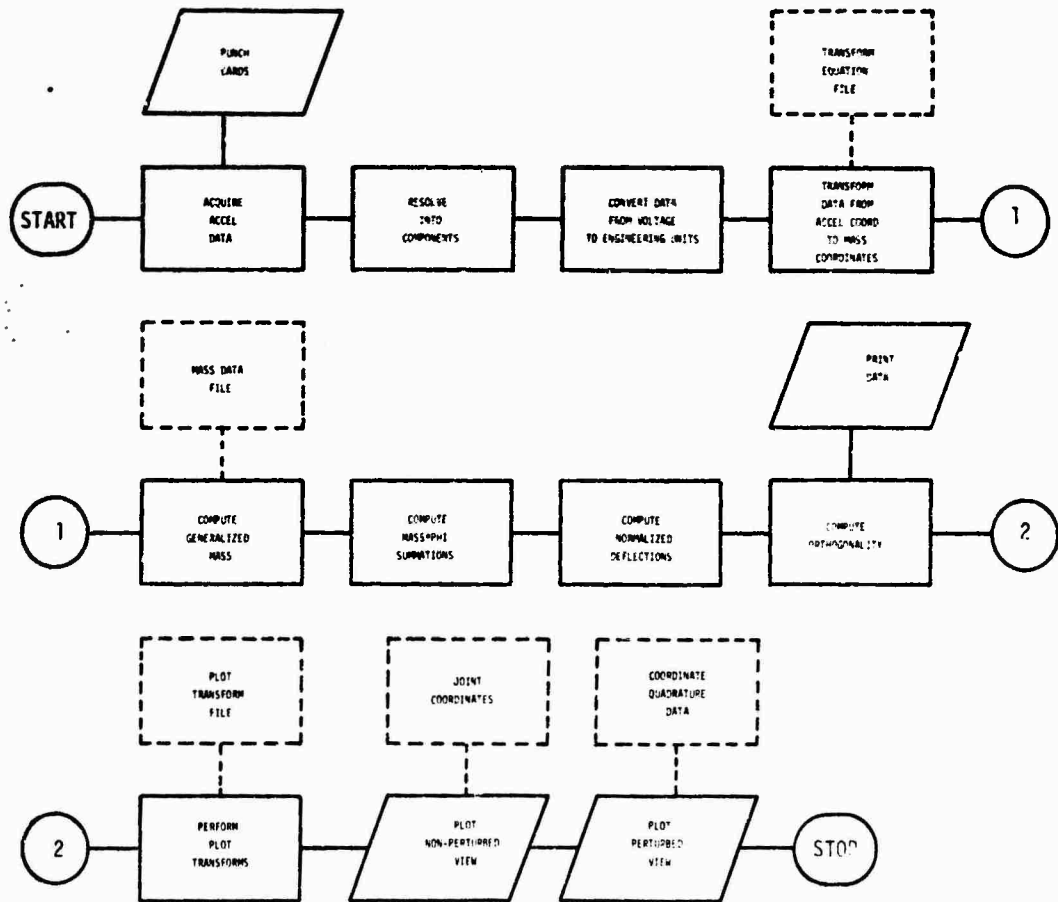


Fig. 7 - COMCAS Software Flowchart

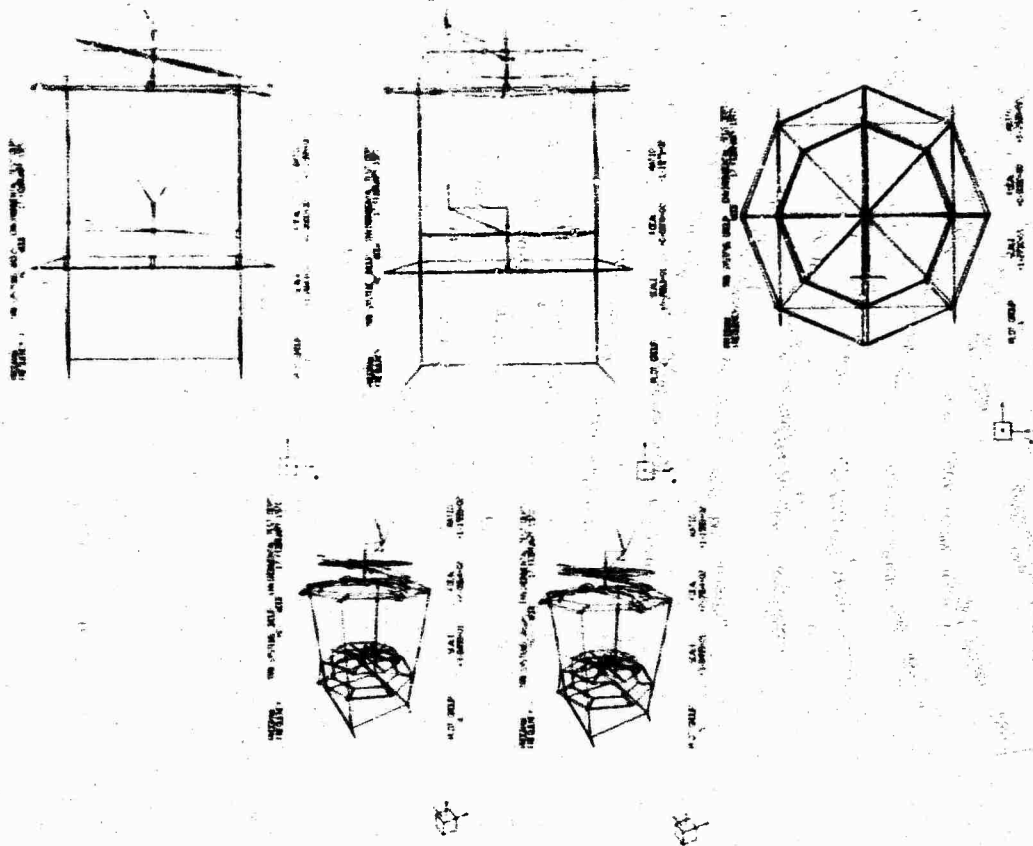


Fig. 8 - Orthographic (Top) and Stereographic (Bottom) Views of a Structure

where n is the number of degrees-of-freedom, m_j denotes the element of the diagonal mass matrix corresponding to the i th degree-of-freedom, and $\theta_{i,j}$ denotes the i th normalized deflection for the j th measured mode.

These calculated generalized coordinate data are listed on a hardcopy printout immediately after data acquisition is complete. A flowchart of these operations is given in Figure 7.

Various methods exist to calculate the damping factor. The most convenient is to determine the frequency points of maximum and minimum coincident response [2]. Looking back to Figure 4, the maximum, ω_b , occurs below resonance and the minimum, ω_a , occurs above resonance. The damping factor, ξ , is a function of the ratio of these frequencies and is given by

$$\xi = \frac{(\omega_a/\omega_b)^2 - 1}{2(\omega_a/\omega_b)^2 + 1} \quad (5)$$

An alternate method [4] is to utilize the relationship based on the logarithmic decrement of the decay curve given as

$$\xi = \frac{1}{2\pi n} \log_e \frac{Y_0}{Y} \quad (6)$$

in which the damping factor is a function of the initial amplitude, Y_0 , and final amplitude, Y , of the peaks of a decay curve, as shown in Figure 5, and n is the number of cycles included within the initial and final amplitude peaks.

As no real advantage is gained by performing these calculations on a computer, since the values must be read from a record, the computations are performed manually.

As soon as the data is reduced and the mode is deemed acceptable, the plotting sequence is initiated. The COMCAS software includes a plot routine which generates three orthographic views and two stereographic views of the structure. Two images appear on each plot: the undeflected structure in black and the perturbed structure in red. Plotting parameters, which are manually entered on the keyboard, are available to allow the structure to be viewed at any angle and at any focal point. Hence, if any key portion of the structure is obscured, the operator need only enter new parameters on the keyboard to

effectively swing the viewpoint around the structure. The plot format is shown in Figure 8 in which the lighter lines, plotted in red on the original plots, indicate the perturbed structure. The stereo plots, when viewed with a stereoscope, provide a three-dimensional view of the structure. This stereo view is very useful when working with higher order modes having complex shapes.

Very often the mass model of a structure is constructed in such a manner that large rigid objects are modeled with a single mass point with multiple degrees-of-freedom. A useful technique in this case is to employ transformations by which the motion at this mass point is projected to synthetic nodes established at the corners, edges or other easily identified points of the object. These synthetic nodes are then also plotted to more clearly define the gross behavior of the object.

APPRAISAL OF SYSTEM PERFORMANCE

A modal survey was recently performed on a large tandem-satellite payload with excellent results. All significant modes met the orthogonality goal of ten percent, which is generally

accepted as a realistic requirement for orthogonality. Minor exceptions to this goal existed in three higher frequency modes. These exceptions were attributed to participation of secondary structure which was not adequately defined in the mass model.

The phase-lock and amplitude servo control systems are very necessary to maintain resonance during data acquisition. Limits imposed on the forcing distribution during dwells was $\pm 5\%$ of the required level and seldom was any readjustment required during the modal dwells.

Co/quad analysis has proved its worth in various tasks. As opposed to the out-dated and extremely inferior technique of observing the total response of each accelerometer to determine resonance, the co/quad technique has proven to be an extremely fast and accurate method of detecting resonance and, in fact, has almost eliminated the need for a large number of exciters to be placed around the structure. Four exciters rated at twenty-five force-lbs have been sufficient to properly excite large and complex structures when the data is resolved into co and quad components before computing generalized coordinate data.



Fig. 9 - Modal Survey Control Room

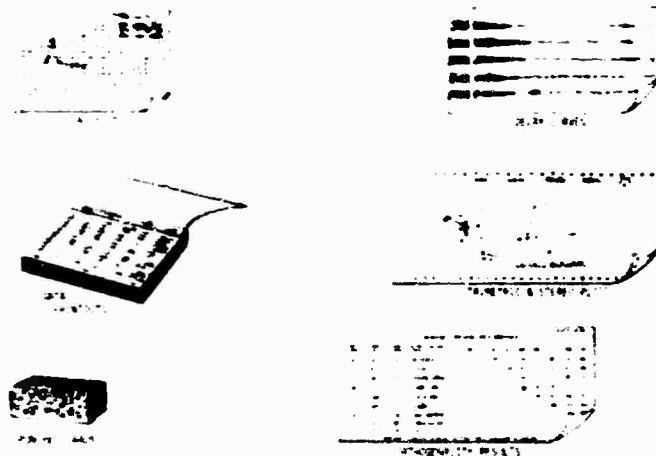


Fig. 10 - Modal Survey Data Package

A real-time data appraisal and documentation capability is a distinct advantage and a necessary safeguard against the jeopardy of tearing down the test setup before poor data can be identified and improved. Modes exhibiting poor orthogonality with previously defined modes were identified immediately after acquisition of response data, the forcing distribution was improved and modal data were again acquired and examined.

Complete visibility of all operations was achieved by locating all consoles and computer I/O devices, with the exception of the line printer, in a control room adjacent to the structure under test. A photo of this control room is included as Figure 9. The CRT/keyboard unit, through which all system activity is directed, can be seen in the foreground. A second CRT/keyboard unit, not shown in the photograph, was available for use by the engineering staff to recall data from previous modes without interfering with system operations.

Immediately after data for the last mode were acquired, a complete package of data was available for loads analysis. This package included raw voltage data, engineering unit data, generalized coordinate data, orthogonality results and modal plots, shown pictorially in Figure 10.

FUTURE SYSTEM UPGRADING

Studies are presently in progress to convert the system to one utilizing sweep-mode techniques. This will allow a modal survey to be accomplished completely in one slow sinusoidal sweep with the computer providing foreground control of the frequency, forcing distribution, data acquisition and purity appraisal. Documentation will be accomplished on a non-interference background basis.

A control technique has been devised [5] which will eliminate the unwanted mass effects of unused exciters. This is important to the overall concept of accomplishing a modal survey in a single sweep since exciters will be required at key locations throughout the structure to allow excitation of all predicted modes. The amplitude and phase of each exciter and the excitation frequency will be controlled by the computer through A/D and D/A interfaces. A conceptual block diagram of the control loop for a single exciter is given in Figure 11. The velocity at a given excitation point is utilized as an indicator of the effect of the exciter for the mode at hand. If it is not assisting in exciting the mode the oscillator input to this channel will be removed; however, the velocity feedback still remains to provide enough energy to the exciter to have it appear to the structure as zero mass. The function of the rest of the system is identical to the present control system. All manual functions, e.g., ranging of the units, selection of inputs, etc., will be eliminated by auto-ranging amplifiers and random-access crossbar switching networks.

The test will proceed by slowly sweeping until the computer determines that a resonance condition is at hand. The resonance will be optimized by varying phase, amplitude and frequency for maximum quadrature peaking of key accelerometers. After data acquisition has been completed, the sweep will resume. Computer foreground activity will continue in search of the next mode while background activity will commence to document the modal data just acquired.

CONCLUSION

The performance of COMCAS during a modal survey of a large complex structure has demonstrated the value of interleaving analog

ACKNOWLEDGEMENTS

The plotting software, an important contribution to the timely completion of COMCAS, was provided through the courtesy of The Aerospace Corporation, El Segundo, California.

The various analytical procedures now performed effortlessly by the computer are a result of a great deal more effort expended by Dick Strom, Chung Hwang and Rich Schlothauer.

APPENDIX A
LIST OF SYMBOLS

Symbol	Definition	Units	Symbol	Definition	Units
F_a	Applied Force	LB	A_m	Acceleration Input to Co/Quad Multiplier Circuit	Volt
A_t	Total Acceleration	G	$m_{i,j}$	Element of Mass Matrix	LB or LB-IN ²
S_{fg}	Sensitivity of Force Amp.	LB/Volt	$[M]$	Mass Matrix	LB or LB-IN ²
G_{fg}	Gain of Force Gage Filter	db	$\delta_{i,r}$	Deflection at Point i of rth Measured Mode	Inch
F_v	Force Level	Volt	$\{A_r\}$	Modal Column of rth Measured Mode	Inch
A_f	Gain of Co/Quad Ch.A	db	G_r	Generalized Mass of rth Measured Mode	LB or LB-IN ²
S_a	Sensitivity of Accel Amp.	G/Volt	$C_{r,s}$	Mass Coupling Between rth and sth Measured Modes	LB or LB-IN ²
G_a	Gain of Accel Filter	db	$\rho_{r,s}$	Magnitude of Mass Coupling Between rth and sth Measured Modes	Scalar
A_v	Acceleration Level	Volt	$\{M\}$	Generalized Mass Matrix For All Measured Modes	LB or LB-IN ²
A_a	Gain of Co/Quad Ch.B	db	$\{ \}$	Modal Matrix Containing Columns For All Measured Modes	Inch
C_v	Coincident Level	Volt ²	$\{M_{r,s}\}$	Generalized Mass Matrix For rth and sth Measured Modes	LB or LB-IN ²
ϕ	Phase Angle Between Applied Force and Total Acceleration	Deg.	$\theta_{i,r}$	Element of Modal Column Normalized to Unity Generalized Mass	$\frac{IN}{(LB-IN^2)^{1/2}}$
Q_v	Quadrature Level	Volt ²	$\{A_r\}$	Modal Column of rth Measured Mode Normalized to Unity Generalized Mass	$\frac{IN}{(LB-IN^2)^{1/2}}$
Co_{fa}	Coincident Component ($5 F_s A_t \cos \phi$)	LB-G			
$Quad_{fa}$	Quadrature Component ($5 F_s A_t \sin \phi$)	LB-G			
Co	Coincident Component ($A_t \cos \phi$)	G			
$Quad$	Quadrature Component ($A_t \sin \phi$)	G			
F_m	Force Input to Co/Quad Multiplier Circuit	Volt			

APPENDIX B

A block diagram of the co/quad analysis system is given in Figure 6. This system operates on signals from a selected reference force gage and the response accelerometers.

Tracking analyzer 1 filters the reference force gage signal and the 100 kc output is applied to the input of Channel A of the co/quad analyzer. Similarly, the 100 kc acceleration signal is applied to Channel B of the co/quad analyzer. After ranging of all units has been optimized, the co or quad output of the co/quad analyzer can be selected as the input to a digital voltmeter to read a voltage which can be converted to the co or quad component of acceleration, with respect to the reference force gage signal, for each selected accelerometer. The filtered D.C. outputs of the force or acceleration tracking analyzers can be selected as the input to the digital voltmeter to read a voltage level which can be converted to the reference force level or accelerometer total response, respectively. Ranges of all units are required to convert the readings from voltage to engineering units.

The co/quad analyzer operates on the force, F , and acceleration, A , signals through phase-shift and filtering networks to give the co and quad components of the acceleration which are defined as

$$Co_{fa} = \frac{FA}{2} \cos \phi \quad B-1)$$

and

$$Quad_{fa} = \frac{FA}{2} \sin \phi, \quad B-2)$$

where ϕ is the phase angle between the applied (reference) force and the total acceleration measured at the selected response accelerometer.

However, the co/quad analyzer also contains a multiplier circuit in which there is a fixed gain of 10, i.e., with force and acceleration inputs having levels and phase angles of

$$\begin{array}{ll} a) F = 0.71 \text{ V rms} & b) F = 0.71 \text{ Vrms} \\ A = 0.71 \text{ V rms} & A = 0.71 \text{ Vrms} \\ \phi = 0^\circ, & \phi = 45^\circ, \end{array}$$

and

$$\begin{array}{l} c) F = 0.71 \text{ Vrms} \\ A = 0.71 \text{ Vrms} \\ \phi = 15^\circ, \end{array}$$

the resulting co and quad outputs are

$$\begin{array}{ll} a) Co = 2.50 \text{ VDC} & b) Co = 1.76 \text{ VDC} \\ Quad = 0 \text{ VDC}, & Quad = 1.76 \text{ VDC}, \end{array}$$

and

$$\begin{array}{l} c) Co = 2.45 \text{ VDC} \\ Quad = 0.66 \text{ VDC}. \end{array}$$

Therefore, the D.C. voltage read at the co and quad output must be divided by 5 to obtain the analog representation of $FA \cos \phi$ and $FA \sin \phi$. In other words, the voltages read at the co and quad outputs actually represent

$$Co_{fa} = 5 FA \cos \phi \quad B-3)$$

and

$$Quad_{fa} = 5 FA \sin \phi, \quad B-4)$$

which will be used in place of equations B-1) and B-2) in the remainder of this discussion.

The force, F_s , imposed on the structure at the reference force gage location is given by

$$F_s = \frac{F_v \times S_{fg}}{10 \text{ Exp}(G_{fg}/20)}, \quad B-5)$$

where F_v is the level of the filtered D.C. output, G_{fg} is the gain of the reference force gage tracking analyzer and S_{fg} is the sensitivity of the force gage amplifier.

The total acceleration, A_t , seen by the selected response accelerometer is given by

$$A_t = \frac{A_v \times S_a}{10 \text{ Exp}(G_a/20)}, \quad B-6)$$

where A_v is the level of the Filtered D.C. output, G_a is the gain of the accelerometer tracking analyzer and S_a is the sensitivity of the accelerometer amplifier.

The voltage read at the Co output which represents $FA \cos \phi$, denoted by C_v , and the voltage read at the quad output which represents $FA \sin \phi$, denoted by Q_v , are given by the following equations, in which F_m and A_m are the force and acceleration inputs to the multiplier circuit and the constant 5 is included to account for the gain of 10:

$$C_v = 5 F_m A_m \cos \phi \quad B-7)$$

$$Q_v = 5 F_m A_m \sin \phi \quad B-8)$$

APPENDIX B
(Continued)

Now, F_m is related to the force applied to the structure, the sensitivity of the force gage amplifier, the gain of the tracking filter and the gain, A_f , of channel A of the co/quad analyzer as

$$F_s = \frac{F_m \times S_{fg}}{10 \text{ Exp}(G_{fg}/20) \times 10 \text{ Exp}(A_f/20)} \quad \text{B-9)}$$

Similarly, the relationship between the total acceleration and A_m , the acceleration input to the multiplier circuit, is given by

$$A_t = \frac{A_m \times S_a}{10 \text{ Exp}(G_a/20) \times 10 \text{ Exp}(A_a/20)} \quad \text{B-10)}$$

where A_a is the gain of channel B of the co/quad analyzer.

Solving equations B-9) and B-10) for F_m and A_m , respectively, and substituting into equation B-7) yields

$$C_v = \frac{5 \times F_s \times A_t \times Y \times \cos \theta}{S_{fg} \times S_a} \quad \text{B-11)}$$

where, for convenience, Y is defined as

$$Y = 10 \text{ Exp}(A_f/20) \times 10 \text{ Exp}(G_{fg}/20) \times 10 \text{ Exp}(G_a/20) \times 10 \text{ Exp}(A_a/20).$$

Likewise, after substitution into equation B-8) the expression for quad is obtained:

$$Q_v = \frac{5 \times F_s \times A_t \times Y \times \sin \theta}{S_{fg} \times S_a} \quad \text{B-12)}$$

Solving equations B-11) and B-12) for $A_t \cos \theta$, denoted by C_o , and $A_t \sin \theta$, denoted by Q_o , and using equation B-5) to eliminate F_s from the expression results in

$$C_o = A_t \cos \theta = \frac{C_v \times S_a \times Z}{5 \times F_v} \quad \text{B-13)}$$

and

$$Q_o = A_t \sin \theta = \frac{Q_v \times S_a \times Z}{5 \times F_v} \quad \text{B-14)}$$

where Z is defined, for convenience, as

$$Z = \frac{1}{10 \text{ Exp}(A_f/20) \times 10 \text{ Exp}(G_a/20) \times 10 \text{ Exp}(A_a/20)}$$

Equations B-13) and B-14) are expressions for the coincident and quadrature components, respectively, of the total acceleration signal, measured at a given response location and applied to Channel B, with respect to a reference force gage signal which is applied to Channel A of the co/quad analyzer.

APPENDIX C

DISCUSSION OF MODAL ORTHOGONALITY

With n mass oriented accelerometers acquiring data from a continuous structure which has been idealized by lumping masses such that n degrees-of-freedom exist, the off-diagonal elements of the corresponding $n \times n$ mass matrix vanish. Should the accelerometers not be located at each coordinate, the same result can be accomplished through the use of transformation equations to translate the measured acceleration from accelerometer coordinates to mass coordinates. Let the diagonal mass matrix be

represented by

$$[M]$$

where the elements

$$m_{i,j} = 0$$

and

$$m_{i,i} = \text{Mass Property of Point } i, \quad i = 1, n.$$

The modal deflections of a measured mode are the elements of a column matrix. This modal column of the n degree-of-freedom system in the rth mode will be represented by

$$\{e_r\},$$

where each element

$$e(i,r) = \text{Deflection at Point } i, i = 1, n.$$

This modal column is also called the rth eigenvector and may be thought of as a vector in n dimension space where each element of the column is a component of the vector in the corresponding coordinate direction. For an n degree-of-freedom system there are n such eigenvectors. Each eigenvector and associated eigenvalue will satisfy the equation of motion for the system in free vibration.

The generalized Mass, G_r , of the system for the rth measured mode is given by

$$G_r = \{e_r\}^T [M] \{e_r\}, \quad (C-1)$$

where the symbol T denotes the transpose of the matrix. An equivalent expression for the above equation is

$$G_r = \sum_{i=1}^n m_i e_{i,r}^2. \quad (C-2)$$

The set of eigenvectors obtained experimentally should be orthogonal in a particular sense, i.e., they should be orthogonal with respect to the mass (or stiffness) weighting matrix. This orthogonality relationship with mass as the weighting matrix, between the rth and sth modes is, in general, expressed as

$$\{e_r\}^T [M] \{e_s\} = 0. \quad (C-3)$$

Mass coupling between the rth and sth mode results in a value other than zero on the right-hand side of Equation C-3) Therefore, the mass coupling, C, between the rth and sth measured modes is defined as

$$C_{r,s} = \{e_r\}^T [M] \{e_s\}, \quad (C-4)$$

or equivalently, by

$$C_{r,s} = \sum_{i=1}^n m_i e_{i,r} e_{i,s} \quad (C-5)$$

The magnitude of mass coupling, $\delta_{r,s}$, between the rth and sth measured modes can be assessed by comparison with the rth and sth generalized masses:

$$\delta_{r,s} = \frac{C_{r,s}}{(G_r \times G_s)^{1/2}} \quad (C-6)$$

The generalized mass matrix will be denoted by the symbol

$$[M]$$

and is defined as

$$[M] = \{e\}^T [M] \{e\}, \quad (C-7)$$

where the lack of a subscript in the modal matrices signifies that the complete set of eigenvectors is included. The generalized mass matrix will contain as the diagonal elements the generalized mass for each mode with off-diagonal elements containing the mass coupling terms.

It is convenient at this point to investigate the result of computing the generalized mass matrix for the rth and sth measured modes. Consider a system having six degrees-of-freedom:

$$\{M_{r,s}\} = \begin{pmatrix} e_{1,r} & e_{1,s} \\ e_{2,r} & e_{2,s} \\ e_{3,r} & e_{3,s} \\ e_{4,r} & e_{4,s} \\ e_{5,r} & e_{5,s} \\ e_{6,r} & e_{6,s} \end{pmatrix}^T \begin{bmatrix} M_1 & 0 & 0 & 0 & 0 & 0 \\ 0 & M_2 & 0 & 0 & 0 & 0 \\ 0 & 0 & M_3 & 0 & 0 & 0 \\ 0 & 0 & 0 & M_4 & 0 & 0 \\ 0 & 0 & 0 & 0 & M_5 & 0 \\ 0 & 0 & 0 & 0 & 0 & M_6 \end{bmatrix} \begin{pmatrix} e_{1,r} & e_{1,s} \\ e_{2,r} & e_{2,s} \\ e_{3,r} & e_{3,s} \\ e_{4,r} & e_{4,s} \\ e_{5,r} & e_{5,s} \\ e_{6,r} & e_{6,s} \end{pmatrix}$$

$$\{M_{r,s}\} = \begin{pmatrix} 1,r & 2,r & 3,r & 4,r & 5,r & 6,r \\ 1,s & 2,s & 3,s & 4,s & 5,s & 6,s \end{pmatrix} \quad \begin{bmatrix} M_1 & 0 & 0 & 0 & 0 & 0 \\ 0 & M_2 & 0 & 0 & 0 & 0 \\ 0 & 0 & M_3 & 0 & 0 & 0 \\ 0 & 0 & 0 & M_4 & 0 & 0 \\ 0 & 0 & 0 & 0 & M_5 & 0 \\ 0 & 0 & 0 & 0 & 0 & M_6 \end{bmatrix} \quad \begin{pmatrix} a_{1,r} & a_{1,s} \\ a_{2,r} & a_{2,s} \\ a_{3,r} & a_{3,s} \\ a_{4,r} & a_{4,s} \\ a_{5,r} & a_{5,s} \\ a_{6,r} & a_{6,s} \end{pmatrix}$$

$$\{M_{r,s}\} = \begin{pmatrix} (-1,r M_1) & (-2,r M_2) & (-3,r M_3) & (-4,r M_4) & (-5,r M_5) & (-6,r M_6) \\ (-1,s M_1) & (-2,s M_2) & (-3,s M_3) & (-4,s M_4) & (-5,s M_5) & (-6,s M_6) \end{pmatrix} \quad \begin{pmatrix} a_{1,r} & a_{1,s} \\ a_{2,r} & a_{2,s} \\ a_{3,r} & a_{3,s} \\ a_{4,r} & a_{4,s} \\ a_{5,r} & a_{5,s} \\ a_{6,r} & a_{6,s} \end{pmatrix}$$

$$\{M_{r,s}\} = \begin{pmatrix} \left(\begin{array}{l} (-1,r)^2 M_1 + (-2,r)^2 M_2 + (-3,r)^2 M_3 \\ + (-4,r)^2 M_4 + (-5,r)^2 M_5 + (-6,r)^2 M_6 \end{array} \right) & \left(\begin{array}{l} a_{1,r} M_1 a_{1,s} + a_{2,r} M_2 a_{2,s} + a_{3,r} M_3 a_{3,s} \\ + a_{4,r} M_4 a_{4,s} + a_{5,r} M_5 a_{5,s} + a_{6,r} M_6 a_{6,s} \end{array} \right) \\ \left(\begin{array}{l} -1,s M_1 -1,r + -2,s M_2 -2,r + -3,s M_3 -3,r \\ -4,s M_4 -4,r + -5,s M_5 -5,r + -6,s M_6 -6,r \end{array} \right) & \left(\begin{array}{l} (-1,s)^2 M_1 + (-2,s)^2 M_2 + (-3,s)^2 M_3 \\ + (-4,s)^2 M_4 + (-5,s)^2 M_5 + (-6,s)^2 M_6 \end{array} \right) \end{pmatrix} \quad \text{C-8) }$$

APPENDIX C
(Continued)

An inspection of C-8) will disclose the presence of the result of Equation C-1) for the rth and sth modes in positions 1,1 and 2,2 respectively, of the diagonal and the result of Equation C-4) in both off-diagonal elements. Hence, the generalized matrix may be characterized by

$$\{M_{r,s}\} = \begin{Bmatrix} G_r & C_{r,s} \\ C_{r,s} & G_s \end{Bmatrix} \quad \text{C-9)}$$

and the non-dimensional magnitude of mass coupling is found by comparing the off-diagonal element with the root of the product of the diagonal elements,

$$\delta_{r,s} = \frac{C_{r,s}}{(G_r \times G_s)^{1/2}},$$

which is identical to Equation C-6).

It is desirable to normalize the elements of each modal column to unity generalized mass for the particular measured mode. This is possible since amplitude is not a property of normal modes. Denoting the normalized modal column of the rth measured mode as $\{\theta_r\}$, each element is obtained by dividing by the root of the rth generalized mass:

$$\theta_{i,r} = \frac{G_{i,r}}{(G_r)^{1/2}} \quad \text{C-10)}$$

In so doing, the denominator of equation C-6) becomes unity and $\delta_{r,s}$ may be calculated simply by performing the summation

$$\delta_{r,s} = \sum_{i=1}^n m_i \theta_{i,r} \theta_{i,s} \quad \text{C-11)}$$

The result of equation C-11) multiplied by 100 gives the mass coupling, or orthogonality, between the rth and sth measured modes in percent.

The futility of attempting to obtain absolutely orthogonal modes, i.e., with zero mass coupling, can be realized by noting the causes of error. The distributed mass of the structure is discretized to form a mass model of the structure. The transformation equations include terms to determine the displacements of the center of gravity and rotations about the principal axes of inertia of each mass element from components of acceleration measured at various locations. The accuracy of the determined mass coupling, or orthogonality, depends on the accuracy of the theoretical mass model, transformation equations and the experimental data.

Caution must be exercised when using orthogonality results to appraise the validity of modal data. Two modes can be orthogonal in the mathematical sense simply because they are physically orthogonal. One, or both, of these modes can be non-normal to the remaining modes of a set even though at first glance they appear to meet orthogonality conditions when considered as a pair without regard to the other normal modes. Orthogonality, then, is a necessary but not sufficient condition that the mode under consideration is a normal mode of the structure.

DISCUSSION

Mr. Gayman (Jet Propulsion Laboratory): As a result of experience with this system and with the overall data processing, have you determined any criteria for judging when an orthogonality check is good or bad or indifferent?

Mr. Salyer: That point is probably open to a lot of interpretation, but our orthogonality goal is ten percent and we have been very successful in meeting that goal. While we have exceeded that goal with some of the higher order modes we have been able to rationalize that out because they are so far displaced from the phenomena which we feel to be important. The participation of these modes is so low compared to the lower frequency modes that we really put most of our time in the lower order modes. The ten percent goal is essentially met.

Mr. Trubert (Jet Propulsion Laboratory): What advantage do you have using the co-quad against phase measurement and amplitude measurement? They are equivalent.

Mr. Salyer: They are equivalent. I feel that our system yields results much quicker. Of course, digital techniques can be employed but it takes considerably longer. One of our requirements is to obtain the results immediately without any transition from tape data or play back through a computer to obtain components of the total acceleration.

Mr. Trubert: What I mean is that instead of using a co-quad you can use a phasemeter and an amplitude meter and get the same answer. We have been doing that at JPL and it works quite well.

Mr. Salyer: I see, you have been using total acceleration and you try to get all of your points either zero or 180 degrees out of phase?

Mr. Trubert: We actually measure the phase.

Mr. Salyer: So you try to get all your points either in or out of phase?

Mr. Salyer: As I explained on one of the slides, the total response obscures the quadrature data.

Mr. Trubert: No, but we do not use the peak to tune; we use the phase to tune.

Mr. Salyer: Well, we have used both.

Mr. Trubert: Instead of measuring x and y you measure the modulus and the phase angle?

Mr. Salyer: I understand what you are saying now. We used that technique at the beginning. The system that we have now is about a third generation system. The technique that you describe is difficult because of the number of Lissajous patterns that you have to look at.

Mr. Trubert: I wonder why you would need a co-quad analyzer when you can do the job with an amplitude and phase meter? If one method has a real advantage over the other I would like to know that.

Mr. Salyer: If you are using amplitude and phase, are you using the phase to convert your total acceleration amplitude into co- and quad- components?

Mr. Trubert: Yes, the computer does that.

Mr. Salyer: The computer does that in real time?

Mr. Trubert: No, not real time, but you do not need that. You measure the amplitude and the phase and then you tune on the phase only. That is the way you tune your mode. I think you are tuning an quad-, are you not?

Mr. Salyer: Yes, we tune on quad-. We use force and acceleration.

Mr. Trubert: That is the same thing, I think.

Mr. Salyer: No. Not unless you go through some mathematical computations and unless those mathematical computations are performed in real time so that it gives a comparable quality of data.

Mr. Trubert: Well, you do not really need the value of your co- or your quad-, you just need a zero angle, then you are tuned.

Mr. Cronkhite (Bell Helicopter Co.): Do you use normal mode data in dynamic response analysis?

Mr. Salyer: The quadrature data is used.

Mr. Cronkhite: How do you obtain the generalized masses?

Mr. Salyer: The generalized mass is an intermediate step in computing the orthogonality.

Mr. Cronkhite: What mass matrix did you use?

Mr. Salyer: It was a mass matrix system that was derived from the actual inertial properties of the structure under test.

Mr. Cronkhite: So you developed a mass matrix for your actual structure?

Mr. Salyer: Yes.

Mr. Cronkhite: Did you use a lumped mass matrix or a consistent mass matrix?

Mr. Salyer: We used a diagonal mass matrix without any off diagonal terms.

Mr. Cronkhite: How does this work in dynamic response analysis? Do you find this adequate?

Mr. Salyer: It worked very well. I think it is the best approach.

OBJECTIVE CRITERIA FOR COMPARISON OF RANDOM VIBRATION ENVIRONMENTS

F. F. Kazmierczak
Lockheed Missiles & Space Company
Sunnyvale, California

Analysis of random vibration requires an objective means of accounting for time and amplitude. Use of the peak exceedence curve, the expected number of cycles to exceed some peak amplitude, provides a technique for including both parameters in measuring the damage potential of environments. The procedure is based on the Rayleigh Distribution of peak amplitudes in narrow bands and provides a simple method for comparing random vibration environments. An extension of this technique, utilizing Miner's Rule, provides a procedure for more accurately measuring the potential fatigue damage. Two detailed examples of how this general methodology is applied are presented.

INTRODUCTION

Equipment for missiles and space vehicles must undergo numerous random vibration environments, both on the ground prior to flight as well as during the actual flight. In order to verify the flight worthiness of equipment, qualification testing is usually performed on mechanical shakers using a test spectrum which is more severe than the total flight item exposure. In order to evaluate this qualification test spectrum, it must be compared to several environments each of which has a different spectrum shape and time duration. The most expedient procedure is to set the qualification test level so that it envelopes all of the environments and to assure that the test time exceeds the total exposure time expected for flight hardware. However, because of the differences in time and amplitude between the various environments this approach is overly conservative and results in testing components at levels which may produce unnecessary failures during testing, thereby increasing the program cost. Therefore, a procedure which incorporates the combined effect of time and amplitude is desirable.

One method for achieving this goal is referred to as the technique of peak counting. This method assumes that the accumulation of peaks as a function of peak amplitude is a realistic measure of the severity of the environment under consideration. The underlying assumption made in the development of the peak count approach is that the vibration signals being analyzed can be described as an ergodic signal, whose instantaneous amplitude is normally (Gaussian) distributed. In practice it is necessary to retain the frequency information obtained from the acceleration spectral density (PSD), and therefore it is also assumed that a broadband random signal whose PSD amplitude varies with frequency can

be treated on a narrow band basis. These assumptions lead to a Rayleigh Distribution for the peaks.

The Rayleigh Distribution is used to derive a peak exceedence curve, which is the number of peaks expected to exceed some amplitude as a function of that amplitude. The peak exceedence curve is used as the common measure to compare the severity or damage potential of different random vibration environments. Two typical examples of how this peak count analysis is applied is given in the discussion that follows.

BASIC ASSUMPTIONS

The assumption that a broadband excitation can be broken down into a series of narrow band signals and each narrow band analyzed individually is considered justifiable since the peak count analysis is used only for comparison between various environments. This analysis is accomplished by comparing each narrow band on a one to one basis using arithmetic operations, i. e., the summing or subtraction of peak exceedence curves in each frequency band as a means of finding the relative severity of different environments. In this context, the analysis requires that all of the narrow bands exhibit the same relative severity before it is assumed that the broadband signals being compared have the same relation. Thus any errors which may be introduced by performing the analysis in narrow bands are consistent for all environments and will have a small effect on the end results.

The size of the bandwidths were chosen by considering the response of a single degree of freedom system. Since the bandwidth of the response of an oscillator can be expressed as a percentage of the center frequency, or equivalently a power scale, an

octave type scale should be used for the peak count analysis. A one-third octave scale is suggested to be consistent with acoustic test data.

In addition to performing the analysis in narrow bands it is also necessary to assume normally distributed signals in order to derive a Rayleigh Distribution for the peaks. Experience with mechanical shakers and reverberant chambers has indicated the validity of this assumption for these environments. Although the normality of flight data has not been directly verified, the outgrowth of this assumption, (i.e., Rayleigh Distribution of peaks) has been examined. Shown in Fig. 1 is a comparison of flight data to a fitted Rayleigh Distribution. Some scattering of data is noted at the high sigma values for the liftoff environment, and this is probably due to the highly non-stationary nature of this event. Although the transonic environment is also non-stationary it varies slowly enough with time so that the peaks do fit a Rayleigh Distribution for the short time interval examined. Since the liftoff environment is a short time duration event for most space vehicles the amount of error introduced by assuming a stationary signal is negligible.

Additional assumptions which are necessary in the application of the peak count technique are consistent with engineering practice. For example it is necessary to assume that shaker testing simulates the input seen on the vehicle, and that the dynamic response of a structure is linearly related to the acoustic field excitation. This acoustic test data may be appropriately scaled.

DERIVATION OF PEAK EXCEEDENCE CURVE

As a result of assuming a normal ergodic process in the narrow bands, it can be shown [1] that the probability density function for peak amplitudes (G 's zero to peak for random vibration) is a Rayleigh Distribution of the form

$$P(G) = G/2 \exp \left[-1/2 (G/\sigma)^2 \right] \quad G \geq 0 \quad (1)$$

$$P(G) = 0 \quad \text{elsewhere}$$

where

$P(G)$ = Rayleigh probability density function

G = peak acceleration amplitude

σ = Grms of random signal in narrow frequency band of interest

The integral of this density function is the cumulative distribution function which when subtracted from unity yields the probability of exceedence. Multiplying the exceedence function by the total number of cycles yields the expected number of peaks which exceed a given amplitude, or the desired peak exceedence curve. The result is

$$N(G) = ft \exp \left[-1/2 (G/\sigma)^2 \right] \quad G \geq 0 \quad (2)$$

where

$N(G)$ = expected number of peaks to exceed amplitude G

f = center frequency of narrow band

t = time duration of signal in seconds

Actually this result predicts the number of cycles, with two peaks occurring per cycle, which is consistent with definitions used for fatigue data.

Although the above result is true only for stationary signals it can also be used to describe the environment even if the Grms level changes with time, as has been demonstrated in Fig. 1. In this case the Grms time history is treated as a step function with a constant Grms for each short time interval. Summing the peak exceedence curves for each time interval yields

$$N(G) = \sum_i t_i \exp \left[-\frac{1}{2} (G/k_i \sigma)^2 \right] \quad (3)$$

where

t_i = duration of time interval, seconds

k_i = rolloff curve expressed as a fraction of the maximum Grms level

In this manner the time varying flight conditions can be more accurately treated.

This peak exceedence curve represents the basic measure which can be used for comparing the relative severity of different environments. The real value in analyzing random vibration by using the peak count method is that the combined effect of different environments can be easily obtained by simply summing the peak exceedence curves for all events of interest, resulting in one curve that represents the total cumulative damage potential for all the environments.

Two typical applications which used this analytical procedure were (1) the derivation of an acoustic spectrum to be used for system level acceptance tests, and (2) the comparison of equipment qualification test spectra to predicted flight environments.

EXAMPLE 1 DERIVATION OF ACOUSTIC TEST SPECTRUM

Objective and Approach

In this application an equipment section was to be acceptance tested by subjecting the entire section to acoustic excitation in a reverberant chamber. Since all the components had already been tested and qualified for flight it was necessary to assure that the acoustic test spectrum to be derived would not result in equipment being exposed to levels which would exceed their proven capability.

The overall approach used to achieve this objective was to analytically solve for the margin available for acoustic testing in each frequency band for each piece of equipment, and to use this margin in deriving the acoustic test spectrum. This margin was expressed as the number of peaks available versus G level and was obtained by subtracting the cumulative exposure (sum of the peak exceedence

curves for all flight environments) from the demonstrated capability (peak exceedance curve for qualification tests). Acoustic testing of a development prototype section had previously been performed and provided the basic random vibration data needed for predicting equipment flight and test environments. An example of this procedure is shown in Fig. 2 which shows the cumulative exposure and the demonstrated capability curves for one of the pieces of equipment for the 315 Hz 1/3 rd octave band. The resulting available life curve shown in Fig. 3 represents the amount of peak exceedances that could be expended during acoustic testing.

Figure 3 graphically indicates one of the difficulties encountered during the analysis. It shows that the available life curve is negative at low G levels, indicating that the piece of equipment did not have any additional capability. This negative region results because the flight environment was a low amplitude relatively long duration environment whereas the qualification test was a high amplitude short duration test. Since a large number of cycles at very low G levels does not substantially contribute to the cumulative damage of box components it was necessary to establish a logical lower bound on the G level. Cycles with amplitudes below this level would not be of interest for the analysis.

ESTABLISHMENT OF UPPER AND LOWER BOUNDS

An examination of the fatigue characteristics of various materials was made to determine if a logical approach could be developed for establishing this lower bound. It is recognized that a fatigue argument is more appropriately applied at the point of interest in the structure, in this case the stress level of piece parts inside a box rather than the vibration input at the base of the box. However, the response of the internal components is very difficult to predict, and would require considerable effort. Further this stress is related to the input and by assuming the stress is linearly related to the G level input, a reasonable and simple approach can be derived. Sufficient conservatism exists in the way the fatigue argument is applied so that any errors induced by this assumption of linearity are considered negligible.

Fatigue is usually examined on the basis of an S-N curve which plots the number of cycles to failure as a function of stress level. Fatigue curves for ferrous alloys will have a characteristic knee at stress levels of 0.2 to 0.6 of ultimate. Below this stress level the number of cycles to failure is indefinitely large. The stress level at which this knee occurs is referred to as the endurance limit, or when normalized to the ultimate tensile stress, the endurance ratio. For non-ferrous material this knee does not usually occur, and in this case the endurance limit is usually taken as the stress level at 10^7 or 10^8 cycles. For the present example the worst case total time duration was about 10 min, and the maximum frequency 2000 Hz so that the maximum number of cycles encountered was (10 min) (60 sec/min) (2000 cycles/sec) = $1.2 (10^6)$ cycles or about an order of magnitude less than the above definitions. Hence, the above definitions of the endurance ratio are within the scope of the analysis.

Endurance limits were obtained for various materials and examination of this data indicated that for most metals an endurance ratio of 0.2 to 0.3 is a reasonable estimate of the lower bound. While a lower value of 0.2 is a reasonable approximation for metals this is not necessarily representative of all materials used in the construction of electronic equipment, which would include fiberglass, plastics, ceramics, etc. Only a limited amount of data was found concerning the fatigue properties of these materials, and this indicated that the fatigue properties of non-metallic materials were not as favorable as metals.

Another important consideration in fatigue is the effects of joints and attach points on the material. Fatigue tests are typically performed using smooth specimens, lacking the holes, sharp points, and attachments characteristic of real equipment. These factors result in local stress concentrations which reduce the fatigue life of the material. To account for the above considerations, and also to account for other possible effects such as temperature, mean stress, etc., it was decided to use an endurance ratio of 0.10 as an engineering approximation of the fatigue life limit of equipment.

Use of this endurance ratio was made in the analysis for determining the lower amplitude limit. Below this limit little cumulative damage is acquired, and therefore peaks below this amplitude are not included in the comparison between environments. In order to use this endurance ratio the ultimate capability of the box must be known. Since the ultimate capability of a box cannot be obtained without data from destructive tests, a conservative approach was used by defining the ultimate strength as the maximum input acceleration peak experienced by the box. This maximum peak is obtained from the demonstrated capability curves for each box by finding that G level for which the expected number of peak exceedances equals 10. Justification for picking this point of the curve is given below. The lower bound, GLB, equals 10 percent of this level.

Since the peak exceedance curve represents the statistical expected value it is necessary to define the ultimate box capability in terms of a confidence level. It is desired to have a high degree of confidence that at least one peak exceeded the defined capability level during the qualification test.

Defining the confidence level as $C(G)$, the probability that at least one peak is greater than G, then $C(G)$ can be expressed as a function of $N(G)$. Let

$N(G)$ = expected number of peaks to exceed G

N_0 = total number of peaks that occur

$P(G)$ = probability that any one peak is greater than the level G

Then by definition

$$N(G) = N_0 P(G) \text{ or} \\ P(G) = N(G) / N_0 \quad (4)$$

Since the probability that one peak is greater than G is $P(G)$ and N_0 peaks occur each with the same probability then this process represents a binomial distribution with

$$C'(G) = 1 - [1 - P(G)]^{N_0} \quad (5)$$

In order to evaluate this confidence level it is necessary to use a normal distribution approximation to the binomial. This approximation is good for $np > 5$ and $n(1-p) > 5$ where n equals the sample size and p = probability of a success (i. e., peak exceeding G). For the present case with $N(G) \ll N_0$

$$np = N_0 \left[\frac{N(G)}{N_0} \right] = N(G) \quad (6)$$

and

$$n(1-p) = N_0 \left[1 - \frac{N(G)}{N_0} \right] \approx N_0 \quad (7)$$

Therefore, this approximation is good for $N(G) > 5$. Using this normal distribution approximation the confidence level is

$$C'(G) = P(Z > G) \quad (8)$$

where Z has a standard normal distribution and is defined as:

$$Z = \frac{x - np}{[np(1-p)]^{1/2}} = \frac{1 - N(G)}{N(G)^{1/2}} \quad (9)$$

In this case $x = 1$ since it is desired to have at least one peak exceed the amplitude G , and $p \ll 1$. For $N(G) = 10$ the confidence level equals 99.78 percent, which is considered more than sufficient for the present analysis.

Since the probability distribution for peaks is a decaying exponential function of the peak amplitude, the number of peak exceedences becomes very small for large G amplitudes, and therefore it was also decided that an upper bound on the range of values for G was necessary to maintain a realistic region of interest. The upper bound chosen was that G amplitude, where with 90 percent confidence, all peaks were below that level. The upper bound, GUB, then occurs where the number of peak exceedences equals 0.1. This can be shown as follows.

Define the confidence level, $C'(G)$ as the probability that all peaks are less than the level G . Since the probability that one peak is less than G is $1 - P(G)$ and N_0 peaks occur, each with the same probability, then this process represents a binomial distribution, and the probability that all peaks are less than G is

$$C'(G) = [1 - P(G)]^{N_0} \quad (10)$$

Since $P(G) \ll 1$, i. e., the probability that any one peak exceeds amplitude G is small, the above expression can be expanded as

$$C'(G) = 1 - N_0 P(G) + \frac{N_0^2}{2!} P(G)^2 - \dots \quad (11)$$

Now substituting the previously derived relation for $P(G)$, Eq. (4),

$$C'(G) = 1 - N(G) + 1/2 N(G)^2 - \dots \quad (12)$$

which is independent of N_0 and therefore represents the confidence level for all frequency bands. For $N(G) = 0.1$, $C'(G) \approx 0.90$ or a 90 percent confidence level that all peaks will be below G amplitude where the peak exceedence curve equals 0.1 peaks.

A schematic of how these upper and lower bounds are applied is shown in Fig. 4. From the demonstrated capability curve the maximum stress capability, G_{max} , is read where $N(G) = 10$ peaks. The lower bound, GLB, equals 10 percent of G_{max} . On the peaks available curve the upper bound, GUB, occurs where $N(G) = 0.1$ peaks. That portion of the curve which is between these bounds is of interest. These bounds are shown on the available life curve in Fig. 3.

DERIVATION OF ACOUSTIC TEST SPECTRUM

Subtracting the cumulative exposure from the demonstrated capability results in a curve referred to as the available life or margin. This curve (solid line in Fig. 5) represents the demonstrated life or the number of peaks available for vehicle acoustic testing. A curve of the form $FT^* \exp(-1/2 G/Grms^*)$, or a Rayleigh Distribution, represents the number of peaks consumed during a vehicle acoustic test of constant amplitude and duration T^* and can be fitted such that it intersects the peaks available curve at both the upper and lower bounds (dashed curve in Fig. 5).

Results of the analysis indicated that the available life curve exceeded a Rayleigh Distribution curve that was fitted to these end points and this fact was used to obtain the acoustic spectrum. This was done by assuming a test time, and then solving for that $Grms$ which will result in the peak distribution curve for the acoustic test passing through either the lower or upper bound, whichever is limiting for the assumed test time.

$$Grms = G \left\{ -2 \ln \left[\frac{N(G)}{TT} \right] \right\}^{-1/2} \quad (13)$$

The $Grms$ level that fits this curve through the upper and lower points can be obtained by substituting the values for GLB, $N(GLB)$, GUB, and $N(GUB)$ into the above expression. That point which yields the smaller $Grms$ represents the limiting case.

Ratioing this $Grms$ level to the predicted maximum flight level results in a delta dB, reference to flight, which the particular box being examined can be tested to during vehicle acoustic tests in the 1/3 octave band under consideration, or

$$\Delta \text{dB} = 10 \log \frac{(\text{Grms})^2}{\text{Grms Ft}} \quad (14)$$

Applying this delta dB to the predicted maximum flight acoustic spectrum yields the desired test spectrum. By varying the test time a curve was constructed representing the maximum level a particular box can be subjected to as a function of time. This is shown in Fig. 6 and indicates that for the example considered as much as 4-1/2 min of acoustic testing at maximum flight levels could be performed on the ground. By examining all the boxes the maximum acoustic levels that the entire equipment section could be subjected to was derived. Using this approach it was possible to establish a spectrum that was nearly 10 dB higher than was considered possible before the analysis, with the new test levels representing a meaningful acceptance test.

EXAMPLE 2 COMPARISON OF QUALIFICATION TEST TO FLIGHT ENVIRONMENT

Objective and Approach

Another typical application using the peak count analysis was comparing a series of qualification test spectra to a predicted flight environment. In this case a new system design made use of a considerable number of components qualified for other programs. As a result much of the equipment did not meet the qualification test requirements of the new program, even though they had already been tested. In order to save the cost of requalifying this equipment a peak count analysis was performed to show that this equipment was flight worthy for the new program.

The approach used was to compare the peak exceedence curves for the qualification tests performed to the curves for the predicted flight environments. If the qualification test data exceeded the flight environments on this basis in all frequency bands then the box design was considered flight worthy; otherwise a retest would be necessary. For most units this approach was sufficient, however for a few of the components the peak exceedence curves intersected as shown in Fig. 7 in one or two frequency bands. Based on engineering judgment the small amount of overlap that resulted was not considered significant and in order to justify this position a refined fatigue argument was developed.

FATIGUE CONSIDERATIONS

The conservative approach described in the former paragraph ignores the fact that fatigue damage can be traded off on an amplitude cycle basis by application of Miner's Rule [2]. The following analysis was developed to apply Miner's Rule to measure the fatigue damage of random vibration, based on the peak distribution data obtainable from the peak count analysis. This fatigue life measure was derived using the base acceleration input and is dependent upon the actual demonstrated capability of the box. Base input was used since this is the most convenient common interface between different environments. Using actual test data to define the maximum capability of the unit assures the conservatism of the analysis, and results in measuring the

fatigue life of the flight environment relative to the fatigue life of the qualification test.

In addition to the assumptions made for the peak count analysis the following two are also required:

1. A fatigue life curve (S-N curve) is a power function (straight line on a log-log plot) passing through the ultimate stress level at one cycle
2. The stress level of internal components in the box is linearly related to the base acceleration input

The first assumption is sufficiently conservative for the range of interest and therefore is considered acceptable. This is graphically shown in Fig. 9 which plots the assumed range of fatigue life curves used in the analysis to the actual fatigue curves for aluminum and magnesium. As can be seen the assumed fatigue curve range is considerably conservative.

The second assumption is considered reasonable since the analysis is based on the statistical properties of random vibration, and the response of a simple oscillator is directly related to the statistical properties of the base input. Although an electronic box is much more complicated than a single degree of freedom system, the errors induced by this simplification are not considered excessive and using this approach results in a practical analytical procedure.

The first assumption results in a relation for the number of cycles to failure as

$$N_f = cS^{-B}$$

which can also be written as

$$N_f = (S/S_{ult})^{-B} \quad (15)$$

where

N_f = number of cycles to failure at amplitude S

S = maximum stress level per cycle

S_{ult} = ultimate stress level of specimen

c = proportionality constant = S_{ult}^{+B}

B = slope of fatigue life curve

The second assumption implies that G/GULT can be substituted for S/S_{ult} or

$$N_f = (G/GULT)^{-B} \quad (16)$$

where

G = base acceleration input (peak amplitude per cycle)

GULT maximum acceleration peak box can withstand for one peak.

Equation (16) gives a measure of the number of cycles to failure as a function of the base acceleration input and the slope of a fatigue curve which would encompass all materials inside the box. In order to apply this equation it is necessary to derive values for the parameters, B and GULT. To do this use is made of Miner's Rule and the demonstrated capability of the box.

Miner's Rule states that the fatigue life consumed can be expressed as

$$FL = \sum_i n_i / N_i \quad (17)$$

where

FL = fatigue life consumed

n_i = number of cycles occurring at some amplitude S_i

N_i = number of cycles to failure at that amplitude S_i

When FL = 1 then all the fatigue life has been consumed and a failure can be expected. This rule is used in the present analysis by assuming that the fatigue life for the demonstrated capability curve is the maximum possible or FL-capability curve = 1. If we define

$$\Delta N(G) = N(G - \frac{1}{2} \Delta G) - N(G + \frac{1}{2} \Delta G) \quad (18)$$

where

N(G) = number of peaks expected to exceed amplitude G, from peak count analysis

$\Delta N(G)$ = density of or number of peaks expected to occur in interval $G - 1/2 \Delta G$ to $G + 1/2 \Delta G$.

Then using Eq. (16) for N_i results in

$$FL = (1/GULT)^B \sum_i G_i^B \Delta N(G_i)_{\text{capability}} \quad (19)$$

Since the fatigue life of the qualification test is assumed to be the maximum possible, then FL = 1 and either B or GULT can be solved for. Unfortunately insufficient restrictions exist in order to solve for both quantities so that it is necessary to assume a range of values for one parameter and then solve for the second.

Physically B is related to the slope of the fatigue curve, with a range of values from 5 to 20. If B is large, then the specimen has a very flat slope or experiences very little fatigue damage even when exposed to amplitudes near ultimate. Since a

fixed distribution of peaks exists for the demonstrated capability data, which is conservatively assumed to have the maximum fatigue life, then it follows that the ultimate G capability of the box does not have to be very large; i.e., peaks with low amplitudes do not contribute significantly to the fatigue life consumed because of the large number of cycles to failure at these low amplitudes. Therefore, an assumed large value for B means a small GULT, and emphasizes the large amplitude peaks.

Assuming a small value for B means the fatigue curve drops very rapidly, or that nearly all peaks, regardless of amplitudes, contribute significantly to the fatigue life consumed. Again since a fixed distribution of peaks is assumed to have a fatigue life of one, it follows that the ultimate capability of the box must be very large in order to balance this "poor" fatigue curve. Therefore, a low value for B leads to a large value for GULT, and emphasizes the low level peaks where most of the cycles occur.

Since either of the above situations is considered possible for base input to a box, the approach used is to assume a range of values for B and then solve for the GULT value as a function of B. These values for GULT are then used in calculating the fatigue life for the environment of interest, as a function of B. It is important to note that GULT is a mathematical parameter used in comparing environments and is not considered to be a realistic measure of the absolute physical capability of the box.

An outline of the overall procedure is as follows:

1. Obtain $\Delta N(G_i)$ from the peak count analysis for exposure and capability environments.
2. Assume a value for B and solve for GULT using the demonstrated capability curve and Eq. (19) with FL = 1. Repeat for range of values of B = 2 to 20.

$$GULT^B = \sum_i G_i^B \Delta N(G_i)_{\text{cap}}$$

3. Using the above values for GULT obtain the fatigue life consumed during the expected environments, i.e., exposure.

$$FL_{\text{exp}} = (1/GULT)^B \sum_i G_i^B \Delta N(G_i)_{\text{exp}}$$

4. If FL < 1 for all values of B, then box has sufficient demonstrated capability. Repeat for all frequency bands.

This analysis was performed for the example shown in Fig. 7 with the results given in Fig. 9. As can be seen the fatigue life consumed during the flight environments, relative to the qualification test, increases at the low and high values of B, corresponding to emphasizing the high G and low G levels respectively. In both these regions a small amount of overlap occurs. The maximum value

calculated for the fatigue life is 0.66 at $B = 20$, indicating that if this fatigue slope applies then the worst case flight exposure will only consume about 66 percent of the fatigue life that was demonstrated during the qualification test. By this means it was possible to prove the flight worthiness of a number of boxes and thus avoid unnecessary retesting and the associated costs.

CONCLUSIONS

The peak count analysis represents a valuable analytical procedure in the analysis of random vibrations, especially in the field of test requirements for equipment mounted in missiles and space vehicles. Reasonable justifications exist for the assumptions which are necessary in developing and applying this analysis, and with these assumptions a simple and practical analysis can be performed from which logical engineering conclusions can be derived. Because the analysis objectively accounts for both time and amplitude as parameters it provides a more realistic means of combining the effects of dissimilar environments.

With the use of additional supporting arguments the general peak count analysis can be applied to a wide variety of problems, of which two examples are

presented. The first example showed how the technique can be applied to derive an acoustic test spectrum for ground tests. In the second example a fatigue argument was developed, utilizing Miner's Rule, in order to compare the relative severity or potential fatigue damage of dissimilar environments.

The examples pointed out the general methodology of applying the peak count analysis. Use of this technique can result in the removal of a considerable amount of unnecessary conservatism in the analysis of random vibration, which leads to more realistic flight predictions, test requirements, and eventual savings in system weight and costs.

ACKNOWLEDGEMENTS

The author wishes to thank A. L. Ikoia for the assistance which he provided in the development of the analytical procedures.

REFERENCES

1. S. H. Crandall and W. D. Mark, "Random Vibration in Mechanical Systems," Academic Press, 1963
2. Milton A. Miner, "Cumulative Damage in Fatigue," J. Applied Mech., pp. A159-A164, Sept. 1945

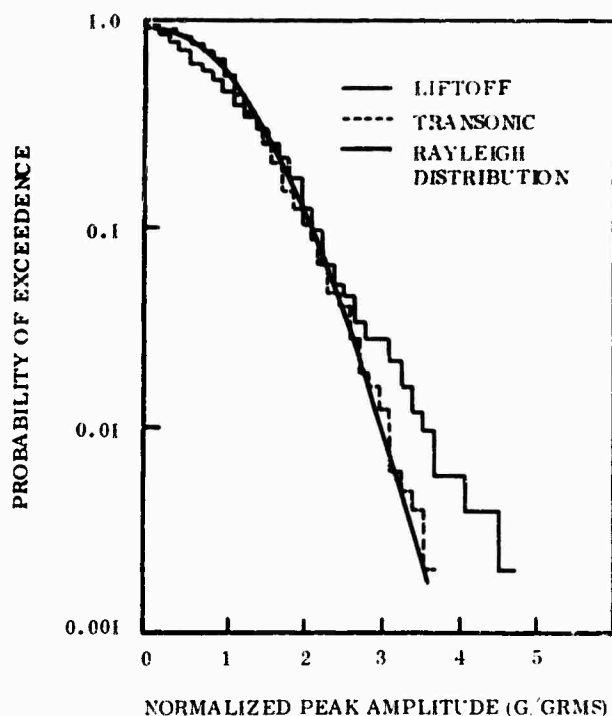


Fig. 1 Comparison of Rayleigh Distribution and Flight Data

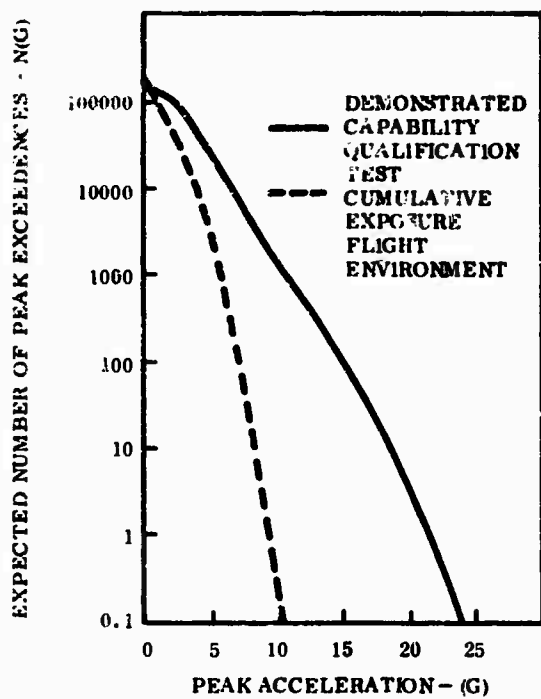


Fig. 2 Peak Exceedence Curves 315 Hz 1/3 Octave Band

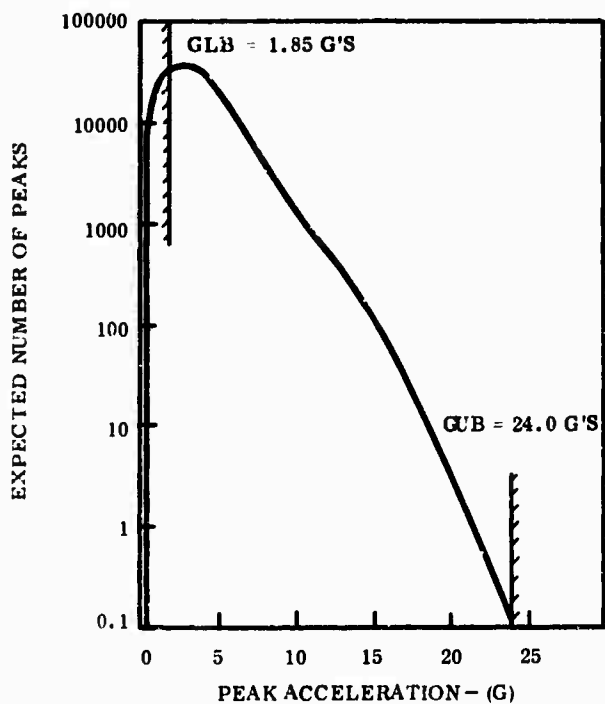


Fig. 3 Number of Peaks Available for Acoustic Testing 315 Hz 1/3 Octave Band

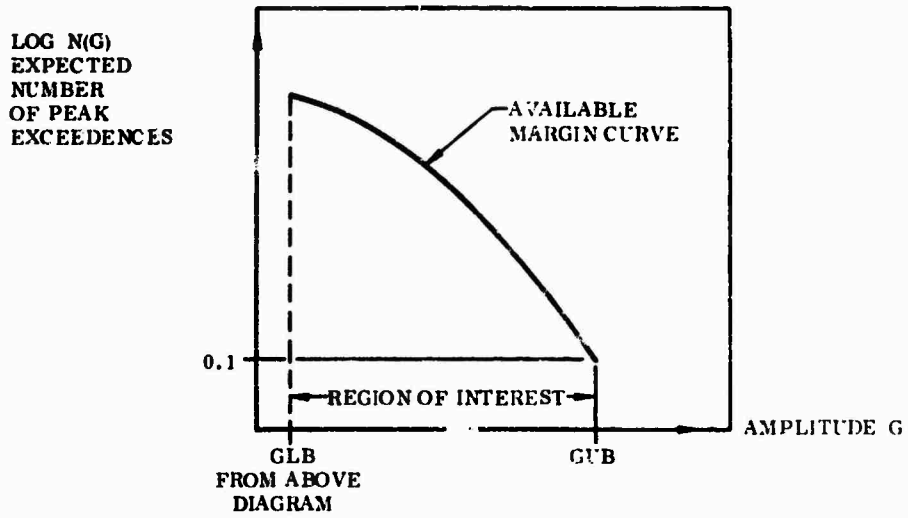
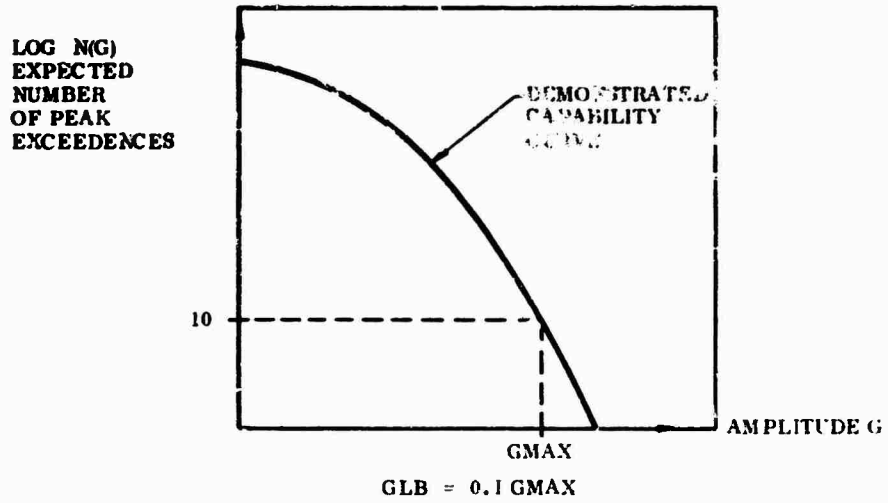


Fig. 4 Definition of Lower and Upper Bounds

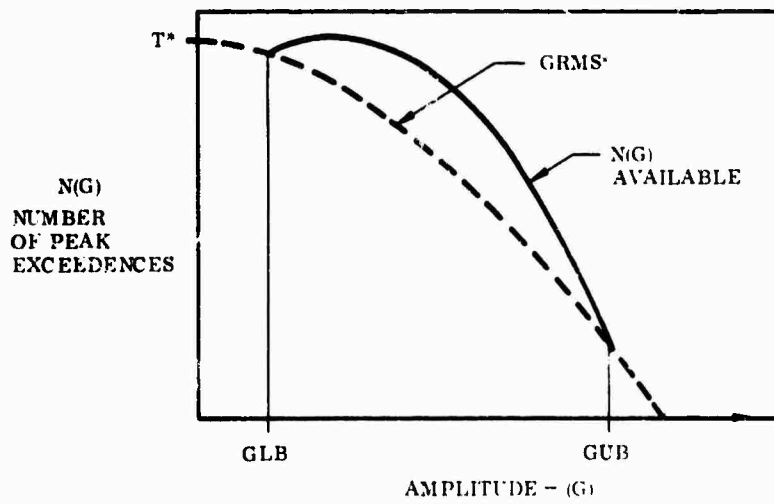


Fig. 5 Derivation of dB vs Time Curve

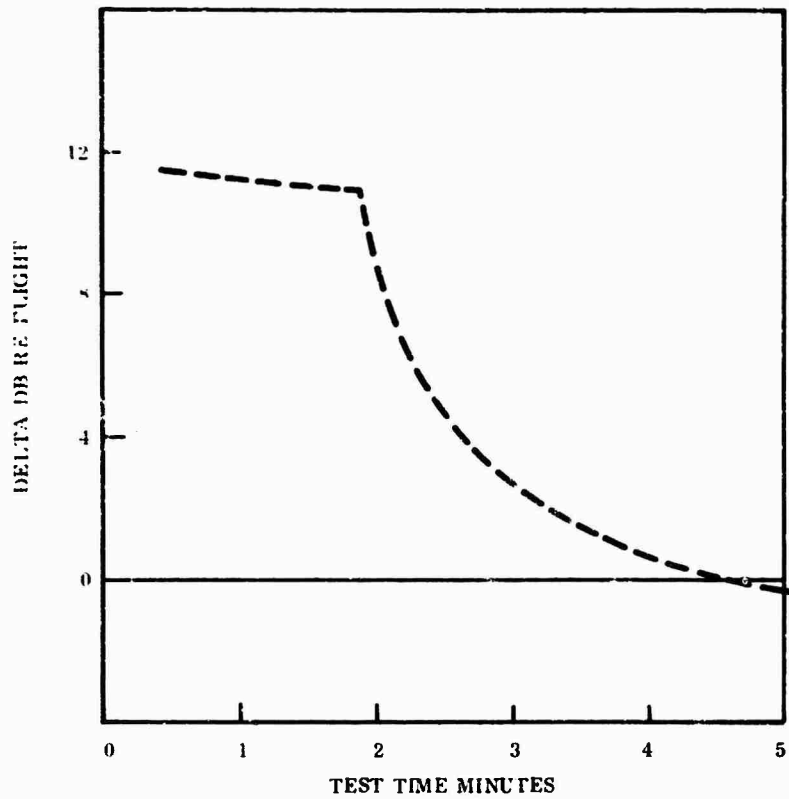


Fig. 6 Maximum Test Amplitude vs Time 315 Hz 1/3 Octave Band

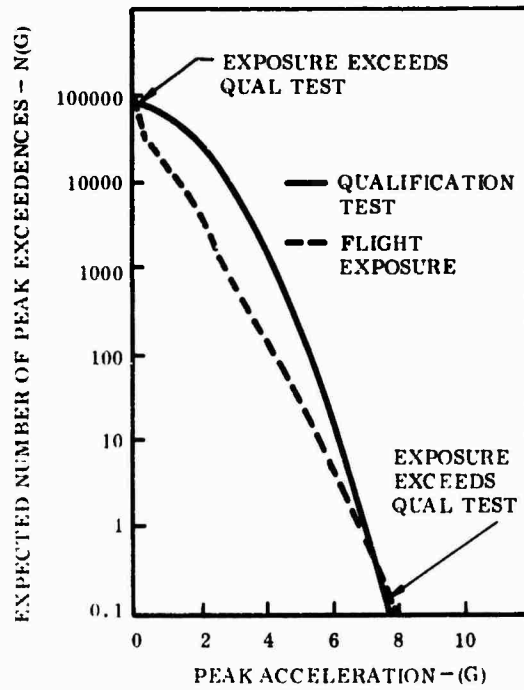


Fig. 7 Peak Exceedence Curves 200 Hz 1/3 Octave Band

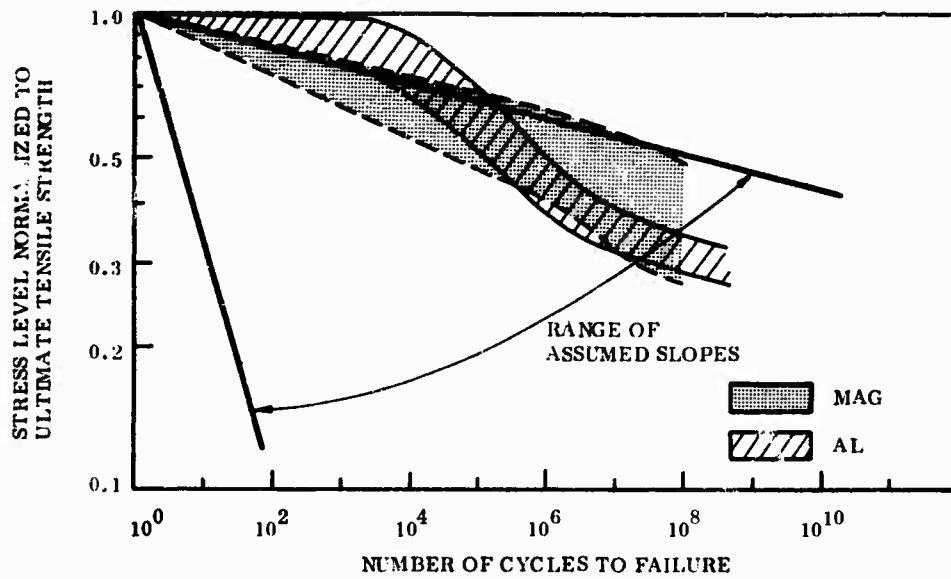


Fig. 8 Comparison of Assumed Fatigue Life Curves to Actual Data

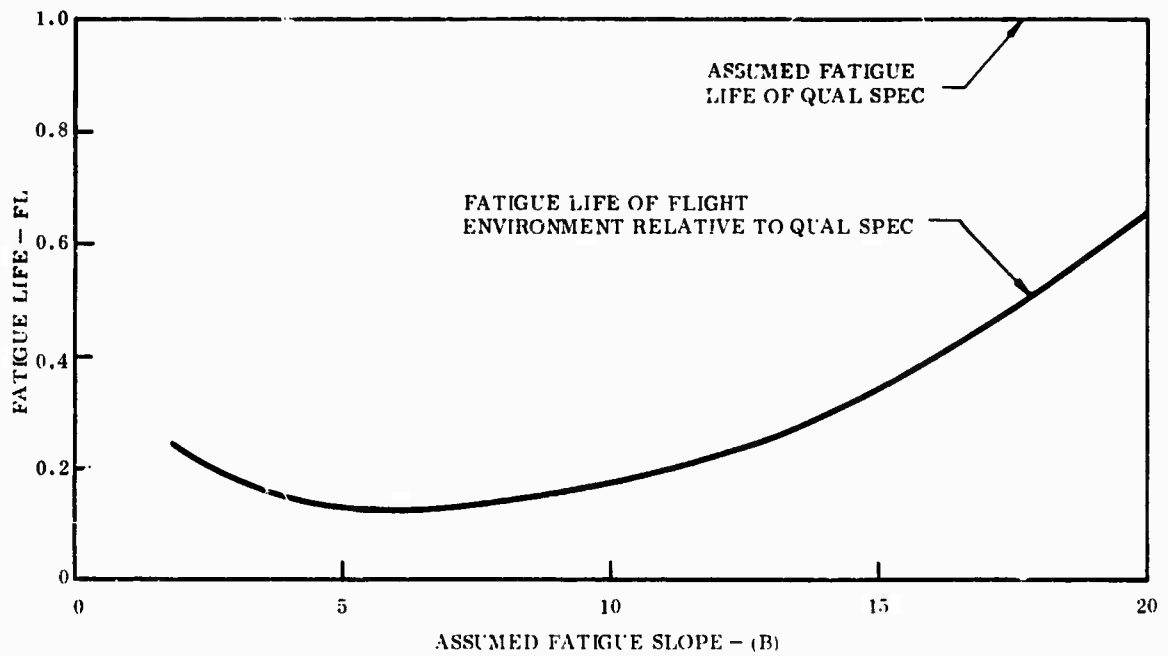


Fig. 9 Fatigue Life of Flight Environment Relative to Qualification Tests 200 Hz Band

DISCUSSION

Mr. Trubert (Jet Propulsion Laboratory): Because you are talking about the number of peaks associated with the levels, I wonder if you are trying to run a fatigue test or an equivalent fatigue test.

Mr. Wrenn: No, we do not want to run a fatigue test at all. We're just associating the number of peaks with essentially the wear that a particular piece of equipment experiences, and we are relating that wear to eventual wearout and failure of that particular box. So we are using it as a tool for evaluating the accumulative exposure that these pieces of equipment see due to random vibration.

Mr. Trubert: You could have a very high level for a small number of peaks or a low level for a high number of peaks. Do you assume it is the same thing?

Mr. Wrenn: They are both handled the same way in the analysis. And this is the trade-off that you can make. You can make comparisons this way objectively rather than nonobjectively.

Mr. Trubert: So this is the same idea as fatigue?

Mr. Wrenn: No, but it is related to fatigue. I should mention in connection with this peak count technique, that the qualification testing of these boxes merely establishes a certain number of peaks that they have seen. They may see far in excess of that before they actually fail. But they have not been proven for that increased number of peaks because their qualification testing has not demonstrated it.

Mr. Galef (TRW Systems): What weighting technique did you use to weight the large number of small peaks against the small number of large peaks?

Mr. Wrenn: Just count the peaks.

Mr. Galef: That is really not sufficient. Certainly two 50,000 psi peaks are more to worry about than one 50,000 psi peak. It is not clear that two 50,000 psi peaks are worse than one 60,000 psi peak.

Mr. Wrenn: First of all we have to realize that we are talking about levels that are of the same

order of magnitude. If you go to non-order-of-magnitude levels, certainly the technique may break down because it assumes it is linearly related to the total exposure. That may not be the case when a box is exposed to a very high level, and then you come in with 0.01 or 0.001 of that level. One must examine the whole technique over again.

Mr. Galef: I thought you were trying to consider the shipping environment along with the flight environment and other environments. This is not the case?

Mr. Wrenn: That is right, we are.

Mr. Galef: But these are orders of magnitude.

Mr. Wrenn: Yes, they are orders of magnitude, but we still feel that the assumptions are valid and at least our flight measurements indicate that they are valid. So you are right. There are some bands where it goes over; we stretch it a little bit. Sometimes we stretch it a lot, but it seems to work. It is a new technique, I should point out. We have not done it this way for a long time and we are starting to explore it. There are lots of improvements that can be made.

Mr. Christensen (Naval Weapons Center): You had failures on qualification test items prior to using this method of analysis. Did you use this method of analysis on spectra applied to your failure samples? That is, you had articles that failed previously and you obviously had envelopes for them. Did you count the theoretical peaks in these envelopes and compare them to the peaks you came up with here?

Mr. Wrenn: This technique in the past has been useful for some very nutsy-boltsy type problems. For example, someone might put a piece of equipment on a shaker and, instead of running for 3 minutes for a test or 1 minute for an acceptance test, he lets it run for 5 minutes, or the shaker runs wild. So here is a person with a box that costs \$60,000, and he wonders whether he can fly it or not. He wants to have a little more confidence that it will perform properly. We use this technique as an engineering tool. Just because the peak count says it is no good it does not mean we are not going to fly it. We want to take a look at the big picture.

THE APPLICATION OF ANALOG TECHNIQUES TO REAL TIME ANALYSIS AND SCREENING OF DYNAMIC DATA

Roger C. Crites
McDonnell Aircraft Co.
St. Louis, Mo.

The necessity of handling large amounts of dynamic data in order to compute complex time variant parameters led to the conception of highly specialized analog computer techniques which enable data analyses and sorting at a small fraction of the time and cost required by a digital computer. These techniques were developed to facilitate ground test assessment of engine-inlet compatibility. The need for, development and successful use of these techniques are described, and potential application to such studies as cumulative fatigue damage and buffet are discussed.

INTRODUCTION

The objective of determining dynamic engine-inlet compatibility from independent tests of engines and scale models of the proposed inlets is to permit selection of compatible designs prior to full scale testing. Successful attainment of this objective substantially reduces the chance of developing an engine and inlet which work well individually but do not perform well together. Fortunately, as it turned out, the amount of data reduction required to achieve this goal by the usual application of digital computer technology represented not merely a high cost, but an impossible cost, both in time and in money.

In resolving the dilemma, a useful philosophy involving the application of special-purpose analog computing techniques evolved. This philosophy has proven useful for other than the original application. It is anticipated that this approach will find profitable employment in many other applications in the aerospace industry.

COMPATIBILITY ASSESSMENT

With the advent of high performance aircraft utilizing an augmented turbofan propulsion unit, airframe-engine compatibility has emerged as a prime consideration in the selection of airframe and engine designs. The very high degree of compatibility necessary to realize the full potential of the aircraft necessitates an inlet-duct design which presents the engine face with a relatively low level of pressure distortion inasmuch as the engine is sensitive to steady state pressure gradients and to fluctuations in the pressure which have a duration time at least as short as one revolution of the compressor. That is, certain pressure patterns or distributions at the compressor face will adversely affect engine performance if that pattern persists for one full revolution of the compressor or longer.

As shown in Figure 1, the independent determination of compatibility essentially involves determining whether or not the proposed inlet design produces any of the pressure patterns which cause instability and loss of engine performance, and if so, to what extent and at what conditions. This is accomplished by analyzing the pressure patterns affecting engine operation and generating explicit mathematical models. The models are

empirical or semi-empirical and are used to establish distortion indices which may be evaluated for any given pressure pattern and indicate the relative "goodness" or "badness" of that pressure pattern so far as the engine is concerned. That is, a particular pressure pattern will yield a numerical distortion index with regard to a particular engine. If the index is below a certain level, engine performance will be unaffected, but if the index approaches this limit or exceeds it, engine performance will suffer.

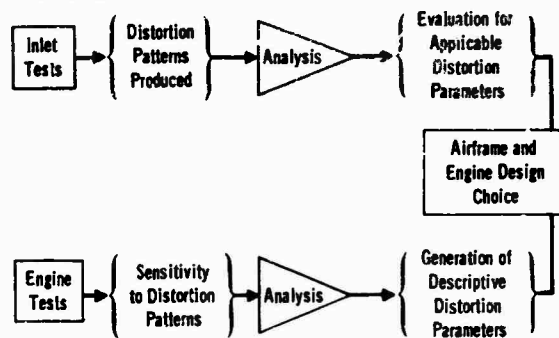


Figure 1 - Independent Selection Scheme

Any inlet design which produces pressure patterns with a very low distortion index for a particular engine is said to be compatible with that engine. Any inlet design which delivers an index above the engine limit value would result in an aircraft which could not fulfill its performance requirements, and regardless of how well the engine and inlet would perform separately, they would be incompatible.

To determine the compatibility of an inlet design with proposed engines, a wind tunnel test of a scale model of the inlet is necessary. The compressor face location is heavily instrumented with total pressure probes. Each probe provides a measurement of the local mean total pressure component, and the local fluctuating or dynamic pressure component. Fifty such probes at the compressor face are typical of the quantity of instrumentation employed. The dynamic components are recorded on a

constant bandwidth multiplex system to provide a high time base correlation between all channels. The steady state components are recorded by the wind tunnel digital data acquisition system.

From this data the distortion indices must be evaluated. Typically, the evaluation must include about 5000 samples per second to be sure of containing the highest frequency of interest. A typical test program consists of about 1000 runs, each 30 seconds long, which are necessary to cover the performance envelope of the inlet. The instantaneous pressures at the 50 probes are used 5000 times per second to calculate several distortion indices. For a single test program such as this, the quantity of raw data that must be fed to a digital computer is about 7.5 billion data values, or, for 10 tests, about 75 billion.

The quantity of data to be analyzed is staggering. And even if the money required to process this quantity of data would have been available, the time required to complete the job would make the aircraft obsolete before it flew. Furthermore, even if the actual data processing could be done in reasonable time at reasonable cost, the result for one run in one test would be 150,000 values of each distortion index computed, or 150 million values per distortion index per test. Each value must be examined to determine if, at any point in the performance envelope, the inlet has produced a pressure pattern incompatible with the engine. If this examination is to be performed by people, one test would require about 125,000 manhours merely to look at the reduced data for only one distortion index. Therefore the cost and time required for data reduction were unreasonable, and in any case, the reduced data would be more than could be reasonably reviewed even if the processing could be accomplished.

It was apparent that an entirely new approach was necessary.

THE ANALOG COMPUTING EDITOR APPROACH

The new approach required a minimization of the quantity of data to be reduced for assessment. This indicated the need for a method of identifying a small time slice (about 0.1 second) which contained the raw data representing the worst pressure pattern, or worst value of distortion index, that occurred during the entire run, and marking this time slice on the data tape. This identification would allow selection of this "worst-case" for digital processing of the buildup and decay of the worst distortion that occurred during the entire run. This precise processing requires only about 3 tenths of 1 percent of the data handling necessary to compute distortion parameters for the full run. Knowing the worst that happened is not quite the same as knowing precisely what happened all the time, but the result is the same. Obviously, if the worst that happened corresponds to a distortion index below the level that produces adverse engine effects, the rest of the run could not produce adverse engine effects, and the inlet and engine are compatible at that run condition. Likewise, if the worst case distortion index is above an acceptable level, the inlet and engine are incompatible for that run condition regardless of how well the inlet operated during the rest of the run.

Besides having some sort of system that locates and marks the worst case time on the data tape, it is very desirable to provide the engineer at the test site with some immediate on-line

data to enable him to assess the progress of the test. Without this data, the test engineer must proceed blindly, with no knowledge of the occurrences during the test until after it is over. Much time could potentially be saved by being able to recognize a problem while still in the field and take corrective action immediately rather than waiting several weeks after the test to discover the need for a minor change.

Figure 2 shows how both of these goals were accomplished. The heart of the system is an analog computer which looks at all steady state and fluctuating total pressures simultaneously as the data comes off the line, and computes instantaneous values of several distortion indices from instantaneous values of all of its total pressure inputs. The lag time associated with the computation is essentially negligible, so that for all practical purposes, the raw data and the computed distortion parameters coexist at the same instant in real time. As a run progresses, the steady state pressures are sampled and remembered.

The fluctuating pressures enter as time histories, and the analog computer produces corresponding time histories of the distortion parameters of interest. This real time distortion is available for monitoring by engineering personnel on a real time display on oscilloscopes. Sections of the time histories of distortion parameters are also recorded for immediate review as oscillograph traces, and a permanent record is made via FM tape. In this manner real time, on site reduced data is available.

A peak detector circuit looks at the output time history of each distortion parameter, which continually updates itself during a run so that its output is always equal to the highest value of distortion index that has occurred up to that point in the run. At the end of the run a button is pushed and the highest value of each distortion index that occurred during that run is displayed on a digital panel meter and printed for permanent record by a digital printer. The peak detector is then reset prior to the initiation of the subsequent run. The time history and worst value of distortion are therefore available on-line in real time as the test proceeds.

In order to determine when the worst case occurs and mark the raw data tape at that instant, a zero crossing comparator and pulse shaping network look at the output of the peak detector. When a peak in distortion exceeds the value locked in the peak detector, the peak detector updates to the higher value, causing the comparator to emit a pulse. The shaping network shapes the pulse into an easily recognized electronic flag. This flag is recorded on the Vidar multiplex system on a blank track. Since the raw data is recorded on the other tracks of the Vidar system, and since negligible time has elapsed from the time the raw data which caused the peak in distortion occurred until the resulting pulse or flag was recorded, the electronic marker on the raw data tape locates the position of the pressure data which caused a peak higher than any preceding peaks in that particular distortion index. The result is a series of pulses recorded on the raw data tape. Each succeeding pulse marks the time that a new high in distortion occurs. When the worst case occurs, the peak detector locks that value in, and since it is the worst case, it will not update again until manually reset for the next run. Therefore, the last pulse, which is generated when the peak detector detects the worst case, represents the location of the data corresponding to the worst distortion, or worst pressure pattern in that run.

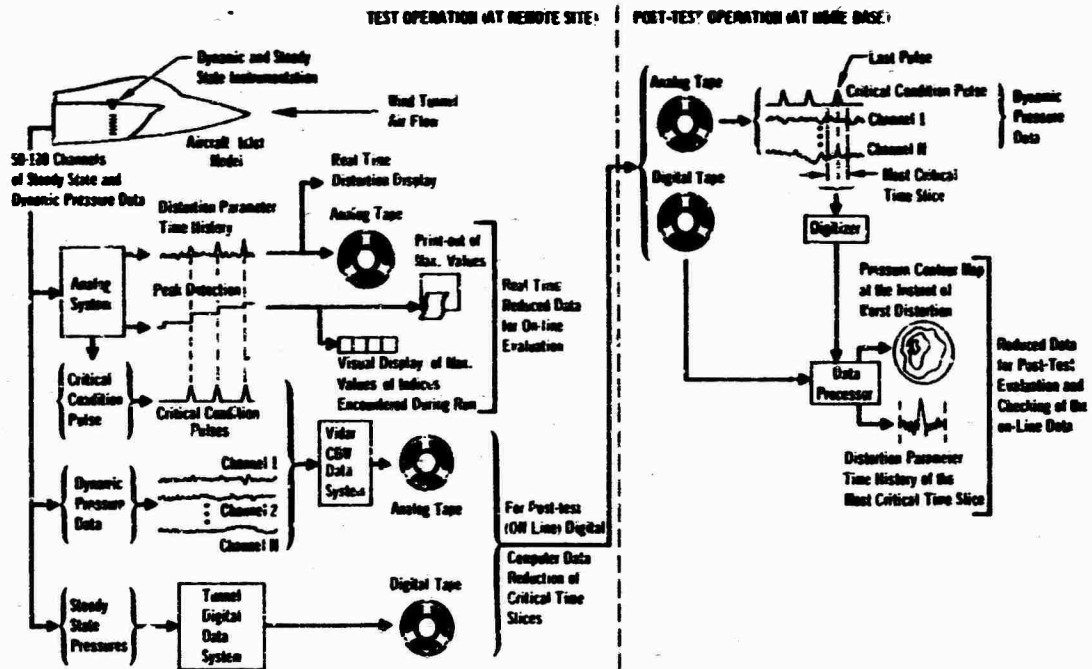


Figure 2 - Total System Application

When the recorded raw data is analyzed (post-test), the data tape is run backward and the critical pulse marker track is monitored. When the first pulse occurs (which will be the worst case pulse because the tape is running backward), an automatic delay system puts another electronic flag on the tape about 50 milliseconds after the pulse. Since the tape was running backward, this new marker pulse is actually 50 milliseconds prior to the time of occurrence of the worst case distortion. The tape is now reversed and run forward. When the new marker pulse is encountered, 100 milliseconds of digitization automatically begin. This time slice that is digitized contains at its center the data which reflects the worst pressure pattern occurring during the entire run.

This digitized worst case time slice is used to obtain computations of the distortion parameters, and to generate pressure contour maps revealing the physical pressure pattern responsible for the worst case distortion index. The values of distortion index obtained by the digital computer can then be compared to that portion of the distortion index time history generated by the analog computer. A typical example of the results of this sort of comparison is shown in Figure 3 for two different distortion parameters. Typically, the deviation between the worst case distortion index obtained by the analog computer, which is available on-line in real time as the test proceeds, and the value obtained by the digital computer from the raw data during post-test operation, is about 5 percent.

Figure 4 is a photograph of the analog computer, which occupies three 19-inch racks. The electronic components utilized in the fabrication of this device are standard, off-the-shelf items, such as integrated circuit operational amplifiers, diode function generators, diode selection networks, etc. The straightforward design of the computer system can be illustrated by a block diagram schematic of one of the simplest distortion parameters that has been used.

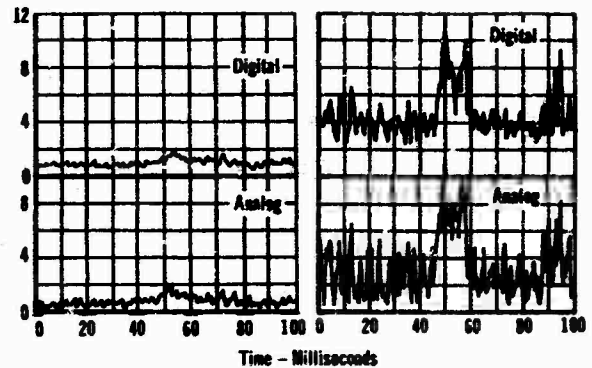


Figure 3 - Comparison of Analog and Digital Computation

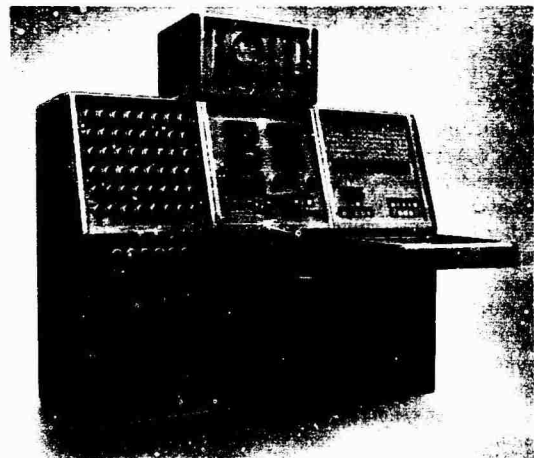


Figure 4 - The Combined Analog Computing System

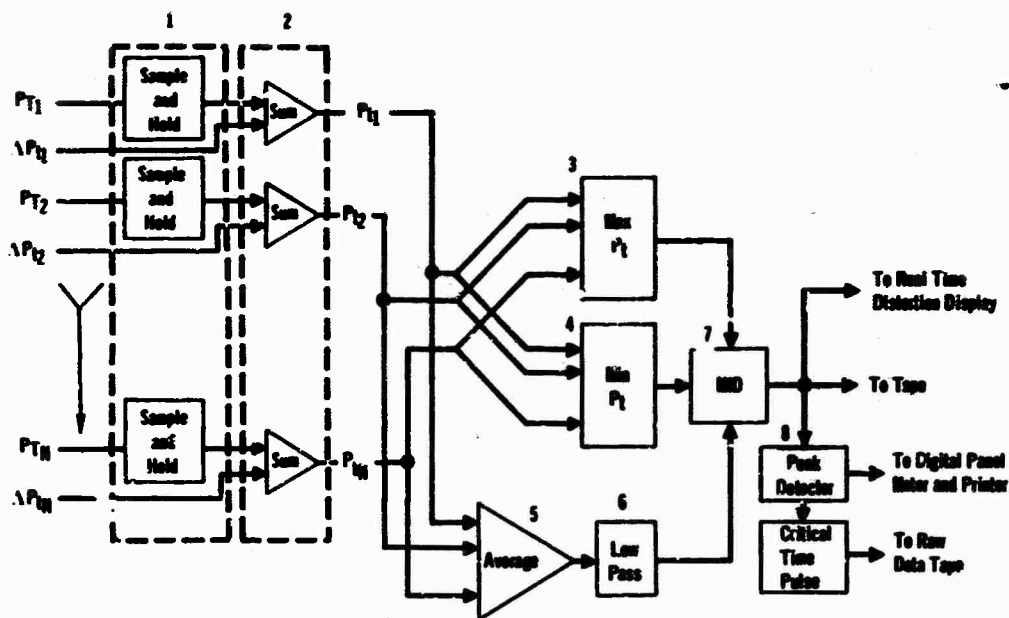


Figure 5 - Analog Calculation of MID

The parameter chosen for the purpose of illustration is defined by Equation (1).

$$MID = \frac{P_{t\max} - P_{t\min}}{\bar{P}_T} \quad (1)$$

where MID is the maximum instantaneous distortion, $P_{t\max}$ is the instantaneous maximum total pressure at the compressor face, $P_{t\min}$ is the minimum instantaneous total pressure, and \bar{P}_T is the average value of the steady state component of the total pressure. This parameter is by far the simplest of the five parameters normally calculated with the analog computer.

As seen in Figure 5, the steady state values of total pressure enter Block 1 and are maintained by a sample-and-hold circuit. The fluctuating pressure components enter Block 2, where they are summed with the steady state values to produce the true dynamic pressure distribution in the inlet. This true dynamic distribution is delivered simultaneously to Blocks 3, 4, and 5. Blocks 3 and 4 are diode selection networks which pass to Block 7 values of the maximum and minimum instantaneous pressure. Block 5 averages all of the dynamic pressures and Block 6 removes the remaining fluctuating component to reveal \bar{P}_T , which is passed to Block 7. In Block 7, $P_{t\max} - P_{t\min}$ is obtained, after which the indicated division is accomplished with the aid of logarithmic diode function generators. The resultant MID time history is displayed on the real time distortion display, recorded on tape and peak-detected. The output of the peak detector is viewed on a digital panel meter and printed on a digital printer, and it is used to drive the critical time pulse marker, as illustrated in Figure 6, to flag the worst case occurrence on the raw data tape. The various other parameters which the computer system employs are calculated in much the same manner but are considerably more involved.

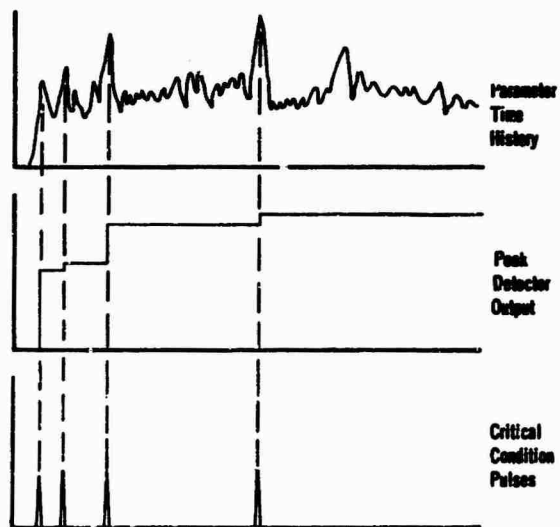


Figure 6 - Peak Detection - Critical Condition Pulses

The analog computer, as shown in Figure 4, has been successfully used on seven major wind tunnel test programs, and will continue to be used. This system provided on-line, real time reduced data with an uncertainty of about 5 percent. It also edited and marked the raw data tape so that the time required to digitally obtain an analysis of the worst thing that happened in each run was reduced by more than two orders of magnitude with corresponding monetary benefits.

OTHER ANALOG SYSTEMS USED

Two other analog systems have been employed with a large measure of success. The first was developed when it was discovered that a considerable quantity of data from a wind tunnel test had been used to calculate some parametric time histories, and after the data reduction was completed, the definitions of the parameters were slightly changed. It appeared that the new definitions would have to be programmed and the parametric time histories simply recalculated from the raw data. Unfortunately, time was not available to accomplish this re-computation. A small analog unit was then developed to apply different weighting functions to the various parameters for obtaining an output parametric time history which corresponded to the new definitions. Tapes of the obsolete parametric time history were played into the analog device, and the output of the system was recorded on another tape deck. In this way the updated reduced data was obtained in 4 days (including design and fabrication of the analog device) as opposed to the estimated 2 weeks required to recompute from the raw data.

The other system was developed in response to the need for obtaining the average value of many true root-mean-square (R.M.S.) pressures in an inlet model. An estimate of the cost and time to digitize and compute the average R.M.S. with a digital computer was compared to the time and cost to compute the same parameter on-line with a special-purpose analog computer. The analog computer provided much greater time savings. The analog system would also provide reduced data on-line as the test proceeded. Cost comparisons revealed that the analog approach, including the cost to build the system, was nearly one order of magnitude lower than the cost to digitize and utilize a large digital computer. Therefore, even if the analog unit was used on only one test and then junked (it wasn't), a considerable savings in money and time would be realized. The analog system was built and used successfully for several test programs.

It must be conceded that the computational accuracy of the digital computer exceeds that of the analog approach. But, with present integrated circuit technology and careful circuit design, analog computational accuracy can be kept within about 2 percent for most applications. When the equations being performed are fairly involved, as with some pressure distortion parameters where calculation of Fourier coefficients (among other things) become involved, the calculation accuracy may drop a few percent. The average true R.M.S. analog system described was verified as having a worst case computational error of about 1 percent.

It must be remembered that calibration of dynamic pressure transducers seldom, if ever, provides for less than 2 percent uncertainty in the raw data. The need for extreme calculation accuracy in such a case is questionable. However, even if extreme accuracy is required, an analog system can perform the function of editor, providing for a much more streamlined digital reduction program, and still obtain a net savings.

Experience to date with dynamic data manipulation suggests the following philosophy (as shown in Figure 7): If a small quantity of dynamic data is to be manipulated, the cost of fabricating an analog system is not warranted, and digital data reduction will prove most economical. If a large quantity of data is to be handled and a calculation uncertainty of 2 percent is acceptable, a special-purpose analog device can usually be

fabricated to accomplish the desired data reduction in much less time, and at a considerable cost savings. If a large quantity of data is to be analyzed but great accuracy of calculation is necessary, it may be possible, depending on the nature of the analysis to be carried out, to perform on-line editing of the raw data and then use digital computation on only critically important data samples.

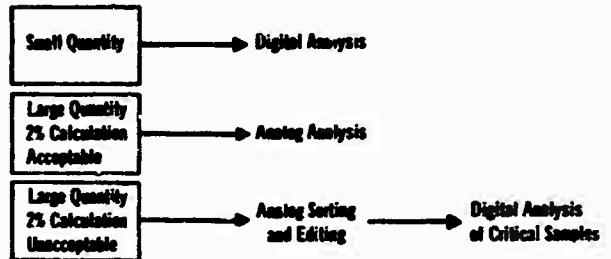


Figure 7 - Reduction of Dynamic Data

ANALOG APPLICATIONS UNDER CONSIDERATION

The analog approach is presently being considered for application to cumulative fatigue damage estimates and buffet studies. Many schemes have been worked out for the estimation of cumulative fatigue damage. Two of the most promising approaches will be discussed here to illustrate the possibilities.

The first scheme, illustrated in Figure 8, uses a spectral weighting approach to estimate cumulative fatigue. Stress, obtained from a properly located strain gage, is passed through an instrumentation amplifier, Block 1, and on to Blocks 2 and 7. The Fourier transform of the stress time history is obtained in Block 7 for about 200 center frequencies simultaneously, over an incremental data time T . The transform is converted into power spectra in Block 8 at the 200 center frequencies and passed to Block 9, which generates the parameter $\omega_n^T/2\pi N_n$. $\omega_n/2\pi$ is the N th center frequency f_{c_n} , and T is the time increment for which the transform was obtained. $\omega_n T/2\pi$ is therefore the product of time and frequency, or effectively, the number of cycles which have occurred at that center frequency for one calculation time T . N_n is the weighting factor for the power which must be ascertained from experimental data, and represents the number of cycles to failure if that power amplitude were maintained. $\omega_n T/2\pi N_n$ is therefore the linear proportional damage sustained during time T , in the bandwidth centered at f_{c_n} . The proportional damage contained in the entire spectra is then summed in Block 10 and accumulated. As time proceeds, the circuit operates sequentially and updates the estimated fatigue damage at T intervals. This approach might be applied to structures where the loading is random or nearly random. Failure would be expected as the accumulated fatigue index approaches unity.

Blocks 2, 3, 4, 5, and 6 do not concern fatigue damage, but represent an overload protector. Block 2 takes the absolute value of the stress, and Block 3 is a peak detector which maintains an output equal to the highest stress peak that has occurred. If the maximum stress exceeds the limit level which is set at Block 5, the comparator, Block 4, activates an alarm circuit which notifies concerned personnel that the item in question is being subjected to loads which could cause immediate and catastrophic failure, not from fatigue but from a simple overload.

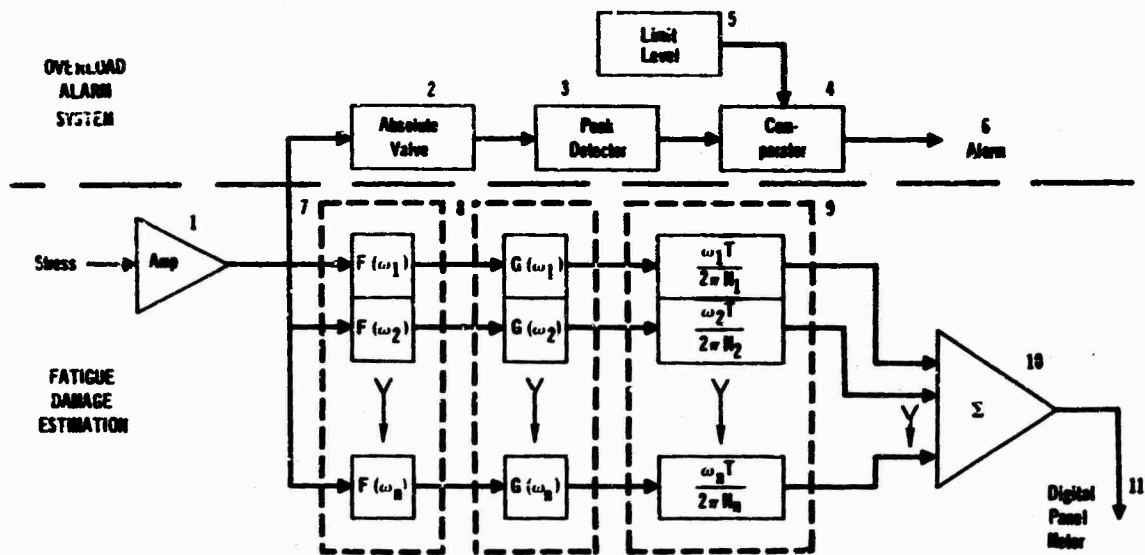


Figure 8 - Fourier Transform Approach to Linear Fatigue Damage Estimation

When the frequency content of the stress time history is fairly well defined and the loading could be described as almost periodic, or distorted modulated sinusoidal, the system shown in Figure 9 might be applied. The stress enters, as before, through an instrumentation amplifier and passes to Blocks 2, 7, and 8. Blocks 2, 3, 4, etc., comprise an overload alarm which is identical to that described for the previous example. Block 7 detects and holds a peak in the time history, and Block 8 detects and holds the value of the valley which follows the peak being held in Block 7. When Block 8 locks its value, Block 9 starts a delay

reset which will dump the values stored in Blocks 7 and 8 and start these elements searching for the next peak and valley. Just before the reset occurs, Blocks 10 and 11 compute amplitude and mean value from the peak and valley being held. The amplitude generates the number of cycles to failure in Block 13, while Block 12 generates a weighting function based upon the mean stress. The product of the weighting factor and the number of cycles to failure is inverted in Block 15 and accumulated in Block 16 upon signal from Block 9. The meter, Block 17, reveals the content of the accumulator. This represents the expended fatigue life as a fractional index.

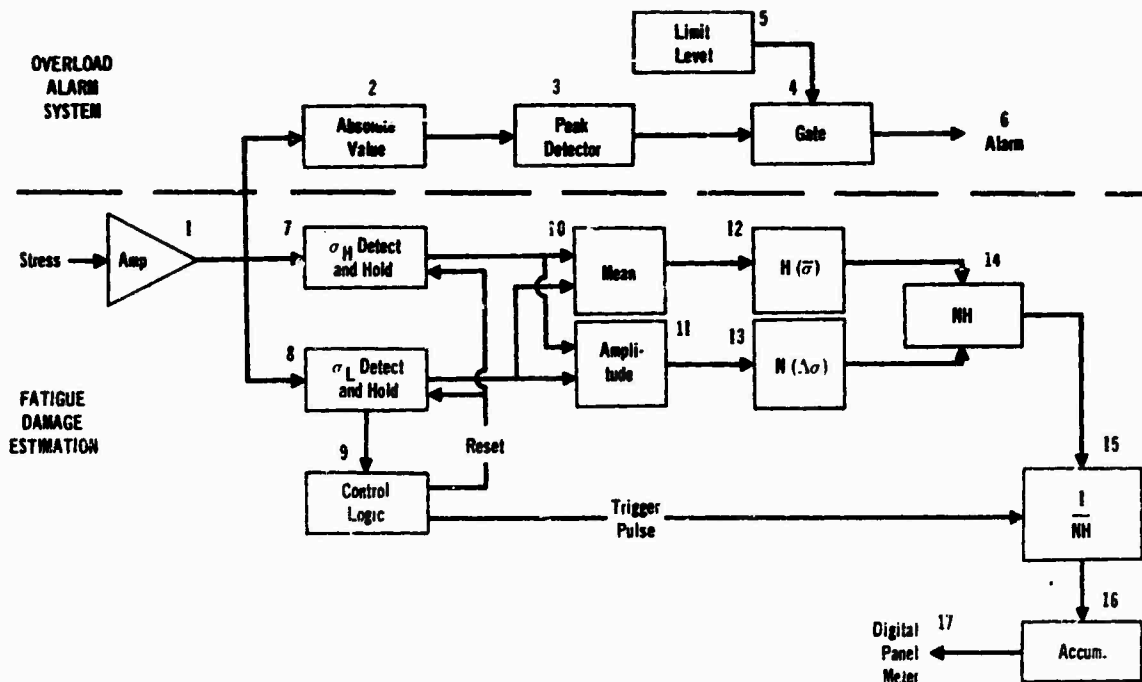


Figure 9 - Discrete Cycle Approach to Fatigue Damage Estimation

This discrete approach is being considered for application to a protection system for internal balances which are used to measure force and moments on scale model aircraft in wind tunnel tests. A series of potentially catastrophic structural failures of the balance components led to a failure analysis which indicated that these failures were due to fatigue. It is anticipated that a fatigue and overload device such as shown in Figure 9, together with an adequate inspection system, could eliminate the danger of a catastrophic failure and possible loss or damage to a very expensive model and an even more expensive wind tunnel.

Application of analog techniques to buffet is still in the speculative stage, but may have real potential. Under consideration at the present time is a scheme which yields on-line statis-

tical analysis of many channels of fluctuating pressure data simultaneously. Also being considered is a system that would allow the engineer to obtain cross-correlations between groups of pressure cells, thereby correlating integrated force patterns rather than individual pressures. The preliminary circuit design and cost analysis on these systems are not complete, and it is therefore not known whether or not they are economically feasible.

SUMMARY

Experience at McDonnell Aircraft Company has proven that in many cases a special-purpose analog device can be constructed and used to reduce dynamic data and/or monitor and edit raw data for later digital computer application with substantial savings in both time and money.

SHOCK LOADING AND HOLOGRAPHIC INTERFEROMETRY IN NDT

R. L. Johnson, R. Aprahamian and P. G. Bhuta

TRW Systems Group
Redondo Beach, California

A brief summary of the principles of holography and holographic interferometry using both the continuous and pulsed laser is given. Photographs of the holographic interferograms obtained of waves propagating in beams and plates are included. The surface displacement of the bodies was obtained from the hologram at specific times and is compared with calculated results. The calculated and experimental results show excellent agreement. Finally, an application of pulsed laser holographic interferometry to nondestructive testing, a subject of great current interest, is included.

INTRODUCTION

Pulsed laser holographic interferometry offers an excellent method for the study of dynamic events. The utility of pulsed laser holographic interferometry is due to the intensity and rapidity of the light pulses produced by the ruby laser. Sufficient intensity for the construction of a hologram can be obtained using pulse widths of as small as 30 nanoseconds and the pulses can be produced at intervals as small as 1 microsecond. As a result the entire process of constructing a doubly exposed holographic interferogram can be completed in a time ($\sim 10^{-6}$ seconds) short compared with the period of natural events. Thus no special precautions need to be taken to ensure stability of platform or ambient air as is necessary when using continuous wave (cw) laser holography. By employing suitable filters and shutters pulsed laser holographic interferometry can be performed in a normal daylight work environment.

This paper contains the results of several experiments to measure the surface displacement caused by the impact loading of beams and plates. The impact loading was effected by striking the surface of the object using a ballistic pendulum. Reference exposure of the surface was made just prior to impact. Subsequent exposure of the film to the ruby laser after selected time intervals resulted in interferograms giving the displacement of the surface at that instant. By making several sequential holograms the displacement time history of the surface wave can be recorded. The data obtained are very accurate since no instrumentation need be mounted on the test object and errors inherent in accelerometer or

strain gages calibration are avoided.

When the plate or beam is not mechanically homogeneous, that is, it contains voids or cracks, the holographic interferograms obtained contain a record revealing the presence of the imperfection. This is because imperfections in the material scatter or diffract the impinging wavefront and act as a secondary source which produces a wavefront that interferes with the wave produced by ballistic impact. As a result imperfect panels or plates will display a characteristic signature on the holographic interferogram. The signature can be used to determine the presence of voids, cracks or imperfections in both homogeneous and composite materials. Thus a nondestructive testing technique of potential wide applicability is available for the purpose of inspecting structures.

An experiment was performed using a composite beam fabricated of aluminum plates and aluminum honeycomb. Selected areas of the honeycomb were debonded from the plate. A pulsed laser holographic interferogram was made of the surface of the plate to record the wave induced by impact of a ballistic pendulum. The interferogram clearly showed the existence of the debonded areas.

TECHNIQUE OF HOLOGRAPHY

The term "holography" is used to describe a means of recording the amplitudes and phases of waves, such as light waves or sound waves. Holography originated with Gabor (Ref. 1) who pointed out the possibility of recording (on a piece of photographic film) the amplitudes and

phases of coherent, monochromatic light waves transmitted through a transparent object. By then projecting light through the photographic film (which is called a "hologram") it is possible to reproduce a three-dimensional image or the original object.

The reproduction of images as Gabor suggested become practical with the advent of the laser as a source of monochromatic, coherent light. In 1964, Leith and Upatnieks (Ref. 2) demonstrated that a three-dimensional image of an opaque object could be reconstructed in a manner similar to that proposed by Gabor. Figure 1 shows a typical set-up of the apparatus used in the Leith and Upatnieks holographic method.

In making the hologram, the light waves from the object (object beam) interact with the light from the mirror (reference beam). When the light from the mirror is in phase with the light from the object, the waves add; conversely, the waves cancel one another when they are out of phase. This type of interaction results in variations in the intensity of the light striking the photographic film (these are spatial variations in intensity, in the plane of the hologram.) Since photographic film reacts to the intensity of light impinging on it, the exposed film gives a permanent record of the interaction of the two light beams.

To reconstruct the image of the object from the hologram, the developed photographic film is illuminated with any monochromatic light source, e.g., the original laser. Now the light interacts with the hologram, and the result is a three-dimensional image of the original object.

HOLOGRAPHIC INTERFEROMETRY

Although image reconstruction was one of the first applications of holography, a technique that has more potential from a research standpoint is "double-exposure holography," which is one form of holographic interferometry (Ref. 3). The essential ideas are as follows: first make a hologram of the object you wish to examine; then subject the object to loads which cause it to deform, and expose the same hologram for a second time. Now when this "double-exposed hologram" is developed and then illuminated, two images are produced: one is from the undeformed body, the other from the deformed body. These light waves (which form the two images) interact with one another, thereby creating interference fringe patterns. By analyzing the fringe patterns, one can determine the surface deformations of the body, which were caused by the applied load. Haines and Hildebrand (Ref. 4) give expressions which show how to relate the interference fringes with the surface deformations of the object. An extensive mathematical description of holographic interferometry was presented recently in Ref. 5.

SHOCK LOADING OF BEAMS AND PLATES

Holographic interferometry is exemplified by pulsed laser holography, which was used to record transverse waves propagating in beams and plates. First, the laser was pulsed once to expose the hologram to the stationary target. Then a stress wave was initiated in the target, and a second laser pulse was timed to expose the hologram when the wave had traveled a given time.

The beam (6061-T6 Aluminum) used in this study measured 6' long x 1" wide x 1/4" thick.

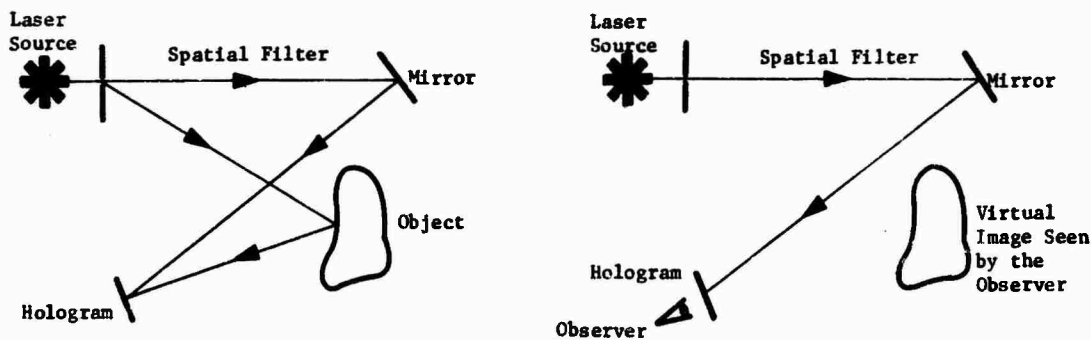


Figure 1 Left: Image Recording Process

Right: Image Retrieval

The experimental set up used to obtain the holographic interferograms of the transverse stress waves in the beam is shown in Figure 2.

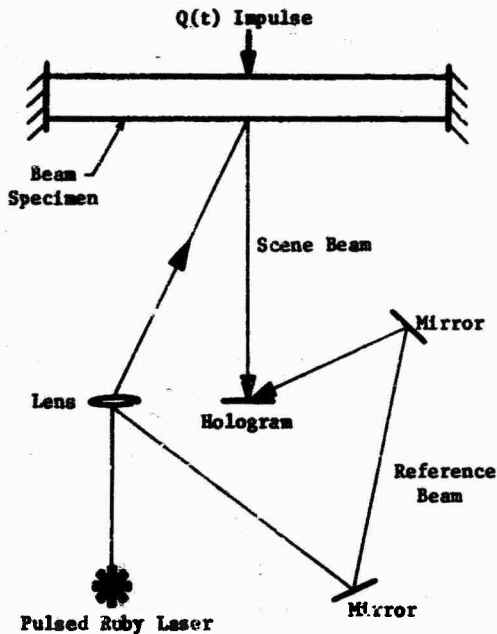


Figure 2 Schematic of Optical Arrangement

Referring to Figure 2, light is passed from the pulsed laser through a negative lens and thence to the front surface of the specimen. This light reflects from the specimen and forms the scene beam for the hologram. Some of the light reflects from the front surface of the negative lens and is directed by mirrors to serve as the reference beam for the hologram. A continuous wave laser was used to align the lens and mirror arrangement and thereby insure uniform illumination of the specimen and the hologram.

A basic experimental problem which had to be overcome was to pulse the laser at a particular time delay, Δ , after initiation of the wave. The timing of the laser was accomplished electronically, using two oscilloscopes with variable time-delays.

The test procedure was to first pulse the laser and make a hologram of the stationary beam, then release the pendulum and initiate the timing sequence to again expose the hologram when the flexural wave was in the beam. Several interferograms were made in this fashion, with time delays of 12.5, 25, and 50 μ sec after initiation of impact. These double-exposure interferograms were later reconstructed by a continuous-wave laser and then photographed. The resulting photos are shown in Figure 3. Qualitatively, the fringes represent constant displacement curves. It is

interesting (but not surprising) to note that at 12.5 μ sec after impact the beam acted much like a plate. This is evidenced by the geometry of the fringe pattern, i.e., circular. At later times, i.e., 25 and 50 μ sec after impact, the fringes indicate the transverse wave is very much plane.

These resulting interferograms may be interpreted to provide quantitative data regarding the surface deformations of the beam resulting from the impact. It may be shown (Ref. 6) that an interference fringe forms whenever the displacement, w , satisfies the condition

$$w = \frac{(2n - 1)\lambda}{2(\cos\theta_1 + \cos\theta_2)}, \quad n = 1, 2, 3, \dots$$

where

λ = wavelength of the laser light, 6943 \AA .

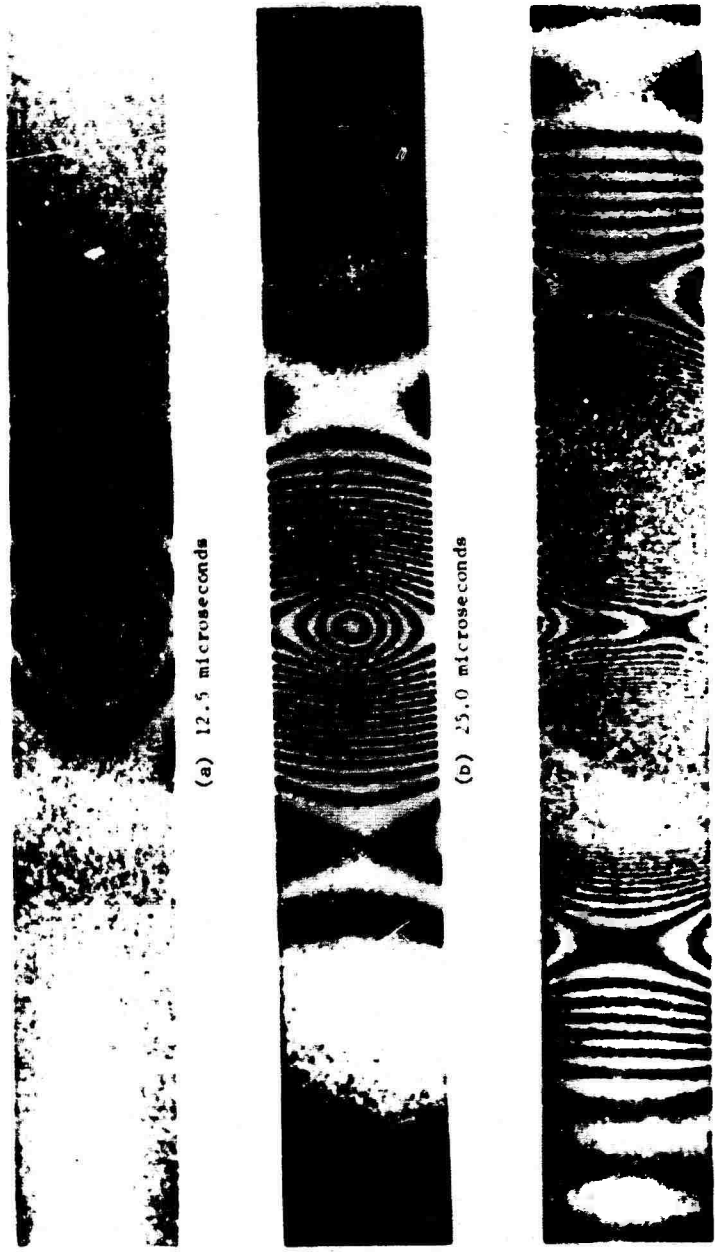
θ_1 = angle between the displacement vector, \vec{w} , and the light illuminating the beam.

θ_2 = angle between the displacement vector, \vec{w} , and the light reflecting from the beam to the hologram.

Data reduction from the interferograms shown in Figure 3 is presented in Figure 4. Also shown in Figure 4 is the beam displacement as determined by a computer program. The model used for the computer program was a one-dimensional beam. This accounts for the greater discrepancy at early times (i.e., 12.5 μ sec when the actual beam acted more like a plate) than at later times.

The same experimental set up used to study the beam was used to study transverse wave propagation in plates. The plate used for this study was made from stock aluminum (6061-T6) measuring 12" square by 1/8" thick. The experimental procedure and data reduction techniques described for the beam are identical for the plate. Eight separate holographic interferograms were made of the transverse waves, differing only in time delays, viz 10, 20, 40, 60, 80, 130 and 150 μ sec after impact. The resulting interferograms are shown in Figures 5 and 6. On at least two occasions, 130 and 150 μ sec, the leading front of the stress pulse reflected from the edges of the plate and began to propagate back toward (but not reaching) the center. This is evidenced by the "rippled" behavior of the fringe patterns on the interferograms. The data reduced from these interferograms are compared with theoretical displacement curves generated by a computer program, Figures 7 and 8. Two-dimensional plate theory was used to model the plate for the computer program. As is evidenced by Figures 7 and 8, good agreement was achieved.

An experiment was performed at TRW using pulsed laser holographic interferometry to



(a) 12.5 microseconds

(b) 25.0 microseconds

(c) 50.0 microseconds

Figure 3 Holographic Interferograms of a Bending Wave in a Clamped-Clamped Beam

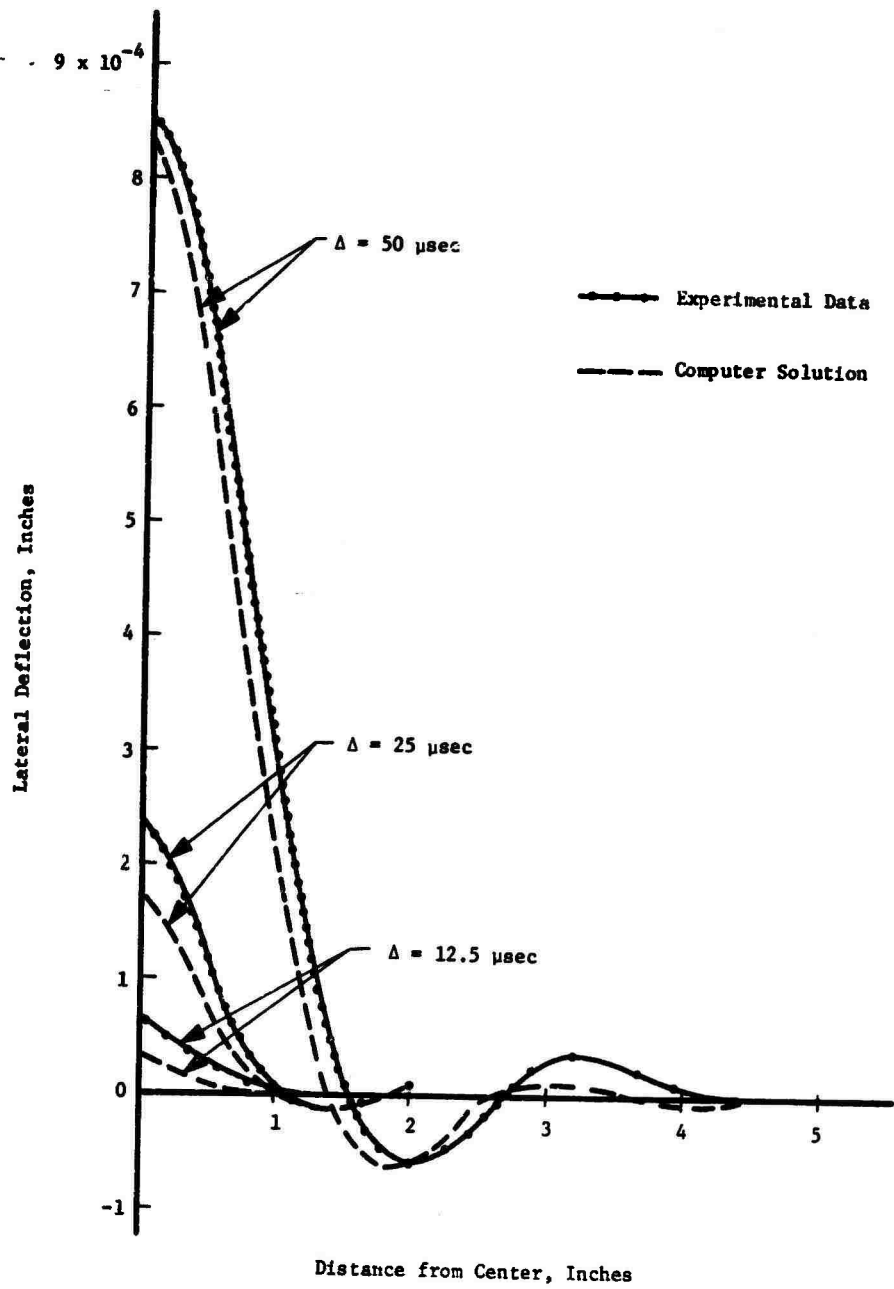


Figure 4 Lateral Deflection (y) vs. Distance Along the Beam (x)



(a) $\Delta = 10 \mu\text{sec}$



(b) $\Delta = 20 \mu\text{sec}$



(c) $\Delta = 40 \mu\text{sec}$



(d) $\Delta = 60 \mu\text{sec}$

Figure 5 Interferograms Showing Bending Wave in the Plate



(a) $\Delta = 80 \mu\text{sec}$



(b) $\Delta = 100 \mu\text{sec}$



(c) $\Delta = 130 \mu\text{sec}$



(d) $\Delta = 150 \mu\text{sec}$

Figure 6 Interferograms Showing Bending Wave in the Plate

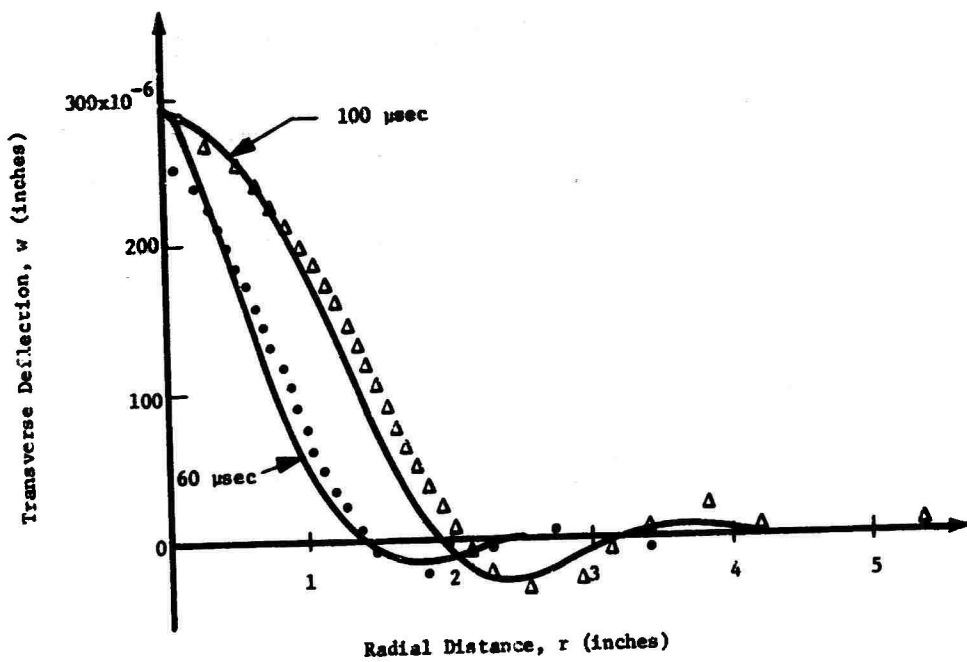
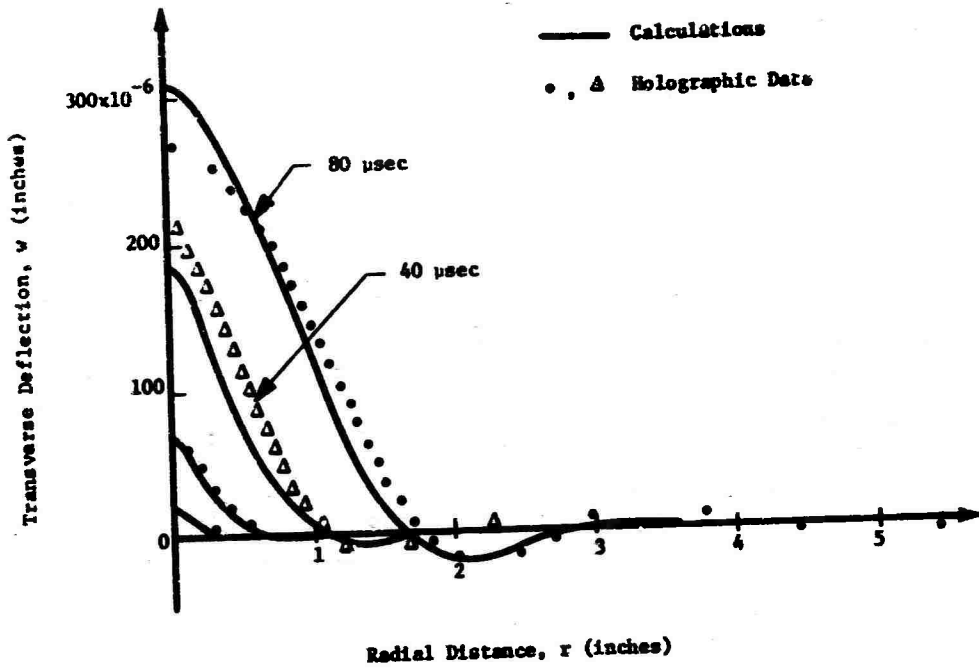


Figure 7 Measured and Calculated Deflection Shapes (Early Times)

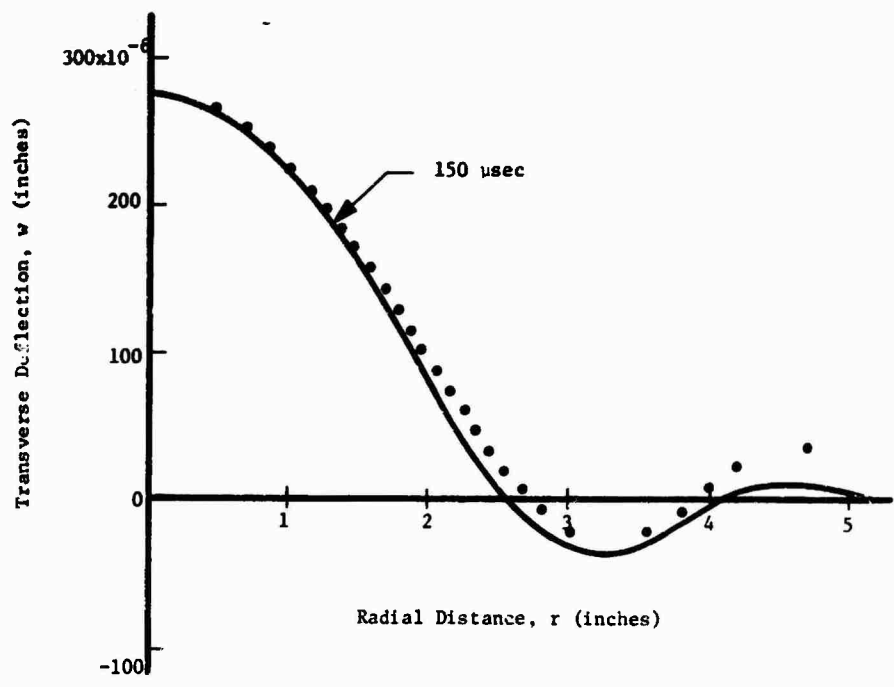
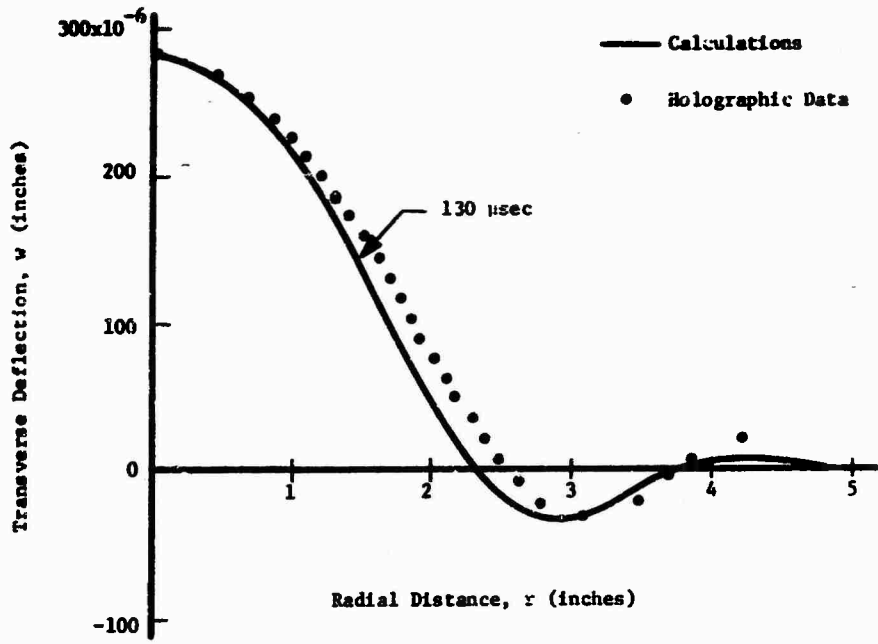


Figure 8 Measured and Calculated Deflection Shapes (Later Times)

nondestructively test a honeycomb panel. The honeycomb panel measured approximately 4" in width, 1/2" in thickness and 18" long. It was constructed out of an aluminum core and aluminum skin. The experimental arrangement used is shown in Figure 9. Referring to Figure 9, light from the pulsed laser was expanded using a simple lens. Light reflected from the honeycomb panel served as an object beam, while light reflected from the mirror served as a reference beam. The honeycomb panel was arranged so that the front surface faced the hologram. A ballistic pendulum was arranged so that it would strike the honeycomb panel from the rear. A multipulsed laser was used to obtain a holographic interferogram. The timing between pulses was arranged so that the first pulse occurred just prior to impact and the second pulse was 80 microseconds after impact. Figure 10a and 10b show the top and front view of the honeycomb panel, respectively. Figure 10c shows a photograph taken of the image reconstructed by the holographic interferogram. The general nature of the fringes is very similar to that obtained during the beam experiments, e.g., Figure 10b. A careful examination of Figure 10c, however, reveals three distinct anomalies in an otherwise smooth fringe pattern. These anomalies verify the existence of the known flaws in the specially prepared sample.

REFERENCES

1. Gabor, D., "Microscopy by Reconstructed Wavefronts," *Proc. Roy. Soc. Series A*, Vol. 197, 1949.
2. Leith, E.M., and Upatnieks, J., "Wavefront Reconstruction with Diffuse Illumination and Three-Dimensional Objects," *J. Opt. Soc. Amer.*, Vol. 54, November 1964.
3. Neffinger, L.O. Wuerker, R.F., and Brooks, R.E., "Holographic Interferometry," *J. Appl. Phys.*, Vol. 37, Feb. 1966, p. 642-649.
4. Haines, K.A., and Hildebrand, B.F., "Surface Deformation Measurement Using the Wavefront Reconstruction Technique," *Applied Optics*, Vol. 5, No. 4, April 1966, pp. 595-602.
5. Brown, G.M., Grant, R.M. and Stroke, G.W., "Theory of Holographic Interferometry," *J. Acoust. Soc. Amer.*, Vol. 45, No. 5, May 1969, pp. 1166-1179.
6. Aprahamian, R., "Some Useful Equations Used in Holography," TRW Report No. AM 70-2, January 1970.

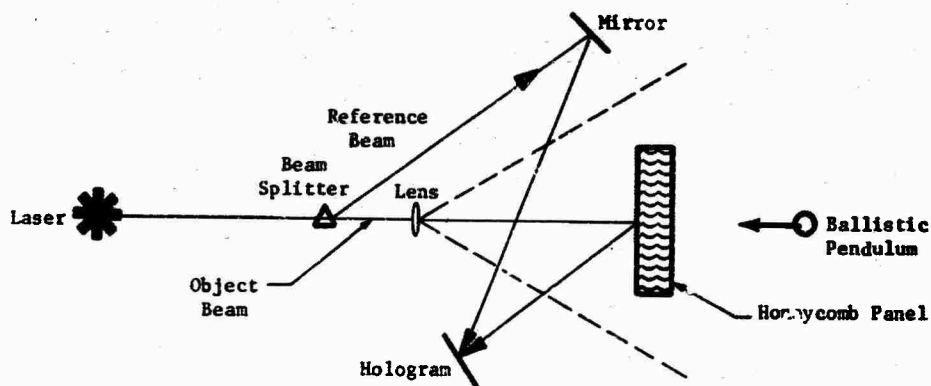
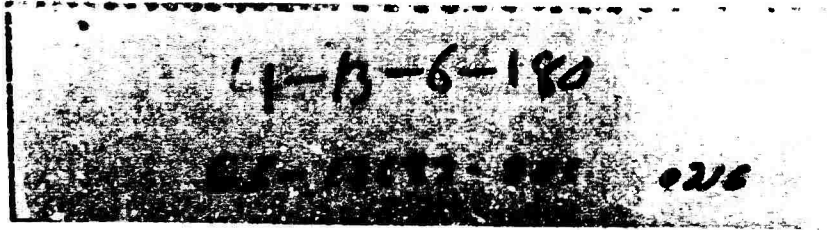


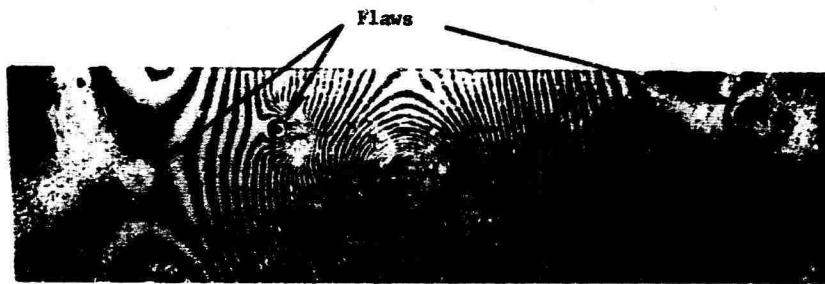
Figure 9 Experimental Setup to Inspect Honeycomb Panels with Pulsed Lasers



(a)



(b)



(c)

Figure 10 NDI of Honeycomb Panels
a) Top view of panel showing the core
b) Front view of panel
c) Holographic interferogram showing defects in the honeycomb panel

DISCUSSION

Mr. Ashley (University of Birmingham): Is it a very tedious procedure to get from the hologram to the displacement data, or is there some sort of automatic data processing involved?

Mr. Johnson: It is tedious the way we did it on this particular case. We finger counted or hand counted the fringes. We thought of techniques where you might use a thin pencil light in a photocell to scan it and count fringes in a raster-like pattern very quickly. I do not know that such a device is actually working though.

Mr. Ripperger (University of Texas): Can you get absolute values of the displacements or are these all relative?

Mr. Johnson: The ones you saw are absolute because the first exposure of the holographic film was made before the beam had moved. You can obtain a relative exposure, too. You can make the first exposure while the beam is in motion and then make subsequent exposures, say, a microsecond later. In this case the interference fringes correspond to the displacement between the two exposures.

Mr. Ripperger: Then you could also get displacement results if the surface you are viewing moves as a plane and you do not have any fringes?

Mr. Johnson: Yes, you can measure in-plane displacements. We have measured both in-plane and out-of-plane displacements.

Mr. Ripperger: That was not what I meant. If the surface that you are looking at moves as a plane you will not see any fringes.

Mr. Johnson: That is right. You have to have a reference point. To picture the mushroom in principle would allow you to find a displacement at every point of the mushroom surface. In the case of the plate experiments, beyond the front of the wave, the plate has not been displaced and so you can start counting fringes from there—that is a zero displacement point.

Mr. Eckblad (Boeing Company): Another practical question: Is this measuring device very sensitive? If you have it in a shock environment observing relative motions is there a way you can get around that? Or apply it?

Mr. Johnson: Continuous wave type holographic interferometry is very slow and you have to have a controlled environment. You need a granite table and a very stable environment. Using pulsed holographic interferometry you can complete the process in a microsecond. Usually this is a time short compared to the lifetime of most natural events, such as wind current changes, and things of that nature. It should be possible to use this type of apparatus in a fairly rough environment if you are using pulsed laser holographic interferometry.

Mr. Eckblad: Is it expensive?

Mr. Johnson: Yes, a pulsed laser costs about \$25,000 to \$30,000 for the laser alone. The film is about a dollar shot, it is not very expensive. It could probably all be reduced to a machine that would be a lot quicker and more functional than the laboratory type of apparatus we are using.

DATA ANALYSIS

A NEW SYNTHESIS TECHNIQUE FOR SHOCK SPECTRUM ANALYSIS

William G. Pollard
Spectral Dynamics Corporation of San Diego
San Diego, California

A new shock spectrum analyzer approach is presented which synthesizes 120 filters to provide primary, residual and maximax shock spectrums. The new technique uses only one single-degree-of-freedom filter. The 120 filter locations are generated by sequentially modifying the input excitation time function 120 times.

DEFINITIONS

Conceptually, shock spectrum is defined as the maximum response of an array of m number of single-degree-of-freedom systems to an input transient excitation. The shock spectrum is composed of two components of information referred to as primary and residual shock spectrums. Primary shock spectrum is defined as the maximum transient response of each single-degree-of-freedom system during the application of the input excitation. The residual shock spectrum is the maximum response of each system after the termination of the input excitation. Shock spectrum, sometimes called composite or maximax response, is the maximum of the combined primary and residual shock spectrum.

SHOCK SPECTRUM ANALYZER TECHNIQUES

There are three common techniques for performing shock spectrum analysis. One of the techniques employs an array of single-degree-of-freedom electronic filters with a transfer function defined by $H_n(S)$. Primary shock spectrum is defined by:

$$\text{Primary Shock Spectrum} = \text{Max} \sum_{n=1}^m \mathcal{L}^{-1} \left[H_n(S) \int_0^{\tau} e(t) e^{-st} dt \right] \quad (1)$$

Where \mathcal{L}^{-1} denotes the inverse Laplace Transform and τ is the time duration of the input excitation, $e(t)$. Residual shock spectrum is defined by:

$$\text{Residual Shock Spectrum} = \quad (2)$$

$$\text{Max} \sum_{n=1}^m \mathcal{L}^{-1} \left[\overline{H}_n(S) \right]$$

Where $\overline{H}_n(S)$ includes the initial conditions of the single-degree-of-freedom filter $H_n(S)$ at time, τ .

A second technique solves the differential equation defined by $H_n(S)$ with an input forcing function, $e(t)$. The m number of solutions equivalent to m single-degree-of-freedom filters is obtained by sequentially incrementing the differential equation coefficients m times. The transient and steady state solutions provide primary and residual shock spectrums respectively.

A third technique relies on obtaining the magnitudes of the Fourier spectrum of the input excitation. A common way of obtaining the Fourier magnitudes is to employ a narrowband, heterodyne type real time spectrum analyzer. Volume 2 of the Shock and Vibration Handbook states that although the shock spectrum and Fourier spectrum are fundamentally different, there is a partial correlation between them. Only residual shock spectrum is analytically related to the absolute magnitude $|F(j\omega_n)|$, of the Fourier spectrum for the special case of a lossless filter, $\zeta = 0$. This relationship is given by

$$\text{Residual Spectrum} \Big|_{\zeta=0} = K u_n \left| F(j\omega_n) \right| \quad (3)$$

where K is a scale factor and u_n is the frequency at which $F(j\omega_n)$ is evaluated. The major

disadvantage of this approach is that primary and maximax spectrums are not obtained. Furthermore, comparison of the output peak responses of the type of filter used in the heterodyne technique with that of a single-degree-of-freedom, low-pass filter, shows that the results do not agree and the heterodyne technique does not yield correct primary spectrum information. For example, if a rectangular pulse of height A is inputted to a low-pass, lossless filter of $\zeta = 0$, the output during the applied pulse is a constant amplitude cosine wave independent of pulse duration with amplitude excursions between 0 and $2A$. For this example, the filter output time response is given by

$$e_n(t) = A(1 - \cos \beta_n t) \quad (4)$$

where β_n is the filter frequency. Now consider the same rectangular pulse to be heterodyned and inputted into a lossless, narrowband filter of the type used in real time analyzers. The filter output during the applied pulse for this case is given by

$$e_h(t) = \frac{AY\beta}{Y^2 - \beta^2} (\cos \beta t - \cos \gamma t), \quad (5)$$

where Y is the heterodyne carrier frequency which is incremented m times to cover the frequency range of interest. Comparing the two results reveals that the responses during the applied pulse do not agree. The filter response for the heterodyne technique is Y dependent as opposed to the constant amplitude response for any β_n . Attractive as this approach is, it is unfortunate that only residual shock spectrum is available from Fourier spectrum information.

NEW SHOCK SPECTRUM ANALYZER APPROACH *

As a preliminary step to describing the new approach, consider the characteristics and responses of an array of m number of single-degree-of-freedom systems as shown in Fig. 1.

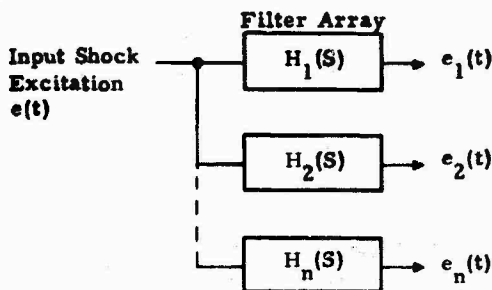


Fig. 1 - Array of Single-Degree-Of-Freedom Systems

* Patent applied for

The transfer function, $H_n(S)$, displayed in the S -plane has the form shown in Fig. 2.

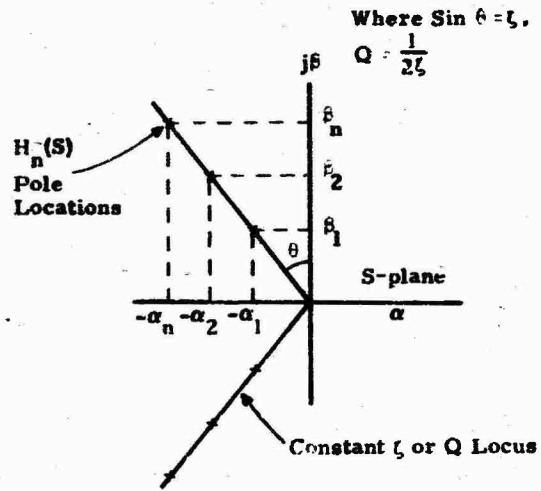


Fig. 2 - Single-Degree-Of-Freedom Filter

The output, $E_n(S)$, in the S -plane is computed by the products of

$$E_n(S) = E(S) H_n(S) \quad (6)$$

where $E(S)$ is the Laplace transform of the input excitation, $e(t)$. The output time response is arrived at by taking the inverse transform.

$$e_n(t) = \mathcal{L}^{-1}[E_n(S)] = \mathcal{L}^{-1}[E(S) H_n(S)] \quad (7)$$

$H_n(S)$ has the form of

$$H_n(S) = \frac{\alpha_n^2 + \beta_n^2}{(S + \alpha_n)^2 + \beta_n^2} \quad (8)$$

for a single-degree-of-freedom system. As seen from the S -plane plot of Fig. 2, ζ is 0 for a lossless system which gives for $H_n(S)$,

$$H_n(S) \Big|_{\zeta=0} = \frac{\beta_n^2}{S^2 + \beta_n^2} \quad (9)$$

For purposes of comparing results of the proposed filter synthesis technique and the single-degree-of-freedom filters defined by $H_n(S)$, the output responses will be computed for a step, a step ramp and a step sine wave as defined in Fig. 3.

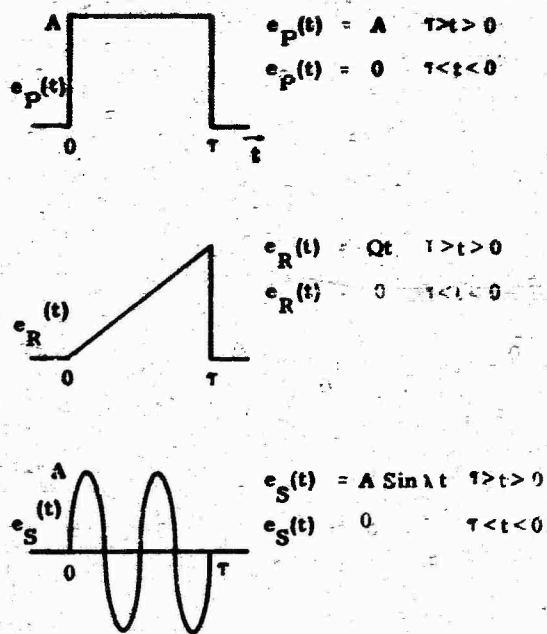


Fig. 3 - Input Excitations

The output responses over the period τ for inputs of $e_P(t)$, $e_R(t)$ and $e_S(t)$ for a filter ζ of zero are respectively,

$$e_n(t) = A(1 - \cos \beta_n t) \quad (10)$$

$$e_n(t) = Q \left(t - \frac{\sin \beta_n t}{\beta_n} \right) \quad (11)$$

$$e_n(t) = \frac{A \lambda \beta_n^2}{\alpha_n^2 - \lambda^2} \left(\frac{\sin \lambda t}{\lambda} - \frac{\sin \beta_n t}{\beta_n} \right) \quad (12)$$

With the filter $\zeta \neq 0$, the output responses over the period τ for inputs of $e_P(t)$, $e_R(t)$ and $e_S(t)$ are

$$e_n(t) = A \left[1 - \frac{(\alpha_n^2 + \beta_n^2)^{1/2}}{\beta_n} e^{-\alpha_n t} \sin(\beta_n t - \psi_1) \right] \quad (13)$$

$$\text{Where } \psi_1 = \tan^{-1} \frac{\beta_n}{-\alpha_n}$$

$$e_n(t) = \quad (14)$$

$$\frac{Q}{(\alpha_n^2 + \beta_n^2)^{1/2}} \left[t - \frac{2}{\alpha_n} \frac{\sin \beta_n t}{\beta_n} + \frac{e^{-\alpha_n t}}{\beta_n} \sin(\beta_n t - \psi_2) \right]$$

$$\text{Where } \psi_2 = 2 \tan^{-1} \frac{\beta_n}{-\alpha_n}$$

$$e_n(t) = \frac{A \lambda (\alpha_n^2 + \beta_n^2)^{1/2}}{[(\alpha_n^2 + \beta_n^2 - \lambda^2)^2 + 4 \alpha_n^2 \lambda^2]^{1/2}} \times$$

$$\left\{ \frac{\sin(\lambda t - \psi_3)}{\lambda} - \frac{e^{-\alpha_n t}}{\beta_n} \sin(\beta_n t - \psi_4) \right\}$$

$$\text{Where } \psi_3 = \tan^{-1} \frac{2 \alpha_n \lambda}{\alpha_n^2 + \beta_n^2 - \lambda^2} \quad (15)$$

$$\text{and } \psi_4 = \tan^{-1} \frac{-2 \alpha_n \beta_n}{\alpha_n^2 - \beta_n^2 + \lambda^2}$$

Eqs. (10) through (15) define the filter output response from $t = 0$ to $t = \tau$ where the maximum peak amplitude during the time τ defines the primary amplitude for filter channel n . The residual would be computed by the use of Eq. (2).

A new technique to synthesize m number of single-degree-of-freedom filters which preserves the correct primary and residual information is under development. The first technique described mechanizes m number of parallel, contiguous filters. The m number of filters are spaced over the frequency range of interest and the closeness of the frequency spacing determines the resolution of the measurement. For example, to cover three decades of frequency with a spacing of 1/12 octave steps requires 120 filters, $m = 120$. Employing the parallel filter approach would require 120 separate filters where each filter is separately tuned for frequency and Q . The proposed synthesis technique fundamentally replaces the 120 filters with only one filter which greatly simplifies instrument maintenance and calibration. A conceptual block diagram showing the approach to generate the equivalent of many different filter outputs with a single filter is presented in Fig. 4.

The input shock excitation, $e(t)$, is entered into the time scale converter which changes the input time scale by a factor a_n . The a_n controller increments a_n in m number of steps to cover a specified frequency range. Each a_n generates a new time function to be entered into the fixed filter, $G(S)$. For each unique a_n , a unique transient and steady state filter response, $e_n(t)$ exists which relates exactly to primary and residual spectrums.

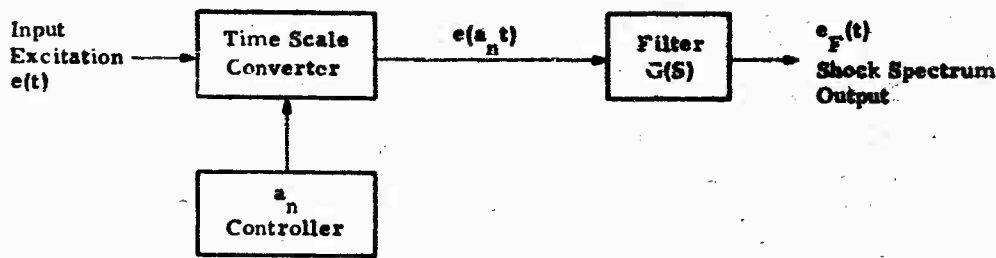


Fig. 4 - Filter Synthesizer

For the system in Fig. 4, the primary and residual shock spectrums are given by

$$\text{Primary Shock Spectrum} = \text{Max} \int_{n=1}^m \mathcal{L}^{-1} \left[G(S) \int_0^{\tau} e(a_n t) e^{-st} dt \right] \quad (16)$$

and

$$\text{Residual Shock Spectrum} = \text{Max} \int_{n=1}^m \mathcal{L}^{-1} \left[\bar{G}(S) \right] \quad (17)$$

where $\bar{G}(S)$ includes the initial conditions at the time of τ/a_n .

A very important aspect of the approach is that the m number of shock spectrum outputs are generated by modifying the input excitation time scale m times and not by changing any physical components or controls to modify filter response. Also the analysis time may be decreased by controlling the minimum a_n . For instance, if a_n were incremented over a range from 10 to 10^6 to cover three decades of frequency, the filter response time would be 10 times faster than the approach using parallel filters covering the same frequency range.

The transforms for the time functions given in Fig. 3 are now recomputed for the new time scale function, $e(a_n t)$, which is the modified time function applied to the filter, $G(S)$. The new transforms for input excitations of a step, a step ramp and a step sine wave are respectively

$$E_P(S) = \frac{A}{S}, \quad E_R(S) = \frac{a_n Q}{S^2}, \quad E_S(S) = \frac{A(a_n \lambda)}{S^2 + (a_n \lambda)^2}$$

The form given by Eq. (7) may be used to compute $e_F(t)$ where

$$e_F(t) = \mathcal{L}^{-1} [E(S) G(S)]$$

and $E(S)$ is defined by $E_P(S)$, $E_R(S)$ and $E_S(S)$ for our analysis.

Over a period τ , the output filter responses for inputs of $e_P(t)$, $e_R(t)$ and $e_S(t)$ for a filter ζ of zero are respectively,

$$e_F(a_n t) = A(1 - \cos \beta t) \quad (19)$$

$$e_F(a_n t) = Q(a_n t) - \frac{Q}{(\beta/a_n)} \sin \beta t \quad (20)$$

$$e_F(a_n t) = \frac{A(\beta/a_n)^2}{(\beta/a_n)^2 - \lambda^2} \left[\frac{\sin \lambda(a_n t)}{\lambda} - \frac{1}{(\beta/a_n)} \sin \beta t \right] \quad (21)$$

With the filter $\zeta \neq 0$, the output responses over the period τ for $e_P(t)$, $e_R(t)$ and $e_S(t)$ are respectively

$$e_F(a_n t) = A \left[1 + \frac{(\alpha^2 + \beta^2)^{1/2}}{\beta} e^{-\alpha t} \sin(\beta t - \psi_1) \right] \quad (22)$$

$$\text{where } \psi_1 = \tan^{-1} \frac{\beta}{-\alpha}$$

$$e_F(a_n t) = \left(\frac{Q}{\alpha^2 + \beta^2} \right) \times \quad (23)$$

$$\left[a_n t - \frac{2}{(\alpha/a_n) + (\beta/\alpha)(\beta/a_n)} + \frac{e^{-\alpha t}}{(\beta/a_n)} \sin(\beta t - \psi_2) \right]$$

$$\text{where } \psi_2 = 2 \tan^{-1} \frac{\beta}{-\alpha}$$

$$e_F(a_n t) = \frac{A \lambda \left(\frac{\alpha^2 + \beta^2}{a_n^2} \right)}{\left[\left(\frac{\alpha^2 + \beta^2}{a_n^2} - \lambda^2 \right)^2 + 4 \lambda^2 \left(\frac{\alpha}{a_n} \right)^2 \right]^{1/2}} \times$$

$$\left[\frac{\sin \left(\frac{\alpha \lambda t - \psi_3}{\lambda} \right)}{\lambda} - e^{-\alpha t} \sin(\beta t - \psi_4) \right]$$

where $\psi_3 = \tan^{-1} \frac{2 \left(\frac{\alpha}{a_n} \right) \lambda}{\left(\frac{\alpha^2 + \beta^2}{a_n^2} - \lambda^2 \right)}$ (24)

and $\psi_4 = \frac{-2 \left(\frac{\alpha}{a_n} \right) \left(\frac{\beta}{a_n} \right)}{\left(\frac{\alpha^2 - \beta^2}{a_n^2} - \lambda^2 \right)}$

In interpreting Eqs. (19) through (24), it is helpful to refer to Fig. 4. If the input excitation, $e(t)$, entering the time scale converter is to be evaluated at some arbitrary time τ , to give $e(\tau)$; the output of the time scale converter $e(a_n t)$, must be evaluated at τ/a_n to yield the same information. For example, if $\tau = 50$ ms then $e(a_n t)$ would be evaluated at 0.5 ms for an a_n of 100. As pointed out, τ may be any arbitrary time; however, for this application to shock spectrum analysis, one of the times of interest, τ , is that time when the input excitation is terminated.

Rewriting Eqs. (19) through (24) evaluated for τ/a_n gives the following set of equations:

For $\zeta = 0$

$$e_F \left(\frac{\tau}{a_n} \right) = A \left(1 - \cos \frac{\beta}{a_n} \tau \right)$$
 (25)

$$e_F \left(\frac{\tau}{a_n} \right) = Q \tau - \left(\frac{Q}{\beta/a_n} \right) \sin \left(\frac{\beta}{a_n} \tau \right)$$
 (26)

$$e_F \left(\frac{\tau}{a_n} \right) = \frac{A (\beta/a_n)^2}{(\beta/a_n)^2 - \lambda^2} \times$$

$$\left[\frac{\sin \lambda t}{\lambda} - \left(\frac{1}{\beta/a_n} \right) \sin \left(\beta/a_n \tau \right) \right]$$
 (27)

For $\zeta \neq 0$

$$e_F \left(\frac{\tau}{a_n} \right) =$$
 (28)

$$A \left[1 + \left(\frac{\alpha^2}{\beta^2} + 1 \right)^{1/2} e^{-\left(\frac{\alpha}{a_n} \right) \tau} \sin \left(\frac{\beta}{a_n} \tau - \psi_1 \right) \right]$$

$$e_F \left(\frac{\tau}{a_n} \right) = \frac{Q}{\alpha^2 + \beta^2} \times$$
 (29)

$$\left[\tau - \frac{2}{\left(\alpha/a_n \right) + \left(\beta/a_n \right)} + \frac{e^{-\left(\frac{\alpha}{a_n} \right) \tau}}{\left(\beta/a_n \right)} \sin \left(\frac{\beta}{a_n} \tau - \psi_2 \right) \right]$$

$$e \left(\frac{\tau}{a_n} \right) = \frac{A \lambda \left(\frac{\alpha^2 + \beta^2}{a_n^2} \right)}{\left[\left(\frac{\alpha^2 + \beta^2}{a_n^2} - \lambda^2 \right)^2 + 4 \lambda^2 \left(\frac{\alpha}{a_n} \right)^2 \right]^{1/2}} \times$$

$$\left[\frac{\sin \left(\lambda \tau - \psi_3 \right)}{\lambda} - e^{-\left(\frac{\alpha}{a_n} \right) \tau} \sin \left(\frac{\beta}{a_n} \tau - \psi_4 \right) \right]$$
 (30)

A term by term comparison may now be made between the sets of equations defined by Eqs. (10) through (15) and (25) through (30). Recall that β takes on m different values, as shown in Fig. 1, to span the frequency range of interest. Note, in comparing Eqs. (15) and (30) that the variable filter terms α and β are duplicated by terms α/a_n and β/a_n . By varying a_n , the terms may be made to take on exactly the same values as the terms defined by α and β . Therefore, in the first technique making α_n and β_n take on m different values by having m different filters, the equivalent may be accomplished by using one filter and letting a_n take on m different values. Further cross comparisons of corresponding terms in the two sets of equations show the same pattern of equivalence, that is

for every τ , τ_n there is an equivalent τ/a and τ/a_n . This demonstrates that at any arbitrary time, the filter amplitude responses of both approaches are the same. Since the two filter forms are the same and both have the same initial conditions at any arbitrary times of τ and τ/a respectively, it follows that the residual responses are the same.

CONCLUSIONS

The method of processing the information through the time scale converter offers considerable flexibility in shock spectrum analysis. Simply by changing the rate of processing the information in the time scale converter, the input frequency range coverage may be changed. Two frequency ranges are made available, one range covering 1 Hz to 1 kHz and the other range 10 Hz to 10 kHz providing the capability to store transients of 1 second and 100 ms dura-

tions, respectively. The filter locations are changed readily by inputting a new set of a 's with different spacing which provides the capability to change the frequency resolution in frequency regions of interest. The number of filter locations may also be increased by increasing the number of a steps; however, the maximum number of filter channels is determined by the filter Q .

The input transient signal is captured and stored in memory which permits viewing of the original input transient. Because of the temporal speed up, the input signal may be displayed without flicker. For example, a 100 ms transient could be displayed at a 100 Hz rate for an a of 10 whereas, without the speed up, the maximum display rate would be 10 Hz. A digital memory stores the 120 outputs of the filter which holds the shock spectrum data indefinitely without decay.

THE ROLE OF LATENT INFORMATION IN INFORMATION
PROCESSING IN MEASURING SYSTEMS

Peter K. Stein
Professor of Engineering
Arizona State University
Tempe, Arizona

The role of latent information in transducers is defined and discussed. All material properties, all coefficients of scalar, vector, tensor, or field quantities, and all transducer performance coefficients are latent information parameters, (LIPs). Such LIPs must be activated so that the information they contain is available for processing in a measuring system.

A systematic study of these LIPs yields a new conceptual model for a transducer, as an information-and-energy-flow device. Information processing (including conversion) is clearly distinguished from energy processing (including conversion). Since measurement is concerned with information flow, this distinction leads to an extension of the Unified Approach to the Engineering of Measurement Systems. A small portion of this approach is presented in this paper, to show that a methodical, systematic approach to the design of measuring systems exists. The presentation shows hitherto unsuspected affinities between transducer families, and hitherto unsuspected transducer families are a natural outgrowth of the methods of investigation presented here. Educational producers and industrial consumers of engineers should be aware that engineers proficient in the new field of Measurement Systems Engineering are being deliberately educated, and are available.

MEASUREMENT

The basic purpose of a measuring system is to obtain information about some state or process being investigated. Information can exist in two forms: Latent and Activated. In both forms it can be identified by the new and original definition of information particularly suitable for measurement engineers, given elsewhere [1, 2] and summarized below:

INFORMATION OF ANY KIND MUST EXIST
on some pattern
of some property
of some wave shape
of some quantity

The quantity on the wave shape of which some pattern of properties identifies the existing information can be in two forms, as shown in Table I.

It must be remembered that information can not be processed without energy transfer, and that every component in a measuring system must be considered in the path of BOTH a flow of information and a flow of energy. To organize and study the field of measurements, the established terminology developed for the Unified Approach to the Engineering of Measuring Systems will be used. A summary of the basic definitions is given below. These are different from current usage and should therefore be studied carefully before proceeding further [1,2,3].

TABLE I: FORMS OF INFORMATION

FORM OF THE INFORMATION	FORM OF THE INFORMATION-CARRYING QUANTITY
Latent Information	Latent Information Parameters (LIPs)
Activated Information	Energy Components and Their Derivatives

DEFINITIONS AND TERMINOLOGY

Transducer:	The smallest information-and-energy processing component in a system, which accepts and emits BOTH energy and information.
Sensor:	The smallest component in a measuring system which contains only information, but emits no energy. Note that it took energy to get the information into the sensor.
Structure:	The network of relationships among transducers or sensors, corresponding to the circuit diagram of the electrical engineer.
Processing:	Operations such as reproduction, conversion, shaping, suppression, enhancement, transmission of information (desired in measuring systems) and energy (a necessary by-product of information processing).
Inputs/Outputs:	The inputs and outputs from all transducers are pairs of quantities, the product of which exhibits the dimensions of energy, and the ratios between which identify certain latent information parameters to be discussed in this paper. Table II illustrates some of these pairs. Tables IV and V show some of the ratios.
Primary Quantity:	That energy component on the wave shape of which some pattern of properties carries information to be processed. (One at each port.)
Secondary Quantity:	That energy component at each port which necessarily co-exists with the primary quantity.
Measurand:	The quantity to be measured, which can be expressed as time and/or space derivatives of the Primary Quantity, or of ratios of such derivatives for the two energy components involved. Tables III, IV, and V illustrate some Measurands.

LATENT INFORMATION [10]

Information which does not exist on an energy component (such as those in Table II), or on a time and/or space derivative of such a component (such as those shown in Table III), is latent information. As such it is not available for processing until it is activated or interrogated. Latent information exists in all transducers by virtue of their latent information parameters. These can be expressed as the ratio of two energy components, or by the ratio of any time and/or space derivatives of these components. In general, all performance parameters of transducers, such as input, output, and transfer coefficients, and all material properties, are latent information parameters. In general, LIP's can be expressed as:

(Latent Information Parameter)

$$= (\text{Material Properties})(\text{Geometric Factors})$$

Some LIPs are functions only of geometric factors such as shape or position; others are functions only of material properties, but in general, both factors are present.

The most common example of latent information is an impedance. Others are elastic modulus, mass, index of refraction, angle of polarization, and all transfer ratios or sensitivities such as the thermoelectric power of a thermocouple, the gain of an amplifier, the gage factor of a strain gage. All coefficients or parameters of scalar, vector, tensor or field quantities are LIPs. Examples are optical birefringence, dielectric constant, electrical resistivity in single-crystal semiconductors for example, plane of polarization, wave propagation velocity, wave reflection and refraction coefficients, etc. [10].

LATENT INFORMATION PARAMETERS

Latent information parameters divide into two groups:

Homogeneous or Single-Port Parameters: LIPs which are expressed as ratios of the time and/or space derivatives of the energy components which co-exist at a single port (entry or exit) of a transducer, are homogeneous. Tables IV, V, and VI illustrate typical examples. Thus this category includes all input and output parameters (sometimes expressible as impedances). Systematic methods exist for identifying possible LIPs. A simple example will be given below.

Given two physical quantities Q_1 and Q_2 selected dimensionally so that:

$$|Q_1| \cdot |Q_2| = |\text{ENERGY}| \quad (1)$$

TABLE II: SOME COMPONENTS OF ENERGY AND POWER

ENERGY FORM	GENERALIZED FORCE (*)		GENERALIZED DISPLACEMENT (*)		GENERALIZED VELOCITY (*)	
	Quantity	Dimension	Quantity	Dimension	Quantity	Dimension
Electrical	Electric Potential (Voltage) E	$L^2MQ^{-1}T^{-2}$	Quantity of Electricity (Charge) Q	Q	Electric Current I	QT^{-1}
Magnetic (*)	Magnetic Potential ϕ	QT^{-1}	Magnetic Flux ϕ	$L^2MQ^{-1}T^{-1}$	Electric Potential (Voltage) E	$L^2MQ^{-1}T^{-2}$
Mechanical Linear	Force F	LMT^{-2}	Translation Displacement x	L	Linear Velocity dx/dt	LT^{-1}
Rotational Mechanical	Moment M	L^2MT^{-2}	Rotation, Angular α	-	Angular Velocity $\omega = d\alpha/dt$	T^{-1}
Acoustic or Fluid	Pressure p	$L^{-1}MT^{-2}$	Volume V	L^3	Volume Flow dV/dt	L^3T^{-1}
Thermal (*)	Temperature θ	θ	Entropy s	$L^2MT^{-2}\theta^{-1}$	Rate of Change of Entropy ds/dt	$L^2MT^{-3}\theta^{-1}$
Chemical (*)	Chemical Potential		Quantity of Material		Reaction Rate	
ENERGY		L^2MT^{-2}	L = length	Note: Luminous Flux ψ is the basic other unit, with dimensions of power, in the system: Mass, Length, Time, Charge, Degree Temperature, Luminous Flux.		
POWER		L^2MT^{-3}	M = mass T = time			

(*) From Ref. 4.

TABLE III: SOME MEASURANDS AS TIME AND SPACE FUNCTIONS OF ENERGY AND ENERGY COMPONENTS

FUNCTION	OF	SYMBOL	YIELDS	SYMBOL	FUNCTION	OF	SYMBOL	YIELDS	SYMBOL
$\frac{\partial(\quad)}{\partial x}$	Force	F	Surface Tension	c	$\frac{\partial^2(\quad)}{\partial t^2}$	Force	F	Load Acceleration	a
	Displacement	L	Strain	H		Displacement	L	Acceleration	a
	Magnetic Potential	ϕ	Magnetizing Field	H		Volume of Fluid	V	Flow Acceleration	a
	Electric Potential	E	Field Strength		$\frac{\partial^3(\quad)}{\partial t^3}$	Displacement	L	Jerk	
	Temperature	θ	Temperature Gradient			()dt	Energy		Action
$\frac{\partial^2(\quad)}{\partial y \cdot \partial z}$	Force	F	Stress	σ	$\frac{\partial^3(\quad)}{\partial y \cdot \partial z \cdot \partial t}$	Energy		Intensity	
	Magnetic Flux	ϕ	Magnetic Field	B		Force	F	Stress Rate	
	Electric Charge	Q	Charge Density			Electric Charge	Q	Current Density	
$\frac{\partial^3(\quad)}{\partial x \cdot \partial y \cdot \partial z}$	Force	F	Specific Weight	γ	$\frac{\partial^2(\quad)}{\partial x \cdot \partial t}$	Displacement	L	Strain Rate	
	Energy		Energy per Unit Volume						
$\frac{\partial(\quad)}{\partial t}$	Force	F	Load Rate		x, y, z are mutually perpendicular directions, x along the direction of the acting quantity; y and z, perpendicular to it.				
	Displacement	L	Velocity	v					
	Magnetic Flux	ϕ	Electric Potential	E					
	Electric Charge	Q	Current	I					
	Fluid Volume	V	Volume Flow Rate						
	Energy		Power						

TABLE IV: SOME LATENT INFORMATION PARAMETERS AS RATIOS OF MEASURANDS:
FOR TIME DERIVATIVES OF ENERGY COMPONENTS

RATIO OF FUNCTIONS	OF	YIELDS	
$\left(\frac{\quad}{\quad}\right)$	$\frac{\text{Force}}{\text{Displacement}}$	$\frac{F}{L}$	Dynamic Stiffness
	$\frac{\text{Displacement}}{\text{Force}}$	$\frac{L}{F}$	Compliance, Receptance
	$\frac{\text{Magnetic Potential}}{\text{Magnetic Flux}}$	$\frac{\phi}{\phi}$	Reluctance
	$\frac{\text{Magnetic Flux}}{\text{Magnetic Potential}}$	$\frac{\phi}{\phi}$	Permeance, (Inductance) A
	$\frac{\text{Electric Potential}}{\text{Electric Charge}}$	$\frac{E}{Q}$	Elastance S
	$\frac{\text{Electric Charge}}{\text{Electric Potential}}$	$\frac{Q}{E}$	Capacitance C
	$\frac{\text{Temperature}}{\text{(Mass)(Specific Heat)}}$	$\frac{\theta}{S}$	Thermal Stiffness [4]
	$\left[\frac{\quad}{\partial t}\right]$	$\frac{\text{Force}}{\partial(\text{Displacement})/\partial t}$	$\frac{F}{v}$
$\frac{\text{Voltage}}{\partial(\text{Charge})/\partial t}$		$\frac{E}{I}$	Resistance R Impedance Z Reactance X_C, X_L
$\left[\frac{\partial(\quad)}{\partial t}\right]$	$\frac{\partial(\text{Charge})/\partial t}{\text{Voltage}}$	$\frac{I}{E}$	Conductance G Admittance Y Susceptance
	$\frac{\partial(\text{Displacement})/\partial t}{\text{Force}}$	$\frac{v}{F}$	Mobility Fluidity
$\left[\frac{\quad}{\partial t^2}\right]$	$\frac{\text{Force}}{\partial^2(\text{Displacement})/\partial t^2}$	$\frac{F}{a}$	Dynamic Apparent Mass
	$\frac{\text{Voltage}}{\partial^2(\text{Charge})/\partial t^2}$	$\frac{E}{\partial I/\partial t}$	Inductance L
$\left[\frac{\partial^2(\quad)}{\partial t^2}\right]$	$\frac{\partial^2(\text{Displacement})/\partial t^2}{\text{(Force)}}$	$\frac{a}{F}$	Inertance
	$\frac{\partial^2(\text{Charge})/\partial t^2}{\text{Voltage}}$	$\frac{\partial I/\partial t}{E}$	Inverse Inductance (Reluctance) r

The general form of a latent information parameter based only on time-functions is:

$$(\text{LIPS}) = \frac{\partial^n Q_1 / \partial t^n}{\partial^m Q_2 / \partial t^m} \quad (2)$$

Since the assignment of Q_1 and Q_2 to specific physical quantities (energy components) is arbitrary and depends on the measurand for each specific case, the LIPs may take forms which are one the inverse of the other. In the LIP, m and n may assume integral values such as 0, 1, 2, etc., where negative values imply integration instead of differentiation. So long as $(n+m) = 0$, the product of the two components of the ratio exhibits the dimensions of energy. The LIP is then considered to be energy based (potential).

If $(n+m) = 1$ by similar argument, the LIP is considered to be power-based, and

if $(n+m) = 2$ the LIP is considered to be based on rate of change of power, a concept for which a single term does not appear to exist. The words energy-acceleration or power velocity are descriptive and will be used. Kinetic energy concepts also appear to apply.

Table VII illustrates the various possibilities for electrical and mechanical systems. It is seen that the many empty spaces identify presently unexplored possibilities. A similar approach applied to the other energy forms of Table II will show that Tables III, IV, V, and VI are just the barest of samples of the possibilities.

TABLE V: SOME MEASURANDS OF RATIOS OF TIME AND/OR SPACE DERIVATIVES OF ENERGY COMPONENTS

RATIO OF FUNCTIONS	OF	YIELDS
$\frac{\frac{\partial(\quad)}{\partial x}}{\frac{\partial^2(\quad)}{\partial y \cdot \partial z \cdot \partial t}}$	$\frac{\partial(\text{Electric Potential})/\partial x}{\partial^2(\text{Electric Charge})/\partial y \cdot \partial z \cdot \partial t}$	Resistivity ρ
$\frac{\frac{\partial^2(\quad)}{\partial y \cdot \partial z}}{\frac{\partial(\quad)}{\partial x}}$	$\frac{\frac{\partial^2(\text{Magnetic Flux})/\partial y \cdot \partial z}{\partial(\text{Magnetic Potential})/\partial x}}{\frac{\partial^2(\text{Electric Charge})/\partial y \cdot \partial z}{\partial(\text{Electric Potential})/\partial x}}$ $\frac{\partial^2(\text{Force})/\partial y \cdot \partial z}{\partial(\text{Displacement})/\partial x}$	Magnetic Permeability μ Dielectric Constant ϵ Elastic Modulus E
$\frac{\frac{\partial(\quad)}{\partial y}}{\frac{\partial(\quad)}{\partial x}}$	$\frac{\partial(\text{Displacement})/\partial y}{\partial(\text{Displacement})/\partial x}$	Poisson's Ratio
$\frac{\frac{\partial^2(\quad)}{\partial y \cdot \partial z}}{\frac{\partial^2(\quad)}{\partial x \cdot \partial t}}$	$\frac{\partial^2(\text{Force})/\partial y \cdot \partial z}{\partial^2(\text{Displacement})/\partial x \cdot \partial t}$	Viscosity η
$\frac{\frac{\partial^3(\quad)}{\partial x \cdot \partial y \cdot \partial z}}{\frac{\partial^2(\quad)}{\partial t^2}}$	$\frac{\partial^3(\text{Force})/\partial x \cdot \partial y \cdot \partial z}{\partial^2(\text{Displacement})/\partial t^2}$	Density ρ
$\frac{\frac{\partial^2(\quad)}{\partial t^2}}{\frac{\partial^3(\quad)}{\partial x \cdot \partial y \cdot \partial z}}$	$\frac{\partial^2(\text{Displacement})/\partial t^2}{\partial^3(\text{Force})/\partial x \cdot \partial y \cdot \partial z}$	Specific Volume

Note that these so-called "material properties" are all ratios of quantities for which the product has the dimensions of energy, power, or rate-of-change of power per unit volume, as shown in Table VI.

TABLE VI
EXAMPLES OF "MATERIAL PROPERTIES" AS HOMOGENEOUS LATEST INFORMATION PARAMETERS: Q₁/Q₂

ENERGY	POTENTIAL ENERGY STORING BEHAVIOR	POWER DISSIPATING BEHAVIOR	KINETIC ENERGY STORING BEHAVIOR
Mechanical	Compression Modulus (Fluid) Elastic Modulus: E Q ₁ = stress or pressure = force per unit area Q ₂ = strain = extension per unit length or contraction per unit volume Q ₁ ·Q ₂ = energy per unit volume	Viscosity Coeff: μ Q ₁ = stress = force per unit area Q ₂ = strain rate = rate of change of extension per unit length of or unit volume per unit volume Q ₁ ·Q ₂ = power per unit volume	Density: ρ Q ₁ = force per unit volume Q ₂ = acceleration of gravity Q ₁ ·Q ₂ = rate of change of power per unit volume
Electrical	Dielectric Constant: ϵ Q ₁ = charge per unit area Q ₂ = potential change per unit length Q ₁ ·Q ₂ = energy per unit volume	Resistivity: ρ Q ₁ = potential change per unit length Q ₂ = rate of change of charge per unit area Q ₁ ·Q ₂ = electrical power per unit volume	
Magnetic	Permeability: μ Q ₁ = magnetic flux per unit area Q ₂ = magnetizing field Q ₁ ·Q ₂ = energy per unit volume		

Note that all these quantities are complex numbers, with a magnitude and a phase. The phase angle of the complex permittivity or dielectric constant, for example, is called the loss angle, and the loss tangent is defined as the angle whose tangent is the imaginary/real part of the complex dielectric constant.

Note that all these quantities exhibit a dependence of both the magnitude and the phase angle, on frequency and on amplitude of the Q₂ quantity. Thus frequency response curves for magnitude and phase, and non-linearity curves, exist. Note also that μ and ϵ are inter-related.

**TABLE VII: A SYSTEMATIC EXPLORATION OF TIME-FUNCTION BASED LIPs
IN MECHANICAL AND ELECTRICAL SYSTEMS**

	LATENT INFORMATION PARAMETERS	MECHANICAL SYSTEMS	ELECTRICAL SYSTEMS
		$Q_1 = \text{Force} = F$ $Q_2 = \text{Displacement} = X$	$Q_1 = \text{Voltage} = V$ $Q_2 = \text{Charge} = Q$
ENERGY-BASED	$\frac{Q_1}{Q_2}$	$\frac{F}{X} = \text{dynamic stiffness or modulus}$	$\frac{V}{Q} = \text{elastance, } S$
	$\frac{Q_2}{Q_1}$	$\frac{X}{F} = \text{compliance or receptance}$	$\frac{Q}{V} = \text{capacitance, } C$
POWER-BASED	$\frac{\partial Q_1 / \partial t}{Q_2}$	$\frac{\dot{F}}{X} =$	$\frac{\dot{V}}{Q} =$
	$\frac{Q_2}{\partial Q_1 / \partial t}$	$\frac{X}{\dot{F}} =$	$\frac{Q}{\dot{V}} =$
	$\frac{Q_1}{\partial Q_2 / \partial t}$	$\frac{F}{\dot{X}} = \text{mechanical impedance}$	$\frac{V}{\dot{Q}} = \text{Resistance, } R$ $= \text{Impedance, } Z$ $\text{Reactance, } X_C \text{ or } X_L$
	$\frac{\partial Q_2 / \partial t}{Q_1}$	$\frac{\dot{X}}{F} = \text{mobility}$	$\frac{\dot{Q}}{V} = \text{Conductance, } G$ $= \text{Admittance, } Y$ Susceptance
RATE-OF-CHANGE-OF-POWER-BASED, ENERGY-ACCELERATION-BASED, OR POWER-VELOCITY-BASED	$\frac{\partial^2 Q_1 / \partial t^2}{Q_2}$	$\frac{\ddot{F}}{X} =$	$\frac{\ddot{V}}{Q} =$
	$\frac{Q_2}{\partial^2 Q_1 / \partial t^2}$	$\frac{X}{\ddot{F}} =$	$\frac{Q}{\ddot{V}} =$
	$\frac{\partial Q_1 / \partial t}{\partial Q_2 / \partial t}$	$\frac{\dot{F}}{\dot{X}} =$	$\frac{\dot{V}}{\dot{Q}} =$
	$\frac{\partial Q_2 / \partial t}{\partial Q_1 / \partial t}$	$\frac{\dot{X}}{\dot{F}} =$	$\frac{\dot{Q}}{\dot{V}} =$
	$\frac{Q_1}{\partial^2 Q_2 / \partial t^2}$	$\frac{F}{\ddot{X}} = \text{dynamic apparent mass}$	$\frac{V}{\ddot{Q}} = \text{inductance}$
	$\frac{\partial^2 Q_2 / \partial t^2}{Q_1}$	$\frac{\ddot{X}}{F} = \text{inertance}$	$\frac{\ddot{Q}}{V} = \text{inverse inductance}$

Inhomogeneous, Inter-Port or Transfer Parameters: LIPs which are ratios between energy components or their time and/or space derivatives, but which exist at different ports (entry or exit) of a transducer, are called interport or inhomogeneous LIPs. If they fulfill the conditions of equations (1) and (2), they are called "Transfer Impedances" for example, to distinguish them from "Point Impedances"--if the very limited, power-based concept of impedance applies to the situation at all. By and large, however, the inter-port parameters will not satisfy equations (1) and (2) or the requirements for homogeneous, intra-port, single-port parameters. Examples would be thermal expansion

coefficients, thermoelectric power coefficients, the gain of an amplifier, gage factor for strain gages, etc. A later section will present a systematic methodology for the study of these LIPs.

GENERAL PROPERTIES OF LATENT INFORMATION PARAMETERS

1. All LIPs are ratios of time and/or space functions of energy components.
2. All LIPs are expressed as partial derivatives at an operating point for the (n-2) dimensions in n-dimensional space, where n is the total number of independent variables

which can affect the LIP. Thus all LIPs are sensitive to the operating point at which they have been determined, the world being non-linear in general. This operating point is governed both by boundary conditions and by initial conditions, as well as by other variables, as will be discussed later. See also Ref. 5.

3. All LIPs are complex numbers, exhibiting a magnitude and a phase angle (of the numerator with respect to the denominator which serves as phase reference).
4. The magnitude and phase angle of all LIPs is a function of the frequency (or rate of change) of the denominator and/or the numerator of the ratio. These characteristics are summarized in frequency-response curves for magnitude and phase (Bode plots, for example, or Nyquist or Root-Locus presentation if preferable [1]).
5. The magnitude and phase angle of all LIPs is a function of the amplitude of the denominator and/or the numerator. These characteristics are summarized in the linearity or non-linearity curves for magnitude (the author has never seen one for phase angle, but it does exist). Naturally, such amplitude-dependence curves must be presented at a stated operating point and at a given signal frequency, just as frequency-response curves only hold at a given amplitude, or a small range of amplitudes in which the system is assumed at least incrementally linear about the operating point, which must be stated.
6. All LIPs present reversible (temporary) and irreversible (permanent) responses to any of the n dimensions which determine them--a fact which can be exploited or deplored as will be shown later. (Also see [6].) Any

TABLE VIII: TYPICAL EFFECTS OF VARIOUS ASPECTS OF THE ENVIRONMENT ON A LATENT INFORMATION PARAMETER

(Note the partial derivatives around an OPERATING POINT in n -dimensional space)

TOTAL DIFFERENTIAL PER UNIT	INCREMENT dx	SLOPE $\frac{1}{R} \cdot \frac{\partial R}{\partial x}$	WHEN REVERSIBLE, THE BASIS OF	WHEN PERMANENT, EVIDENCE OF PAST HISTORY OF
$\frac{dR}{R}$	R Electrical Resistance	$R = \rho \frac{L}{A}$ ρ = resistivity L = length A = area		If $dR = 0$, a precision resistor
$\frac{1}{R} \cdot \frac{\partial R}{\partial \theta} \cdot d\theta$	θ Temperature	Thermo-resistive coefficient Resistance-temperature coeff.	Resistance thermometer; thermistor	Heat treatment, cure cycle, firing temp., etc.
$\frac{1}{R} \cdot \frac{\partial R}{\partial \epsilon} \cdot d\epsilon$	ϵ Strain	Piezo-resistive coefficient Strain sensitivity Resistance-strain coeff.	Resistance strain gage	Cold work, fatigue damage, mechanical history
$\frac{1}{R} \cdot \frac{\partial R}{\partial p} \cdot dp$	p Pressure	Resistance-pressure coeff. Bridgman coefficient	Bridgman pressure transducer; carbon microphone, etc.	Hydrostatic pressure
$\frac{1}{R} \cdot \frac{\partial R}{\partial H} \cdot dH$	H Magnetic Field	Magneto-resistive coeff.	Magnetic field resistance sensors	Magnetic field
$\frac{1}{R} \cdot \frac{\partial R}{\partial I} \cdot dI$	I Luminous Intensity	Photo-resistive coefficient	Photo-resistive detectors	Luminous Intensity
$\frac{1}{R} \cdot \frac{\partial R}{\partial h} \cdot dh$	h Humidity	Humidity-resistance coeff.	Humidity sensors, resistance-based	Humidity
$\frac{1}{R} \cdot \frac{\partial R}{\partial c} \cdot dc$	c Fractional Concentration of chemical element	Composition effect on resistance	Concentration or Species determination	Progressive corrosion; degree of cure in polymers
$\frac{1}{R} \cdot \frac{\partial R}{\partial s} \cdot ds$	s State Phase, Structure	Usually discontinuous function of phase or structure change (amorphous/crystalline)	Studies of material state, phase, or structure	Same as reversible
...				

TABLE IX: TYPICAL ENVIRONMENTAL EFFECTS ON THE PARTIAL DERIVATIVES OF LATENT INFORMATION PARAMETERS

(Note the effect of a change in operating point in one dimension on the slopes in all dimensions)

PARTIAL DIFFERENTIAL PER UNIT	INCREMENT dx	RATE OF CHANGE OF SLOPE: The Effect of (dx) on the Strain Sensitivity or Piezo-Resistance Coefficient	WHEN REVERSIBLE, Effect of (X) on the Calibration of the Strain Gage:	WHEN PERMANENT, Evidence of past (X):
$\frac{1}{R} \left(\frac{dR}{d\epsilon} \right)$ =	ϵ Strain	Strain sensitivity, piezo-resistance coefficient, resistance-strain coefficient	Electric resistance strain gage	
$\frac{1}{R} \cdot \left[\frac{\partial(\partial R/\partial \epsilon)}{\partial \theta} \right] \cdot d\theta$ +	θ Temperature	Temperature effect on gage factor or calibration	Temperature effect on gage factor	Heat treatment for metals
$\frac{1}{R} \cdot \left[\frac{\partial(\partial R/\partial \epsilon)}{\partial \sigma} \right] \cdot d\sigma$ +	σ Strain	Effect of strain on the gage factor	Non-linearity of calibration	Past cold work
$\frac{1}{R} \cdot \left[\frac{\partial(\partial R/\partial \epsilon)}{\partial p} \right] \cdot dp$ +	p Pressure	Effect of pressure on gage factor	Pressure effect on gage factor	Pressure history
$\frac{1}{R} \cdot \left[\frac{\partial(\partial R/\partial \epsilon)}{\partial H} \right] \cdot dH$ + ...	H Magnetic Field	Effect of magnetic field on gage factor	Magnetic-field effect on gage factor	Magnetic field history

Note, for example, that $\frac{1}{R} \left[\frac{\partial(\partial R/\partial \epsilon)}{\partial \epsilon} \right]$ is a very sensitive indicator of total accumulated fatigue-damage (cold work) in the S/N "Fatigue Gage," although it is not the primary read-out used.

TABLE X: TYPICAL EXAMPLES OF VARIOUS ASPECTS OF THE ENVIRONMENT ON A LATENT INFORMATION PARAMETER

TOTAL DIFFERENTIAL PER UNIT	INCREMENT dx	SLOPE $\frac{1}{V} \cdot \frac{\partial V}{\partial x}$	WHEN REVERSIBLE, THE BASIS OF	WHEN PERMANENT, EVIDENCE OF PAST HISTORY OF
dV/V =	V Volume	$V = A \cdot L$ or $V = \frac{m \cdot R \cdot \theta}{p}$ A = area L = length m = mass of gas R = gas constant These are typical expressions for volume		
$\frac{1}{V} \cdot \frac{\partial V}{\partial \theta} \cdot d\theta$ +	θ Temperature	Volumetric thermal expansion coefficient	Fluid-filled thermometers such as gas, mercury-in-glass, etc. (State change)	Change in structure or phase
$\frac{1}{V} \cdot \frac{\partial V}{\partial p} \cdot dp$ +	p Pressure	Volumetric pressure coefficient (compressibility)	Barometer	Change in structure (ex. twinning of iron crystals)
$\frac{1}{V} \cdot \frac{\partial V}{\partial L} \cdot dL$ +	L Length	Sensitivity of volume to change in length	When cylinder position is used as measure of volume in PV engine studies	
$\frac{1}{V} \cdot \frac{\partial V}{\partial A} \cdot dA$ +	A Area	Sensitivity of volume change to area change		
$\frac{1}{V} \cdot \frac{\partial V}{\partial F} \cdot dF$ +	F Force	Sensitivity of volume to force change	Load cell: mercury-filled hollow cylinder with open sight glass	
$\frac{1}{V} \cdot \frac{\partial V}{\partial s} \cdot ds$ + ...	s Chemical reaction or state	Sensitivity of volume to chemical reaction or state	Phase change or structure change in a material	Shrinkage of polymers during cure. Correlates with degree of cure

remnant effects must be identified. The problems here are closely allied to the past history of the material and/or geometric factors which determine the LIP [5].

TYPICAL MANIFESTATIONS OF LATENT INFORMATION PARAMETERS

Tables VIII, IX, and X show a limited number of possibilities of latent information parameters. It is important to note the systematic method by which such effects can be investigated.

First select a latent information parameter, such as electrical resistance. Secondly, list a number of independent variables which may affect it. Thirdly, express an incremental change of the LIP (total differential) as a sum of the partial differentials multiplied by the incremental change of each variable.

Table VIII identifies the effects of temperature, strain, pressure, magnetic fields, luminous intensity, humidity, fractional concentration of chemical elements (composition) and state, phase, and structure, on electrical resistance. Each of the partial derivatives can be used as a transducing process from some energy component or measurand into latent information (resistance change). Such effects may be temporary or permanent, with uses as indicated. This approach identifies the earlier statement [6] that all transducers respond in all ways they can to all factors of the environment. The measurement engineer's job is to enhance the desired responses to the desired environmental factor and to suppress all other environment-response combinations. Table XI identifies the possibilities. The processes of enhancement and suppression have been treated extensively elsewhere [1,5,6]. Table XII illustrates the problems for a bonded resistance strain gage, in summary [7].

Typical permanent effects of extreme utility to computer-memory applications, and which are controllable, are just being discovered and brought to commercialization [8,9].

Table IX illustrates that each of the partial derivatives is itself a function of a number of independent, environment-controlled variables, and that the various second-order partial differentials exist to act as possible transducer bases or as sources of confusion, noise, interference, or whatever name one gives to anything but the desired response of the transducer to the desired environmental factor to be observed today [6]. It should be noted that individual references which describe actual case histories and numerical values for each of these effects are to be found in large number in the Strain Gage Encyclopaedia [7], when strain gages are the sensor of interest. To the author's knowledge, this approach has not been extensively applied in a systematic manner to any other type of sensor or transducer. These references will not be cited here.

Table X illustrates some of the independent variables affecting the volume within a defined region of space. Note that each of these partial derivatives, in turn, depends on a host of others.

Numerous examples from the published literature regarding evidence of state of cure, cure cycle, and post-cure effects in plastics and ceramics (firing-cycle instead of cure), as they are evidenced by volumetric changes, which create havoc in strain gage installations, are covered in the Adhesives discussion in the Strain Gage Encyclopaedia, for example [7].

Table XII illustrates some of the possible responses of a resistance strain gage to just a few environmental factors. It should be noted that any undesired change in resistance of the

TABLE XI: POSSIBLE ENVIRONMENT-RESPONSE COMBINATIONS IN A TRANSDUCER

ENVIRONMENTAL ASPECT OR FACTOR	TRANSDUCER RESPONSE			
	SELF-GENERATING (*)		NON-SELF-GENERATING (*)	
	Temporary	Permanent	Temporary	Permanent
Desired (Measurand)				
Undesired (Sum total of all other factors)				

(*) See Table XIII, Fig. 1, and the accompanying discussion

Note that only one of the eight combinations shown above is SIGNAL--the desired response to the desired environmental factor. Hence there are seven environment-response combinations which are noise levels. Note that there is never only ONE noise, also note that systematic methods of documenting the presence or absence of noise are available [1,6].

TABLE XII: ENVIRONMENT-RESPONSE COMBINATIONS FOR ELECTRIC RESISTANCE STRAIN GAGE

ENVIRONMENT	RESPONSE SYSTEM TO THE ENVIRONMENT			
	NON-SELF-GENERATING RESPONSE		SELF-GENERATING RESPONSE	
	Permanent Evidence	Temporary Response	Permanent Evidence	Temporary Response
Mechanical Strain	<p>Cold-work-induced resistivity change follows cold-work in excess of past peak.</p> <p>Cyclic strain (fatigue) produces cold work which may result in resistivity change.</p> <p>Cold work also affects gage factor and resistance-temperature coefficient.</p>	<p>Piezo-resistive response, which is desired.</p> <p>$\Delta R/R = K \cdot \epsilon$</p> <p>$\epsilon$ = mechanical strain input ΔR = strain-induced electrical resistance change R = initial gage resistance K = gage factor or calibration constant</p> <p style="text-align: center;">[SIGNAL]</p>	<p>Yielding after plastic deformation</p>	<p>Piezoelectric effect. Charge accumulates as response to input strain/displacement.</p>
Temperature Change, Gradient, Level, or Rate of Change	<p>Temperature level, time at temperature, rate of change, etc., influence phase transformations, inter-granular corrosion, alloy migration to grain boundaries, etc. All of these effects affect resistivity at room temperature, resistance-temperature coefficient and gage factor.</p>	<p>Resistance-temperature coeff. of the strain gage when bonded to a specific specimen, can be maintained near zero for particular specimens in specific temperature ranges. This self-compensation is achieved by control of the resistance-temperature coeff. of the strain gage filament.</p>	<p>Changes in dimension due to heat-treatment, grain size change, etc.</p>	<p>Thermal expansion in filament creates strain even for self-compensated gages. Thermoelectric effects at lead junctions. Match for thermal time-constant difference or temp. gradients.</p>
Magnetic Fields	<p>In certain materials such as nickel alloys, permanent property changes may occur, such as resistivity and resistance-temperature coefficient changes.</p>	<p>Magneto-resistive effects interfere with strain-induced resistance measurement.</p>	<p>Permanent dimension changes are possible depending on magnetic domain alignment.</p>	<p>Magneto-strictive forces on filament. Electro-magnetic induction in filament.</p>
Electric Fields		<p>Electro-resistive effects.</p>		<p>Charges induced by the field couple into signal path, directly or capacitively thru shield.</p>

filament which is temporary is misinterpreted as a load-induced strain, and any permanent resistance change (due to resistivity change) is misinterpreted as specimen yielding, plastic buckling, or permanent set of a mechanical joint or of a bad gage installation. With all these effects coexisting and all dependent on the past history of the specific strain gage installation [5], the amount of confusion possible in the data is frighteningly large. Systematic approaches exist for controlling all these effects, and documenting whether or not at any instant during a test they affect the data [1,6,7].

Strain gages are used as examples throughout this article, because the author's background permits him to make more definitive statements about this sensor than any other. Note that the problems are all-pervasive and that the background which permits an understanding of one sensor automatically permits an appreciation of the problems associated with any sensor [5].

It should be noted that among methods for suppressing the undesired responses, or the responses to undesired environmental factors, are subtractive cancellation through common mode rejection, minimizing by division through a variety of deviation-minimizing structural arrangements, and information conversion [1,5,6]. In addition, an operating point may be selected, such that the particularly troublesome partial derivatives are effectively zero (i.e., at a maximum or minimum). This approach has been illustrated both for test rig design and transducer design [20,1], and involves a combination of material selection and geometric considerations. This method is called self-compensation, and its application yields, for example, self-temperature-compensated devices such as tuning forks, strain gages, etc.

A GENERALIZED TRANSDUCER CONCEPTUAL MODEL [10]

All transducers exhibit latent information parameters which must be activated before the information they contain is available as a pattern of properties of a wave shape of an energy component, or its time and/or space functions. The simplest conceptual model which accounts for the above facts is illustrated in Figure 1.

Two energy components arriving at the Major Input port create changes in LIPs within the transducer; such changes occur about a given operating point or initial condition. The definition of the Major Energy Input is that input port at which LIP-variations are induced.

Two energy components arriving at the Minor Input port interrogate the LIP in the transducer, or activate the latent information and carry it through to the output port where two energy components emerge. One of these (the Primary Quantity) carries the desired information on some pattern of some property of some wave shape of some time and/or space function of that energy component.

There are now four distinct possibilities as summarized in Table XIII. One of the two input ports is usually controlled by design of the transducer and/or the measuring system. Thus an example of a design-controlled Major Input or LIP is the nature of the material-property discontinuity of thermoelectric power across the junction of a thermocouple. An example of a design-controlled Minor Input is the constant-voltage, constant-frequency excitation of a linear, variable, differential transformer. If both input ports are design-controlled, a source (voltage oscillator, for example, or constant temperature bath) results. If neither input port is design-controlled, either a computing

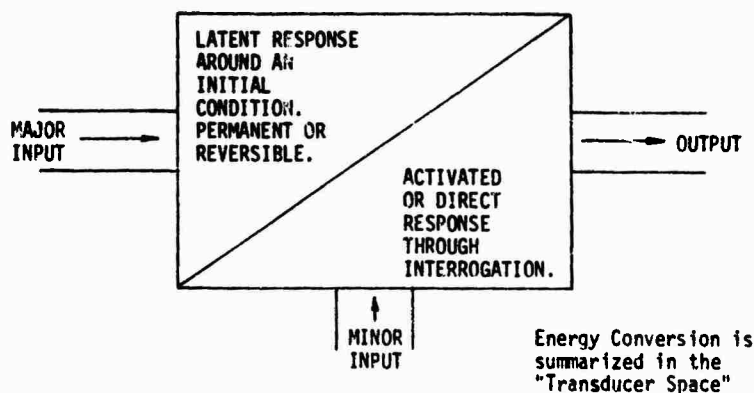


FIGURE 1

TRANSDUCER RESPONSES: ENERGY AND/OR INFORMATION CONVERSION

TABLE XIII: TYPES OF RESPONSES

MAJOR INPUT \ MINOR INPUT	DESIGN-CONTROLLED	ENVIRONMENT-CONTROLLED
DESIGN-CONTROLLED	Source or Standard	Self-generating Response
ENVIRONMENT-CONTROLLED	Non-Self-Generating Response	Multiplier, Computing Element or a Problem.

element exists or a problem (noise levels, according to the definition in Table XI).

The other of the two input ports is usually environment-controlled; that is, deliberately (hopefully) affected by the desired environmental factor to be observed with the transducer. Conditions at this port are therefore labelled Environment-Controlled. For a thermocouple, the Minor Input is under environment-controlled conditions. For a differential transformer, the displacements (and forces) which move the core, provide differential magnetic reluctance paths (latent information) within the LVDT; it is therefore identified as having an environment-controlled Major Input.

By common practice, the words SELF-GENERATING (or active) RESPONSES are applied to transducers with design-controlled latent information parameters or Major Inputs, and the words NON-SELF-GENERATING (or passive) RESPONSES are applied to transducers with design-controlled Minor Inputs. Note that this transducer model shows for the first time the indisputable relationships between these responses, and the brutal fact that every transducer will quite obviously exhibit both responses simultaneously. This fact serves as the basis for the noise-documentation techniques previously reported [1,6,10]. A more comprehensive model to account for the behavior of real transducers is shown in Ref. 10.

ENERGY PROCESSING

Energy processing within a transducer involves the possibility of any energy components (or any of their space and/or time functions) appearing at any of the three minimum number of ports of a transducer. If one tabulates energy forms as:

- Chemical
 - Optical
 - Mechanical
 - Electrical
 - Thermal
 - Magnetic
 - Acoustic/Fluid
 - Nuclear
- } 2 components for each form

then 8^3 major sets of possibilities exist within which there are numerous variations. The first organized systematic approach to the presentation of these possibilities was given in the Transducer Space concept [1]. The method is based on pioneering work by Lion [11] modified to account for the latent information nature of transducers. Since energy processing in measuring systems is not the topic of this paper, no further discussion will be given.

In subsequent examples cited in this paper, an indication of the energy processing mechanisms in specific transducers will be given.

INFORMATION PROCESSING

Information can exist on patterns in time and/or space of a total of 8 properties (involving three wave shapes--constant levels, sine waves and pulses). There are thus 32 possible combinations [1,2] and therefore as many forms in which information can exist, without even starting to count the number of patterns or codes which have been used. Each of these 32 basic information forms has specific advantages and specific limitations, such that 32 measuring systems, each based on a different form, can be assembled, calibrated, and yield 32 different answers when exposed to the same measurand. A methodical approach to the study of some of these factors has been given elsewhere [1,7,15]. It is important to note here that the conversion of information-form from one of the 32 possibilities to another is frequently desired as a method of noise suppression or signal enhancement [1,6,10] or as a means of stacking a number of channels of information side by side in the time or frequency domains [1], or for storage.

It can be shown that information conversion in a transducer is ONLY POSSIBLE when the design-controlled input to that transducer is not a constant level. Thus DC-fed devices of all kinds are not capable of information conversion. Table XIV identifies the transducer operating modes in which information conversion is possible, and those in which it is not, and suggests possible symbols for their presentation in measuring system schematics. [DC = static = constant level = zero frequency = stationary]

TABLE XIV: INFORMATION CONVERSION

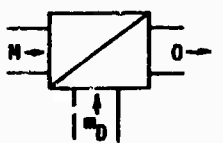
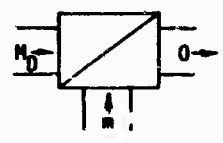
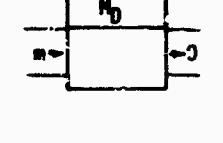
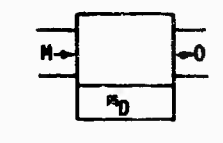
POSSIBLE		NOT POSSIBLE	
			
Non-self-generating response with time-dependent minor input	Self-generating response with time-dependent, controlled, major input. D = design-control	Self-generating response with DC major input, time-independent, design-controlled	Non-self-generating response with DC minor input, time-independent, design-controlled

Table XV illustrates both self-generating and non-self-generating responses for electric LIP-based transducers with resistance, capacitance and inductance LIPs.

These principles apply to all transducers, and it has been shown, for example, that zero-based mechanical pulse carriers, working simultaneously with PAM and PFM information forms, can be made to yield data not obtainable in any other way [1,14]. It has also been shown as far back as 1956 that under certain conditions the pulse repetition rate, or sine wave frequency, of the

carrier can be a fractional part of the signal frequency, and all of the information contained in the signal can still be retrieved [1,15]. An example of this method applied to a mechanical-pulse-carrier system is given in References 14 and 15, which anticipate the operating principle which the sampling oscilloscope and many signal averagers used today.

A systematic study of measuring systems according to the principles given in this paper reveals a number of possibilities which either contradict directly, established textbook statements,

TABLE XV: TYPICAL EXAMPLES OF DESIGN-CONTROLLED MAJOR AND MINOR INPUTS FOR ELECTRICAL "LIP"s

LATENT INFORMATION PARAMETER "LIP"	MAJOR INPUT	MINOR INPUT	OUTPUT	COMMON NAME FOR THE TRANSDUCING PROCESS
Electrical Resistance	Unit change in displacement: strain	Current DESIGN-CONTROLLED	Voltage	Resistance strain gage; resistance devices related to linear or angular displacement, of all kinds, such as potentiometer devices
	Displacement DESIGN-CONTROLLED	Voltage	Voltage	Electrical chopper, if design-controlled displacement makes and breaks a contact; from zero to infinite resistance, periodically
Electrical Capacitance	Unit change in displacement: strain	Voltage DESIGN-CONTROLLED	Charge	Capacitive strain gage, if voltage is non-DC. Capacitive velocity gage (rate-of-change-of-strain gage) for DC Minor Input
	Displacement DESIGN-CONTROLLED	Voltage	Charge	"Vibrating reed electrometer" or Vibrating Capacitor, for sinusoidal displacements [Ref. 12]
Electrical Inductance	Unit change in displacement: strain	Current DESIGN-CONTROLLED	Voltage	Inductive strain gage for non-DC Minor Input. Velocity gage for DC Minor Inputs
	Displacement DESIGN-CONTROLLED	Current	Voltage	Magnetic modulator and Second Harmonic Generator [Ref. 13]

Note that in these examples the Major Input always presents potential-energy-storing aspects at its input, whereas from the Minor Input and from the Output, the transducer "looks" like a power dissipating element (primarily) for resistive devices; like a potential-energy-storing device (primarily) for capacitive devices; and like kinetic-energy-storing devices (primarily) for inductive devices.

or which yield entire new families of transducers which have not yet been conceived. Experimental evidence indicates that the textbook statements are often incomplete and sometimes erroneous. The new transducer families which are possible [10] are only held up by developments in materials research. It turns out that modulated piezo-electric devices and thermocouples are entirely possible, but that these require materials with properties diametrically opposed to the ones now being exploited--hence materials research is not progressing in the direction to permit the construction of modulated thermocouples and piezo-electric devices. The fact that they will work when the materials become available is established beyond doubt [10].

EXAMPLES OF TRANSDUCER FORMULATIONS ACCORDING TO THE UNIFIED APPROACH

This section gives the information-and-energy-flow schemas for several common transducers, according to the Unified Approach to the Engineering of Measuring Systems and the conceptual transducer model reported in this paper.

The devices cited are:

1. turbine-type flow-meter
2. mercury-in-glass thermometer
3. piezoelectrically based transducers

4. thermocouple
5. electric resistance-based sensors
6. vacuum tubes as voltage-controlled resistors

For each category, the following information is given:

- A. Type of response desired: self-generating or non-self-generating.
- B. Energy components involved at the various ports.
- C. Latent information components involved.
- D. Information form involved at the various ports.
- E. Measurand and its relationship to the energy component.
- F. Information processing involved.
- G. Energy processing involved.

An incrementally linear mathematical model for the transducer is given, for some of the devices. The coefficients within this model are LIPs, as will clearly be recognized.

The basic method for generating the coefficients which are required is taken from Ref. 1. The coefficients themselves are taken from References 1, 4, 16, 17.

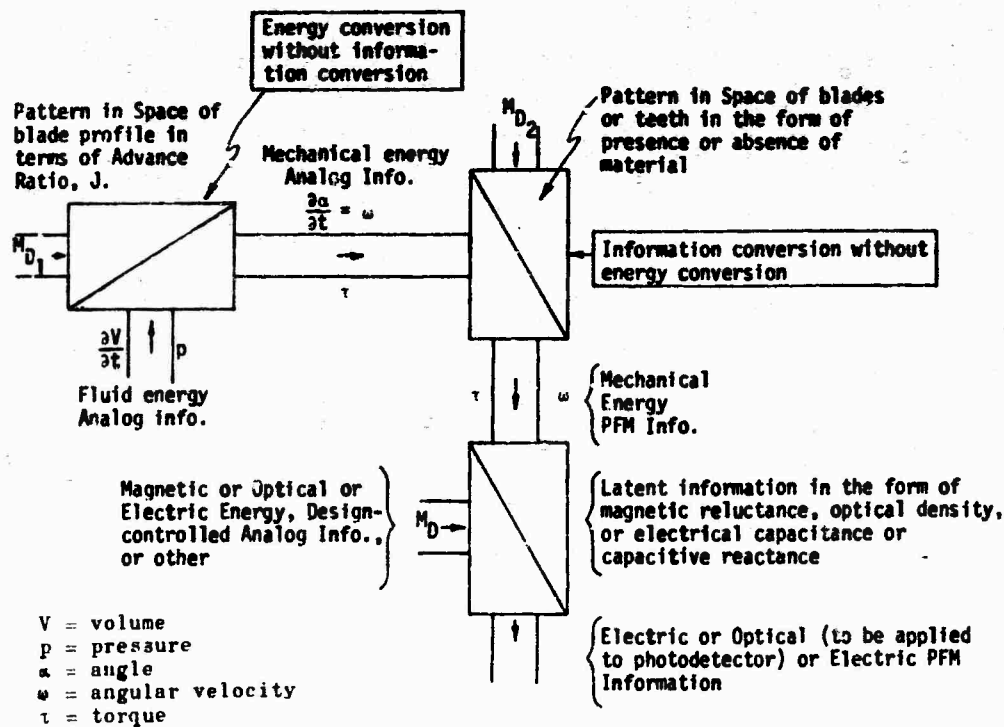


FIGURE 2
A TURBINE-TYPE FLOW-METER AS INFORMATION AND ENERGY PROCESSING COMPONENT

A Turbine-Type Flow-Meter as Information and Energy Processing Component (See Figure 2). Fluid energy in the form of flow rate and pressure act on the air-foil blades of the "turbine" and create a rotational speed of the rotor, against a restraining torque. The flow-speed relationship is governed by the advance ratio (J) of the air-foils. The restraining torque is governed by bearing friction and back-reactions from the design-controlled minor input of the last stage of energy conversion (ex. magnetic forces).

By distributing material in space in a pattern of presence-or-absence of material, the analog velocity is converted into PFM information. The number of blades on the rotor identify the angular increments which can be detected or the frequency of blade passage for a given rotor analog speed.

The pattern of presence/absence of material is converted into

- an electrical output by detecting blade passages with a monopole pick-up which provides a permanent magnet (analog minor input) surrounded by a coil, such that the passage of each blade evokes an electrical pulse.
- an optically-induced electrical signal by having the blades interrupt a light-beam focused on a photocell.
- an electrical output created when each blade interrupts an electrostatic field, or when each blade produces a change in capacitive reactance when it passes.

A Mercury-in-Glass Thermometer as Information and Energy Processing Device (See Table X). For a tube of constant area and under constant pressure, in the absence of external forces (centrifugal, magnetic, etc.) and abutting against an initial volume filled with a liquid:

Initial condition or operating point:

At temperature θ_0 the liquid occupies volume V_0 . All of the liquid is assumed at constant temperature at all times.

The temperature-induced volume-increment can be expressed by geometric factors:

$$dV = A \, dL \quad A = \text{area of the tube}$$

and by material properties

$$dV = \frac{\partial V}{\partial \theta} \cdot d\theta$$

Hence:

$$\frac{dL}{d\theta} = \frac{1}{A} \cdot \frac{\partial V}{\partial \theta}$$

$$\frac{dL}{d\theta} = \frac{V_0}{A} \left[\frac{1}{V_0} \cdot \frac{\partial V}{\partial \theta} \right] = C_2$$

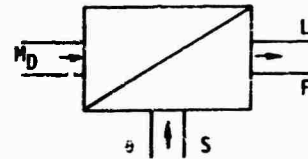


FIGURE 3

For high transfer ratio $dL/d\theta$ it is necessary to start with the largest volume V_0 of a liquid with high volume thermal expansion coefficient, being pushed into a tube of the smallest area, A.

- S = entropy
- F = force
- M_D = design-controlled major input: V_0 ; $(1/V_0)(\partial V/\partial \theta)$; A
- θ = temperature increment starting from θ_0

$$L = C_1 F + C_2 \theta \quad \text{a linear model around the operating point. Assuming that there is no opposing force, F:}$$

$$S = C_3 F + C_4 \theta$$

$$L = C_2 \theta \quad \text{the relationship between output length and}$$

$$S = C_4 \theta \quad \text{the thermal input characteristics.}$$

The assumption of constant force can be approximated extremely well in real liquid-filled thermometers.

Piezoelectrically-Based Transducers.

Piezoelectricity: Some crystals which are anisotropic, such as quartz and tourmaline, generate a charge when mechanically strained. The effect is reversible and phase sensitive. A displacement applied to such crystals with asymmetrical charge distributions causes a relative displacement of positive and negative charges within the lattice. This effect produces equal and opposite charges on the faces of the crystal.

Ferroelectricity: On a polycrystalline scale, there are zones of spontaneous polarization similar to the local domains in ferro-magnetic

materials. These zones are partially oriented by the application of an external electric field. A ferroelectric material, once polarized, can be considered an artificially piezoelectric material. Electrically, it is anisotropic.

For a given natural or artificially induced polarization:

Independent variables, F = force
 V = voltage

Dependent variables, δ = displacement
 Q = charge

Linearly, or incrementally linearly around an initial condition or operating point:

$$\delta = C_1 V + C_2 F$$

$$Q = C_3 V + C_4 F$$

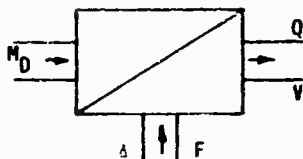


FIGURE 4

$$C_1 = \left. \frac{\delta}{V} \right|_{F=0} \text{ or } \left. \frac{d\delta}{dV} \right|_{F_0} = \frac{L_j}{L_i} \cdot d_{ij}$$

$$C_2 = \left. \frac{\delta}{F} \right|_{V=0} \text{ or } \left. \frac{d\delta}{dF} \right|_{V_0} = \frac{L_j}{A_i} \cdot S^E$$

$$C_3 = \left. \frac{Q}{V} \right|_{F=0} \text{ or } \left. \frac{dQ}{dV} \right|_{F_0} = \frac{A_j}{L_j} \cdot \epsilon_{jj}$$

$$C_4 = \left. \frac{Q}{F} \right|_{V=0} \text{ or } \left. \frac{dQ}{dF} \right|_{V_0} = \frac{A_j}{A_i} \cdot d_{ji}$$

$$\frac{C_3}{C_1} = \left. \frac{dQ}{d\delta} \right|_{V=0} \text{ or } \left. \frac{dQ}{d\delta} \right|_{V_0} = \frac{A_j}{L_i} \cdot \frac{1}{g_{ij}}$$

$$= \left. \frac{F}{V} \right|_{\delta=0} \text{ or } \left. \frac{dF}{dV} \right|_{\delta_0} = \frac{A_j}{L_j} \cdot \frac{1}{g_{ij}}$$

L = length dimension related to geometry of the material.

A = area dimension related to geometry of the material.

i, j = subscripts identified with directions.

d = piezoelectric strain constant for the material.

S^E = compliance, which is higher for short-circuit conditions (here) than for open-circuit ones.

ϵ = dielectric constant, which is higher for free end (here) than fixed end conditions.

$d_{ij} = d_{ji}$ since the process is considered reversible.

g = Piezoelectric stress constant, higher for free than fixed end conditions (free end here).

Design-controlled major input: Polarization and geometry. Initial condition identified by subscripts "o".

Table XVI identifies the symbols employed in defining the piezoelectric material properties. Note that reversible transducers such as piezoelectric ones illustrate the effects of boundary conditions on calibration data most effectively. The Golden Calf Effect [18] of using calibration data under boundary conditions different from those for which they were determined is serious. Thus, the input coefficient C_2 , the compliance, is higher for short-circuit conditions than open-circuit ones, indicating a lower resonant frequency and a different frequency response curve for the mechanical characteristics of the piezoelectric device for charge-amplifier readout than for voltage-amplifier readout. Similarly, the input boundary conditions determine the output coefficient C_3 , the internal capacitance of the device. Thus under free-end input conditions of zero force, the capacitance is higher than for fixed-end conditions of zero allowable displacement. Since the cable-capacitance corrections for piezoelectric devices are determined by the transducer output capacitance, and that capacitance depends on the clamping conditions under which the piezoelectric material is constrained, problems may arise. These problems are among many discussed in the literature on the subject [19] but hardly demonstrated as simply as in the preceding section.

A Thermocouple According to the Gradient Approach (See Figure 5). The thermoelectric effect is one of voltage generation along homogeneous electrical conductors in temperature gradients. Thermocouples take advantage of the effect by maximizing the differential-voltage generating ability of materials of different history, electrically connected.

This differential history is most often one of chemical composition, but heat treatment and cold work are known to produce differential

TABLE XVI: TYPICAL SYMBOLS EMPLOYED IN DESCRIBING PROPERTIES OF PIEZOELECTRIC MATERIALS [17]

These symbols identify properties of materials and not of physical elements made from the materials

S_{11}^D — open-circuit electrodes
 — stress in 1 direction
 — strain in 1 direction

S_{33}^E — short-circuited electrodes
 — stress around 3 direction
 — strain in 3 direction

$$\text{COMPLIANCE} = \frac{\text{STRAIN}}{\text{STRESS}}$$

All stresses other than the stress involved in one subscript are held constant. Also applied as noted (*).

ϵ_1^T — constant stresses on the material (no forces, ex.)
 Free end.
 — Electrodes \perp 1

ϵ_3^S — constant strains on the material; no deformations in any direction. Fixed-end conditions.
 — Electrodes \perp 3 axis

$$\text{DIELECTRIC CONSTANT} = \frac{\text{(CHARGE DENSITY)}}{\text{(ELECTRIC FIELD)}}$$

Relative dielectric constant, $K = \epsilon/\epsilon^0$ ϵ^0 = for vacuum

k_{15} — stress or strain is in shear around the 2 axis
 — Electrodes \perp the 3 axis

k_p — this subscript used only for ceramics; electrodes \perp 3 axis, stress or strain equal in all directions \perp 3 axis

ELECTROMECHANICAL COUPLING

d_{33} — piezoelectrically induced strain, or applied stress in 3 direction.
 — Electrodes \perp 3 axis

d_h — stress applied equally in 1, 2, and 3 directions, (hydrostatic). Electrodes \perp 3 axis for ceramics, and \perp 2 axis for lithium sulfate

$$\text{PIEZOELECTRIC STRAIN CONSTANT} = \frac{\text{STRAIN}}{\text{APPLIED FIELD}}$$

$$= \text{SHORT CIRCUIT CHARGE/ELECTRODE AREA/APPLIED STRESS} \quad (*)$$

g_{31} — applied stress or piezoelectrically induced strain is in the 1 direction.
 — Electrodes \perp 3 axis

g_{15} — applied stress or piezoelectrically induced strain in shear around 2.
 — Electrodes \perp to 1 axis

$$\text{PIEZOELECTRIC STRESS CONSTANT} = \frac{\text{STRAIN}}{\text{APPLIED CHARGE/ELECTRODE AREA}}$$

$$= \frac{\text{FIELD}}{\text{APPLIED STRESS}}$$

(*) Axis of poling field = 3. Shear around 1 = 4, around 2 = 5, shear around 3 = 6

thermoelectric properties even in materials of identical chemical composition. Very minor changes in chemical composition in any material may produce drastic changes in its thermoelectric behavior [6].

From Moffat: [Chapter 18, Ref. 1]

The voltage generated in a loop made of two homogeneous conductors of different thermoelectric power:

$$E_{net} = \int_0^L \epsilon_1 \cdot \frac{\delta t}{\delta x} \cdot dx + \int_L^0 \epsilon_2 \cdot \frac{\delta t}{\delta x} \cdot dx$$

$$dE = \epsilon \cdot \frac{\delta t}{\delta x} \cdot dx$$

If ϵ is not a function of distance (homogeneous conductors), spatial dimensions may be replaced by thermal limits at the spatial limits:

$$E_{net} = \int_{T_1}^{T_2} \epsilon_1 \cdot dt + \int_{T_2}^{T_1} \epsilon_2 \cdot dt$$

$$= \int_{T_1}^{T_2} (\epsilon_1 - \epsilon_2) dt$$

$$\epsilon = \left(\frac{dk}{dT} - u \right)$$

ϵ = Absolute value of electromotive force.

k_p = Peltier coefficient.

If the thermoelectric power is not a function of temperature or distance along the conductors:

$$E_{net} = (\epsilon_1 - \epsilon_2)(T_2 - T_1)$$

x = incremental distance.
 u = Thompson coefficient.
 t = incremental temperature.
 T = absolute temperature.

This information is tabulated for various ϵ -pairs and T_1 values.

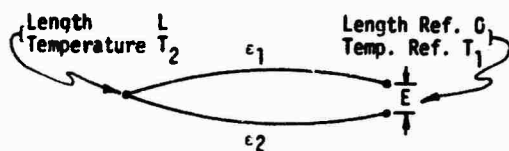


FIGURE 5

A Thermocouple According to the Unified Approach Modelled as a Single Component.

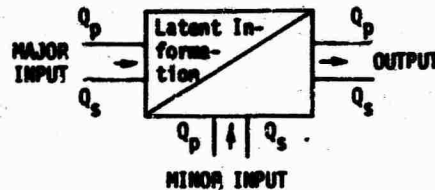


FIGURE 6

Major Input:

Design-controlled by material selection of k_p, c_p .
 Usually fixed and time-independent.

Minor Input:

Primary quantity:

Temperature difference, $\theta = T_2 - T_1$
 Temperature level T (absolute)
 Reference temperature T

Secondary quantity:

Entropy S^1

Thermal energy.
 Usually in analog form.

Output:

Primary quantity:

Potential difference E
 Current I

Electrical energy.
 Usually in analog form.

Energy Conversion:

Thermal-electrical at constant material properties.

Information conversion:

Not possible at constant material properties.

Relationships [4]:

$$E_T = Z_{11} \cdot I + \left[\frac{k_p}{c_p} \right] S$$

$$\theta = - \left[\frac{k_p}{c_p} \right] \cdot Q + \left[\frac{T}{c_p} \right] S$$

- k_p = Peltier coefficient
- C_p = heat capacity (*)
- Z_{11} = adiabatic resistance of the junction
- Q = charge flowing through the interface
- E_T = thermal emf generated

A Thermocouple According to the Unified Approach Modelled as a Differentially Coupled System [5].

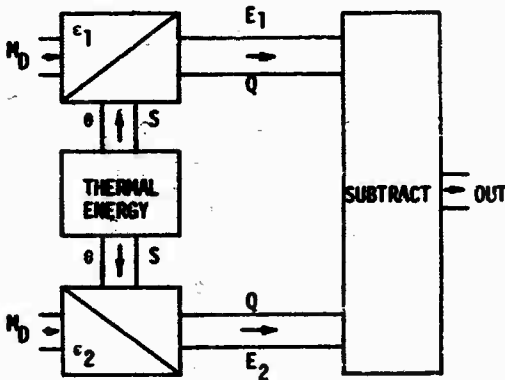


FIGURE 7

$$E_1 = \int_0^L \epsilon_1 \frac{\partial t}{\partial x} \cdot dx + \int_{T_1}^{T_2} \epsilon_1 \cdot dt + \epsilon_1(T_2 - T_1) = \epsilon_1 \theta$$

$$E_2 = \int_0^L \epsilon_2 \frac{\partial t}{\partial x} \cdot dx + \int_{T_1}^{T_2} \epsilon_2 \cdot dt + \epsilon_2(T_2 - T_1) = \epsilon_2 \theta$$

$$OUT = (E_1 - E_2) = \theta(\epsilon_1 - \epsilon_2)$$

General Case for Electrical Resistance Based Detectors. Given an electrical resistance detector for which the relationships between environmental factor, q_1 , and electrical resistance can be expressed in the following form:

$$R = R_0(1 + K \cdot \Delta q_1)$$

(*) The heat capacity at constant pressure,
 $C_p = m \cdot c_p$

c_p = specific heat at constant pressure
 m = mass

which is often expressed:

$$\frac{\Delta R}{R_0} = K \cdot \Delta q_1$$

or as:

$$\frac{1}{R_0} \cdot \left(\frac{\partial R}{\partial q_1} \right) = K$$

the q_1 -coefficient of resistance.

R_0 = the initial value of resistance at condition q_{10}

R = the final value of resistance at condition $q_1 = q_{10} + \Delta q_1$

ΔR = the resistance change ($R - R_0$)

Δq_1 = the q_1 -change ($q_1 - q_{10}$)

Given an electrical Minor Input to interrogate the sensor resistance, or to activate it, as shown in Figure 8, and a resulting electrical output. Voltage detection is very common, and is illustrated. It implies current excitation, also shown.

Figure 8 models the device as an energy and information processing transducer, assuming incremental linearity about an operating point identified by subscripts "0".

Select as independent variables, since they can usually be easily controlled: q_1 , i , and I .

The governing relationships then are:

$$(e - e_0) = k_1(q_1 - q_{10}) + k_2(i - i_0) + k_3(I - I_0) \quad (1)$$

$$(V - V_0) = k_4(q_1 - q_{10}) + k_5(i - i_0) + k_6(I - I_0) \quad (2)$$

$$(q_2 - q_{20}) = k_7(q_1 - q_{10}) + k_8(i - i_0) + k_9(I - I_0) \quad (3)$$

For the sample circuit illustrated, $V = e$ so that equations 2 and 3 are identical and $k_1 = k_4$, $k_2 = k_5$, $k_3 = k_6$.

Evaluating the coefficients k_1 , k_2 , k_3 as examples:

$$k_1 = \frac{\Delta e}{\Delta q_1} \text{ for } \Delta i = \Delta I = 0$$

$$e_0 + \Delta e = (I_0 - i_0)(R_0 + \Delta R)$$

$$\Delta e = (I_0 - i_0)(\Delta R)$$

but

$$\frac{\Delta R}{R_0} = K \cdot \Delta q_1$$

hence

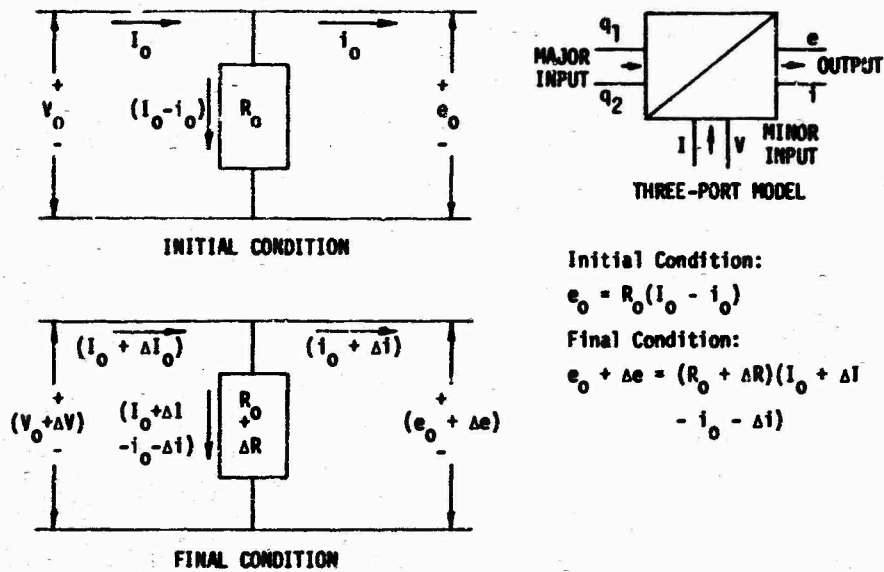


FIGURE 8

$$k_1 = \Delta e / \Delta q_1 = (I_o - i_o)(R_o)(K)$$

or for $i_o = 0$, open-circuit conditions:

$$\Delta e / \Delta q_1 = I_o \cdot R_o \cdot K$$

$$k_2 = \Delta e / \Delta i \text{ for } \Delta q_1 = 0 (R = R_o), \text{ and } \Delta I = 0$$

$$e_o + \Delta e = (I_o - i_o - \Delta i) R_o$$

$$\Delta e = -\Delta i \cdot R_o$$

$$k_2 = \Delta e / \Delta i = -R_o$$

$$k_3 = \Delta e / \Delta I \text{ for } \Delta i = \Delta q_1 = \Delta R = 0$$

$$e_o + \Delta e = (I_o + I - i_o) R_o$$

$$e = I R_o$$

$$k_3 = \Delta e / \Delta I = R_o$$

Hence equation (1):

$$\Delta e = R_o(I_o - i_o)K \cdot \Delta q_1 - R_o \cdot \Delta i + R_o \cdot \Delta I$$

For a constant-current source $I = 0$ and for open-circuit read-out conditions, $i_o = \Delta i = 0$, so that

$$\Delta e = R_o \cdot I_o \cdot k \cdot q_1$$

Initial Condition:

$$e_o = R_o(I_o - i_o)$$

Final Condition:

$$e_o + \Delta e = (R_o + \Delta R)(I_o + \Delta I - i_o - \Delta i)$$

This represents the maximum voltage output from a resistance sensor of the type discussed here, in any electrically passive network (circuit or structure).

The Vacuum-Tube as a Voltage-Controlled Resistor. The linearized approximation of a triode is shown below. The pertinent characteristics are:

$\mu = (\Delta E / \Delta e)$ at constant plate current, the Amplification Factor

$r_p = (\Delta E / \Delta I)$ at constant grid voltage, the Plate Resistance

E_c = the cut-off voltage

E_b = plate voltage

I_p = plate current

R_o = total resistance at the operating point = E_o / I_o

From the illustration (Figure 9) it is seen that

$$E_o = E_c + I_o \cdot r_p + \mu \cdot e_o$$

Dividing by I_o ,

$$R_o = r_p + (E_c / I_o) + (\mu / I_o) \cdot e_o$$

As the grid voltage changes by Δe , a resistance change ΔR occurs:

$$\frac{\Delta R}{\Delta e} = \frac{1}{I_0} = K \quad \text{in units of volts at } E_b \text{ / milliamps at } I_0 \text{ per milli-volts at } e.$$

Overall, then:

$$R_0 + \Delta R = R = \left(r_p + \frac{E_c}{I_0} + K e_0 \right) + K \cdot \Delta e$$

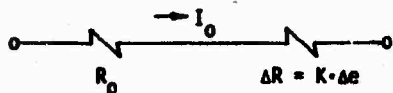


FIGURE 9

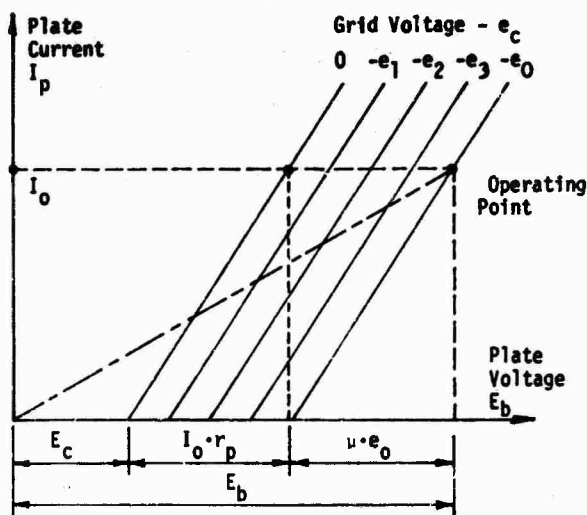
The vacuum tube has been modelled as a VOLTAGE-CONTROLLED RESISTOR. It should be noted that for some vacuum tubes, geometric relationships between grids, plate, and cathode, are the basis of the transduction process, notably in the vacuum-tube accelerometer. In that case, an acceleration-sensitive resistor results as model, and the variations of μ and r_p with acceleration must be determined, since all other parameters now remain fixed.

Note that the voltage-controlled resistor model of a vacuum tube does not supplant the incremental-voltage-source model used by electrical engineers. It is an additional aid in unifying and understanding the behavior of energy and information processing elements--i.e., transducers.

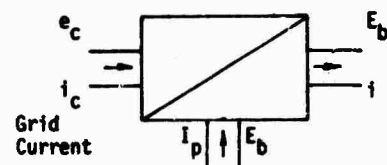
Similar models can be constructed for transistors, diodes, and any component normally modelled in electrical engineering. A differential amplifier then becomes a Wheatstone Bridge, and all analyses of bridge circuits apply directly.

The structure (circuit) into which the vacuum tube is placed for activation of its latent (resistance) information, will determine whether the more convenient model is:

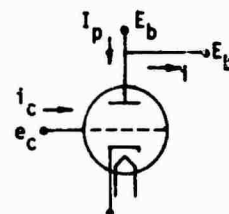
$$R = R_0 + K \cdot \Delta e \quad \text{or} \quad \frac{\Delta R}{R} = \left(\frac{K}{R_0} \right) \cdot \Delta e$$



LINEARIZED APPROXIMATION OF A TRIODE



TRANSDUCER CONCEPTUAL MODEL



PHYSICAL MODEL

FIGURE 10

THE VACUUM-TUBE AS A VOLTAGE-CONTROLLED RESISTOR: ILLUSTRATIONS

LATENT INFORMATION PARAMETERS: HOW THEY MANIFEST THEMSELVES

The appearance of LIPs as input, output, or transfer coefficients of scalar, vector, tensor, and matrix expressions has been identified in a previous section. A brief survey of how LIPs appear in several common systems will be presented in this section.

A. In Linear, Lumped Parameter Systems.

Many components of measuring systems are used in frequency ranges or to time scales where they can be modelled as lumped parameter (at least incrementally) linear components with reasonable success. Many links in the measurement chain, including such devices as load cells, accelerometers, pressure transducers, thermocouples, many amplifiers, some filters, and even certain distributed parameter links such as cantilever beams, etc., can be modelled by one or a combination of linear differential equations with constant coefficients, of the first and second order. This simple, common example of the manifestation of LIPs is discussed below. Let the modelling relationship be:

$$\alpha \frac{d^2 Q_2}{dt^2} + \beta \frac{dQ_2}{dt} + \gamma Q_2 = Q_1(t) \quad (4)$$

where α or γ may equal zero for first-order systems, and where $Q_1(t)$ is the excitation, input, forcing function, service condition, or stimulus. The dimensions of each term of the equation are those of Q_1 and it must be emphasized that Q_1 and Q_2 have been selected according to the dimensional relationship of Equation (5), yielding

$$|Q_1| \cdot |Q_2| = |\text{Energy}| \quad (5)$$

Latent information parameters (LIPs) such as defined in Table VII:

$$\alpha = \frac{Q_1}{d^2 Q_2 / dt^2} \quad (6)$$

$$\beta = \frac{Q_1}{dQ_2 / dt} \quad (7)$$

$$\gamma = \frac{Q_1}{Q_2} \quad (8)$$

Equation (4) can also be rewritten as:

$$\alpha \frac{d^2 Q_2}{dt^2} + 2 h w_n \alpha \frac{dQ_2}{dt} + w_n^2 \alpha Q_2 = Q_1(t) \quad (9)$$

For first-order systems, two formulations are possible:

$$\beta \frac{dQ_2}{dt} + w_0 \beta Q_2 = Q_1(t) \quad (10)$$

$$\alpha \frac{d^2 Q_2}{dt^2} + w_0 \alpha \frac{dQ_2}{dt} = Q_1(t) \quad (11)$$

The following definitions of the characteristics of these equations apply:

$$w_n = \sqrt{\gamma/\alpha} \quad \text{the undamped natural frequency of the second order system, Eq. (9)} \quad (12)$$

$$h = \frac{\beta}{2\sqrt{\gamma\alpha}} \quad \text{the damping ratio of the second order system, Eq. (9)} \quad (13)$$

$$w_0 = (\gamma/\beta) \quad \text{the characteristic frequency, also known as the break-point, 3-dB point, frequency limit, 70.7% response point, etc., of the first order system, Eq. (10)} \quad (14)$$

$$w_0 = (\beta/\alpha) \quad \text{the characteristic frequency of the first order system, Eq. (11)} \quad (15)$$

$$\tau = (\beta/\gamma) \quad \text{the time-constant for the first-order system, Eq. (10)} \quad (16)$$

$$\tau = (\alpha/\beta) \quad \text{the time-constant for the first-order system, Eq. (11)} \quad (17)$$

It can be shown that the energy stored in the LIPs identified above in Equations (6), (7), and (8), or the energy dissipated as power in them, is directly associated with each LIP as follows: [1]

Energy stored in an α -element: =

$$\frac{1}{2} \alpha \left(\frac{dQ_2}{dt} \right)^2 \quad \text{stored as a rate of change in kinetic form.} \quad (18)$$

Energy stored in a γ -element: =

$$\frac{1}{2} \gamma (Q_2)^2 \quad \text{stored as a level, in potential form.} \quad (19)$$

Energy stored in a β -element: =

None energy is dissipated as power.

Hence, one can associate each of these parameters with certain physical responses in the system they model. It should be noted that each of these parameters may contain a collection of

modelled linear lumped-parameter elements. Thus it is not unusual in mechanical systems, for example, to find a certain combination of masses, springs, and dampers as expressing the α -term, for example. The exact form of each parameter depends on the system components and the system structure, where the concept of "structure" is used to identify the relationship between the components, sometimes called the circuit or the network.

In recognition of these possibilities, the following nomenclature has been adopted for the study of such systems, when the study is based on energy-flow (Eq. 5) rather than the more standard power-flow concept used in most textbooks. A comprehensive and basic treatment of the energy-flow approach is given in Ref. [1].

- α = kinetic energy storing parameter for the system described in Eq. (4)
- β = power dissipating parameter for the system
- γ = potential energy storing parameter for the system.

The system characteristics tabulated in Eqs. (12) through (17) are independent of the forcing function in linear systems. The frequency dimensions are in radians/second and could be called angular velocity. In distributed parameter systems, characteristic linear velocity (wave front velocity) will appear in place of w_0 or w_n .

B. In Linear Systems with Parameters Distributed along One Spatial Dimension.

Sometimes the individual components identified in the earlier sections can not be specifically separated because they are continuously distributed and no one component can be made to predominate in the time-or-frequency-scale of the operating conditions of the transducer. A simplified version of the equations governing a typical one-dimensional system of this type is given below for the model illustrated in Figure 11. The equations are written for voltage and current, for which the product is power rather than energy. This distinction from the formulation of Equation (3) should be noted. Let:

- r = resistance per unit length of an electrical cable
- l = inductance per unit length of the cable
- c = capacitance per unit length of the cable
- g = conductance per unit length of the cable.

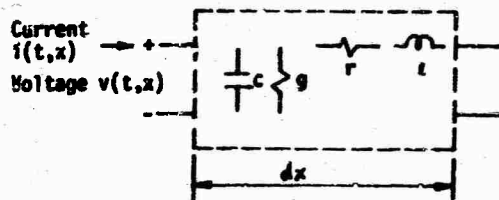


FIGURE 11

MODEL FOR AN INCREMENTALLY LINEAR LENGTH OF CABLE

The governing equations are [1]:

$$\frac{\partial^2 i}{\partial t^2} + \frac{a^2}{\mu} \cdot \frac{\partial i}{\partial t} = a^2 \frac{\partial^2 i}{\partial x^2} - g \cdot a^2 \frac{\partial v}{\partial x} \quad (20)$$

$$\frac{\partial^2 v}{\partial t^2} + \frac{a^2}{\delta} \cdot \frac{\partial v}{\partial t} = a^2 \frac{\partial^2 v}{\partial x^2} - r \cdot a^2 \frac{\partial i}{\partial x} \quad (21)$$

The above equations are a formulation of the wave equations, and a cable operated in a frequency region or to time scales where these effects predominate is called a transmission line. The following system characteristics are identified in Eqs. (20) and (21).

$$a_0 = \sqrt{1/(lc)} \quad \text{the wave front (linear) velocity} \quad (22)$$

$$Z_0 = \sqrt{l/c} \quad \text{the characteristic impedance which governs the reflection and refraction phenomena at each end of the cable, or where discontinuities in geometry or material properties occur.} \quad (23)$$

$$\gamma^2 = \frac{(s+\delta)(s+\mu)}{a^2} \quad \text{the propagation function which determines the time delay, attenuation, and distortion of the wave as it propagates.} \quad (24)$$

$$s = \quad \text{the Laplace operator.} \\ \delta = r/l \quad \text{a power dissipating parameter of the cable.} \quad (25)$$

$$\mu = g/c \quad \text{a power dissipating parameter of the cable.} \quad (26)$$

$$\epsilon = \frac{1}{2}(\mu+\delta) \quad \text{governs the attenuation of the wave.} \quad (27)$$

$$\zeta = \frac{1}{2}(\mu-\delta) \quad \text{governs the distortion of the wave.} \quad (28)$$

The attenuation of the traveling wave is given by α and its distortion by β . For zero c , all frequency components of the wave travel at equal velocity. There is no distortion because the electrical and magnetic energies are in balance at the time the wave strikes, and no adjustments are necessary. For non-zero c , each frequency component of the wave travels at its own velocity, always less than a_0 , and the adjustment to energy unbalances cause wave shape distortion.

For a mechanical bar of length L , area A , density ρ , and elastic modulus E , the equivalent quantities would be:

c equivalent to k the compliance per unit length

z equivalent to m the mass per unit length

$$k = \frac{1}{A \cdot E} = \frac{1}{A \cdot E} \text{ on a per-unit-length basis (29)}$$

$$m = A \cdot L \cdot \rho = A \cdot \rho \text{ on a per-unit-length basis (30)}$$

Thus:

$$a_0 = \sqrt{E/\rho} \text{ the so-called speed of sound or celerity in a uni-dimensional geometry (31)}$$

$$Z_0 = A \cdot \sqrt{E \cdot \rho} = \frac{A \cdot E}{a_0} \text{ the dynamic stiffness (32)}$$

Not enough is usually known about the internal damping mechanisms in materials, so that the mechanical equivalents of the resistance and conductance per unit length are usually neglected and assumed as zero.

It can be seen that the physical quantities which affect any of the LIPs r , k , c , or g , or their mechanical equivalents, will affect a number of aspects of overall system performance characteristics. Examples of these are reflection and/or refraction phenomena at discontinuities, through effects on Z ; wave front velocity; time delay; attenuation or distortion of the wave in the medium. The activation of latent information can therefore occur through any of a number of mechanisms.

It should be emphasized that the traveling wave equations identify pairs of traveling waves. This concept agrees with the transfer of energy or its rates of change, such as power. The common neglect of one member of such a pair can lead to data that appear unexplainable and irrational. The problems arising in the measurement of traveling strain waves in mechanical structures, with electric resistance strain gages, when the displacement-wave is not remembered, is an excellent example of such a case [1]. The displacement wave moves the strain gage very rapidly, albeit by a microscopic amount; any magnetic flux lines, such as the

earth's, which cut the rapidly moving loop (or loops) of conducting filament representing the strain gage, create self-generating responses into the measuring system. These responses occur to the same time scale as the strains to be observed, and their magnitude is in the neighborhood of a millivolt for normal conditions; this represents a sizeable noise level which must be dealt with. The standard noise-documentation methods inherent in the Unified Approach are the only methods available for handling this problem [1, 6].

C. In Linear Systems with Parameters Distributed in 2 or 3 Spatial Dimensions.

A wave is a disturbance moving through a medium. For transverse waves, particles move perpendicular to the direction of wave propagation. For longitudinal waves, particles move parallel to the direction of wave propagation, the proposition already examined for one-dimensional geometries in Case B, above. Surface waves in two-dimensional cases, include circular or elliptical motion of the particles. In the general 3-dimensional case, waves transmitted across a boundary may be subjected to effects such as the following:

- the wave may travel at a new speed.
- the excitation may travel at a new wave length or frequency.
- the wave may propagate in a new direction.
- the wave may propagate in a new plane of polarization (for transverse waves).
- only a portion of the energy in the wave may penetrate the new medium from the source-medium: the refracted portion.
- a portion of the energy in the wave may be reflected back into the source-medium: the reflected portion.

For one-(spatial)-dimensional waves, the reflection and refraction coefficients, identifying those portions of a specific energy-component which are reflected into the source medium, or transmitted into the receiving medium, are governed by the characteristic impedances or dynamic stiffnesses, Z_0 , of each medium at the contact interface. The wave propagation velocities are governed by the values for a_0 in each medium.

In a large solid, dilatational or longitudinal waves propagate at a velocity

$$a_L = a_0 \sqrt{\frac{1-\mu}{(1+\mu)(1-2\mu)}} \text{ where } \mu = \text{Poisson's ratio for the medium (33)}$$

and rotational disturbances or shear waves, producing particle motion perpendicular to the wave propagation direction, propagate at a velocity:

$$a_s = a_0 \sqrt{\frac{1}{2(1+\nu)}} \quad (34)$$

Along a free boundary, Rayleigh surface waves are propagated much like on a fluid surface, and are attenuated rapidly with depth and as a function of frequency.

In more complicated systems such as those associated with electromagnetic fields in optical, electrical, and magnetic systems, where properties such as index of refraction are described by second order tensors, additional effects may occur, which can be defined as latent information parameters. In two-dimensional space, a change in the direction of a ray is possible, and in three-dimensional space, changes in the orientation of a plane wave may occur. Such angular effects are especially associated with refractive indices and with polarization effects. Thus latent information can be activated by the determination of changes in angle of polarization of components of the traveling-wave pair, as in photoelasticity or in the Kerr cell.

When latent information is activated by interrogating it with a Minor Input, the process is sometimes referred to as the modulation [2] of the Minor Input by the latent information parameter. Some of the pertinent considerations for electro-optic modulators are discussed below [21,22]. There are two basic types of light-modulators--temporal and spatial. Temporal modulators vary electro-magnetic characteristics such as phase, frequency, amplitude, etc. Spatial modulators vary the physical qualities of the light beam such as direction, intensity, beam width, etc. This division is consistent with information being carried on patterns in space or time of properties of wave shapes of energy components [1,2,3]. In the temporal electro-optic modulators, two types of retardation can occur: linear retardation, called the Pockels effect, and quadratic, called the Kerr effect. The following material properties and parameters are important in electro-optic materials selected for modulator design [21,22]. Note that many of these can act as LIPs.

The electro-optic coefficient (r) relates the induced birefringence to the applied electric field. The refractive index (n) determines the speed of light in the medium, the reflection losses at its surface, and the "figure of merit" (n^3r) for electro-optic modulation. The transmission properties determine the spectral region available for modulation. The relative dielectric constant (ϵ) determines the capacitance of the crystal and the speed of electric fields in it. The loss tangent ($\tan \delta$) determines the electrical loss (modulation power) in the crystal.

The electrical resistivity (ρ) relates to space charge effects and heating of the medium. Crystal symmetry determines the non-zero electro-optic, piezoelectric, and photoelastic coefficients and the applicability of the crystal to specific device configurations. The photoelastic and piezoelectric properties determine the frequencies of undesired piezoelectric resonances and relate the clamped to the unclamped (fixed-end to free-end boundary conditions) electro-optic coefficients. The thermal conductivity of the medium determines the deleterious birefringence due to thermal gradients in the crystal heat by electrical or optical sources.

The refractive index in an absorbing medium is a complex number

$$N = n + j \cdot k \quad (35)$$

$n = c/v$ the refractive index defined as the ratio of the phase velocity of electro-magnetic radiation in vacuum, (c), to the phase velocity of the same radiation in the material, (v).

k is the extinction coefficient or absorption index.

Both n and k are frequency-dependent, or wavelength dependent. They also depend on temperature, pressure, nuclear radiation, and material preparation techniques, which is especially important for thin films.

It is seen that many of the material properties cited above, could be used as LIPs of either permanent or reversible types. It is equally apparent that certain effects desired for one application may be undesired for others.

D. Other Possibilities in Linear Systems.

Other possibilities exist, for example in piezoelectricity. The parameters which define the property of piezoelectricity are called third-order tensors, because they relate first-order tensor (the electric moment produced) to the stress applied (a second-order tensor)[23]. The number of such parameters varies from one to 18, depending on the materials involved. In a semi-conductor, the piezo-resistive effect is described by stating the relationship between a stress tensor and an electric resistance tensor. It can be shown that the piezo-resistive tensor (the basis of the electric resistance strain gage) is a fourth rank tensor which, in general, contains 81 terms. It has been stated that if a shear stress is applied to a suitable form of semiconductor material, the property that changes is the ratio of an electrical field component to a perpendicular current density component [24]. In the absence of a shear stress, this ratio has a value of zero. Since the material most frequently used for semi-

conductor strain sensors is silicon which has a cubic structure, only three terms of the tensor are retained, and these are of the fourth rank tensor type. They may each be used as LIPs.

E. Non-Linear Systems.

In non-linear systems all of the parameters discussed in earlier sections now become amplitude-dependent. Thus each amplitude of strain propagates at its own velocity dependent on the tangent-modulus $E^* = d\sigma/d\epsilon$ at the strain amplitude being considered, even for one-dimensional mechanical traveling waves such as treated in Section 8 above.

In general, non-linear systems are frequency-creative in that the frequency-content of an emerging output signal need bear no resemblance to the frequency-content of input energy-components. Such effects can all be used as LIPs for information processing (modulation). In many cases they represent undesired environment-response combinations which are to be suppressed. The general noise-documentation methods of the Unified Approach apply to these cases [6].

ACTIVATION OR INTERROGATION OF A LATENT INFORMATION PARAMETER

Evidence of the latent information contained in a LIP can only be obtained by interrogating it with an energy component, and obtaining as a response another energy component. The information obtained in that LIP will be carried on some pattern of some property of some wave shape of that output energy component. The possibilities of activation are so numerous that a systematic study of them is given elsewhere [10]. Suffice it to say that a single, lumped-parameter capacitor, for example, can have the LIP it contains activated in at least the following ways.

1. Measurement of the value of C itself as charge per volt.
2. The time constant of a first-order system into which it is inserted.
3. The characteristic frequency of a first-order system into which it is inserted.
4. The capacitive reactance at a known frequency, in a circuit.
5. The magnitude of the impedance formed with a known series resistance.
6. The phase angle of the impedance formed with a known series resistance.
7. The damped natural frequency of a second-order system into which it is inserted.
8. The rate of decay of the transient response of a second order system into which it is inserted. (Not applicable for capacitance.)
9. The resonant frequency of a specific portion of a second-order system into which it is inserted, perhaps maintained at forcing frequency by means of a closed-loop feedback arrangement.
10. The maximum dynamic magnifier for one of the energy-storing responses in a second-order system into which it is inserted.
11. Any properties in any of the multitude of bridge circuits into which the capacitor might be inserted.

The systems cited above may be excited with a transient, such as a step, with a sine wave, or with DC. In the DC-excited system, a time-dependent LIP (or capacitance, in this case) is required, resulting in a linear differential equation with time-dependent coefficients, the responses of which carry the LIP-information on an energy component.

DEDICATION

This paper is respectfully dedicated to the memory of

WILFRID L. WALSH

for many years associated with
The A. V. DeForest Laboratory
for Experimental Stress Analysis
MASSACHUSETTS INSTITUTE OF TECHNOLOGY
Cambridge, Massachusetts

friend and teacher who first inspired me with the possibility that making measurements was a respectable occupation of which one could be proud. "Doc" had a hand in the development of the bonded resistance strain gage, of magnetic particle inspection, and of the brittle coating method of stress analysis.

REFERENCES

1. Stein, Peter K., Measurement Engineering, Vol. I, Basic Principles, Stein Engineering Services, Inc., Phoenix, Arizona, 6th edition, 1970 (1st edition, 1962).
2. Stein, Peter K., Sensors as Information Processors, Research/Development, June 1970, pp. 34-40.
3. Stein, Peter K., The Engineering of Measuring Systems, Jnl. of Metals, Oct. 1969, pp. 40-47.
4. Ostrovskij, Elektrische Messtechnik, Grundlagen einer allgemeinen Theorie, VEB Verlag, Berlin, 1969. Transl. by D. Hoffman from the original 1965 Soviet edition.
5. Stein, Peter K., The Role of the Individual in Transducer Society, SESA Paper at the Fall 1970 Meeting, Boston, Mass., and tutorial paper at the First Measurement Science Conference, California Polytechnic Institute, San Luis Obispo, California. Publication No. 22, Laboratory for Measurement Systems Engineering, Arizona State University, Tempe, Arizona 85281.
6. Stein, Peter K., The Response of Transducers to Their Environment, Shock & Vibration Bull. Vol. 40, No. 7, 1969, pp. 1-15, also Proc. 6th Transducer Workshop, IRIG, Range Commanders Council Document 112-70, White Sands Missile Range, N. M., 1970, pp. 91-106, and Proc. Strain Gage Technical Comm., S.E.S.A., of Oct. 28, 1968, S.E.S.A., 1970.
7. Stein, Peter K., The Strain Gage Encyclopedia, Vol. II of Measurement Engineering, Stein Engineering Services, Inc., Phoenix, Arizona, 1962 (out of print).
8. Lessing, Lawrence, Great Hopes from Ovshinsky's Little Switches Grow, Fortune, Vol. LXXXI, No. 4, April 1970, pp. 110-114, 122-124.
9. Taylor, George W., Feasibility of Electro-optic Devices Utilizing Ferroelectric Bismuth Titanate, Proc. IEEE, Vol. 58, No. 8, Aug. 1970, pp. 1220-1229.
10. Stein, Peter K., Information Processing in Measuring Systems, Publ. No. 20, Laboratory for Measurement Systems Engineering, Arizona State University, Tempe, Arizona, April 1970.
11. Lion, Kurt S., Instrumentation in Scientific Research, McGraw-Hill Book Co., New York, 1959.
12. Palevsky, Swank and Grenchik, Design of a Dynamic Condenser Electrometer, Rev. of Scientific Instruments, Vol. XVIII, May 1947, p. 298.
13. Williams, F. C., S. M. Noble, Fundamental Limitations of Second Harmonic Magnetic Modulators, Proc. of I.R.E., Vol. 97, Aug. 1950, pp. 445-484.
- 14a. Stein, Peter K., Strain Measurement on Ball Bearings in Operating Gas Turbines, Strain Gage Readings, Vol. II, No. 4, Oct.-Nov. 1959, pp. 3-20.
- 14b. Stein, Peter K., Strain-Gage-Based Shaft Whirl Instrumentation in Gas Turbines, Strain Gage Readings, Vol. IV, No. 3, Aug.-Sept. 1961, pp. 3-12.
- 14c. Stein, Peter K., Measuring Bearing Strain, Instruments & Control Systems, Vol. 37, No. 11, Nov. 1964, pp. 132-139.
15. Stein, Peter K., Notes and Lectures for the advanced Measurement Systems Engineering Course, ME 462, Arizona State University, Tempe, Arizona, Laboratory for Measurement Systems Engineering.
16. Neubert, H. K. P., Bilateral Electromechanical Transducers: A Unified Theory, Royal Aircraft Establishment Report TR 68248, Oct. 1968, Farnborough, England.
17. Clevis Corporation literature on Piezoelectric Materials. Bedford, Ohio, 44146.
18. Stein, Peter K., Traceability--The Golden Calf, Measurements & Data, Vol. 2, No. 4, July-Aug., 1968, pp. 97-105; Proc. Western Regional Conference for 1968, ASQC, Milwaukee, Wisconsin, 1968, pp. 109-121.
19. Schloss, Fred, Bulletins 1-10, Wilcoxon Research Corp., Bethesda, Maryland 20014.
20. Moffat, Robert J., Uncertainty Analysis, paper distributed at the 1970 Short Course on Measurement Engineering in the Thermosciences, Stanford, California.
21. Hilek, J. T., S. J. Welles, Linear Electro-optic Modulator Materials, Electronic Properties Information Center Publication S-14, Jan. 1970, Hughes Aircraft Co., Culver City, Cal., Air Force Materials Lab. Contract F33615-68-C-1225.
22. Moses, A. J., Refractive Index of Optical Materials in the Infrared Region, EPIC Pub. DR-166, Jan. 1970, AFML Contract F33615-69-C-1225 [See Ref. 21 for details].
23. Condon, E. U., and Hugh Odishaw, editors, Handbook of Physics, McGraw-Hill Book Co., New York, 1958, sections by E. U. Condon.
24. Dean, Mills III, and Richard Douglas, editors, Conventional and Semiconductor Strain Gages, Academic Press, New York, 1962, chapters by A. Kurtz.

TEST FACILITIES

USBR VIBRATION TEST SYSTEM

R. M. McCafferty
U. S. Bureau of Reclamation
Denver, Colorado

This paper describes the electrohydraulic vibration test system of the Bureau of Reclamation, Denver, Colorado. The testing facility, testing equipment, control equipment, instrumentation, and analysis equipment of the system are discussed. Testing and analysis methods used on the present testing program are also covered.

INTRODUCTION

The United States Bureau of Reclamation (USBR) of the Department of Interior has installed a vibration test system at its Engineering and Research Center, Denver, Colorado. The system, under the control of the Division of General Research, is used to study the effects of simulated earthquakes and other dynamic forces on test specimens. Primarily, it has been used for determining the structural response of reinforced concrete specimens. Programs are being considered for other dynamic problems such as structure-foundation interaction, hydrodynamic effects, dynamic material properties, and response of steel structures.

The specific equipment discussed in this paper was purchased to perform a certain function based on given specifications. In no manner may this paper be considered an endorsement of the equipment.

TEST FACILITY

Vibration equipment consisting of a double-acting ram, power supply, and electronic control equipment was first ordered in February 1966. About four months later, it was received, inspected, and installed in a temporary location where it was used in two testing projects 1, 2. It was realized from the beginning that an efficient and versatile testing facility would require a permanent installation and periodic addition and updating of equipment. Random testing capability was acquired when additional control and analysis equipment were delivered in July 1967;

however, the permanent facility was not completed until January 1969. Figure 1 shows a plan view of the 53-ft. 4-in. by 42-ft. testing facility. An overhead 5-ton crane, mounted on rails near the 26-ft. 8-1/2-in. high ceiling, is used for moving test specimens and equipment. Horizontal speeds of either 10 or 20 feet per minute (fpm) and lifting speeds of either 7 or 21 fpm are available.

A major feature of the building is the 250-ton seismic mass. The reinforced concrete mass is 28-ft. by 17-ft. by 5-ft. 8-3/4-in. with a 5-ft. by 5-ft. by 12-ft. buttress at one end. The entire mass was constructed monolithically in one day. Surrounding the mass is a 2-ft. wide trench covered with steel grates. The grates and upper surface of the mass are at floor level for ease in movement of test specimens, equipment, and personnel. Plan and section views of the seismic mass are shown in Figure 2.

Eleven steel plates are post tensioned to the mass to provide a smooth and level surface for mounting exciters and test specimens. Ten plates are horizontal and one 4-ft. by 4-ft. 6-in. by 8-in. thick plate is mounted vertically on the buttress. The horizontal plates on the mass consist of three 7-ft. by 6-ft. by 4-in. thick plates along each long side and three 4-ft. 6-in. by 4-ft. by 8-in. thick plates and one 7-ft. 6-in. by 4-ft. by 4-in. thick plate located along the centerline. All plates were positioned with preset 1/2-in. leveling bolts and grouted in place. A non-shrink grout was mixed with very little water and hand tamped into a 3/4-in. space under the plates.

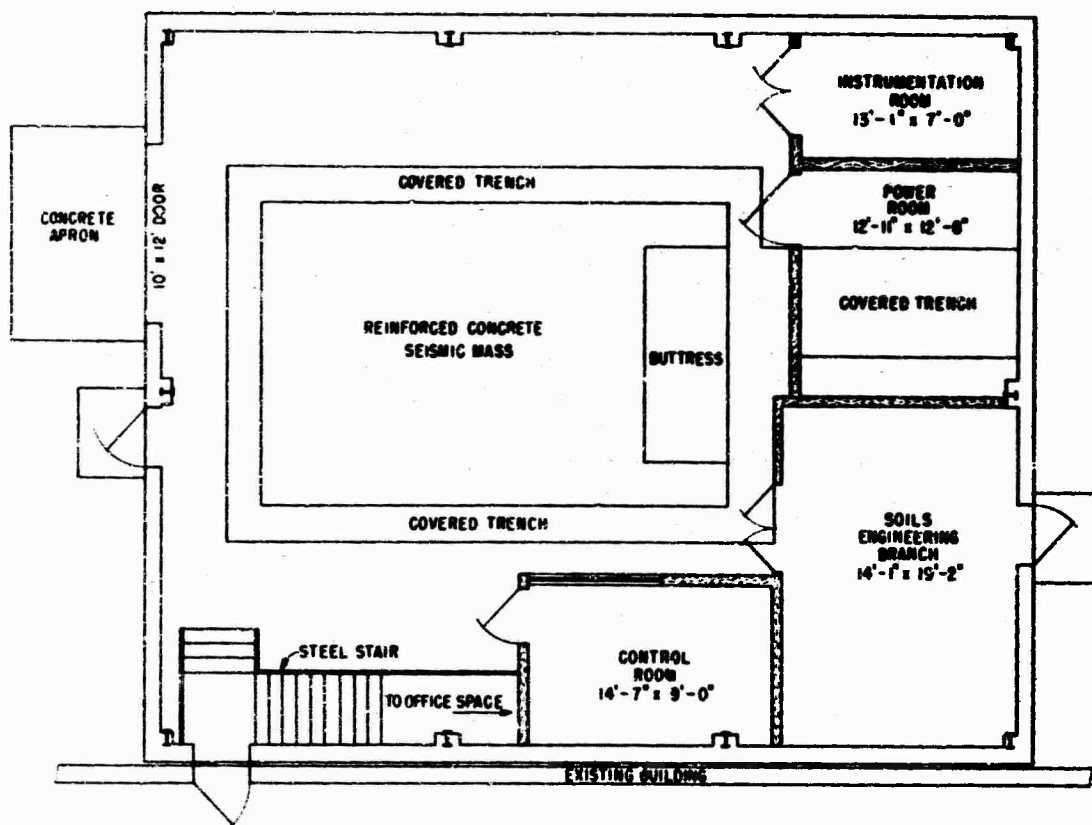


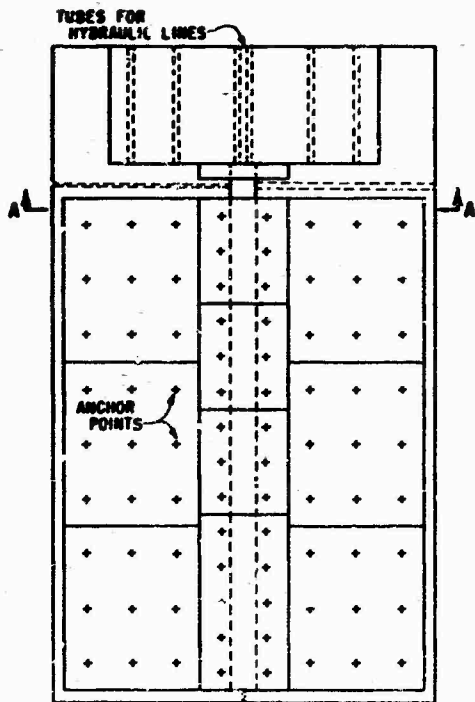
Figure 1 - Plan View of Testing Facility

All plates have a No. 135 finish and the horizontal plates are within 0.02-in. of a level plane. The buttress plate is perpendicular to the horizontal plane and the centerline of the mass.

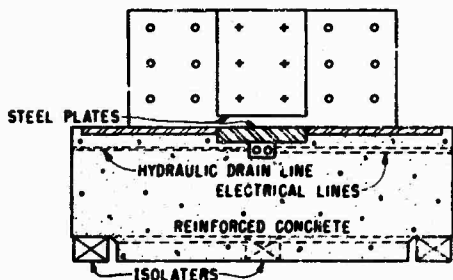
The 4-in. thick plates along the long sides of the mass are each post tensioned with nine 1-1/4-in. diameter anchors which are 2-ft. 8-in. long and anchored in the concrete by 5-in. by 3-in. by 1-1/4-in. steel plates. Anchors for the plates along the centerline are 2-in. diameter bolts and 2-ft. 8-in. long with a 7-in. by 7-in. by 2-in. anchor plate. The buttress plate is anchored similarly except that the 2-in. anchors go through the buttress and are secured with a plate and nut. Each bolt was post tensioned in two stages to 10 kips for the 1-1/4-in. anchors and 25 kips for the 2-in. anchors. The nuts are recessed and the excess anchor ground off below the finished surface. Provision was made for future addition of a steel plate on

each side of the buttress plate for special testing requirements. Since no attempts have been made to remove the plates, there is no experience on the ease of removing or replacing them. The quality of the grouting surface below the plates is unknown.

The seismic mass is isolated from its 21-in. thick reinforced concrete foundation by an air operated Barry isolation system. The system has 25 model AL255-12 isolators located in a notch (see Fig. 2) around the bottom edge of the mass. Twelve isolators are located along each long side and one is in the center under the buttress. Three master isolators, one under the buttress and one at each corner farthest from the buttress have height sensing devices. Each master determines the air pressure required at its location to maintain a 3-point level seismic mass. The remaining isolators are divided into three groups as slaves each pressure controlled by its master isolator. By



PLAN



SECTION A-A

Figure 2 - Seismic Mass

presetting the required height, the isolators maintain a given plane as the external load varies. Several isolators and the covered trench around the mass are shown in Figure 3.

The isolation system is capable of supporting 625,000 pounds (lbs) with an air pressure of 100 pounds per square inch (psi). The resonant frequency of each isolator is 1.4 Hertz (Hz) and magnification at resonance is less than 1.5. At 5 and 10 Hz, the system transmits to the foundation 35 and 7 percent



Figure 3 - Isolation System

respectively of the applied dynamic energy. Above 35 Hz, the transmissibility is less than one percent. For operation below 5 Hz the isolation system is generally turned off and the seismic mass rests on its foundation.

An 8-in. by 14-in. channel (see Fig. 2) for hydraulic lines runs just below the center steel plates from the buttress to the far end of the mass. An opening at the buttress allows access to the channel. Two pipes enter the channel through two 3-in. diameter holes under the buttress. These pipes carry oil to and from the rams. Four connection points along each pipe are available to connect hoses which are attached to the ram. For vertical operation of an exciter several feet from the channel opening, additional pipelines can be installed or one of the center plates may be removed for access to a connection point.

Three additional holes connect with the channel. One 3-in. diameter hole runs from the channel at a point near the buttress toward the control room. It contains control and instrumentation cables. A 1-in. diameter hole runs from the channel in the opposite direction of the 3-in. hole and contains a small hydraulic drain hose. A drain hole is also provided at the end opposite the buttress to prevent any accumulation of liquids in the channel.

For large test specimens access to the air-conditioned testing area is through a 12-ft. by 10-ft. wide leaf-type door (see Fig. 1). If one enters from the adjoining building which is at a higher elevation, steel stairs lead down to the testing area or up to an office and a heating, air-conditioning, and air-compressor equipment room.

Other rooms in the facility include

an instrumentation room for preparing instruments and gages and for storing supplies and tools. A soundproof room contains the hydraulic power supply. This room has a removable ceiling to provide access with the crane for equipment maintenance. It is not air-conditioned but has an exhaust fan to circulate outside air. The control room has a separate air-conditioning system and is also soundproof. To provide the maximum cooling of the equipment, air enters at the floor level under the cabinets and circulates up and out through ceiling vents. All operating controls are located in this room. Instrumentation and control lines enter the room through a trench which connects to the trench around the mass. Communication is provided between the control room and the testing area by an intercom system. The test facility also contains an area in which the USSR Soils Engineering Branch conducts dynamic tests on soils.

TESTING EQUIPMENT

Two hydraulic rams (or exciters) designed to produce dynamic or static forces were purchased from Bolt, Beranek, and Newman, Inc. The rams are shown in Figure 4 and their ratings are listed in Table 1. The 1-in. stroke ram, which is rated at 50 kips, has a Team model SV-200 servovalve to electronically control the flow of hydraulic oil. Hydrostatic bearings, located around the circumference at each end of the 5-1/2-in diameter piston, provide the capability to carry side loads. A shear force up to 5.2 kips or a 41 inch-kip moment may be safely transmitted to the ram. The 10-in. stroke ram, rated at 30 kips, has a Moog model 72-103 servovalve but no hydrostatic bearings. A clevis or other device must be attached to the 3-in. diameter piston to eliminate side loads.

For either exciter, a hydraulic

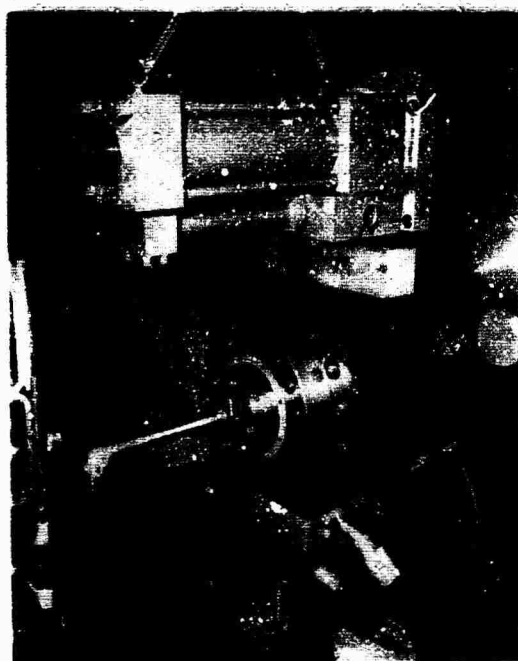


Figure 4 - Hydraulic Exciters

power supply provides oil up to 70 gallons per minute (gpm) at a maximum of 3000 psi. The power supply with a 10-horsepower (hp) priming pump and a 125-hp main pump is shown in Figure 5. A 200-gallon (gal) reservoir, water-cooled heat exchanger, pressure regulator, and accumulators are other features of the power supply. Other piping, two accumulators, and a pressure regulator are bolted to a 1/2-in. steel plate attached to the reinforced concrete block wall. Pipelines to the seismic mass are located in a trench under the reservoir and are connected

TABLE 1
Performance Characteristics of Hydraulic Rams

Ram Number	1	2
Vector Force - lbs	50,000	30,000
Stall Force - lbs	77,000	37,500
Stroke - in.	1	10
Maximum Velocity - ips	18	30
Maximum Frequency - Hz	400	100

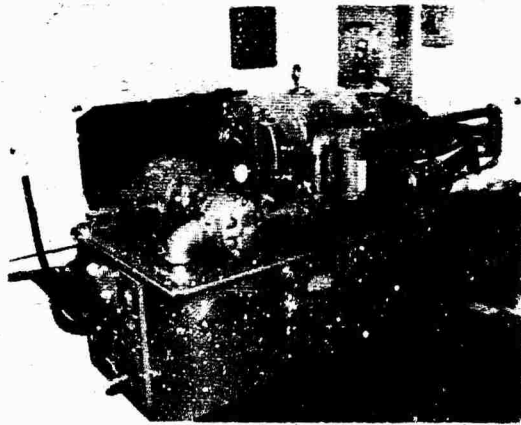


Figure 5 - Hydraulic Power Supply

by flexible hoses to the pipes going through the holes under the buttress. Supply pipes are 1-1/2-in. diameter and the return pipes are 2-in. diameter. Both pipes are rigidly attached to the floor to eliminate vibrations due to pressure pulses and hose vibrations. To keep the oil as clean as possible, it is filtered by 30-micron filters after the priming pump and by 10-micron filters after the main pump. Also, a magnetic device is located in the reservoir to remove metallic particles from suspension.

For supporting test specimens, ten hydrostatic bearing slip tables, Teas models 1830T-8 and 1830V-8, provide an almost frictionless sliding surface. Each table is capable of supporting 10 kips in tension or compression with a spring stiffness of 8×10^6 pounds per inch. All tables have a 1-1/8-in. limiting displacement and can carry a 1.75 foot-kip moment in the vertical plane of movement. Three tables (model 1830V-8) are used primarily to limit lateral displacement. They also can resist a roll moment of 0.88 foot-kips. The remaining tables (model 1830T-8) are intended primarily to carry vertical loads and can resist a roll moment of 1.66 foot-kips. They also limit lateral movement to ± 0.05 in. Hydrostatic slip tables with 10-in. strokes are planned for use with the long-stroke ram.

A hydraulic power supply for the slip tables provides oil at 0.6 gpm and 2500 psi to float the moving elements. A suction pump returns the oil to a 10-gal reservoir. The power supply is located in the trench behind the buttress end of the seismic mass. Pressure and suction hoses extend halfway along

both sides of the mass and terminate at the floor level with quick disconnect connections. During operation, additional hoses lead from these connections to manifolds. Other short hoses are then connected to the slip tables. Oil will not be returned to the reservoir unless care is taken to keep the return lines below the overflow level of the slip tables.

CONTROL EQUIPMENT

Most of the electronic equipment is located in the air-conditioned control room. Figures 6 and 7 show the desk console, one- and two-bay instrumentation cabinets, and other equipment on the shelves.

For general sin wave dynamic testing two oscillator systems are available. Both may be operated either individually or simultaneously to drive two exciters in a closed-loop configuration to maintain a preset acceleration, velocity, or displacement level. The oscillator

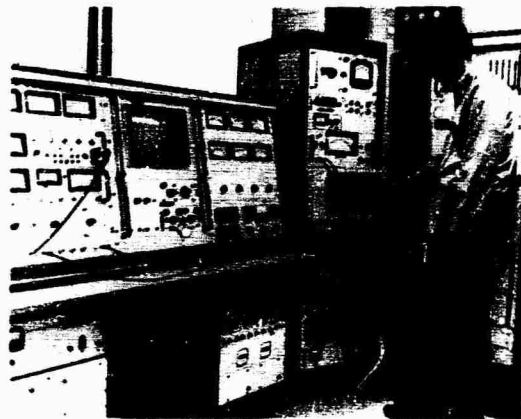


Figure 6 - Control Equipment

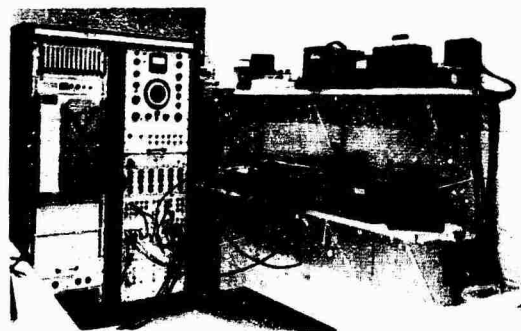


Figure 7 - Testing Equipment

purchased initially was a Bruel and Kjaer model 1039. It produces a sinusoidal signal from 5 to 5000 Hz or from 5005 to 10,000 Hz. Logarithmic sweep rates at 132 different speeds range from 0.3 to 335 degrees per min on a circular 220-degree scale. The regulation speed of the compressor may be manually set at 10, 30, 100, 300, 1000, or 3000 db per sec. Also the oscillator can automatically select one of the above levels at specific crossover frequencies. Crossover from control of displacement to acceleration or of velocity to acceleration may be made between 8 and 1000 Hz. Great care is required in setting the crossover frequency to minimize the jerk-effect produced at the exciter. Closed-loop control of acceleration from an accelerometer signal can only be performed above 10 Hz.

An Unholtz Dickie model ATC-6 averager may be used in conjunction with the above oscillator. It has the same regulation speeds and can select either the largest or a weighted average of up to six accelerometer signals to control the exciter. In the averaging mode, the unit is phase insensitive.

When the vibration test system was expanded, Spectral Dynamics oscillator control units models SD104 and SD105 were purchased. Sinusoidal, triangular, or square wave forms may be generated in five ranges from 0.005 to 50,000 Hz. Either logarithmic or linear sweep rates may be selected. Continuously variable rates are available from 0 to 720 degrees per min for the logarithmic sweep and 0 to 1000 Hz per sec for the linear sweep. The regulation speed in the manual mode is continuously variable from 10 to 3000 db per sec. In the automatic mode, the regulation speed varies as a function of frequency from a lower limit of 10 db per sec to a manually set upper limit of 300 to 4000 db per sec. Automatic thump-free crossover is possible from displacement to acceleration up to 200 Hz or from velocity to acceleration up to 1000 Hz. The unit continuously monitors both control values and the crossover occurs when the acceleration reaches a preset level. DC signals proportional to frequency are available for plotting on X-Y recorders. Electronic filters, which are described under ANALYSIS METHODS, may be included in the closed-loop to clean up noisy signals. An unstable control condition may occur if the regulation speed is set greater than eight times the filter bandwidth or if the filter is operated at a frequency less than one half of its bandwidth.

Two random noise generators may either individually drive the system or

provide signals to a Ling model ESD-13 equalizer. The equalizer has 13 filters with bandwidths from 10 to 50 Hz over the frequency range of 10 to 450 Hz. The random noise signals may be shaped by adjusting slide wire controls of the various filters. A 14-channel FM magnetic tape recorder is available to provide a control signal. One channel is wired so that while its output is driving the system the remaining channels can be used to record data. Special tapes have been obtained with four recorded earthquakes at different time scales. Both acceleration and displacement records are available.

A curve follower, Data Trak model FGE-5110, was purchased to generate arbitrary shape signals but at this time has not been used. The desired wave form is drawn on special 8-in. wide paper. The paper may be several feet long for one test or only the circumference of the drum for a repetitive fatigue test. A set of gears can vary the chart speed in 13 steps from 2-1/2 to 40 in. per min. The curve follower has a maximum following rate of 7 in. per sec (ips) and has a full scale output of 2.5 volts. The signal may either drive the system or be recorded on the tape recorder. If recorded, the time scale may be altered by playing the tape at a speed different than the recording speed.

Several protection devices are included to automatically shut down the system whenever certain functions are in error. The main and priming pumps are shut down if there is a loss of pressure, loss of hydraulic fluid, or the pressure of the slip table power supply drops below 2250 psi. An electronic protection unit, Spectral Dynamics model SD123, protects a test specimen from over or under testing. It senses the RMS value of an accelerometer signal. If the signal is greater than or less than a predetermined value, the driving signal is automatically and smoothly attenuated by 80 db. The preset over or under amount can vary in nine fixed steps from 1.0 to 6.0 db from the preset RMS acceleration value.

INSTRUMENTATION

A wide variety of instruments is available to measure the response of test specimens. Presently accelerations can be measured with any of the following USBR accelerometers: (1) Nine Columbia model 302-6, (2) Six Bruel and Kjaer type 4332, (3) Two Endevco model 2260-250-10 and (4) One Kistler model 808K. The Columbia and Bruel and Kjaer accelerometers are used for general

testing. The Endevco accelerometers are a strain-gage type and have presently not been used. The Kistler accelerometer is used as a calibration standard and has the capability to be directly mounted to another accelerometer. Amplifiers for the accelerometers consist of six Unholtz Dickie model 9P-1 voltage amplifiers and six Columbia model 9000 charge amplifiers. Two portable amplifiers, Columbia model 9001 and Kistler model 504A, are available. Accelerometers are normally attached to the test specimens with Endevco model 2983B insulated mounting studs, magnets, or a high quality cement.

Dynamic displacements are measured by a group of linear variable differential transformers (LVDT) and calibration and static movements are measured with either an LVDT or dial gage. LVDT's with a range from 0.1 to 1.0 in. are immediately available and units with longer stroke capabilities are obtainable. Relative rotation of two points (up to ± 20 degrees) may be measured with three Cleveite Brush model 3306 transducers. A universal 50-kip load cell can be installed between the exciter and test specimen. Its output, which is proportional to load, may be used in a closed-loop to control the exciter. Other transducers are capable of measuring load, pressure, and strain.

For accelerometer calibration two methods are available. For a complete calibration over the usable frequency range, an electrodynamic exciter, MB Electronics model PM50, driven by a model 2250-MB power amplifier is available. This exciter has a force rating of 50 lbs and may also be used to test small specimens or for demonstrations. Values of peak-g versus frequency are plotted on X-Y or X-Y-Y recorders. For a quick calibration check, a General Radio model 1557-A calibrator, which operates at only 100 Hz and up to 2-g's is used. Output from the accelerometer and amplifier under calibration is displayed on a Ballentine model 321 true RMS voltmeter in a peak mode to provide a calibration of X volts-peak per g-peak. All accelerometers are given a complete calibration every year or whenever indicated necessary. Before testing a new specimen, accelerometers to be used are given a quick calibration check.

ANALYSIS METHODS

Most of the data are presently analyzed electronically; however, in the future more complicated methods involving the digital computer will be required. The accelerometer and other data are generally recorded on the

14-channel FM tape recorder. Depending upon the duration and frequency of the data to be recorded, tape speeds are selected as either 60, 30, 15, 7-1/2, 3-3/4, or 1-7/8 ips. A voice channel can be used to record pertinent information for ease in identifying data on the tape. Several strip chart recorders and a direct writing oscillograph, both utilizing galvanometers, are available for recording high frequency signals.

During sinusoidal testing, results of one or two accelerometers are generally displayed on X-Y recorders as a peak-g versus frequency curve. This curve is obtained by electronically filtering the acceleration signal with Spectral Dynamics model SD1012 and SD28 filtering equipment. Filter bandwidths of 1-1/2, 10, and 100 Hz can be used with the above two-channel system. The filters operate as peak filters with a center frequency corresponding to the systems operating frequency. Data recorded on the tape recorder can later be analyzed in the same manner.

Electronic integrators are capable of integrating an acceleration sinusoidal signal to obtain the velocity and displacement. Instantaneous peak values of each quantity are displayed on separate meters and the velocity and displacement wave forms are also available. Six additional meters display peak acceleration values from preselected accelerometers.

Some analog to digital (A-D) capability presently exists. DC voltage readings of 160 per minute for a four-channel continuous scan to 95 per minute for a single channel scan can be obtained and punched on paper tape. The information on the paper tape can then be transferred to a magnetic tape for use on a computer. A high-speed A-D system is being considered to directly generate a digital magnetic tape.

Additional electronic equipment for data analysis and general usage is located in the control room. Two logarithmic converters are available and used when there is a large range of values and more accuracy of lower values is required. A phase meter is available for determining the phase angle between two signals. Also resonant frequencies may be found by observing when the phase angle between the driving and response signal is 90 degrees. Additional equipment consists of oscilloscopes, a digital multimeter, and a frequency counter.

TESTING TECHNIQUES

The vibration test system is



Figure 8 - tests of Beam-Column Connection

presently being used to conduct dynamic tests of reinforced concrete beam-column connections. The project is designed to evaluate the amount of hoop reinforcing steel required in the joint region under dynamic loads. The testing arrangement for the specimen in relation to the exciter and other equipment is shown in Figure 8. A test fixture (the steel tubes and plates around the concrete specimen) was constructed instead of a large one piece shaking table. Shaking tables are being used and constructed in several other vibration facilities. It is difficult to design a shaking table which would be versatile enough for all projects. Therefore, the USBR constructs a special fixture for each testing program to keep total weight to a minimum. This procedure allows larger specimens to be tested and higher acceleration levels to be attained.

The present test fixture may be considered a form of shaking table since it moves on top of eight slip tables. At the ends of the specimen, the center slip table restricts lateral movement. A 2-in. high-strength steel rod tapered down at one point to 1-in. diameter serves as a fuse or moment limiting element at the exciter (see Fig. 4). The slip tables carry the shear load and the fuse is designed to fail at the limiting moment capacity of the exciter.

The horizontal portion of the concrete specimen represents a column while the remainder represents a beam of a reinforced concrete frame building. To simulate dead load and support conditions of the prototype structure, an axial load is applied to the column by a hydraulic ram and four high-strength rods. Each end of the column is simply supported on three sets of steel balls and the center is simply supported on two slip tables.

Tests on each specimen begin with a static load applied at the beam end to determine a stiffness value from measured loads and displacements. Linear sweep tests simulating steady-state sinusoidal input are then conducted to determine the natural frequency and damping value. The natural frequency of the test specimen is varied by applying different amounts of mass to the free end of the beam. Normally, several linear sweep tests are conducted for each mass condition while the mass is varied in six steps from 0 to 1100 lbs. The mass consists of a series of steel plates bolted together to attain a maximum height of 18-in. The uncracked natural frequency is reduced from about 44 Hz with zero mass to about 22 Hz with the 1100 lb mass. During this series of tests, care is taken to maintain the excitation intensity below the value

required to produce cracks.

An earthquake such as El Centro NS (1940) is then selected with a time scale such that the natural frequency of the specimen is within the predominant frequencies of the earthquake spectrum. The tape recorded earthquake is then used to excite the specimen at a level to produce some cracking. The static and dynamic sweep tests are then repeated to determine the amount of damage that has occurred. Next, the earthquake is programmed at a greater magnitude to produce a high level of damage or possibly failure of the specimen. Static and dynamic sweep tests are again performed to determine the additional damage. If failure has not occurred, sinusoidal tests of a given duration, magnitude, and frequency range are conducted. These tests are designed to provide excitation that is always near the resonant frequency of the specimen. To accomplish this, the frequency of the exciting force is slowly swept downward from the last measured resonant frequency to a predetermined value. This change in frequency is included to simulate the reduction in resonant frequency that results as additional cracks are developed in the concrete.

In the past tests after major cracking has occurred, the natural frequency with the maximum mass has reduced to about 10 Hz. Measured damping values have varied from a very small amount up to about 4 percent of critical with major cracks in the concrete.

Sweep test data are analyzed by plotting and digitizing the peak-g versus frequency curve. Digital computer programs are used to obtain damping values from the digitized curve and to obtain natural frequencies of an analytical model. In the future earthquake input will be digitized and used to analytically predict the single degree of freedom response of the specimen for comparison with the measured response. All of the results are used to determine how specimens, with various amounts of hoop reinforcing steel, withstand identical dynamic loads.

Presently the capability to which the test system can duplicate an earthquake

type input has not been fully studied. Visually it appears that the recorded acceleration wave form for the El Centro earthquake compressed by a factor of 5 agrees quite well with the acceleration input. The records have not been digitized for input to a computer for computation of the simulated earthquake spectrum.

CONCLUSIONS

The USBR vibration test system after several years of development and progress, is now operational in a new test facility. It is capable of testing a wide variety of specimens from very small to quite large masses. The upper specimen size limit is restricted only by available space or the exciter rating. There are some functions that cannot be performed but most are possible with the addition of equipment presently being manufactured. The greatest deficiency of our equipment is the difficulty encountered at frequencies less than 5 Hz in some instances and 10 Hz for other pieces of equipment. The high frequency range capability of the control equipment is generally not used in our structural testing.

The vibration test system was assembled essentially from components presently used by the aerospace industry. The system is capable of performing most civil engineering tests where the dynamic response of structural elements or models are to be studied. Future projects may include the hydrodynamic effects on submerged structures, structure-foundation interaction, or the effects of nonstructural elements in frame structures.

1/ R. M. McCafferty, "Transmission Cable Wear Rate Due to Preformed Spacers under Dynamic Load," U.S. Bureau of Reclamation, Report No. C-1230 (April 1967).

2/ G. L. Butler, "Static and Dynamic Load Test of Target System, External Tow Gunnery A/A37U-15," U.S. Bureau of Reclamation, Report No. C-1244 (July 1967).

DISCUSSION

Mr. Isada (University of Buffalo): In how many directions or how many degrees of freedom can you test this specimen?

Mr. McCafferty: We are presently limited to one degree of freedom or one direction. We nor-

mally use slip tables that are limited to one direction. We have two shakers and all of the control equipment necessary to operate them simultaneously, but we do not plan to do this in the near future. It is possible to excite in two directions, but there are many other problems involved.

MULTI-DEGREE OF FREEDOM MOTION SIMULATOR SYSTEMS FOR TRANSPORTATION ENVIRONMENTS

T. K. DeClue, R. A. Arore and C. E. Deckard
Wyle Laboratories
Hurtsville, Alabama

This paper presents a discussion on multi-degree of freedom motion simulation systems used to simulate ground transportation and aircraft environments. The paper describes the approach used at Wyle Laboratories to design vibration test environments from which meaningful test results can be obtained. A description of four types of systems, two presently in operation and two under study, is presented.

INTRODUCTION

Tests of items of equipment are conducted in the laboratory for one, or more, of several reasons:

- Control of conditions
- Control of test scheduling
- Simplification of analysis
- Repeatability
- Economy
- Safety

The value of the laboratory test is directly related to the fidelity with which the service environment can be reproduced during test; if the reproduction is faithful, then the test item responses are duplications of those experienced in service and test results can be directly equated to actual performance.

If, however, the laboratory environment differs from that found in service, the test results are only indications of what might happen.

This paper describes the approach used at Wyle Laboratories to design vibration test environments from which meaningful test results can be obtained. The design is an iterative process and, like most engineering efforts, frequently requires re-evaluation and compromise. The philosophy of design is as important as the actual design, and will be explained first.

DESIGN PHILOSOPHY

The Wyle Laboratories approach to the design of a dynamic test starts with an evaluation of the impor-

tant aspects of the service environment; i.e., the origins, transmission paths and coupling modes of the forces acting on the specimen during service.

The goal is to reproduce the service environment in all important respects. When it is not possible to reproduce certain aspects of the environment, for example, the long-term inertial forces acting on major components of an item, the effects of that part of the environment are simulated by some acceptable method. When portions of the environment are simulated, the mechanism of simulation may introduce artifacts, or deviations from precise realism of the test item response. The importance of any test artifact must be considered both during the test design and test data evaluation to weigh the validity of the test results.

The object is to assess the magnitudes and frequency spectra of the forces and couple them to the specimen through impedances similar to those of the support used in service. If possible, the actual support hardware will be used in order to provide a duplication of the service boundary conditions. The more complex the test item and its support hardware are, the greater is the need for accurate boundary reproduction and the more difficult it is to provide simulation of the boundary through manipulation of the inputs.

The first step in the design of the test is, then, to determine how large a section of the entire system, of which the specimen is a part, can be accommodated within the laboratory space and exciter force limits and subjected to the boundary dynamic environment.

The second step is to determine how many degrees of freedom of motion are to be allowed and excited in the specimen. Again, we go back to the evaluation of

the service environment for our answers. We should, of course, allow and excite motion in all degrees of freedom available to the specimen in service. Because of equipment and mechanical limitations, it is often not possible to achieve this goal and compromises must be made.

As each compromise is identified, the effects of the compromise upon the test realism must be evaluated as well as the possibility of achieving the same result by some other means. If we cannot accurately determine that the lack of realism will not reduce the value of the test, we must reproduce the effects and accept the artifacts.

Several designs are discussed in the balance of this paper; although quite different in size and construction, they are alike in that they allow for a high degree of reproduction of the dynamic service environment and introduce very few artifacts. Fidelity of reproduction is maintained by accommodating the entire test item, be it a five pound radio or a fifty ton tank, and providing realistic inputs in several degrees of freedom.

Where, through analysis or instrumentation of the actual environment, it was found that motion does not occur in or about one, or more, of the axes, those degrees of freedom are restrained. Typical of this is the yaw axis restraint imposed on the railcar simulator and roll, pitch and yaw restraint in the helicopter simulator.

The restraints imposed at the fore and aft motion of the test items in the designs of the tank road test simulator and the wheel/rail dynamics simulator do not, as they might first appear, impose restrictions on the dynamic environment. They are, in fact, necessary to maintain fidelity by providing a reference point for the inertial image and, thereby, assure that the dynamic forces and reactions are properly transferred across the profile/vehicle interface.

In all cases, the approximate gross mechanical properties of the external environment to which the test item is exposed in service are maintained in the simulator restraints and force coupling arrangements. This has been done either by selection of mechanical components with the proper spring/mass characteristics, or by electronically modifying the input signals to the simulator, or by both methods simultaneously.

FIVE DEGREES OF FREEDOM RAILCAR SIMULATOR

Introduction

A five degrees of freedom railcar simulator has been constructed and placed in operation at Wyle Laboratories, Huntsville. This simulator will accept

entire vehicles and structures such as equipment shelters and transportation containers. The first test program using this system entailed simulation of the railcar shipping dynamics on automobiles to develop solutions to railcar shipping damage problems.

Railroad Automotive Transporter Environment

Two railroad auto transport cars consisting of one "low tri-pak" and one "standard tri-pak" were instrumented to determine vibration characteristics over the railroad bed between the Midwest, and Los Angeles, California. The primary purpose of the trip was to obtain data of the vibration induced into the automobile at the tires, in each of three mutually perpendicular axes during transportation. Accelerometers were attached on the platform at two automobile positions on each of the two railroad cars and interconnecting cables installed to the instrumentation system located in the caboose. Figure 1 shows the installation. Vertical acceleration measurements were made at each of the four automobile tire locations, and longitudinal and lateral acceleration measurements made at the center of the automobile. The accelerometer data were recorded on magnetic tape during the forty-eight hour trip.

Upon return of the test tapes to the Wyle/Huntsville Facility, the tapes were played back on an oscillograph and the traces examined for significant amplitude indications. Several of the high amplitude areas were then selected for computer analysis. Figure 2 presents a typical PSD plot.

Based upon the data analysis, a set of accelerometer outputs (six channels) were selected to be re-recorded on a second tape which was used as the test control tape. The control tape was produced by selecting portions (approximately one and one-half hours total) of the trip and recording them three times on one reel. The four and one-half hour test control tape could then be played into the simulator six times which was equivalent to a 27-hour trip covering 1700 miles.

Simulator Design and Fabrication

The railcar simulator consists of the following:

- A platform constructed from a section of a tri-pak railcar using minimum stiffening and restraint so that the test platform would exhibit similar high frequency local responses to those of the actual railcar platform.
- Six hydraulic actuators with associated servo valves, displacement feedback transducers, hydraulic power supply, and control electronics. Four actuators were positioned in the vertical axis and two actuators were

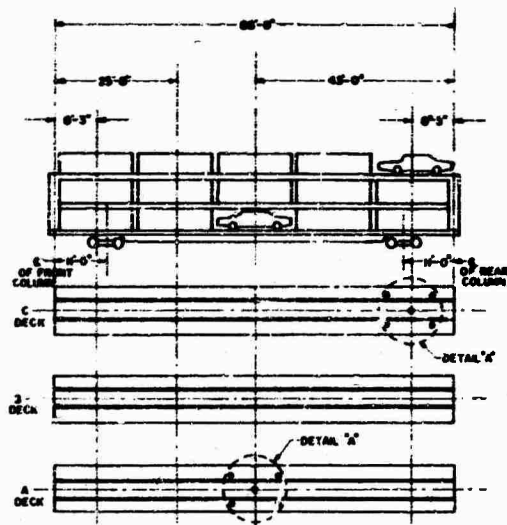


Figure 1. Typical installation of two railcars

horizontally oriented to impart motion through the c.g. of the platform in the lateral and longitudinal directions. Figures 3 and 4 show the simulator setup.

- Fixturing, air springs, spherical bearings, and a parallel cable assembly.
- Automobile tie-down devices to establish the proper relationship of the chain tie-down from the vehicle underbody to the tie-down track on the railcar deck.

The vertical and longitudinal actuator displacement capacity required was 4.0 inches and the lateral actuator displacement capacity 8.0 inches. The actuator force requirements were 13,600 pounds for the lateral and longitudinal actuators and 27,400 pounds for the vertical actuators. Frequency response was 0.5 to 25 Hz. The structural beams used to react the actuator loads were pre-loaded into existing reaction masses and designed to be resonance free in the 0.5 to 25 Hz frequency range.

Spherical bearings were located at each end of each actuator to provide unrestrained dynamic inputs. A parallel cable assembly (concept similar to that used on drafting boards) was installed to provide straight line lateral and longitudinal movement. This prevented yawing of the simulator during test. An air spring system was used to support the static load. Each air spring was connected to a reservoir for the purpose of lowering the air spring system resonance to less than 0.5 Hz.

Thus, the system was capable of providing motion in the three orthogonal directions as well as pitch and roll rotational directions.

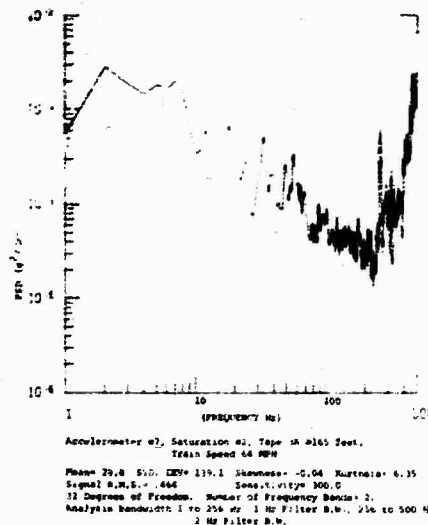


Figure 2. Typical PSD plot of acceleration data (lateral measurement)

Test Operation

Motion control was accomplished by reproduction of the dynamic displacements of the railcar. The recordings of the accelerometer signals obtained during rail transport on magnetic tape were played back to the system through double integration electronics, thereby transforming the acceleration signals to displacement signals. The signals were then sent through closed loop servo control electronics to the six actuators which provided lateral and longitudinal motion plus vertical motion at the four corners of the test platform. The actuators responded to the displacement signals, reproducing the motion at the actuator input points corresponding to the data transducer locations on the railcar platform. Thus, the actual railcar displacements, as recorded from the field data, were duplicated in real time on the motion simulator and the equivalent of a Midwest to West Coast railway shipment was simulated within a period of approximately 27 hours.

THREE DEGREES OF FREEDOM VIBRATION TEST SYSTEM

Introduction

A three axis vibration test system has been developed and placed in operation by Wyle to simulate helicopter flight environments. The system originated from a requirement by the United States Army Aviation Test Board, Fort Rucker, Alabama to create a vibration environment in the laboratory that is representative of the vibration environment encountered by the AN/ARC 115 radio set when installed in on OH-58 helicopter.

Flight Data Acquisition

The OH-58 helicopter radio set (AN/ARC 115)



Figure 3. Railcar simulator (top view)



Figure 4. Railcar simulator (bottom view)

was instrumented with seven piezoelectric accelerometers and two thermocouples to monitor the in-flight vibration and temperature environment. Four accelerometers were attached to the instrument panel adjacent to the radio to monitor the vibration input to the radio. Three accelerometers were attached to the rear of the radio case to monitor actual radio response. The sensitive axes of the accelerometers were oriented parallel to the longitudinal, lateral and vertical axes of the radio face plate. Figure 5 shows the accelerometer locations and orientations. One thermocouple was located approximately one inch behind the radio case to measure free air cabin temperature. One thermocouple was attached to the rear of the radio case to measure operating temperature.

A 14-channel tape recorder was used on board the aircraft to record all accelerometer output data. During the flight tests, one channel was reserved for voice commentary concerning general test conditions and event time. A 1 kHz reference signal was recorded on a second channel to provide a real time base for data analysis and a check on recorder tape speed.

A 1 kHz acoustic calibrator was used to produce a constant amplitude audible tone for periodic transmitter modulation checks during flight testing.

Two complete flight profiles were performed at Fort Rucker, Alabama. The following profiles were representative of actual conditions which were being encountered during flight testing on the OH-58 helicopter at Fort Rucker.

Flight Profile No. 1

- One-minute hover (3 feet)

- Seven-minute flight at maximum velocity attainable, not to exceed VNE (velocity never exceed) at 1500 ft. MSL (mean sea level)
- Simulated diving firing with 60 degree bank, 180 degree side entry and right pull up
- Twenty-minute loitering at 60-70 knots
- Diving firing with 60 degree bank, 180 degree side entry and right pull up
- Twenty-minute loitering at 60-70 knots
- Simulated diving firing with 60 degree bank, 180 degree side entry and right pull up
- Twenty-minute loitering at 60-70 knots
- Diving firing with 60 degree bank, 180 degree side entry and right pull up
- Twenty-minute loitering at 60-70 knots
- Simulated diving firing with 60 degree bank, 180 degree side entry and right pull up
- Twenty-minute loitering at 60-70 knots
- Diving firing with 60 degree bank, 180 degree side entry and right pull out
- Seven-minute flight at maximum velocity attainable not to exceed VNE at 1500 ft. MSL
- One-minute hover (3 feet)

Flight Profile No. 2

This mission was conducted in the same manner as Flight Profile No. 1 with the following exceptions:



Figure 5. Accelerometer locations during flight test

- a. The simulated diving firing and diving firing order was reversed.
- b. All diving pull-ups were to the left.

Vibration data were continuously recorded on tape during take-offs, dash to VNE, each phase of the flight profiles and landings. Cabin temperature, radio set case temperature, and transmitter carrier output and modulation were periodically measured and recorded throughout each flight test. At the conclusion of each flight test, the taped records were played back through the on-board tape recorder and visually displayed on an oscillograph. This allowed examination of the recordings to assure the acquisition of proper data and provided a means of determining the need for repeating a test or correcting any anomalies prior to further testing.

The vibration data obtained during the actual flight test were reduced to X-Y plots, oscillograph records, and computer analyzed power spectral density (PSD) plots. These data were analyzed and reviewed with Fort Rucker personnel. Figure 6 shows typical PSD plots of accelerometer data.

The data channels with the highest level of vibration in each of the three mutually perpendicular axes, and with the best representation of the flight vibration environment were isolated and selected to provide the vibration input to the vibration fixture during the laboratory simulated flight test. A master tape recording was prepared by duplicating these specific portions of the flight test tapes in order to provide a two-hour profile of the helicopter during flight.

Laboratory Simulation of Flight Vibration Environment

The radio sets were mounted by their normal

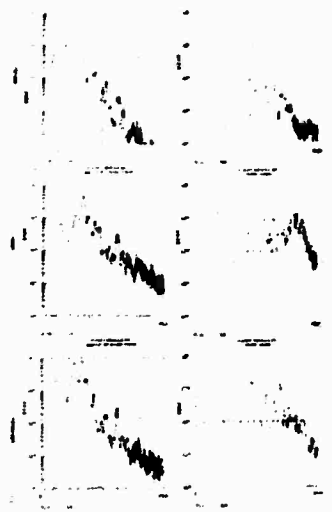


Figure 6. Typical PSD plots (AN/ARC 115)

means to a three axes vibration test system as shown in Figures 7 and 8. The three axes vibration test system consists of three electrodynamic exciters and a square aluminum mounting plate that provides an attachment for the test specimen as well as input points for the three orthogonal vibration test axes. Simultaneous excitation and stability are realized by the fact that although motions are unrestrained in the three orthogonal axes, they are restrained in the three roll axes. This is accomplished by using specially designed drive adaptors that are axially stiff and laterally soft.

During testing, the master tape recording containing the profile was played into a control system, and each of the three axes signals routed to its respective exciter system. Figure 9 shows the control system. The taped signals were amplified and passed through filter networks which compensated for fixture and exciter resonances. A master control unit was incorporated to provide start up and shut down of the entire system.

Three control accelerometers were located on the vibration fixture (one for each exciter). The output signals from the accelerometers were monitored during testing to insure proper vibration levels and observe any anomalies. Periodically during the test, the output signals from the control accelerometers and the tape input signals to the three axes system were recorded and analyzed on a digital computer. The data generated from the simulator tests compared favorably with the data generated during the flight test. The electrical operation of the radio test sets was checked at the start and end of each profile. This functional test consisted of the following measurements:

- Transmitter carrier output
- Transmitter carrier modulation

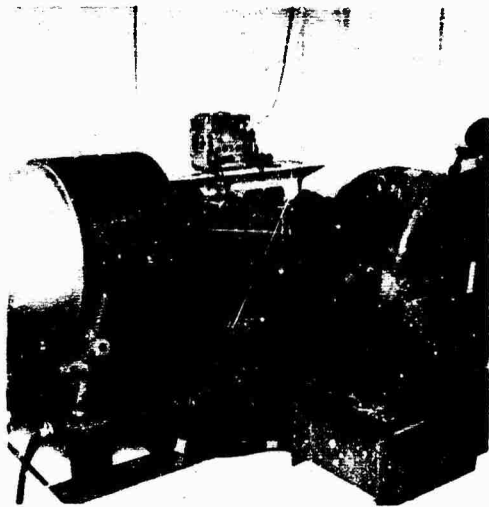


Figure 7. Helicopter simulator test setup (overall view)

- Input voltage
- Case temperature
- Ambient temperature

The operational characteristics of the on-board helicopter radio equipment were determined for a duration of 1500 hours of testing.

FIFTY TON TRACKED AND WHEELED VEHICLE ROAD SIMULATOR

Introduction

Wyle Laboratories was awarded a contract by the Army Tank Automotive Command to determine the feasibility for the design and construction of a road simulator for testing large size vehicles up to and including the M-60 tank. Initially, the effort involved the investigation of two system concepts that seemed most practical for accomplishing the requirement. The investigation then developed to the point where one system was selected for the final, more detailed feasibility study. Though the primary task was to determine the optimum system that would deliver the maximum operational parameters, the system itself would be an integral part of a large testing laboratory. Consequently, such things as system layout, heating, cooling, exhausting techniques, accessibility and noise levels were factors of considerable importance.

Operational Parameters

The operational goals of the system were established by the Army Tank Automotive Command and were considered as design criteria for the feasibility study. These parameters are as follows:



Figure 8. Helicopter simulator test setup (close-up view)

- Vehicle weight 50 tons
- Maximum vehicle velocity 50 mph
- Maximum point loading at any one vehicle road wheel 80,000 lbs.
- Maximum bump height 12 in.
- Minimum bump spacing to bump height ratio 1.5 to 1.0
- Maximum vertical velocity of bump profile 270 in. per sec.
- Maximum vehicle acceleration rate 0 to 20 mph in 10 sec.
- Maximum incline 30 per cent grade

Simulation of vertical and tangential loads into the vehicle road wheels were required. Each side of the simulator was to be independently controlled for bump profile. No special requirements were set for simulation of vehicle braking. The vehicle was to be remotely controlled while under test.

Concept Description

The two basic systems initially investigated with regard to fulfilling the operational requirements were:

- Electrohydraulic System

This system, shown in Figure 10, utilizes twelve electrohydraulic exciters for system excitation. These exciters generate extremely high forces and operate satisfactorily over the range of frequencies required for road test simulation. System performance is a function of the pressure and flow capacities of the

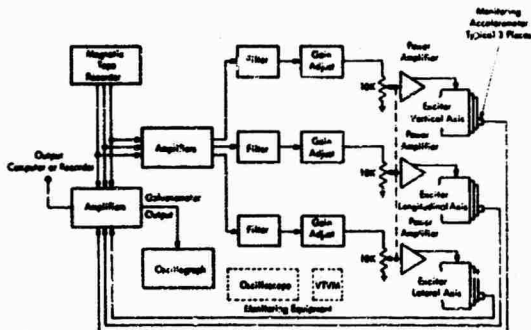


Figure 9. Helicopter simulator control system

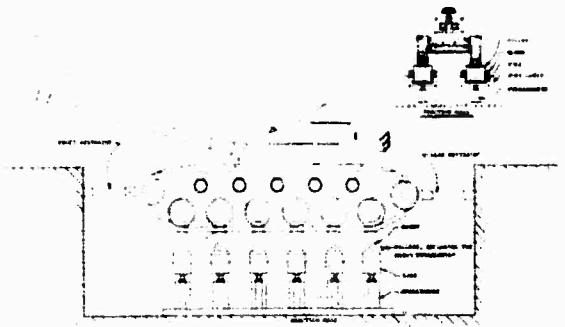


Figure 10. Road simulator hydraulic system concept

pumping system as well as the area and stroke of the vibrator exciters. Complex electronic servo-systems are utilized to program and control the operation of the exciters.

The maximum operating conditions set forth in the design requirements call for an average hydraulic flow rate of 557 gpm per exciter. These exciters would be sequentially programmed to provide some repeating type input to the vehicle. Each exciter extension would terminate in a yoke which holds a motor dynamometer. The torque of these devices would be controlled to present a simulation of the gross terrain profile to the vehicle.

This system would display a requirement for maximum power when simulating maximum bump and climbing conditions. Calculations show this maximum power requirement to be 9,084 hp. Assuming eighty per cent efficiency of the hydraulic pump driving motors and motor dynamometers, the total primary electric power would be 8,500 kva.

• Mechanical System

The second concept involved using a mechanical system employing two "endless belts" similar in function to a large tank tread. Road surface profiles could be programmed on these belts, which would then be driven under the wheels of stationary vehicles.

The most practical concept for this approach involves providing a series of linked

carriages beneath the vehicle, with each containing steel plates that could be actuated vertically to simulate a bump input. This concept is shown in Figure 11.

Extension of the plates would be accomplished with a long stroke hydrashaker for each track. Road profile wavelengths could then be programmed in increments of multiples of the thickness of the steel plates. Each plate would be extended an amount determined by the basic program above the link surface, located in place and driven under the wheels of the vehicle. Before returning to the program position again, the plates would be unlocked and returned to their bottom position.

The system would exhibit a requirement for maximum power when simulating vehicle acceleration and bump conditions simultaneously. The power required by the drive motors to simulate the maximum specified acceleration is estimated to be 800 horsepower. Calculations show that should maximum bump simulation be required during vehicle acceleration, the total power requirement would be 3,028 hp. Again, assuming eighty per cent pump and motor efficiency, the total primary electrical power requirement would be 7,830 kva.

The mechanical system was selected for the total feasibility study based upon a comparison between the two concepts and because of its versatility and lesser power demands.

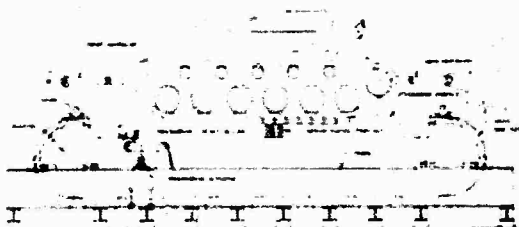


Figure 11. Road simulator mechanical system concept

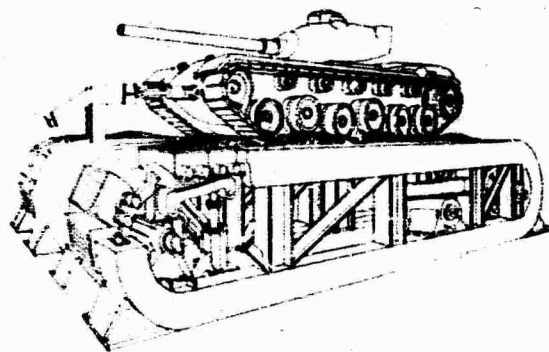


Figure 12. Pictorial view of road simulator

Mechanical System Description

The total system concept is more readily understood by separating the basic configuration into its major components. Figure 12 gives a pictorial view of the system. A description of the basic system components follows:

● Mechanical Configuration

The mechanical configuration includes all members, linkages, bearings and mechanisms that are employed to present a variable bump to the tank tracks. The conceived system provides two separate treadmills, one for each side of the vehicle. Each treadmill consists of a series of carts supported on bearing rollers. The carts are linked together and form a brake chain which is pulled under the vehicle by large sprockets. The carts are pulled along the underside of the assembly, up over the opposite end sprocket and then repeat the sequence.

Each cart contains profile simulating plates of a given thickness and length. Immediately prior to passing beneath the vehicle track, each plate may be programmed to some desired height and locked into place with a rack assembly. When utilizing a variable type program, the plates are unlocked and deprogrammed immediately prior to encountering the programmer. Thus, the programming sequence is:

- Release the Plate Locks
- Deprogram the Plates
- Program the Plates

● Apply the Plate Locks

System flexibility also provides the capability for programming the plates for one revolution and allowing them to retain this configuration while the vehicle and simulator velocities are varied.

● Hydraulic System

Programming of the bump plates is accomplished by the use of two, six inch stroke, 33,000 force-pound hydraulic exciters. Having determined the operational requirement of 135 inches per second peak velocity, each of the two hydrosolvers employed would require 440 gpm peak flow or 200 gpm average flow at 3,000 psi. The system comprises a closed loop piping configuration that starts and terminates in a low pressure oil reservoir.

● Drive Motors

The power requirement for each drive motor is established as being approximately 400 horsepower. Further, the drive motors should display the following characteristics:

1. Constant torque from 0 to 40 per cent of maximum speed. Maximum torque developed at 40 per cent speed equal to 400 hp.
2. Speed and torque control at all speeds.
3. Motors must possess the ability to drive as well as absorb energy on a re-generative basis during that portion of test when the tank is simulating

on uphill climb.

The 400 horsepower requirement resulted, primarily, from the vehicle acceleration requirement. When considering the 150 per cent, one minute overload capability of the proposed DC motors, it becomes feasible to employ a 300 hp rated drive motor for each side of the system.

● Control System

The total control system is comprised of the three basic subsystems shown in Figure 13. These subsystems are:

1. Vehicle engine control
2. Terrain and system velocity control
3. Profile simulation control

● Reaction Mass

The required reaction mass platform dimensions have been defined as 25 feet by 50 feet. The design is predicated on a 5 g acceleration at the c.g. of the 50-ton vehicle to be tested. Also, operational criteria anticipate a peak force of 1,000,000 pounds of short duration.

Reinforced concrete with reinforcing structural steel running horizontally, vertically and diagonally, should be used. Preferably the entire concrete mass should be poured at one given time to ensure a homogeneous and continuous block with no artificial disjunction due to manufacturing processing. The concrete reaction mass should be sandwiched vertically between two steel plates, thus realizing the following advantages:

1. The top plate gives a solid anchorage for the system frame.
2. The sandwich construction of the reaction mass design insures a better use of the material as a lumped mass system, and therefore, gives a higher mechanical impedance value in the frequency range where mass controls.
3. The bolts and plates will give some degree of concrete pre-stressing, which allows the material to possess higher values of Young's modulus, E, and modulus of rigidity, G. Both E and G play important roles in wave propagation in the concrete material.
4. Provision of local mass should wave phenomena occur inside concrete reaction mass.

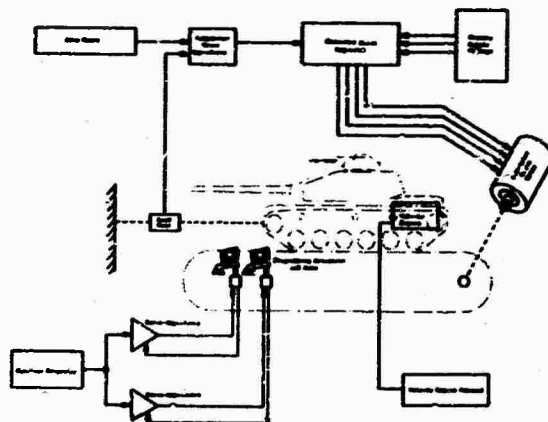


Figure 13. Road simulator control system

5. Further prevention of concrete failure in tension.

● Data Acquisition

One of the outstanding advantages of performing road tests under simulated conditions in the laboratory is the ability to accurately define and evaluate vehicle response characteristics. This can only be totally accomplished by establishing the measurement parameters that are required to adequately define these desired responses. Available vehicle test literature have indicated these parameters to be:

1. Acceleration and stress of critical chassis and suspension members.
2. Dynamic wheel loads.
3. Vehicle velocity and acceleration.
4. Engine torque and rpm.

The choice of basic type of data system (analog or digital) rests upon the total number of channels contemplated, the desire for real-time acquisition, system flexibility and expansion.

WHEEL/RAIL DYNAMICS TEST FACILITY

Introduction

Within the last several years, the American public has become aware of the basic problems that have begun to plague our conventional transportation systems. Both auto and air traffic problems have increased to the point where our Government has deemed it necessary to legislate certain actions that would alleviate these conditions.

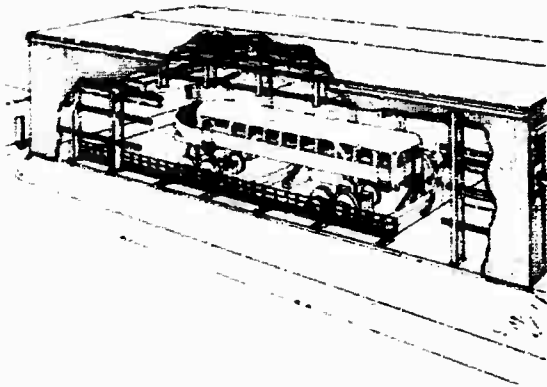


Figure 14. Pictorial view of wheel/rail test facility

Concurrently, parallel solutions have been sought. This approach has led to the consideration and acceptance of high speed train systems as a basic transportation medium, and industry has been given the mandate to develop high speed trains with operating speeds up to 300 mph.

To meet this goal demands that giant technological strides be taken in a short period of time. As is true in any technology, these strides can only be accomplished by highly trained personnel and the proper equipment. Of immediate, paramount importance is the controlled investigation of wheel/rail dynamic phenomena. In May of this year, Wyle Laboratories/Huntsville was awarded a contract by the Federal Railroad Administration for the design, fabrication, installation and operation of a wheel/rail dynamics test facility. Though this facility is to initially concern itself with the investigation of high speed wheel-on-rail vehicles, subsequent efforts shall also include the capability for testing tracked air cushioned vehicles. In essence, the primary function of the facility is to reproduce as many of the vehicle/wheel/rail environmental conditions as are possible, as well as simulate all the known remaining environmental attributes. Further, sufficient operational flexibility shall be provided to afford a tool for experimentation in those areas where little knowledge is now available. Figure 14 shows a pictorial view of the wheel/rail test facility.

Presently, the program is in the preliminary design phase. Pueblo, Colorado has been selected as the location for the facility. The facility is scheduled to be fully operational approximately two years from now.

Facility Requirements

Design of the facility is predicated on the following maximum vehicle and track characteristics:

Vehicle (Powered or Unpowered)

Weight	400,000 lbs.
Horsepower	8,000 hp
Length	200 ft.
Width	20 ft.
Height	20 ft.

Track

Gage	4'8" to 8'0"
Superelevation	10°
Vertical Displacement	6 in.
Lateral Displacement	6 in.
Frequency Range	dc to 50 Hz.

Dynamic Environment

Dynamic environment is an all-inclusive term meant to portray the total dynamic phenomena that are to be considered in the design of the test facility. If the facility is to accomplish its true purpose it must effectively simulate these phenomena. Additionally, the facility should display versatility, reliability and provisions for later changes or expansions. A listing of the dynamic phenomena is now given:

1. Local Track Effects
 - Geometric irregularities
 - Surface conditions of wheels and rails
 - Compliance and damping
2. Track Geometry
 - Tangent track
 - Spiral entry
 - Superelevated curves
 - Grade
3. Train Induced Dynamic Phenomena
 - End coupling loads
 - Braking loads
 - Accelerating loads
 - Aerodynamic loads
4. Self-Induced Forces and Motions
 - Truck yaw oscillations
 - Truck-car body interactions

- Adhesion, creep and slip
- Centrifugal forces
- Gyroscopic forces

Simulator Motions

Consideration of reproducing the above phenomena in the test facility has led to the preliminary design of a basic platform which contains a circular roller for simulating the flat rail. Six hydraulic actuators are used to impart controlled motions to the platform and wheel/roller interface in six degrees of freedom. Thus, the total system consists of a series of these platforms, or modules, with each module being capable of providing motions in six degrees of freedom for the roller under each wheel of the test vehicle.

As stated, the roller module is the unit whose primary function is to represent a continuous rail and its associated properties at the train/wheel interface. It is therefore necessary to describe the roller module motions relative to this interface. In addition to the local interface coordinate system, an additional reference coordinate system, fixed in space, must be established to define the initial position of the local orthogonal triad. This reference coordinate system is assumed to be oriented at the center of the track roadbed. Figure 15 illustrates the two coordinate systems in which all possible motions of a given roller module can be described. Table I defines the simulation mode, degrees of freedom and the specific coordinates associated with the motions required for simulation.

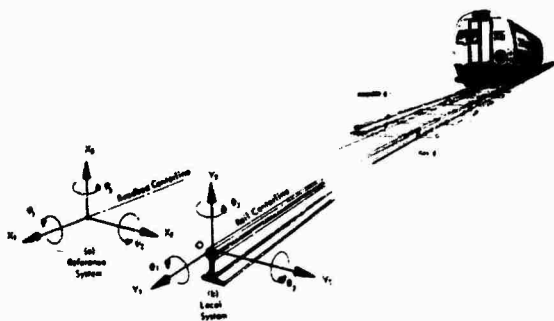


Figure 15. Wheel/rail simulator coordinate system

Mechanical System

An elevation view of the six degree-of-freedom concept is shown in Figure 16.

Essentially, there are three vertical actuators and three horizontal actuators per module. The vertical actuators provide motions in the vertical direction and rotational motions in roll and pitch. The longitudinal actuator is used for imposing longitudinal motion; while the lateral actuators provide lateral and yaw motions. The rail-simulating roller is positioned along the longitudinal centerline of the platform and is supported by two bearings which are rigidly attached to the platform.

The rail-simulating roller is driven by an off-board drive system utilizing an electrical motor and flywheel. The total drive system consists of the following elements:

- Drive motor
- Flywheel
- Drive shaft
- Hydraulic vane coupling
- Constant velocity coupling
- Drive motor/flywheel coupling
- Flywheel support bearing
- Hydrostatic spline

For unpowered vehicles, the drive motor supplies the necessary power to turn the flywheel and the roller through the drive shaft. The total rotational inertia of the flywheels is sized to simulate the longitudinal inertia of a moving vehicle. Coupled to each roller (on-board the platform) is a hydraulic vane coupling. Its purpose is to provide controlled velocity changes to the roller (to nullify the decrowning effect) without requiring controlled speed changes in the drive motors.

Torsionally stiff, constant velocity couplings are used to connect the two rollers under each axle. This same type coupling is used to connect the flywheels (located off-board the platform) to the rollers. This coupling allows the transmission of high torque with minimum velocity error. A hydrostatically lubricated spline is included between each pair of constant velocity couplings which provide an axial degree of freedom to accommodate variations in distance between shaft-connected components due to platform motions.

Hydraulic System

Based on present information, facility layouts are being made to accommodate a 5,000 gpm, 3,000 psi hydraulic system. Present information and analyses show that a ten module (one module per wheel of an eight wheeled vehicle, and one module per each end

TABLE I

MOTIONS REQUIRED FOR SIMULATION

Simulation Mode	Specific Coordinates	Simulation Mode	Specific Coordinates
Vertical irregularities of tangent track	Y_3 translation θ_2 rotation (pitch)	Superelevated spiral track	Y_1 translation Y_2 translation Y_3 translation θ_1 rotation (roll) θ_3 rotation (yaw) $\Delta\Omega$
Lateral irregularities of tangent track	Y_2 translation θ_3 rotation (yaw)		
Combined vertical and lateral irregularities of tangent track	Y_2 translation Y_3 translation θ_2 rotation (pitch) θ_3 rotation (yaw)	Superelevated spiral track with vertical and lateral irregularities and warp superimposed	Y_1 translation Y_2 translation Y_3 translation θ_1 rotation (roll) θ_2 rotation (pitch) θ_3 rotation (yaw) $\Delta\Omega$
Tangent track with crowning compensation*	Y_1 translation $\Delta\Omega^\dagger$		
Vertical irregularities with crowning compensation on tangent track	Y_1 translation Y_3 translation θ_2 rotation (pitch) $\Delta\Omega$	Superelevated spiral track with vertical and lateral irregularities, crowning compensation, and warp superimposed	Y_1 translation Y_2 translation Y_3 translation θ_1 rotation (roll) θ_2 rotation (pitch) θ_3 rotation (yaw) $\Delta\Omega$
Lateral irregularities with crowning compensation on tangent track	Y_1 translation Y_2 translation θ_3 rotation (yaw) $\Delta\Omega$		
Combined vertical and lateral irregularities with crowning compensation on tangent track	Y_1 translation Y_2 translation Y_3 translation θ_2 rotation (pitch) θ_3 rotation (yaw) $\Delta\Omega$		

*Crowning refers to the wheel on the crown of the roller, i.e., the position where the axes of rotation lie in the same vertical plane. In a wheel/rail simulator in which circular rollers are substituted for flat rails, the equilibrium of a truck becomes unstable once the wheels have departed from the crowns of the rollers as the truck yaws.

† $\Delta\Omega$ signifies a change in roller rpm. In the case of crowning compensation, this would only involve a small and temporary perturbation about the steady-state rpm and in a direction dictated by the sense of the decrowning translation, whereas, during superelevation and simulated curve negotiation, $\Delta\Omega$ signifies a change in the steady-state rpm in order to compensate for the effectively "longer" outer rail.



Figure 16. Elevation view of six degrees-of-freedom concept

coupler) would require a 3,000 gpm system while an eighteen module system would require a 5,000 gpm system.

Reaction Masses

Concepts call for a fixed reaction mass on one end of the test area, with a movable reaction mass on the other end of the area. Present plans call for a total reaction mass weight of approximately 18,000 tons.

Control System

The control system determines the performance of the actuator module system under all conditions of varying loads. This system must be adaptive to changing load environments, which affect the reproduction of static track irregularities, track input impedances, and vehicle induced dynamic track irregularities while suppressing artifacts which result from the simulation processes.

The nonstationary nature of the coupled vehicle/wheel/rail interaction processes predicates an adaptive control system. A hybrid system offers the best approach to the successful accomplishment of a general control system which can adapt to the evolutionary characteristics of the processes to be controlled in real time. The control system is schematically illustrated in Figure 17. The hybrid system comprises the following modular sections: source profile generator, adaptive filtering, coordinate conversion, inverse system transfer function, signal conditioning, digital monitor and processor, inverse coordinate conversion (optional), the necessary feedback networks, including inverse track impedance transfer function, and the inter-communication coupling with other control system modules.

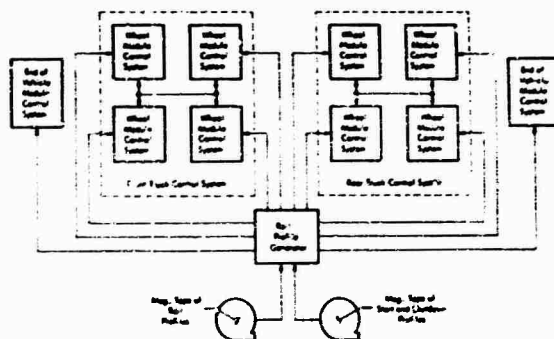


Figure 17. Wheel/rail simulator control system

Facility Layout

Figure 18 presents the total facility layout. This layout illustrates the test area as well as the associated areas required for efficient facility operation. Presently conceived are two bridge cranes, of 100 tons lift capacity each, that will be used to off-load the test vehicle from the spur track onto the test machine. This process is reversed when testing is accomplished.

Though the layout is predicated on both immediate and future requirements, the facility will be designed to allow for future physical expansion.

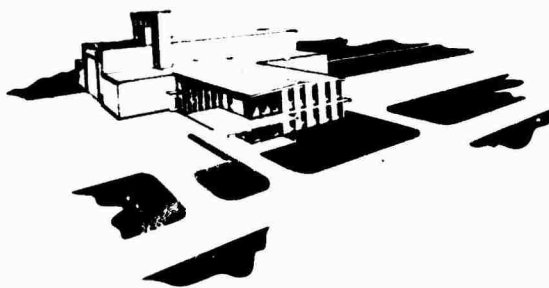


Figure 18. Wheel/rail test facility layout

DISCUSSION

Mr. Kana (Southwest Research Institute): On the three degree-of-freedom simulator for the helicopter environments you did not say very much about how equalization is accomplished. Would you elaborate on that, and in particular, indicate whether you ran into any problems that were different from what one would anticipate for a one degree-of-freedom system with a broad band input?

Mr. Arone: The control system for the helicopter simulator included filter networks for equalizing out the mechanical resonances of the exciters and the fixtures. Several trials were necessary in order to obtain a one-to-one correspondence from the tape input to the controls to the output of the

fixture. Again this was a compromise and is a best-effort type of situation. The basic limitations in one degree-of-freedom system compared to the three degree-of-freedom system are the frequency response, and, of course, the duplication of the field environment. The frequency response in our system was extremely good from the range of 5 Hz. to around 150 Hz. Above 150 Hz., the control was more difficult to achieve. In a single degree of freedom system this would be easier to obtain. However, having to make our system a three degree-of-freedom system, the restrictions imposed by the basic stingers, as we call them—the attachments—gave us some problems in those areas. We have a patented design on some stingers which allow three degree-of-freedom testing simultaneously.

DESIGN AND FABRICATION OF AN AIRCRAFT SEAT CRASH SIMULATOR

Nelson M. Isada
State University of New York at Buffalo
Buffalo, New York

The crashworthiness of aircraft seat and passenger-restraint systems may be determined by means of crash simulation in a laboratory. This study is primarily on the design and fabrication of a variable slope inclined plane crash simulator for the purpose of: (1) testing models and prototypes of aircraft seat and passenger-restraint systems, and (2) validating mathematical models of the dynamics of aircraft seats and restraint systems. The crash simulator consists of: (1) a crash cart, (2) a swiveled inclined ramp with tracks, (3) a decelerating device of sandwich coil springs, (4) a reinforced concrete abutment, and (5) accessory equipments such as quick release and latching mechanisms.

INTRODUCTION

In evaluating the crashworthiness of aircraft seat and passenger-restraint systems it is necessary that the effect of the high deceleration inputs to the seat and passenger-restraint system be reduced so that the chances of survival during a crash landing and rapid egress afterwards can be increased. It is also hoped that the probability of detachment of passenger seats and their backs from their mounts during crash landings will be minimized through energy dissipation and pulse reshaping of the shock input from the airframe.

To attain the foregoing broad objectives two parallel programs [Refs. 1 and 2] were followed, namely (1) an analytical program and (2) a laboratory crash simulation program. This paper discusses the progress of the laboratory program. This program consisted primarily of the design and construction of variable slope inclined plane crash simulator for the purpose of: (1) testing models and prototypes of aircraft seat and passenger-restraint systems, and (2) validating the mathematical models developed in the analytical program.

A search of the literature revealed the existence of several crash simulators. These crash simulators vary in complexity - some simple and others very sophisticated facilities. However, most of the crash simulators

have been designed to simulate level (horizontal) crashes. Hence, this study was made to simulate variable impact angles.

A small-scale crash simulator was built and tested by the writer and Swiatosz [Ref. 1], then a decision was made to design and build a larger version which can accommodate two aircraft seats subjected to a 15g half-sine deceleration pulse. This full-scale crash simulator is shown in Figures 1 and 2. The major components of this simulator are: (1) a 6 ft. wide by 7 ft. long flat top steel cart with five wheels on each side and weighing 2600 lbs. unloaded; (2) a swiveled inclined ramp with tracks supported by a steel superstructure about 30 ft. long, 18 ft. high and 8 ft. wide; (3) a decelerating device made of sandwiched steel coil springs and reversible wedges for change of impact angles; (4) a reinforced concrete abutment, weighing about 60 tons, with removable top; and (5) accessory equipments such as the center guide mechanism, a quick release and latching mechanism, and lifting (electric winch) devices.

The design and fabrication criteria for this simulator consisted of a fixed construction budget, limited time, simplicity, safety, minimum maintenance, the possibility of relocation and further development. The major technical specifications were: (1) Loaded weight of cart, 4,000 lbs.; (2) Peak deceleration of cart, 15 g's; (3) Deceleration duration, 0.1 sec.;

(4) Normal impact angle (slope of ramp), 15 degrees; (5) Maximum travel on ramp, 18 ft.; (6) Maximum drop height of cart, 9 ft.

The instrumentation used to test the full-scale crash simulator consisted of piezo-electric accelerometers connected to charge amplifiers which are in turn connected to a multichannel oscillograph by means of shielded cables. More detailed descriptions of the components of this crash simulator and the results of crash tests will now be given.

THE CRASH CART

The crash cart, shown in Figure 2, is the central portion of the crash simulator because its dimensions and characteristics affect the remaining components of the system. For example, the width of the cart affects the location of the tracks which in turn affect the width of the supporting structure; the weight of the cart affects the characteristics of the decelerating device and the capacity of the electric hoist.

As mentioned earlier, the cart should be able to accommodate a two-passenger aircraft seat. This specification imposes a 400 lb. (weight of two passengers plus weight of seat) load on the cart. In order for the dynamic interaction between the cart and the load to be acceptable a total weight to load ratio of ten was chosen. This required a total loaded weight (cart + load) of 4,000 lbs.

In addition to the above specification it is also desirable that the cart be able to accommodate geometrically three rows of seats so that the effects of restraint systems (belts and/or inflatable air bags) may be investigated. This additional requirement was met by building a cart with a flat steel top 6 ft. wide by 7 ft. long by 1/2 inch thick. The larger length than width dimension is satisfactory from the standpoint of stability against yawing (horizontal turning) of the cart during a test run.

The third specification for the cart was to distribute the load as evenly as possible. For this purpose, ten wheels (five on each side) with polyurethane elastomer tires (to cut down on noise) were used. The wheels are held by one-inch diameter axles.

A fourth major specification for the cart is rigidity. This requirement was met by using 6" x 4" x 1/2" angle irons for outside braces, a 6" I-beam for center brace, and 6" x 1/2" bent plates for cross bracing as shown in Figure 4. In addition, the front of the cart was made rigid by welding five eight-inch I-beams and a one-inch bumper plate to it as shown in Figure 3 and Figure 4.

INCLINED RAMP AND SUPERSTRUCTURE

The first requirement imposed on the ramp was variable slope. To meet this specification a swiveled ramp, shown in Figure 5, was selected. This ramp can be inclined from 0° to 30° about a 3-inch diameter pin.

The second requirement for this ramp is for it to be able to carry the crash cart and its load. To this end one 12-inch channel on each side, weighing 20.7 lbs. per foot, was used. Each channel is supported by eight-inch wide flange (8 WF) columns every 6 ft. as shown in Figures 5 and 6.

The third specification for the ramp is for it to be able to carry the cart wheel tracks and the center guide rails. The arrangements are shown in Figure 6. This figure shows the 5-inch channel track attached to the 12-inch channel carriage and the center guide rail attached to the channel cross braces.

The fourth requirement imposed on the ramp is rigidity. This specification was met by the use of channel braces and tie rods as shown in Figure 7.

The primary functions of the superstructure are to support the ramp and the lifting devices. The superstructure, shown in Figure 8, is made of five 8-inch wide-flange columns (8 WF24 @ 6' -0" o.c.) on each side and joined at the top by an angled 8-inch wide flange beam (8 WF17). Each side is braced vertically by 1-inch diameter tie rods and 5-inch wide flange beams (5 WF16). The two sides of the superstructure are joined together at the top by 5-inch wide flange beams (5 WF16) and braced diagonally by 2 1/2" x 2 1/2" angle irons. Knee braces are provided at the end columns.

DECELERATING DEVICE

The decelerating device must meet two major requirements, namely, (1) a capability to change the angle of impact and (2) a capability to produce a pulse duration of 0.1 sec.

The first requirement was met by using five reversible steel bumpers (wedges) made from 8-inch beams as shown in Figure 9. These bumpers are bolted to the reinforced concrete abutment. The upper arrangement, shown in Figure 9, is for an impact angle of 30 degrees whereas the lower portion is for a horizontal impact. The bumpers for a 15-degree impact are made of uncut 8-inch beams. The spacings of these bumpers match the spacings of the cart bumpers.

The pulse duration requirement was met by building a sandwiched steel coil springs as shown in Figure 10. This figure shows a steel plate joining the forward ends of the coil springs and anchored to the 8-inch wedges. There is another plate joining the rear ends of the coil springs. The rear face of the sandwiched springs slide along the wheel tracks to prevent falling off. The springs used in this initial study are automotive suspension springs with an average spring rate of 200 lbs. per inch each. The springs are removable (a maximum of eighteen springs can be used) so that the spring rate can be varied to meet the pulse duration requirement. The spring rate needed is (See Figure 11)

$$\text{Required } K_s = \pi^2 W / g \tau^2$$

where

K_s = simulator spring constant, lbs./inch

W = cart weight, lbs.

g = gravitational acceleration, inches/sec²

τ = pulse duration, sec.

The foregoing equation has been derived from the free vibration solution of an undamped linear spring with no initial deformation and then impacted by a rigid mass.

REINFORCED CONCRETE ABUTMENT

The major requirement in the design of the abutment is that it must be stable, i.e., the motions must be negligible. To meet this requirement several physical considerations were made. One is that the mass of the abutment must be large compared to the mass of the cart. A mass ratio of 30 was chosen as practical. This mass ratio requires that the abutment must weigh around 120,000 lbs. (60 tons). The most logical choice is a reinforced concrete abutment. The dimensions of this abutment are shown in Figures 12 and 13. This concrete abutment is made up of three parts (see Figure 12), namely, (1) an existing concrete pad (11' 6" wide by 7'0" long by 4'0" deep) formerly used as a machine foundation; (2) a newly poured stepped continuous pile (11'6" wide by 3'0" long, stepped down to 1'0" by 7'0" deep) and (3) a removable top (11'6" wide by 10'0" long, plus a concrete striker wedge, by 3'0" high). The existing machine foundation was used to increase the mass of the abutment, the stepped continuous pile was poured to insure that the abutment does not move dangerously, the removable top feature was added for possible relocation and further development, and a concrete striker wedge with anchor bolts were added to provide an inclined face for and to anchor the steel wedges.

ACCESSORY EQUIPMENTS

Several accessory equipments are needed for the proper operation of the crash simulator. One is a pair of guide mechanisms (or hooking devices) attached to the underside of the cart. The mechanism, shown in Figure 14, provides cam followers to roll against the guide rails mounted on the inclined ramp as shown previously in Figure 6.

Another accessory equipment is the latching and release mechanism shown in Figure 15. This mechanism is made of a curved plate attached to the rear of the cart and a pneumatic cylinder with a spring-mounted plunger. The cart latches when the plunger and the hole in the curve plate align. The cart is released by providing compressed air to the pneumatic cylinder to overcome the friction between the curved plate and the plunger.

A third accessory equipment is the cart recovery device. The device chosen is an electric winch with a stainless steel cable hooked to the cart in order to pull the cart up the incline. The electric winch is mounted at the end of the inclined ramp.

A fourth accessory equipment is a pair of chain hoists for changing the slope of the ramp. These hoists are mounted on the top brace of the superstructure.

CRASH SIMULATOR TESTS

Crash tests made with the full scale crash simulator proved out the adequacy of the design and the instrumentation. Hence, the crash simulator is now ready for the testing of prototype (full scale) passenger seats.

The instrumentation used to test the full-scale crash simulator consisted of piezo-electric accelerometers connected to charge amplifiers which are in turn connected to a multichannel oscillograph by means of shielded cables as shown in Figure 16.

Two seats were used to test the full scale crash simulator. One was a school bus seat that was readily available and full size. The seat was mounted on the cart similar to the way the seat is mounted on a school bus. The mounted seat can be seen in Figure 3. Although the crash simulator performed satisfactorily, the school bus seat did not because the seat cushion was thrown about when subjected to a cart deceleration of 3.77g. The cart deceleration for this test was recorded and is shown in Figure 17, together with the time base pulses energized by micro switches which were triggered by the cart. In this test, ten automotive coil springs were used in the decelerating device. Inspection of the

school bus seat cushion showed that the clamping attachment was very weak, indicating a need for the development of rational specifications for school bus seats.

In view of the above, another seat was used. An automotive seat, which was also available, was mounted on springs simulating the stiffness of aircraft seats. Another modification was the addition of eight springs to the previous ten springs in the decelerating device. Crash tests were then performed by varying the drop height of one foot to a drop height of four feet. The results of the measured peak decelerations are shown in Figure 18. Also shown in Figure 18 are the calculated peak decelerations based upon free fall impact velocity and the free vibration of an ideal spring-mass system. Both results agree closely. The small discrepancies can easily be attributed to rolling friction. Also shown in the figure is the distance travelled by the cart before impact along the 15-degree inclined ramp.

CONCLUSIONS

As a result of this study, some new information has been gained and what we believe to be a unique crash simulator facility has been built. Some of this new information and the components of the crash simulator have been discussed. Briefly, it can be concluded that: (1) A simple, rugged and effective variable slope inclined plane crash simulator can be designed and built for use to test full scale aircraft seats and passenger-restraint systems; and (2) commercially available transducers, instrumentation, recording devices and photographic equipment can be used gainfully in crash simulation tests.

ACKNOWLEDGMENT

The author would like to thank the U.S. Public Health Service (Grant No. EC 00287, formerly UI 00669) and the Department of Mechanical Engineering, (State University of New York at Buffalo) for supporting this study.

The author also wishes to acknowledge the cooperation of his colleagues and students, especially to Dr. R. Mates, Dr. R. Ketter, Professor P. Mohn, Professor Y. Sarkees, Messrs. E. Swiatosz, G. Brundage, K. Siwiecki, D. Patrawala, F. Ho, R. Lees, J. Kowalski, W. Slater, R. Gromada, T. Less, H. Wagner, H. Sheehe, and W. Willerth; to Mrs. M. Smits and Mrs. G. Cocuzzi for typing the manuscript; to his wife Beatriz for her editorial help; to Aerotec Industries, Inc. for supplying the aircraft seat drawings; and to Holler Bros., Inc. and Sen-Wel Industries, Inc. for their help in the construction of the crash abutment and superstructure.

REFERENCES

1. Isada, N. and Swiatosz, E., "Analysis of the Dynamics of Aircraft Seats During Crash Landings", ASME Paper No. 66-WA/SAF-1, American Society of Mechanical Engineers, New York, November, 1966.
2. Isada, N., "Dynamic Response of Aircraft Seat and Restraint Systems", Final Report, Department of Mechanical Engineering, State University of New York at Buffalo, Buffalo, New York, August, 1969.

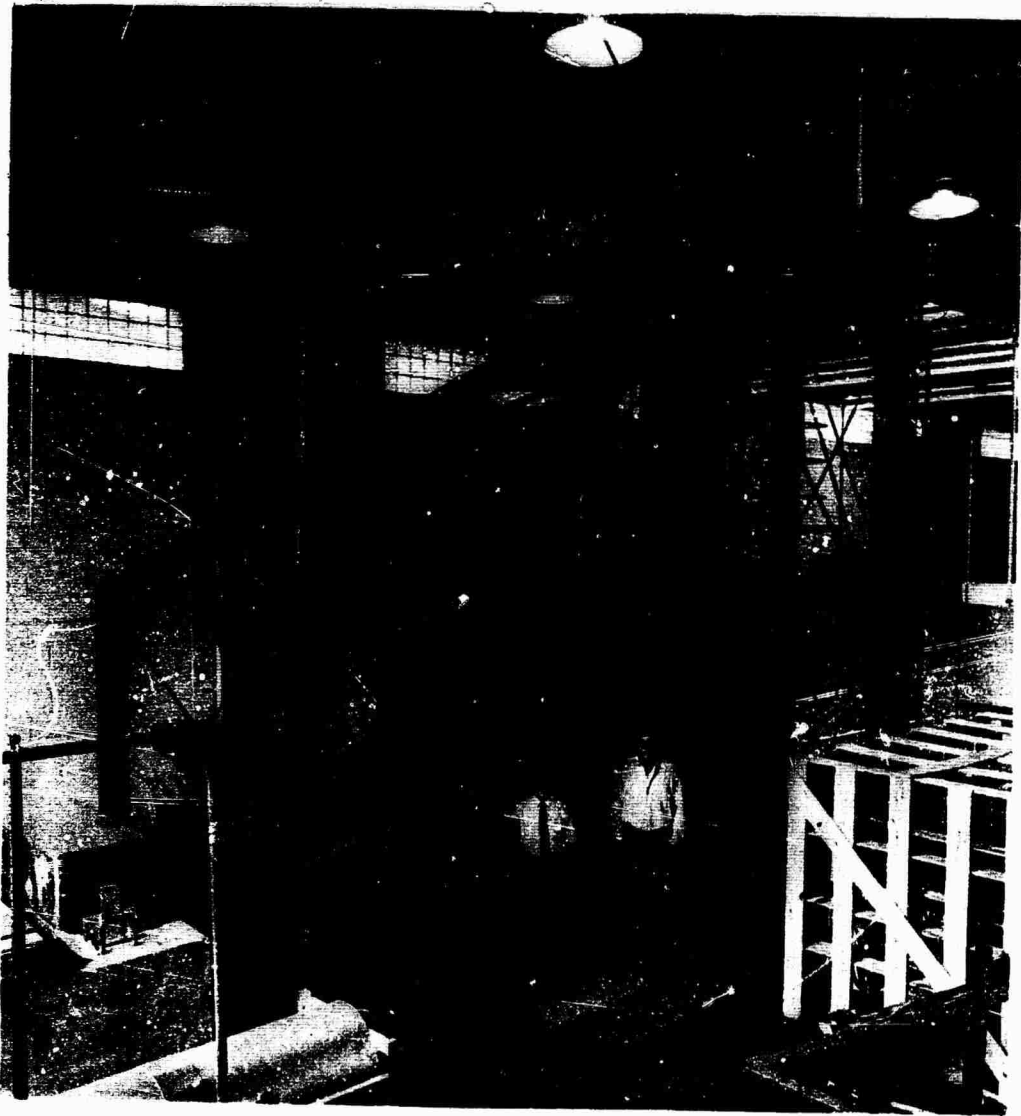


FIGURE 1. INCLINED PLANE CRASH SIMULATOR

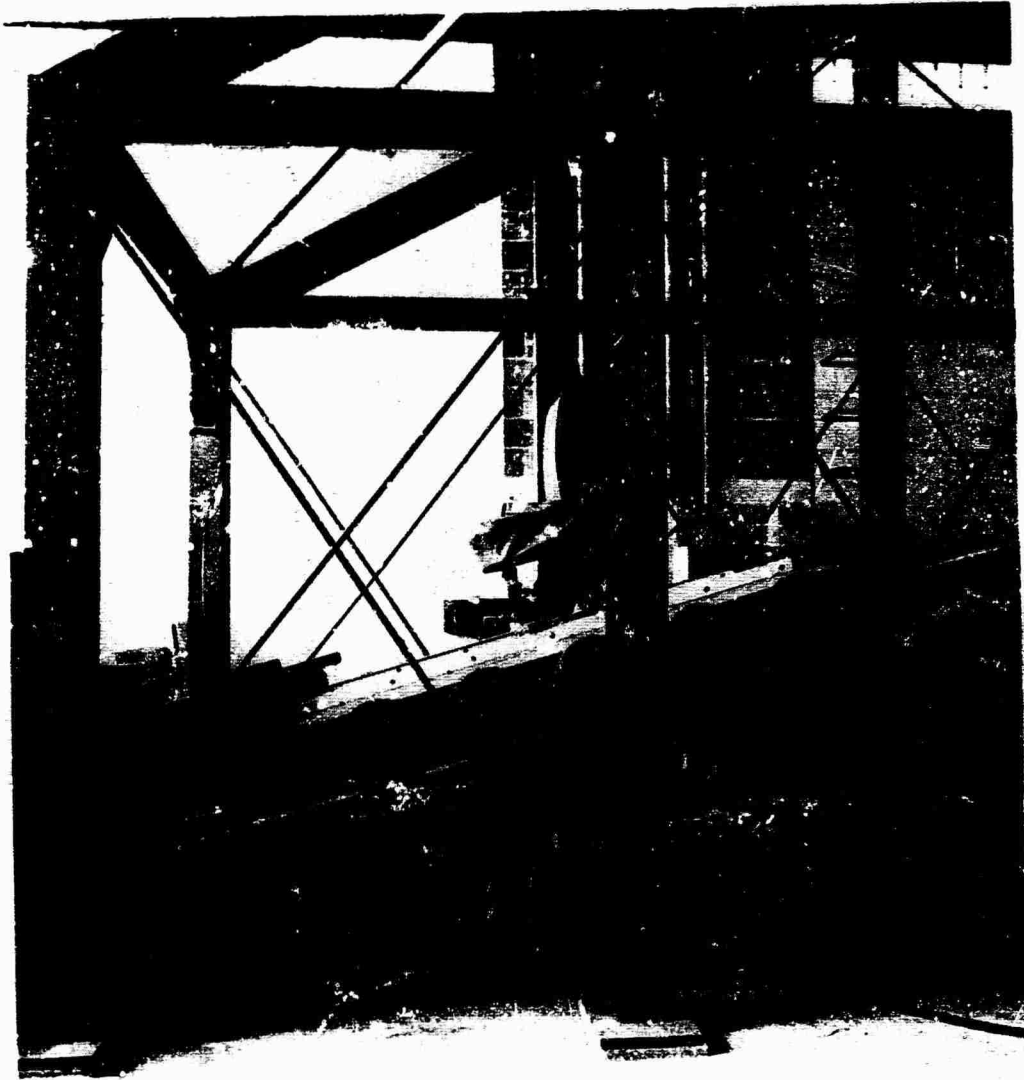


FIGURE 2. SIDE VIEW OF THE CRASH SIMULATOR



FIGURE 3. THE CRASH CART WITH SEATS

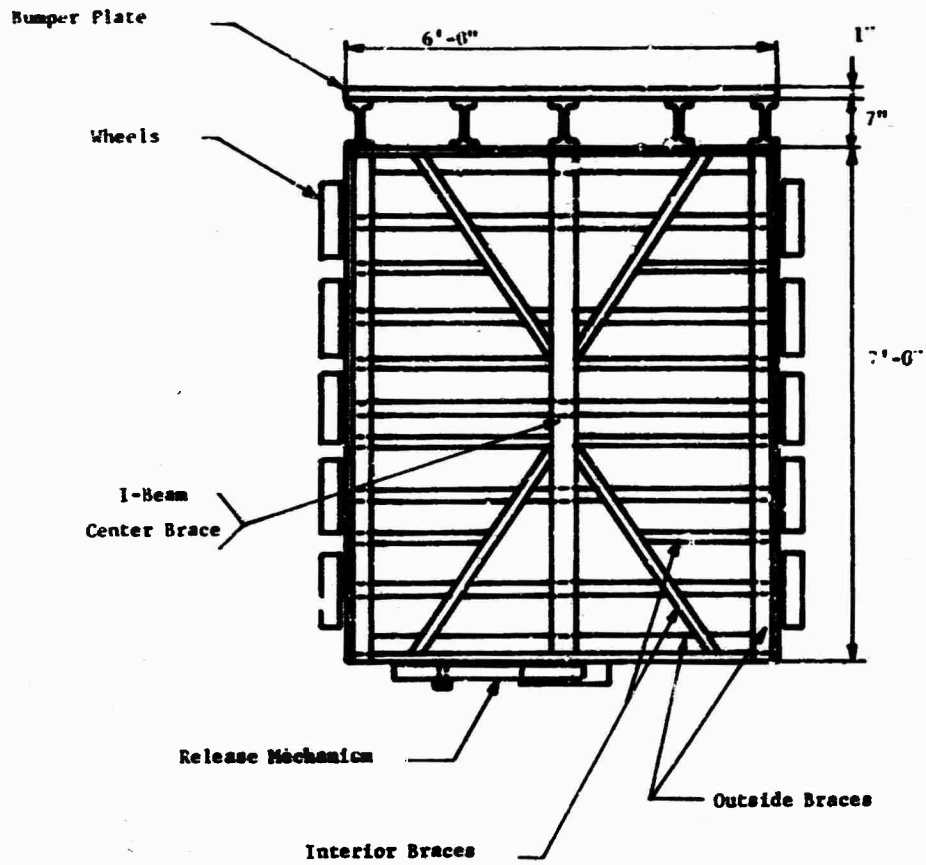


FIGURE 4. TOP VIEW OF CRASH CART WITH TOP PLATE REMOVED

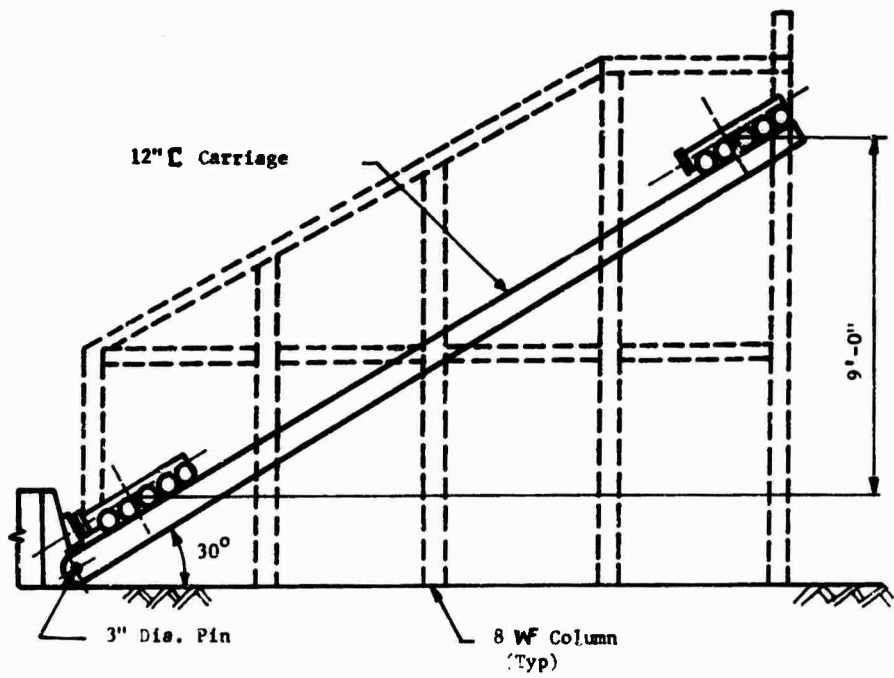


FIGURE 5. SIDE VIEW OF SWIVELED RAMP

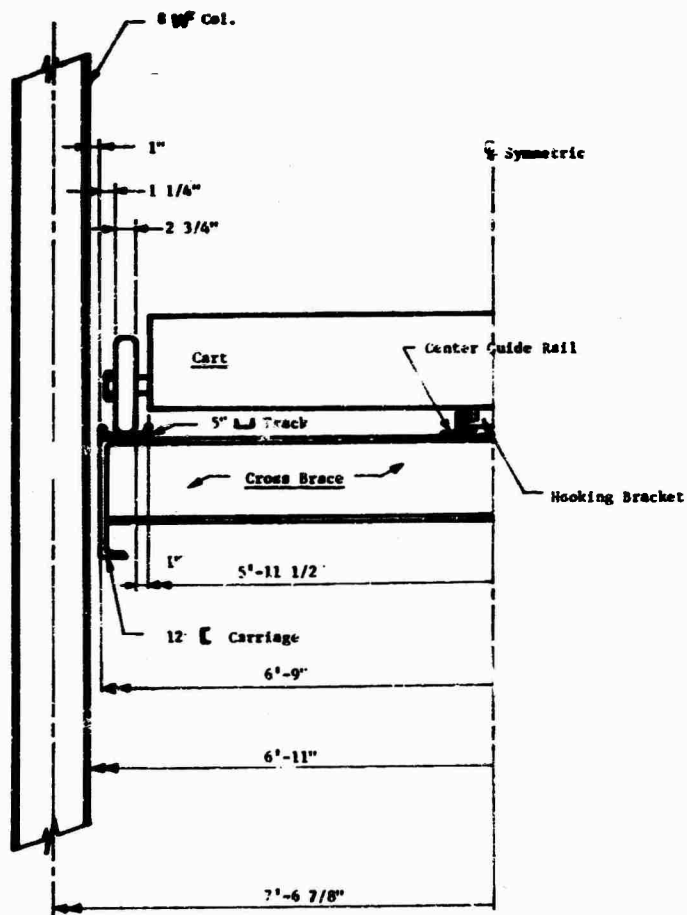


FIGURE 6. CROSS SECTIONAL VIEW OF RAMP

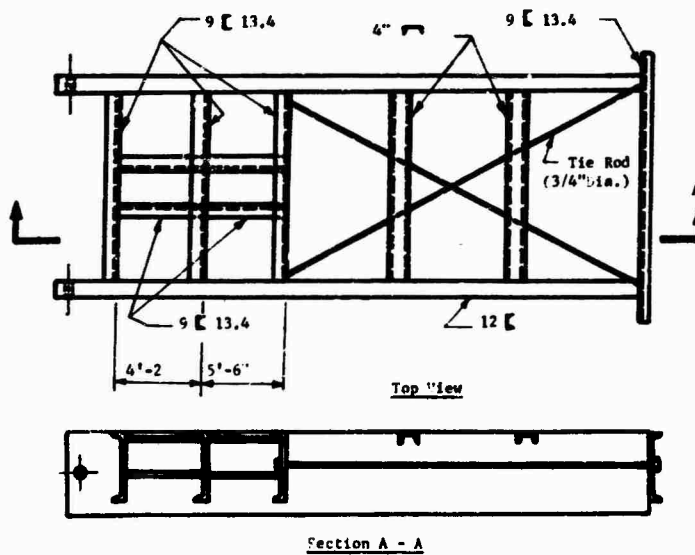


FIGURE 7. PLAN VIEW OF RAMP

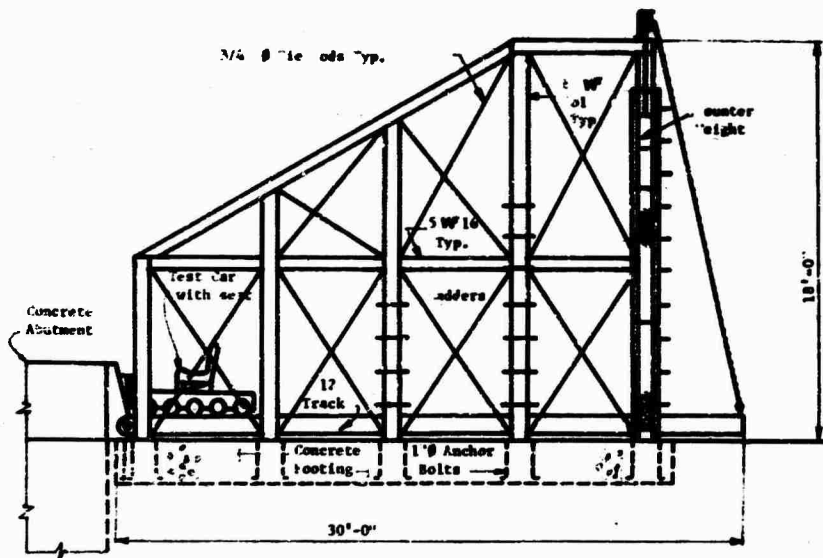


FIGURE 8. SUPERSTRUCTURE STRUCTURAL ARRANGEMENT

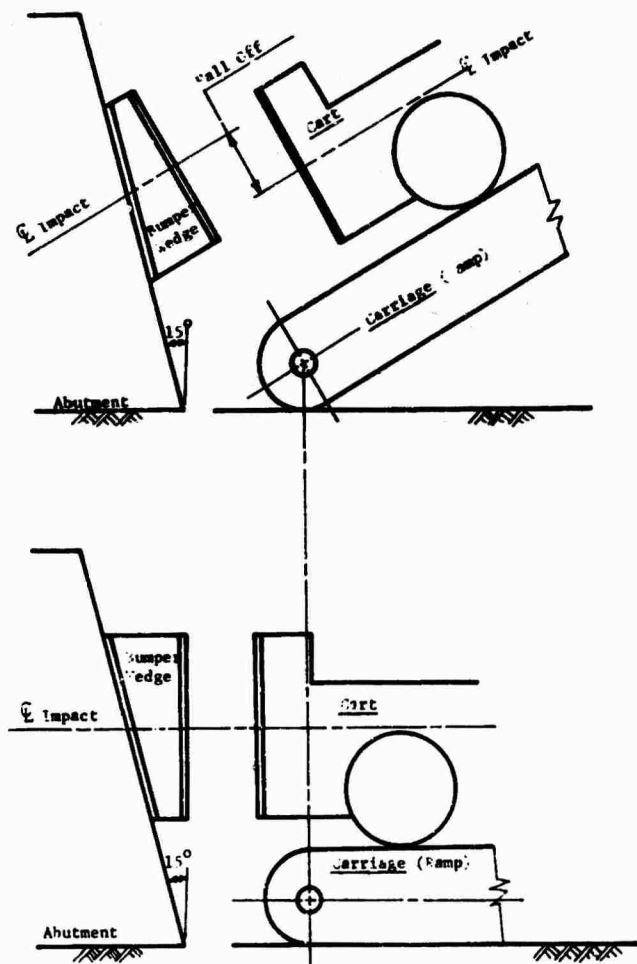


FIGURE 9. REVERSIBLE STEEL BUMPER WEDGES

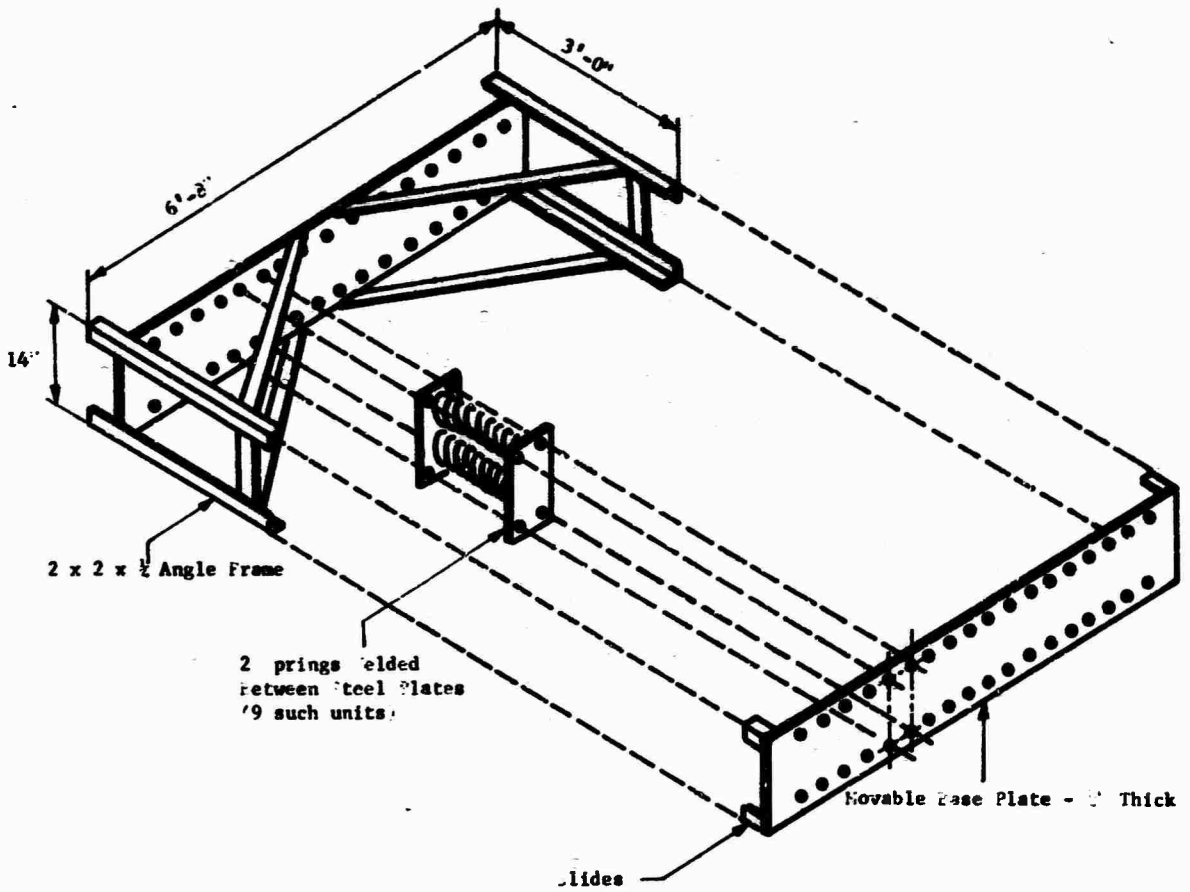


FIGURE 10. DECELERATING DEVICE. SANDWICHED STEEL COIL SPRINGS.

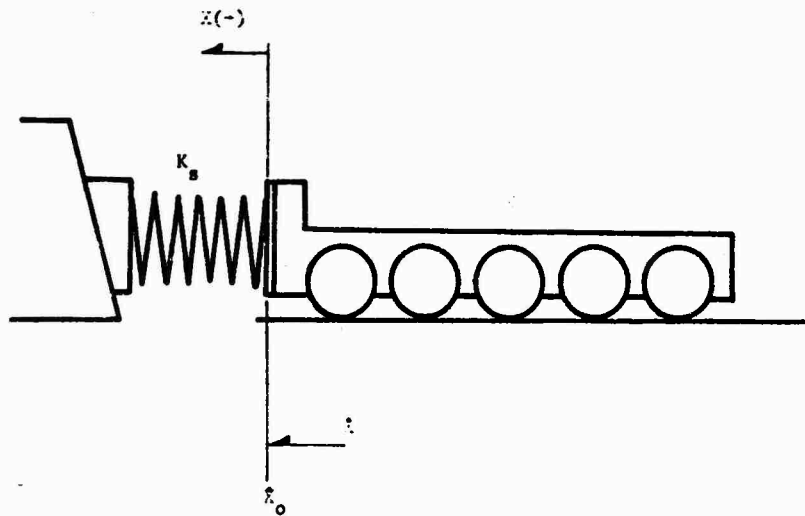


FIGURE 11. DYNAMIC MODEL OF CART AND DECELERATING DEVICE

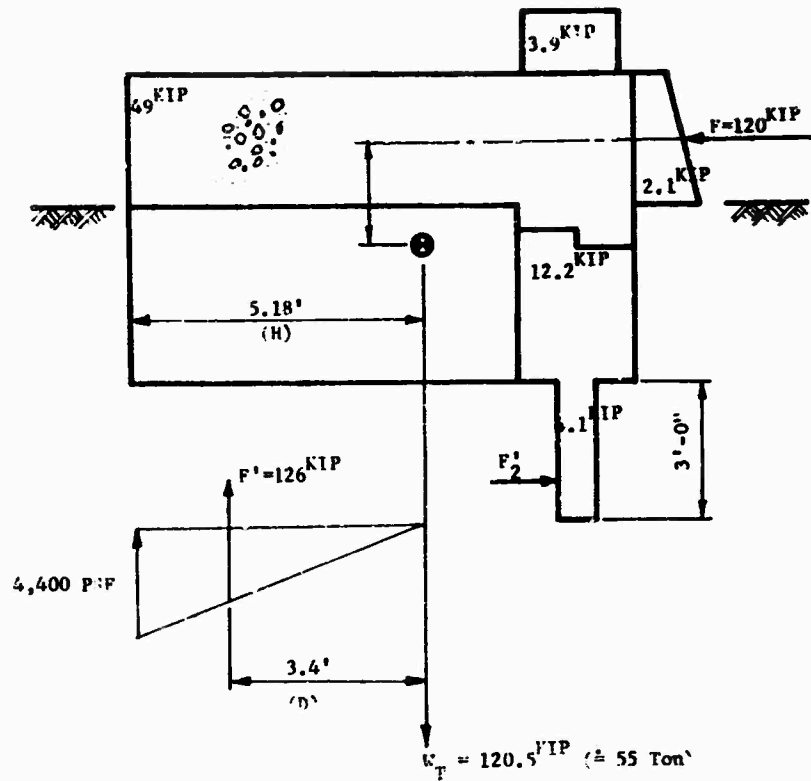


FIGURE 12. SIDE VIEW OF CONCRETE ABUTMENT

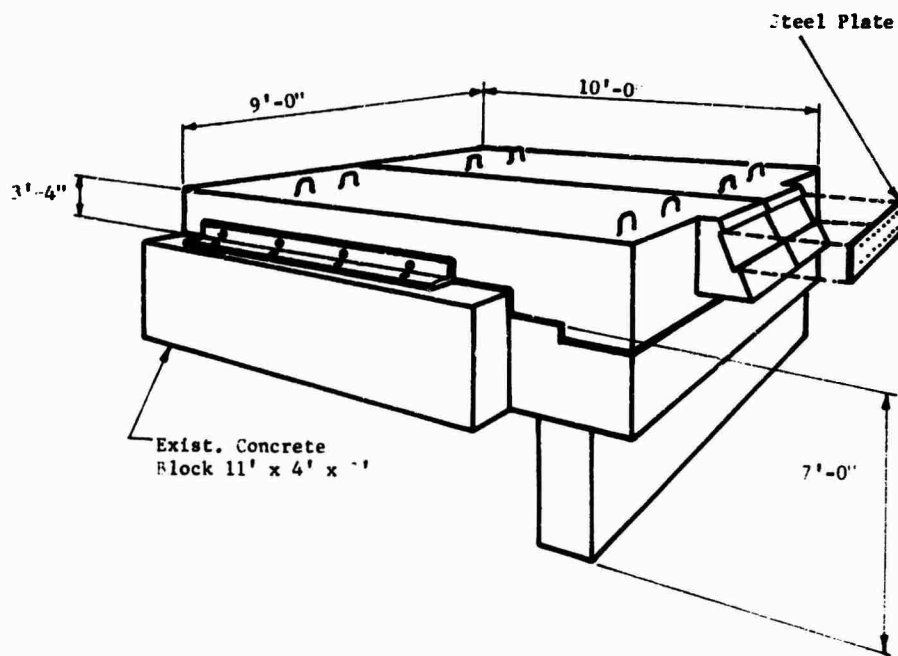


FIGURE 13. ISOMETRIC VIEW OF CONCRETE ABUTMENT

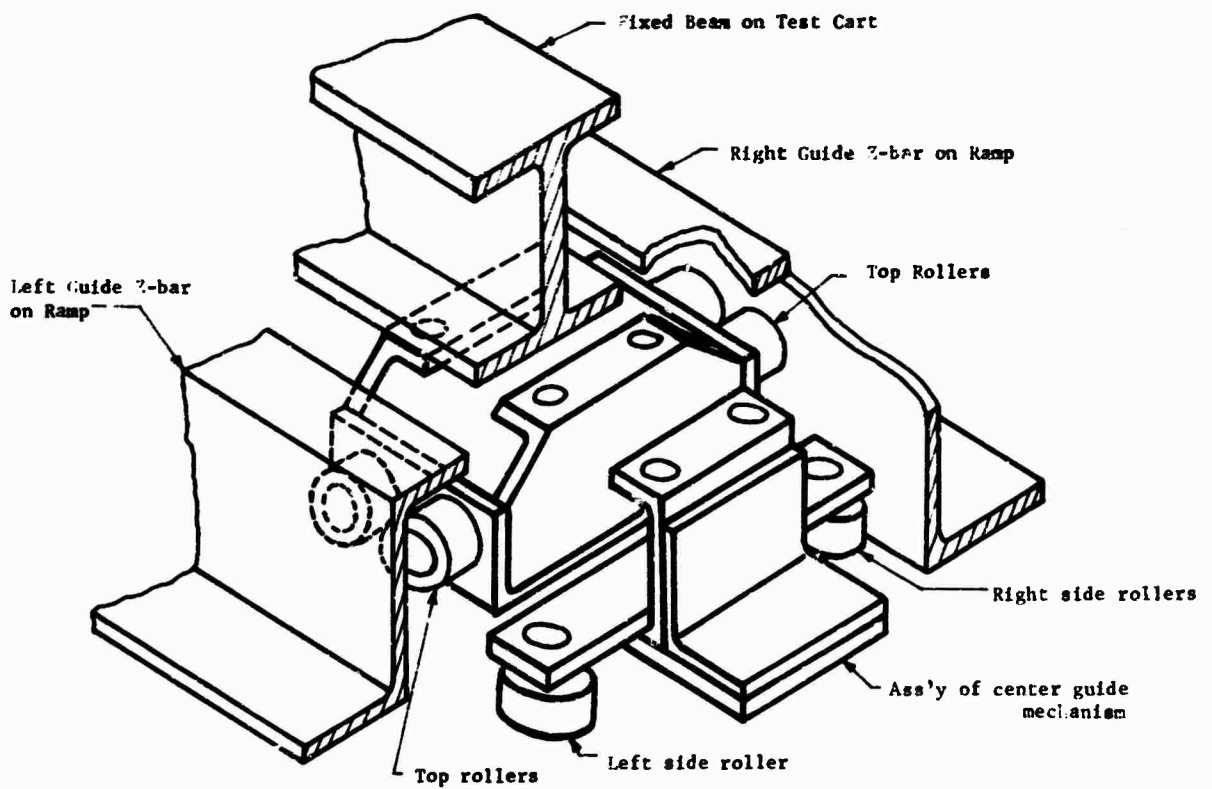


FIGURE 14. CENTER GUIDE MECHANISM

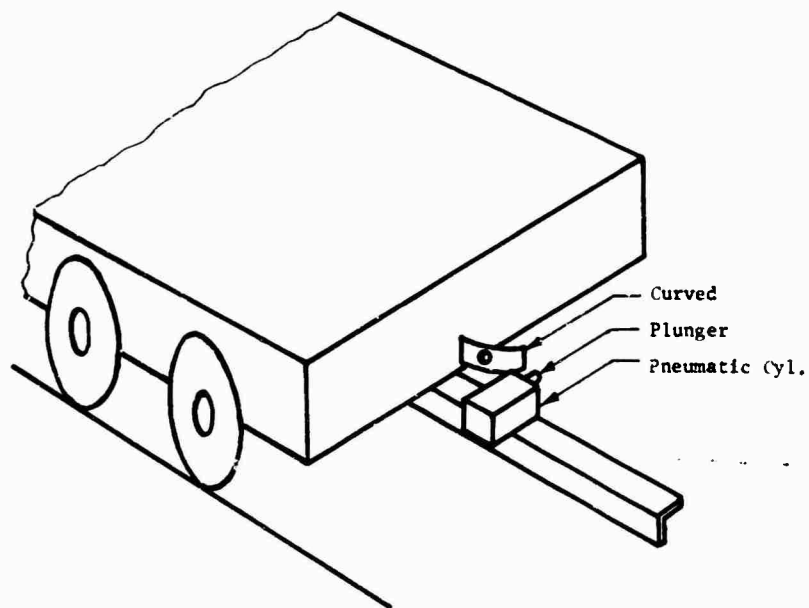


FIGURE 15. LATCHING AND RELEASE MECHANISM

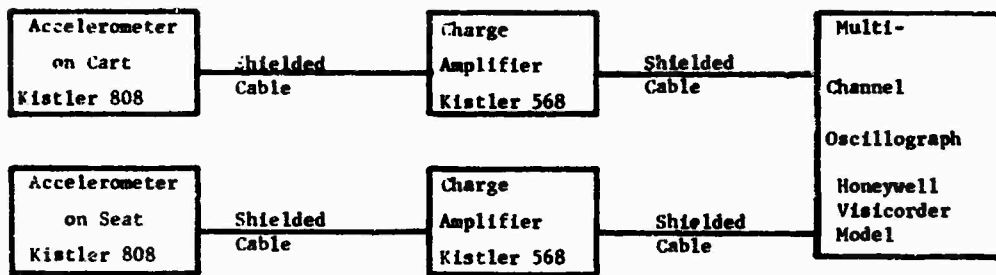


FIGURE 16. INSTRUMENTATION SYSTEM

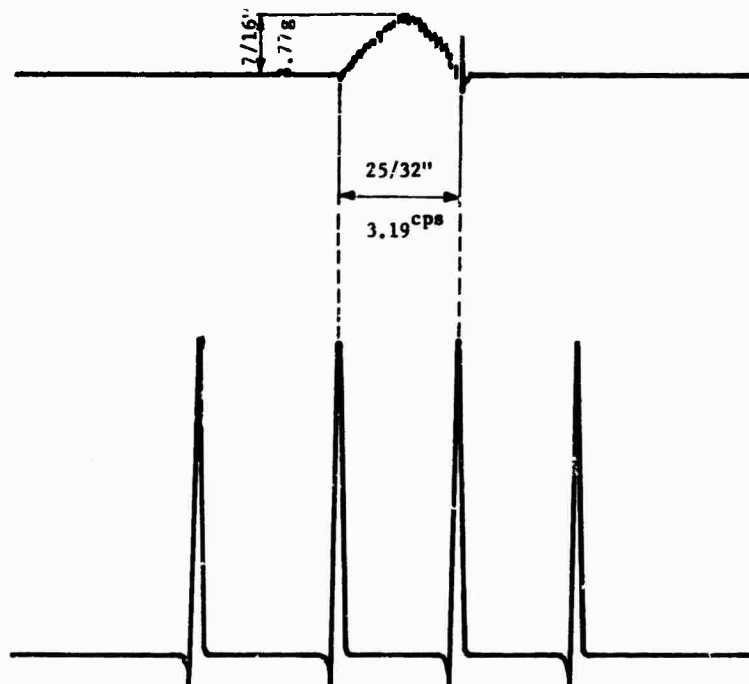


FIGURE 17. RECORDED CART DECELERATION AND TIME BASE WITH SCHOOL BUS SEAT AS LOAD (TRACED FROM TEST RECORD)

DROP HEIGHT	LENGTH ON SLOPE (For 15°)	IDEAL CART G _m *	ESTIMATED CART G _m	PULSE HEIGHT (MEASURED)	MEASURED** CART G _m
1' - 0"	3' - 10½"	6.54 g	5.9 g	0.703"	6.0g
1' - 6"	5' - 9 5/8"	8.01 g	7.2 g		
2' - 0"	7' - 8 3/4"	9.25 g	8.3 g	0.980"	8.4g
2' - 6"	9' - 7 3/4"	10.32 g	9.3 g		
3' - 0"	11' - 7"	11.32 g	10.2 g	1.125"	9.7g
3' - 6"	13' - 6"	12.23 g	11.0 g		
4' - 0"	15' - 5 3/8"	13.08 g	12.7 g	1.56"	13.4g

*G_m = Peak Cart Deceleration

**Conversion Factor: 8.62 g/inch

FIGURE 18. PEAK DECELERATIONS OF CART FOR VARIOUS DROP HEIGHTS.

DISCUSSION

Mr. Keefe (Kaman Sciences): You said you designed your simulator for 15 g's, is this a representative number for crashing airplanes?

Mr. Isada: Some specifications say 8 g's, newer ones say 10 g's, but we feel that aircraft

seats should be designed for at least 15 g's. If the seats and the restraint systems can withstand the impact, even if the shell collapses, we feel that the passenger has a better chance of surviving.

"DESCRIPTION OF A SHOCK AND VIBRATION DISPLACEMENT AMPLIFIER"

D. Cerasuolo, J. Chin
Raytheon Company
Sudbury, Massachusetts

This paper describes the technique used by the authors to simulate the large displacement low frequency dynamic environments found in massive ground based installations. The technique utilizes a conventional electrodynamic shaker and readily available commercial test equipment. A prototype of the Shock and Vibration Displacement Amplifier was assembled and tested. The performance and theory of operation of this prototype system are discussed.

INTRODUCTION

Recent developments in this country's National Defense Policy and consequently the U.S. Armament industry have brought about changes in requirements for survivability of equipments in battle environments. Among these are large displacement low frequency dynamic environment found in the massive ground based installations such as that Raytheon Company is presently involved with. These programs require displacements as high as 10 inches at frequencies as low as 2 cps.

The bulk of equipment available to perform dynamic tests are electrodynamic shakers. These equipments are inherently displacement limited. Displacement limits are generally in the fraction of an inch to one inch and a fraction range for nearly all exciters of this type in use today. A few large displacement exciters have been built but are of the single thruster type design and severely payload limited. Hydraulic shakers which lend themselves to large displacement low frequency applications require large expensive installations, and lack the flexibility of an electrodynamic shaker system, especially at the higher frequencies. Because of this and the requirement, we were given to perform these large displacement low frequency tests, the system herein described was developed.

THEORY OF OPERATION

The concept upon which the system is based i.e., utilizing the phenomena of resonance to achieve displacement amplification, is not new. However, the method we used to implement and control the phenomena is unique. The following schematic will help illustrate the method:

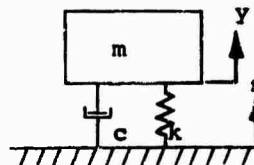


Figure 1

The system can be assumed analogous to the single degree of Freedom System of Figure 1. The electrodynamic shaker is represented by the support and the test item by the mass. The forces acting on the mass are the spring force = $k(s-y)$ and damping force = $c(\dot{s}-\dot{y})$, assuming "y" is greater than "s". Using $F = ma$, the equation of motion is:

$$(1) \quad m\ddot{y} = k(s-y) + c(\dot{s}-\dot{y})$$

where: s = the displacement of the support

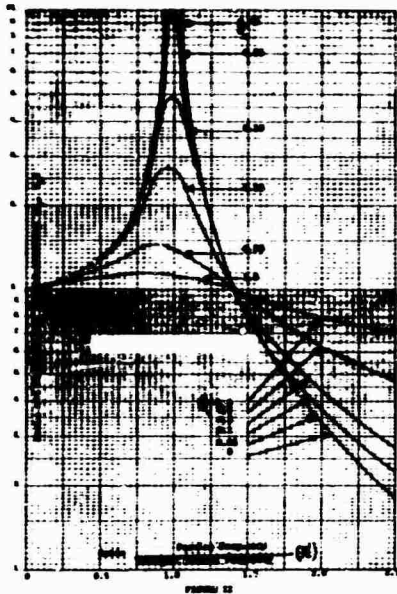
y = the displacement of the mounted body

The factor "k", the system spring constant and "c", the viscous damping are the parameters we will control to achieve the desired response for a damped sine shock test or swept sine vibration test. Solution to the differential equation in terms of the amplitude ratio (referenced to as transmissibility T_D):

$$(2) \quad T_D = \frac{|Y_0|}{|S_0|} = \frac{1 + [2(w/\omega) (\zeta)]^2}{\sqrt{[1 - (w^2/\omega^2)]^2 + [2(w/\omega) (\zeta)]^2}}$$

where: The undamped natural frequency $\omega = \sqrt{k/m}$

and damping constant $(\zeta) = c/c_c$ (c_c is the critical damping) are the system parameters in terms of "k" and "c". Plots of this equation for various values of ζ are shown in Figure II



At resonance $w/\omega = 1$, the transmissibility is a maximum and the equation becomes:

$$(3) \quad T_D = \frac{1 + (2 \zeta)^2}{(2 \zeta)^2}$$

The absolute displacement $(s + y)$ of the mounted body is then entirely dependent on the damping, the ratio varying between infinity (∞) for an undamped system and $(s + \sqrt{5/4})$ for a critically damped system. Therefore,

by adjusting the "k" of the system so that the ratio of "w" which is the forcing frequency to ω is unity, a condition of resonance is obtained whereby the displacement is amplified as a function of the system damping. In our system we have utilized air springs whose "k" is continuously variable as a function of gaseous pressure enabling us to "tune" the system in its dynamic state. A schematic of the prototype mechanical amplifier is illustrated in Figure III.

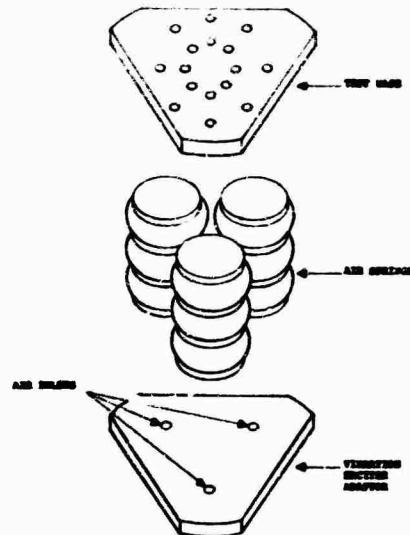


FIGURE III - MECHANICAL AMPLIFIER

For the damped sinusoidal shock testing, the exponential decay rate of the transient disturbance of the mounted body is also a function of the system damping. Since the system damping is not continuously variable in a controllable manner--our system simulates the decay rate desired e.g., $\zeta = 0.1$ expressed in a percentage as 10% of critical (C_c). This is achieved by controlling the decay rate of the input forcing frequency with the amplitude modulator.

In the Swept Sine Vibration Mode, the system must be continuously tuned to resonance while sweeping the frequency. This is achieved by utilizing the phase relationship of the displacement of the mounted body to that of the support.

Again referring to Figure I the expression for the displacement of the mounted body "M" is:

$$(4) \quad y = y_0 \cos (wt + \psi_2)$$

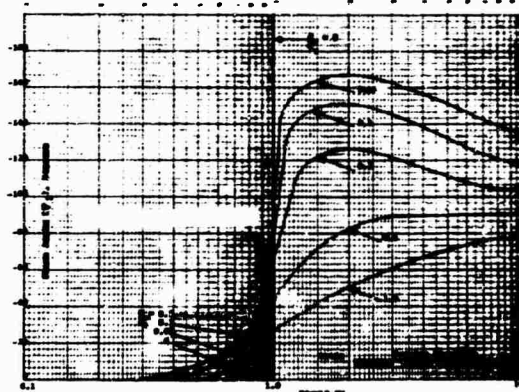
ψ_2 is the phase angle between the displacement (or acceleration) of the mounted body "M" and the support. The solution to this equation in terms of the tangent of the phase angle:

$$(5) \quad \tan \psi_2 = \frac{-2 \zeta (\omega/\omega_n)^3}{[1 - (\omega^2/\omega_n^2)] + [2(\omega/\omega_n) \zeta]^2}$$

where all terms are the same as in Equation (2). Again evaluating the expression at resonance:

$$(6) \quad \tan \psi_2 = \frac{-1}{2\zeta}$$

* A plot of this equation for various values of C/C_c is shown in Figure IV below

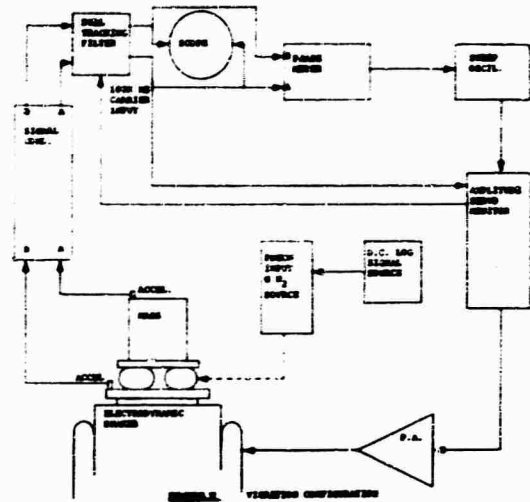


It can be seen then that the phase angle is also a function of the damping ratio and approaches 90° at resonance with no damping i.e., $\zeta = 0$. The angle varies between approximately -27° for a critically damped system ($\zeta = 1$) and -90° for an undamped system. In our system with $\zeta = .1$ this phase angle is -79° . It is this phase angle which we use to control and maintain the system at resonance with the sweeping frequency.

DESCRIPTION OF SYSTEM

The complete system consists of an electrodynamic shaker/amplifier which includes the Amplitude Servo

Monitor and the Oscillator. The Shaker System transducers and signal conditioning equipment are all part of the normal existing vibration laboratory equipment. The addition of the Mechanical Amplifier, Resonance Dwell Phase Meter, Dual Tracking Filter, and GM_2 Pneumatic source completes the system as shown in Figure V.



1. Steady State Vibration - Swept Sine Operating Mode:

In the steady state vibration mode, the shaker system amplitude servo monitor and oscillator are set up as in a normal test to suit the dynamic conditions required. After start up of the shaker, the air springs are tuned to resonance as indicated by the proper phase angle on the phase meter, and/or lissajous pattern on the oscilloscope. This is usually done at the lowest desired test frequency. The tuning is accomplished by admitting gaseous nitrogen from a high pressure gas source through a regulator to set the desired pressure on the air springs. Acceleration or/displacement transducers mounted on either side of the displacement amplifier provide a signal to the phase meter through a dual channel tracking filter. The tracking filter is used both for cleaning the signal i.e., removal of unwanted noise, and to utilize the heterodyning of the 100Kc, carrier for frequencies below 5 cps, the low frequency design limit of the phase meter. These signals "A" from the output (mounted body) side and "B" from the input (shaker top side) are fed through the signal conditioning (charge amplifier) system for normalization and or gain adjustment, then through the tracking filter to the

phase meter. Signal "A" is also sent from the tracking filter to the servo monitor for continuous control of the test item to the required specification.

After tuning to resonance, the phase meter - which contains an integral resonant dwell circuit - is placed in the "Preset" mode which nulls the output to the sweep oscillator. This procedure accomplishes the control of the oscillator by the resonant phase angle between the input and output of the mechanical amplifier. The oscillator is controlled by an error signal provided by a change in the preset phase angle in the resonant dwell phase meter.

The phase error is generated by a change in pressure at the air springs constantly "detuning" the system. The phase meter, continuously correcting for the detuning, drives the oscillator to resonance, resulting in a swept sine frequency "at tuned resonance" proportional to the rate of change of gas pressurization. The oscillator signal is processed through the servo monitor to the power amplifier which drives the shaker, controlling the input as a function of the response.

The pneumatic input to the air springs is provided by a regulated high pressure gaseous nitrogen GN_2 source. A pressure transducer (Figure VI) controlled by a DC signal proportional to oscillator frequency admits gas to provide the proper tuning as a function of time. The controlled gas flow into the air springs determines the sweep rate.

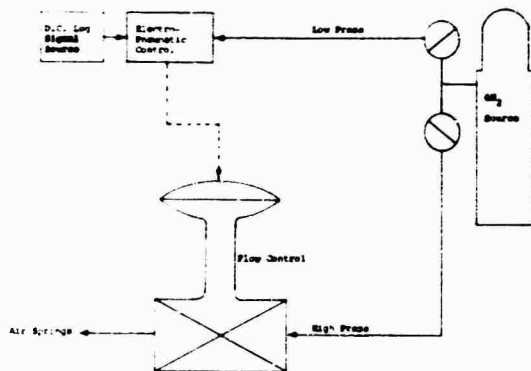


FIGURE VI PNEUMATIC INPUT SYSTEM

A photograph of a typical test setup is shown below

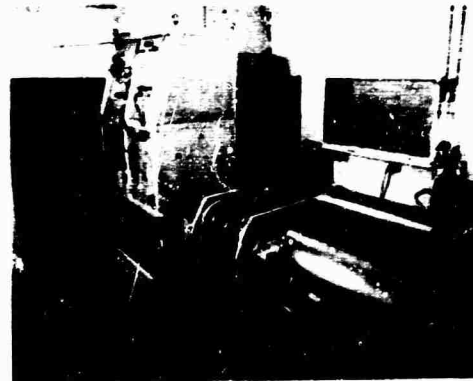


FIGURE VII-PHOTOGRAPH OF A TYPICAL TEST SETUP

2. Results:

Tests on the system have resulted in displacement amplifications as high as 11 inches at 3 cps and 10 inches at 7.5 cps at sweep rates of 2-1/2 octaves per minute between frequencies of 3 cps to 22 cps. The system is limited by the performance capabilities of the electrodynamic shaker system. These results are shown in the accompanying test data. (Figure VIII)

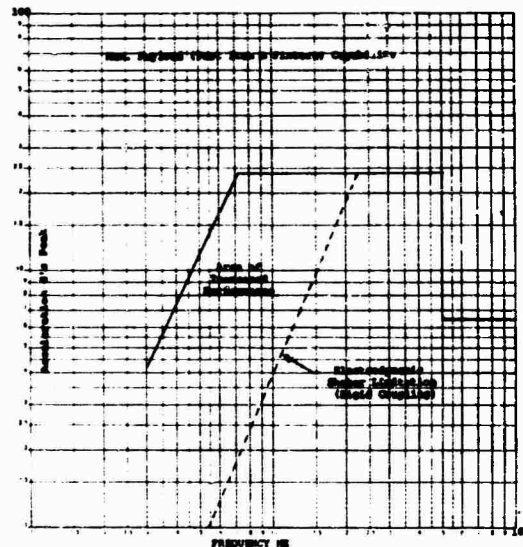


FIGURE VIII SWEEP SINE VIBRATION PROFILE

3. Shock Mode of Operation:

In the Shock Mode of Operation, the system is "tuned" to resonance at a discrete frequency in a similar manner, with the set up shown as in

Figure IX. The amplitude modulated signal source delivers a sine burst at the desired frequency and decay rate to the power amplifier to excite the shaker. The resulting displacement is amplified through the air spring mechanical amplifier to the desired level by adjusting the peak amplitude of the input signal. This is accomplished by (See Figure X) applying a sine burst of the desired frequency from the function generator where it is time phased and triggered in the variable delay. The pulse gate passes the number of cycles desired and sets the decay rate as delivered by the ramp voltage generator. The amplitude modulated signal is then fed into the power amplifier to excite the shaker.

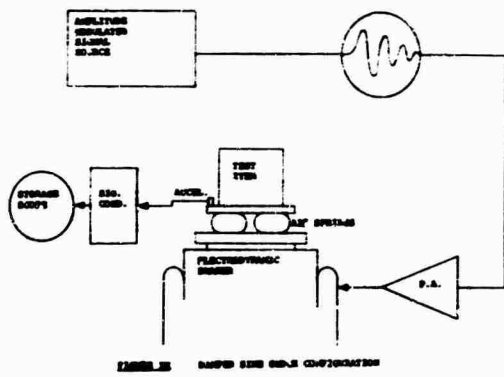


FIGURE IX - AMPLITUDE MODULATED SIGNAL SOURCE

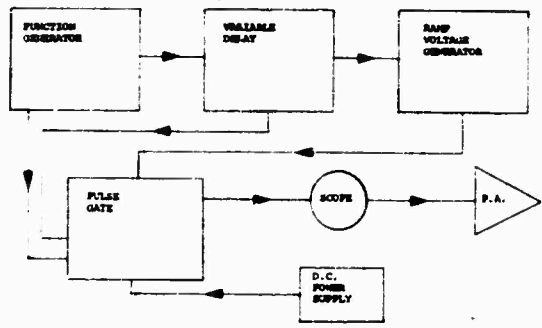
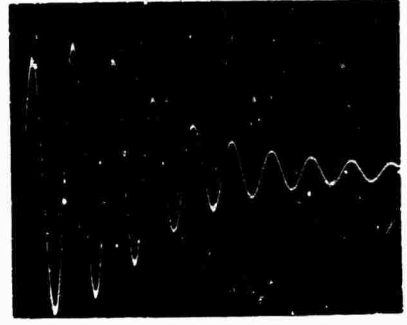
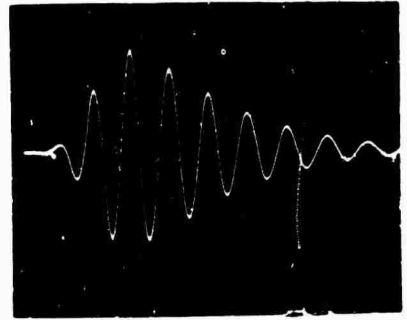


FIGURE X - AMPLITUDE MODULATED SIGNAL SOURCE

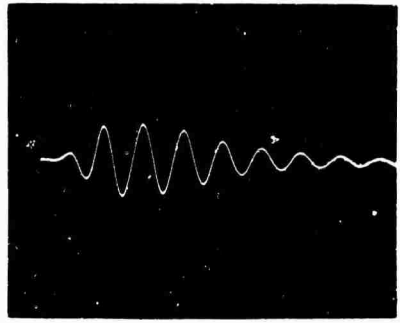
Amplifications of greater than 10:1 have been accomplished. Displacements of 11 inches at 3 cps on the mounted body have been achieved. The results are shown in Figure XI through XIII.



Sensitivity: Vertical 200mv/cm (5 Hz)
FIGURE XI - AMPLITUDE MODULATED 5HZ SINUSOID



Filtered Input (5Hz Bandwidth)
Sensitivity: Vertical (1.49/cm), (5Hz)
FIGURE XII - DAMPED SINE SHOCK INPUT TO TEST ITEM



Filtered (5Hz Bandwidth)
Sensitivity: Vertical (1.47/cm), (5Hz)
FIGURE XIII - ELECTRO DYNAMIC SHAKER ARMATURE

DISCUSSION

Mr. Galef (TRW Systems): I am surprised at your very good results on the damped sinusoid. Here we are dealing with a lightly damped system which takes some time to build up to resonance, and I would expect it to reach its peak value quite a few cycles later in time and then to damp out quite slowly. How does the theoretical calculation of that ten percent damped system compare to what you actually got?

Mr. Cerasuolo: This is a function of the electrodynamic shaker itself, and of the mounted test mass and the shaker armature—the load to be overcome. Would you show slide 12 again please? The peak amplitude is not reached on the first cycle. It will take as many cycles as are necessary to overcome the inertia. Notice that the peak amplitude is reached on approximately the second cycle. This is a limitation which you have to live with unless you have got enough force capability to handle it.

Mr. Galef: That is the input. I am concerned about the other side of the air bag. I would expect the peak not to be reached until the fifth or sixth cycle.

Mr. Cerasuolo: The actual test does produce some delay in the peak, but not five or six cycles. It depends on how much inertia you have to overcome, and the damping of the system. We are trying to achieve the buildup of resonance. As you say, there is a limitation in that instead of producing an exact damped sinusoid, sometimes in order to get the peak you have to start it initially with one or two cycles of a lower amplitude to build up to the peak.

Mr. Sernez (IBM): Your picture shows horizontal tests. Did you also do the same type of test in the vertical direction?

Mr. Cerasuolo: Yes, we have done it in all three axes. The vertical axis is much more impressive but unfortunately I did not bring the photograph with me.

Mr. Sernez: How do you manage the one inch maximum travel on the shaker with the high amplification of the specimen?

Mr. Cerasuolo: Are you referring to the stability of the system in the vertical mode?

Mr. Sernez: Yes. Do you use a dc bias to maintain a position?

Mr. Cerasuolo: Oh, I see what you mean. We do relieve the mass in excess of 1,000 pounds on the shaker so that the system will not bottom out.

Mr. Sernez: One more question. You indicate results at 3 Hz. Do you rate your vibration system and operate the exciter at 3 Hz.?

Mr. Cerasuolo: Yes, we do operate the exciter at 3 Hz. At low frequencies one can not use the rated output as an actual parameter of the shaker.

Mr. Sernez: Do you actually get a sinusoidal shape out of the shaker at 3 Hz.?

Mr. Cerasuolo: Yes, we do.

Mr. Jobe (Bell Labs): This may be an unfair question. Your paper was directed to sine testing. We use the shaker for electrodynamic shock tests. Have you had any experience or have you used this as an amplifier in order to be able to get more shock output from a shaker of this nature?

Mr. Cerasuolo: It will not work. Do you mean for something like a pyrotechnic shock or a single sinusoid pulse type test?

Mr. Jobe: Pyrotechnic shock is what I meant.

Mr. Cerasuolo: We could reproduce a dc pulse type test but a pyrotechnic shock—which is in essence an oscillatory transient—can not be handled by this because it is essentially a low frequency system and it just will not respond.

ARTILLERY SIMULATOR FOR FUZE EVALUATION

H. D. Curchack
Harry Diamond Laboratories
Washington, D. C.

A unique facility for fuze testing has been constructed that simultaneously provides linear and angular accelerations as they are applied in rifled artillery. The fuze is electrically interrogated during this time and subsequently while the angular velocity is maintained. This second report on the simulator describes the progress made in four years and the work still to be done. A description of the device and status of the major components is followed by evidence of the correspondence of test conditions with those of field firings, a discussion of instrumentation, a description of table-top simulators, and discussion of the advantages of the present technique and areas for future development.

INTRODUCTION

Centrifuges, spinners, gas guns, actuators and rocket sleds have been constructed for laboratory simulation of the forces experienced by fuzes or fuze components when launched or fired. Of these, gas guns and spinners are frequently used by engineers concerned with the environment experienced by such spinning artillery fuzes as may be fired from howitzers, recoilless rifles, or certain mortars. In one gas-gun technique, the fuze is slowly accelerated to a predetermined velocity and then decelerated by impact with a known target. This rapid deceleration simulates the setback of the field fired projectile. The main advantages of this technique are that the fuze is immediately available for inspection and the cost and problems associated with recovery in the field are eliminated. In spinners the fuzes are rotated at the angular velocity appropriate to the weapon, and optical or electrical observations are made of performance. Some spinners use low inertia or other means to duplicate the angular accelerations experienced in the field.

This paper describes a unique facility called the Artillery Simulator which unites the features of the gas gun and the low inertia spinner so that setback and spin acceleration

occur simultaneously. Although a description of this device has been previously published [1,2], it is repeated here because circulation of these documents was limited and the description is necessary to understand this paper. However, all the results are new and some new equipment is described herein. Also described are automatic testers for production-line evaluation of fuze components employing the techniques developed [3,4].

THE CONCEPT

A system is desired that simultaneously applies linear and angular accelerations to a fuze or fuze component as is done to projectiles fired from rifled barrels. The angular velocity achieved is maintained, as in the case of a projectile in flight, and the performance of the component is electrically monitored for a period representing the flight time. Our approach is as follows.

A hollow cylindrical tube is rotated about its longitudinal axis at a desired angular velocity. A projectile (which we shall call "bird" to distinguish it from the actual projectile used in the field) enters the tube at a given linear velocity. Within the tube, the bird is linearly

decelerated while being angularly accelerated until it has stopped linearly and has acquired the angular velocity of the spinning tube. Furthermore, at some time during this process an electrical circuit is completed that allows continuous monitoring of the fuzing component within the bird.

Although interdependent, the problems associated with this approach are readily enumerated and must be properly resolved. It is necessary to provide:

(1) The requisite linear velocity to the bird without disturbing the fuze component. (Gas gun)

(2) A tube, of bore sufficient for testing fuze components, that can rotate at a representative angular velocity. (Spinner or Spin-catcher)

(3) A stopping mechanism to decelerate the bird properly while minimizing the forces transmitted to the bearings (Mitigator-Momentum Exchange)

(4) Electrical circuits from the bird to the spinning tube to remote instrumentation. (Readout)

THE GAS GUN

A method of setback simulation often used at Harry Diamond Laboratories is to first accelerate a bird in a 96 ft gun and then stop it within a few inches in a target of lead blocks [5,6]. The velocity attained in the gun is chosen so that the peak deceleration on impact as recorded by a copper ball accelerometer [7,8,9] is comparable with typical field conditions. This facility has proved its usefulness in the development of many electromechanical fuzing systems, because the fuze designer has a readily available test that his fuze has to survive before satisfactory field performance can be expected.

If we assume our simulated acceleration (impact acceleration) to have an average, a , then the velocity, v , to produce a given a in the stopping distance, s , is approximately

$$v = \sqrt{2as} \quad (1)$$

This is the velocity we need to attain in the gas-gun in terms of simulation parameters a and s . Assume that the velocities of interest can be obtained in an almost constant acceleration gun, therefore

$$v = \sqrt{2AL} \quad (2)$$

where A is the acceleration and L is the length of the gas-gun. Since, as previously stated, the gun force or acceleration is to be small compared with the stopping force or simulated acceleration.

$$s/L = A/a \ll 1 \quad (3)$$

For ideal simulation of field conditions, the bird containing the fuze component should be stopped in a distance equivalent to the length of the field artillery piece from which the component is fired. If the artillery barrel is 10 ft, s should be approximately 10 ft and from previous consideration L should be greater than 500 ft. The available space limited our gas gun to an L of 30 ft which reduced s to about 6 in. and limits v to \sqrt{a} where a is in ft/sec² and v is in ft/sec. For a maximum a of 10,000 g (320,000 ft/sec²), v is less than 600 ft/sec, which is easily attainable in gas guns.

The bore of the gun was chosen to be 2 in. because this is large enough to accommodate many fuzing components yet small enough to allow for an easily constructed rotating catch tube.

The original gun had a barrel constructed from two butt-welded steel tubes with 1/4 in. walls. This was replaced in 1969 with a honed stainless steel barrel. The driver is a converted 3.2ft³ air storage tank. The bird is generally a right circular cylinder 4 in. long and weighs between 1 and 2 lb. The bird is inserted into the end of the gun up to a pin that protrudes into the tube. A mylar diaphragm is placed over the muzzle of the gun, and the barrel is evacuated. The bird, diaphragm, and pin are sealed with O-rings. The gun can be fired in either of two ways. The pin may be pulled without attaching the driver to the gun. In this case the 14.7 psi atmospheric air pressure propels the bird. Furthermore, there is effectively no pressure difference across the bird as it leaves the gun which, as will be seen, is a distinct advantage. The second method involves attaching the driver to the barrel, evacuating this tank through an auxiliary vacuum system, pressurizing it with the proper amount of helium gas, and then pulling the pin. Helium is used because its light molecular weight makes it more efficient than air and it is safer than the most efficient gas, hydrogen. Although there has

been no need and therefore no effort to obtain velocities higher than 600 ft/sec, a velocity of 2500 ft/sec with a 1-lb bird is a conservative upper limit for the gun.

The construction features of the gun that are most important so far as ease of operation and assurance of performance are embodied in three assemblies (1) the breech and release mechanism, (2) the gun barrel and (3) the muzzle (diaphragm and vacuum section).

The breech section is an extension of the gun barrel containing a release pin and various vacuum seals. The bird is loaded into the breech simply by inserting it into the (effective) end of the gun. Since 99% of the shots fired do not use the driver tank, this is all that is required to "load" the gun. After the gun has been evacuated, an electrically controlled pneumatic cylinder withdraws the 0.5-in. diameter steel release pin, which fires the bird.

The driver tank is used simply by rolling it forward and attaching it with fast-acting clamps. This speed of operation is important in certain extreme temperature and telemetry testing and will be further discussed.

The gun barrel bore was trepanned from two 17-ft stainless steel bars that were subsequently turned down to 4-in. O.D. The bore of each section was then honed to 2.013 in. over its entire length. This type of fabrication was used to maintain dimensions over the extended lengths, and the heavy wall prevents kinking and allows the gun to be aligned over its entire length (using optical techniques) to a few thousandths of an inch. The ends of the section were machined to mate with each other and the breech and muzzle section resulting in a gun about 33 ft long.

The vacuum section (Fig. 1) is located at the muzzle end of the gun and contains an oversized inside diameter for about one inch from the gun exit. The purpose of this "reservoir" is to provide a volume for any gas (that may either be in the gun prior to firing or may blow by the projectile) to fill without undue buildup of pressure. This is done to get maximum performance of the gun. The vacuum system attaches to the gun at this section.

The 0.001-in. mylar diaphragm material is obtained on 200 ft rolls, 4 in. wide. It is pulled down from a reel across the muzzle of the gun and is clamped to the vacuum section by a door and a latch.

SPINNER

For proper simulation the spinner (spin-catcher) must rotate the bird about its longitudinal axis, and therefore the bird must be a reasonably close fit to the bore of the tube. For this reason a 3-ft section of the same steel tubing used for the gun barrel was chosen for the first tube. The outside of the tube was then machined to be concentric with the inside, a ball bearing was mounted at each end, and a sheave as provided for a single v-belt.

This assembly was then mounted (by the bearings) on a heavy steel platform, and a variable speed motor was provided to impart a drive for the tube. The complete spin-catcher was installed about 14 in. from the muzzle of the gas gun. Aligning was accomplished with a specially machined tube that fit closely within the gun and spin-catcher tube. The current spin-catch tube is considerably more complex than this tube but only in detail.



Fig. 1. Muzzle of gun.

The two major considerations for the location of the spin-catcher were that the device be close enough to the muzzle so that the bird would enter without hitting the tube wall, yet far enough so that the driver gas is adequately vented and does not continue to push the bird within the spin-catch tube. A set of curves showing the drop distance due to gravity as a function of horizontal free travel distance and horizontal velocity [1] revealed that for an arbitrary minimum velocity of 200 ft/sec, there would be a drop of 0.005 in. in a distance of 1 ft.

THE METHOD OF STOPPING (MITIGATED-MOMENTUM EXCHANGE)

The conventional HDL air gun technique of stopping the projectile uses lead blocks stacked in a massive steel chamber rigidly attached to a concrete floor. This brute-force method is of no use in the spin-catcher. If the catch tube is filled with lead and sealed so that the lead cannot come out the far end, the entire momentum impulse will have to be borne by the bearings. Such thrust forces would be intolerable. Rather than build thrust bearings into the device (which might be of doubtful utility for high impulses and would undoubtedly decrease the upper rotational limit of the tube) it was decided to use a momentum transfer system.

If an elastic impact occurs between two identical masses in which initially one mass is moving and the other is at rest, the result is that the moving mass stops while the other mass leaves with the initial velocity. (Such an impact is often demonstrated on the billiard table.) There is no expectation that at gas-gun velocities, we will have elastic impacts, but by the proper choice of masses and degrees of inelasticity, the bird can always be brought to rest within the spin-catcher while transferring its momentum to a mass that is ejected and eventually stopped by lead blocks.

To catch the bird in these inelastic impacts, it is necessary to devise an effective way to absorb the energy not carried off by the momentum exchange mass, or "mem", and to produce the simulated acceleration. Currently, we use either a column of plywood blocks or other mitigators [10,11] as an intermediary between the bird and the mem with very effective results. About 3000 birds have been caught successfully.

After the bird is caught, it is held by friction only within the spin-catcher. Therefore, if the driver gas does not readily expand and dissipate between the muzzle and the spin-catcher, it will blow the bird through the tube. This explains the desirability of keeping as low a pressure as possible within the gun. If the range of velocities is to extend upward so that gas at higher pressures is used, the spin-catcher will undoubtedly have to be moved further from the muzzle.

THE READOUT SYSTEM

To demonstrate the feasibility of the spin-catch method, the first 100 shots were made in a catcher with no readout capability. A simple readout system was then designed to extend the system development. This required construction of a second spin-catcher and modification of the bird. The idea behind the readout is to split the spin-catch tube longitudinally into two or more sections, each insulated electrically from the other and each connected to its own slip ring (Fig. 2) and external brush assemblies.

The bird (Fig. 3) is insulated to preclude its forming any electrical path between sections and carries on it the same number of contacts as there are segments in the catcher. These contacts are allowed limited outward motion and are activated by centrifugal, spring or setback forces.

As soon as the bird enters the spin-catcher and starts rotating or decelerating, the contacts move outward radially, each contacting a single section. If the bird does not achieve the tube's angular velocity immediately, there is relative motion across the sections so that each channel of information is retarded one step for each section traversed. The main advantage of such a design is that it is insensitive to the longitudinal location of the bird, assuring readout as long as the bird is caught.

The present readout spinner (Fig. 4) is constructed of four stainless steel readout sections assembled with bakelite insulators. The readout section length is 32-in. and the overall length is 40-in. The slip rings are coin silver, and three carbon brushes are mounted in parallel on each slip ring. Conventional ball bearings that are oil-mist lubricated are used. The spinner is honed to 2.013 in I.D.

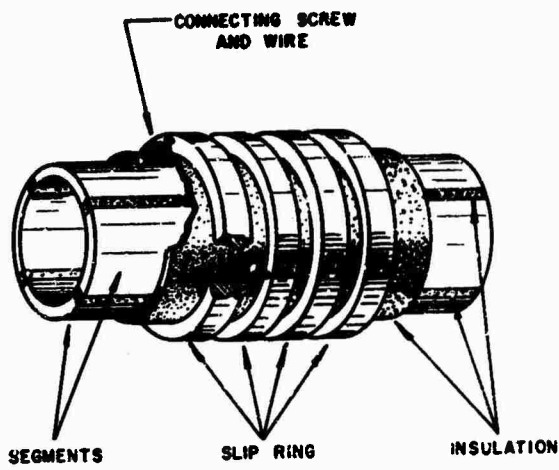


Fig. 2. Readout section diagram.

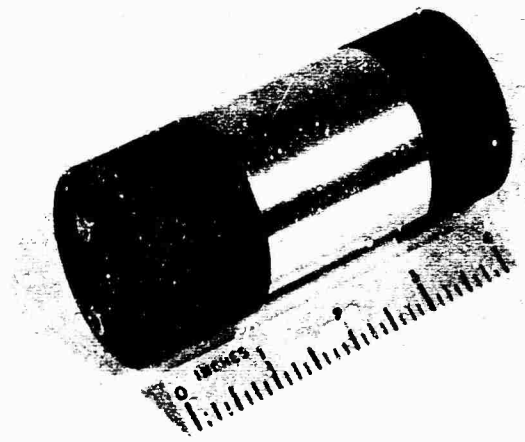


Fig. 3. Readout bird. The two bright discs at the 4-in. mark are the contacts.

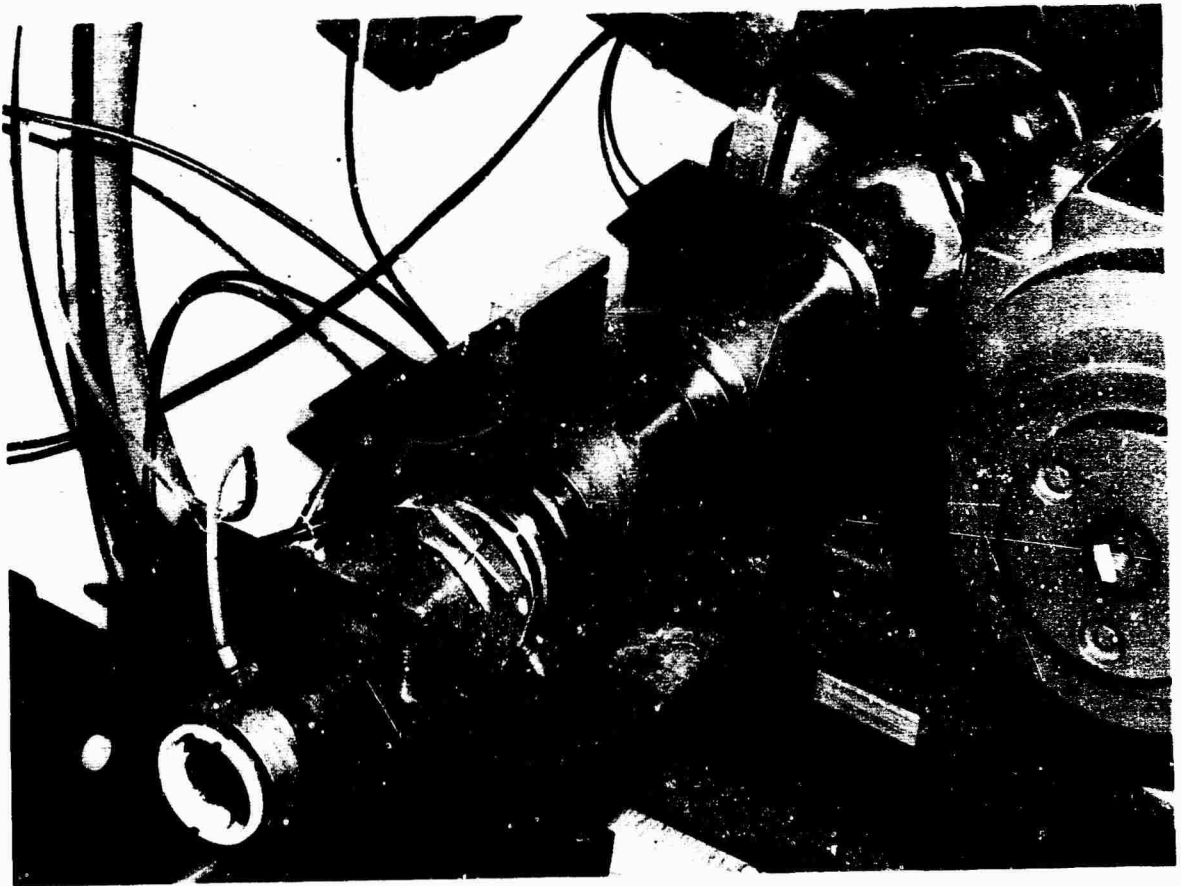


Fig. 4. Spinner.

The top test speed used with this spinner is 130 rps. Above this speed, flexing causes considerable runout of the middle of the tube and excessive vibration. Although the tube has been dynamically balanced, the construction features do not allow sufficient rigidity for balance to be maintained. The dangers in using the equipment are the noise generated on firing, and the spinning mem which at higher spinner speeds sometimes ricochets out of its catch box. For this reason the spinner, muzzle of the gun, and mem catch box are in a reinforced concrete room.

FIRING PROCEDURES

The actual firing procedure is as follows. The test conditions, "G", spin and impact velocity are established. This determines the type of mitigator and mem. These are positioned within the spinner close to the bird entrance. New diaphragm material is placed in the diaphragm section, the bird is inserted into the breech, the valve connecting the vacuum system to the gun is opened, (if the driver tank is to be used it is attached, evacuated and pressurized) the spinner is turned on and the release pin is withdrawn. The spinner is run for as long as necessary following impact. From the time the bird is inserted into the breech until it is fired is about one minute. For temperature conditioned birds, this time is decreased by inserting a separate nose piece into the breech and then attaching the remainder of the bird after the gun barrel is evacuated. After the shot the spinner is stopped and the bird and mitigator are pushed out of the spinner. The data recorded includes all masses, bird and mem velocity and mitigator type and change in length.

GAS GUN PERFORMANCE

We define a perfect gun as one in which the acceleration is constant, since this would be the gun with the lowest peak acceleration for any given length gun and muzzle velocity. Looked at in a slightly different way, this is the shortest gun possible for a given peak acceleration and muzzle velocity. In the design of a facility, the length of the gun needed is an important consideration in cost as well as space. Therefore, we define the efficiency of the gun, R , to be equal to the ratio of actual muzzle velocity to ideal velocity, i.e. velocity attained in a perfect gun. Reference

1, Appendix B contains predictions of gas-gun velocities and bounds for the theoretical efficiency. The efficiency is a function of dimensionless velocity $u = v/c$ (where c is the sound speed of the gas used in the gun) and the specific heat ratio, γ .

A constant diameter gun [12] is one in which the gun diameter is maintained both upstream and downstream of the bird for effectively infinite lengths. The theoretical properties of such guns are expressible in closed form and therefore provide insight and a basis for qualitative decisions. Oversized reservoir guns [13-16] are somewhat more efficient. Ideally, the maximum values of u would be 3 and 5 for γ 's of 5/3 and 7/5. Practically, however, the efficiency R is down to 0.1 at u 's of 1.5 and 1.9. This implies that a gun at least 10 times longer or with 10 times the acceleration of the ideal gun would be needed to achieve these velocities. It therefore appears most attractive to concentrate on guns with as small a value of u as possible and impose a practical limit on u of about 1.

An infinite chambrage gun [14,16] is one in which the diameter of the gun in the pressure chamber is very large compared with the barrel diameter. Our guns when evacuated and driven by room air would be considered infinite chambrage. When the tank is used the chambrage is about 6. The constant diameter gun has a chambrage of unity.

Two assumptions implicit in the derivation of the performance of the guns are that friction does not slow the bird nor does any gas blow by the bird. In our initial tests one or two O-rings were used on the projectile to serve as a vacuum seal and to minimize blowby. The velocity when two O-rings were used indicated lower efficiency than expected while one O-ring results were only slightly more efficient. Furthermore, the velocity changed with the type of O-ring used as well as with the different O-rings of the same lot. For this reason the O-ring was transferred from the bird to the gun, and the bird and gun diameters were critically controlled to reduce blowby. Results with this system with an air driver gas, infinite chambrage, and a honed barrel yield efficiencies within 2% of theoretical up to velocities of 350 ft/sec [17].

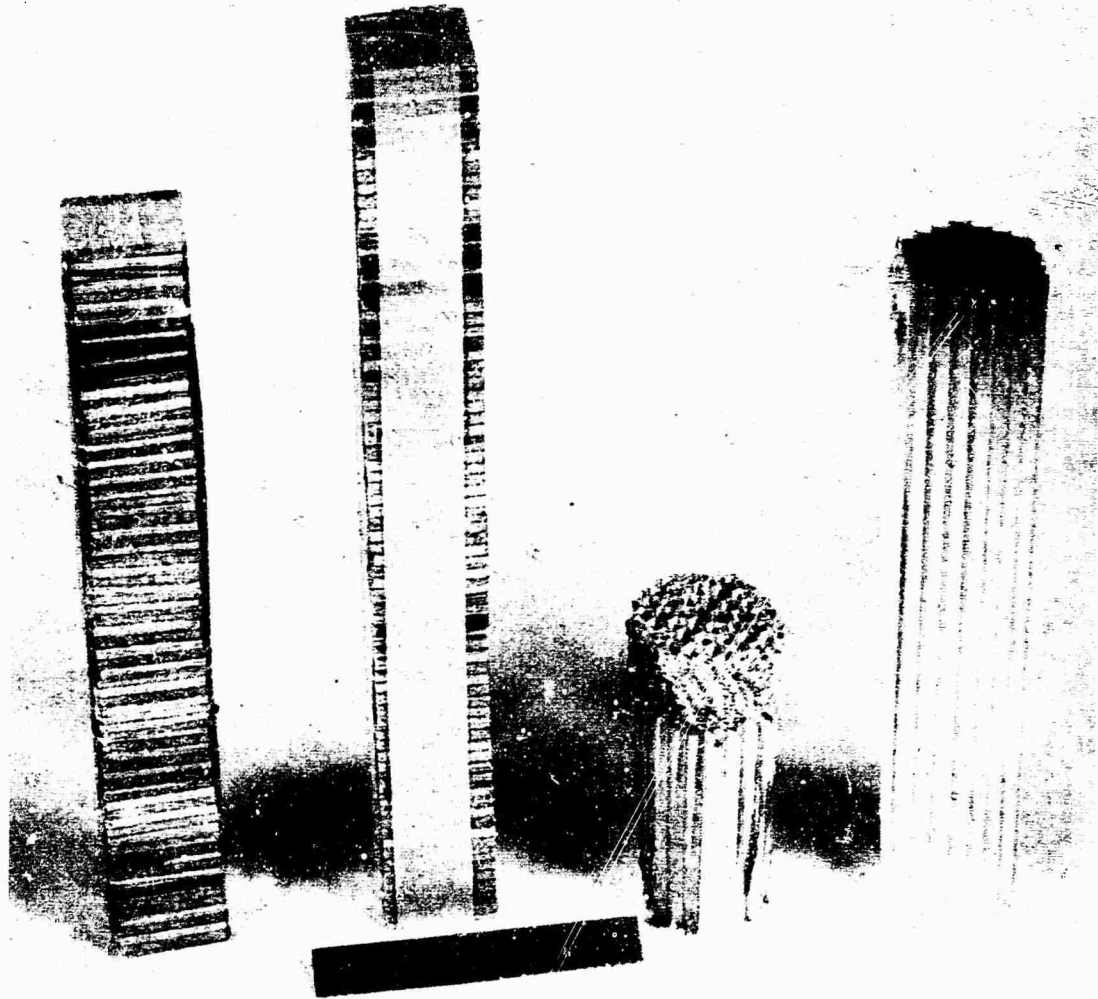


Fig. 5. Plywood and aluminum honeycomb mitigators before and after impact.

SPIN CATCHER PERFORMANCE

The first spin-catcher with read-out had two segments and performed well. It was used in over 2000 tests with no apparent deterioration of bearings or brushes. This is even more noteworthy since several bad impacts occurred immediately after changing over to this catcher. Bad impacts may occur for a number of reasons. The most damaging is caused by a misalignment between gun and catcher. Unless alignment is adjusted periodically a bird or the catcher can be considerably deformed by the impact. Reasonable caution avoids

this. However, a more usual cause of improper bird entry to the spinner can be traced to a slight rotation of the bird which is caused by asymmetric diaphragm failure. This type of defect is minimized if the bird is long enough so that its trailing edge is still guided by the gun barrel during diaphragm penetration. However we still have some engagement of the leading edge with the spinner wall even with considerable care. For this reason a conical teflon entrance piece is used as a guide at the adit to the spinner.

STOPPING MECHANISM PERFORMANCE, LINEAR AND ANGULAR ACCELERATION

The stopping mechanism has performed very satisfactorily in that very little data have been lost due to the bird bouncing back out or going through the catcher. However, how well we are simulating artillery firing requires investigation of the linear and angular accelerations.

An analysis of linear momentum and energy conservation equations applied to this impact problem [1] led to the conclusion that the plywood impacts could be considered completely inelastic. This leads to the conclusion that the bird velocity never goes to zero and we cannot stop it. Actual experience has shown however that to bring the bird to rest a mem of about six times the mass of the bird is required for wood impacts and ten times the mass of the bird is required for aluminum honeycomb (standard or tubular type). Figure 5 shows wood and honeycomb mitigators before and after impact.

Conservation equations reveal that for an impact in which the bird is brought to rest

$$E_L/E_M = 1 - (m/M) \quad (4)$$

where E_L is the energy absorbed during impact

E_M is the maximum energy that could be absorbed

m is the bird mass

M is the mitigator and mem mass combined

However (from [1])

$$E_L/E_M = 1 - \epsilon^2 \quad (5)$$

$$\therefore \epsilon = m/M \quad (6)$$

where ϵ is the coefficient of restitution for the impact.

Therefore we have empirically determined the coefficients of restitution and fractional energy loss to be 1/6 and .97 for wood impacts and 1/10 and .99 for honeycomb impacts.

The fact that E_L/E_M of .97 is less than the values measured previously ([1]p 36) is attributed to the fact that the measured mem velocity in these experiments is too low. This is because the mem has been decelerated by friction while traveling through the spinner before the mem velocity is measured.

CORRELATION WITH FIELD TESTS

The actual deceleration profile experienced by the bird has not as yet been measured in these experiments, however, techniques are being developed to do this (See INSTRUMENTATION Section). Values calculated from impact velocity, masses, and crush of the mitigator [1,11] have been the primary data output. For levels up to 5000 G, there is a strong correlation between simulator results and field results on certain fuze components. There is insufficient data at higher G levels to know if the correlation still exists. In the field the higher G's are accompanied by spin rates currently unobtainable in our equipment. Most testing in our equipment is at the lower accelerations.

One case in point is the PS115 power supply, a fuze device activated by simultaneous linear and angular accelerations and prolonged spin. The entire power supply or its capsule (the container that stores the electrolyte) has been tested in its various forms in 81 shots in the simulator since its development began in late 1965. It has also been alternately tested about 530 times in the 4.2 mortar, 90 times in the 155 howitzer and about 50 times in each of the 75, 105 and 175 howitzers. Whenever the field conditions were comparable to simulator test conditions, the results were remarkably similar.

The cost of the \$17 simulator shots many of which included readout in excess of 5 minutes was less than \$10,000 (about \$10 per shot). The cost of the equivalent field tests cannot be estimated because some of the simulator tests are not achievable in the field. This is discussed further in the ADVANTAGES Section.

Outside of the correlation between field and simulator data for the power supply discussed in the previous section, quantitative angular acceleration measurements are only now being made. The results to date are fragmentary and will be the subject of a future report. However, the proposed measurement techniques are described in the INSTRUMENTATION Section.

HARD-WIRE READOUT PERFORMANCE

Tests run on the spinner which involve readout have involved fuze power supplies of various types. Generally these tests have been at about 50 rps and good low-noise traces have been recorded. Figure 6

is a typical readout of an experimental power supply. Trace A is the signal channel; trace B, the noise channel. The calibrations for this shot are 10 volts per major division for the A trace and 0.2 volts per major division for the B trace. The time base is 2 seconds per major division. A zero-time signal appears on traces A and B as the bird enters the spinner. The power supply is automatically electrically loaded after 6 seconds and unloaded after 10 seconds. This appears as a slight drop in voltage on trace A and as spikes on trace B. This test was at 44 rps and 1860 G. The power supply temperature was 145°F. There is some expected noise generated during power supply activation and may be ignored. The noise signal contains power supply noise as well as brush noise from the spinner. The total noise amplitude is less than 40 millivolts which is acceptable regardless of the cause. The brush noise does increase with spin rate and is sometimes objectionable at spins over 100 rps. Because we want to extend our spin rate to over 300 rps and also because good contact between the bird and spinner is not established until about 5-30 millisecond after impact, a hardened telemetry system has been developed for readout.

TELEMETRY

The 240-MHz telemeter [18] utilizes three information channels, IRIG A, C, and E. An exploded view of the telemeter projectile (Fig. 7) shows the linen base phenolic projectile, an aluminum radiation shield, transmitter, a signal processor, and nickel-cadmium power supply. The prime purpose of this unit was to investigate power supply performance during its activation phase. Under certain conditions this critical phase may precede the establishment of good contact for hard wire readout. The second important consideration is that the brush noise problem is circumvented.

The telemeter is turned on just before firing. Since the projectile "for vacuum firing" protrudes from the breech a dipole antenna at the breech allows the receiver to be tuned to the broadcast frequency. A second antenna in parallel with the breech antenna is wound in a helix around the spinner. (See Fig 4) The transmitter which has been used in about 30 shots has remained locked to the receiver during every test.

INSTRUMENTATION

Outside of vacuum and pressure measurements which are made in a

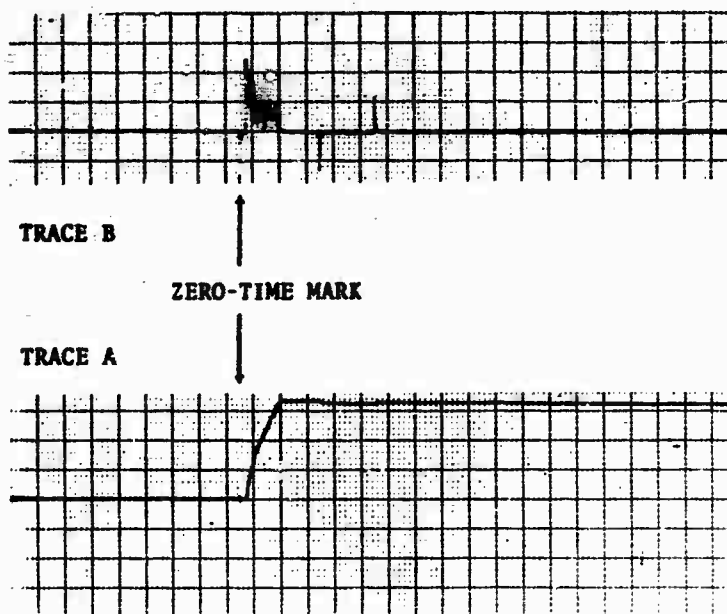


Fig. 6. Power supply readout. Trace A is the signal channel (10 volts per major division). Trace B is the noise channel (0.2 volts per major division). The time axis is 2 seconds per major division.

routine way, most measurements concerning the dynamics of the bird have led to difficulties which in some cases are still unresolved.

Bird Impact Velocity Measurements

The impact velocity is computed from a time of flight measurement made by optical detectors spaced twelve inches apart in the free flight region between the gun exit and spinner adit. Since the calculated acceleration depends upon the square of this measurement [1], it is important that it be accurately measured. However the bird on occasion would rip out a piece of diaphragm which may trigger one or both of the photocell circuits producing measurements that are in error by as much as $\pm 5\%$ in a system with better than 1% expected accuracy. Therefore many erroneous readings were assumed to be proper. It was not until occasional velocity measurements produced gun efficiencies a few percent greater than expected from theory that a closer look revealed the problem. All measurements now are monitored by oscilloscope in such

a manner as to reveal when the trigger is improper and how much the time of flight must be corrected. Bird velocity measurements now for "vacuum" operation are reproducible to better than 1% for any bird and atmospheric pressure. (On a rainy, low pressure day, the birds are measurably slower than on a clear, high pressure day.)

Piezoelectric Accelerometer Measurements

Trailing wire techniques have been used in guns as long as 100 ft at the Harry Diamond Laboratories to make impact acceleration measurements. It was not until measurements were made in short vacuum guns [19,20] to verify predicted impact results that discrepancies were again noted. In these tests the wire is connected to the accelerometer before, during and after impact. The first difficulty that appeared was a random zero shift of the terminal base line sometimes positive, sometimes negative, of as much as 30% of the pulse amplitude (Fig. 8). This was traced to overloading of the shock amplifier by high

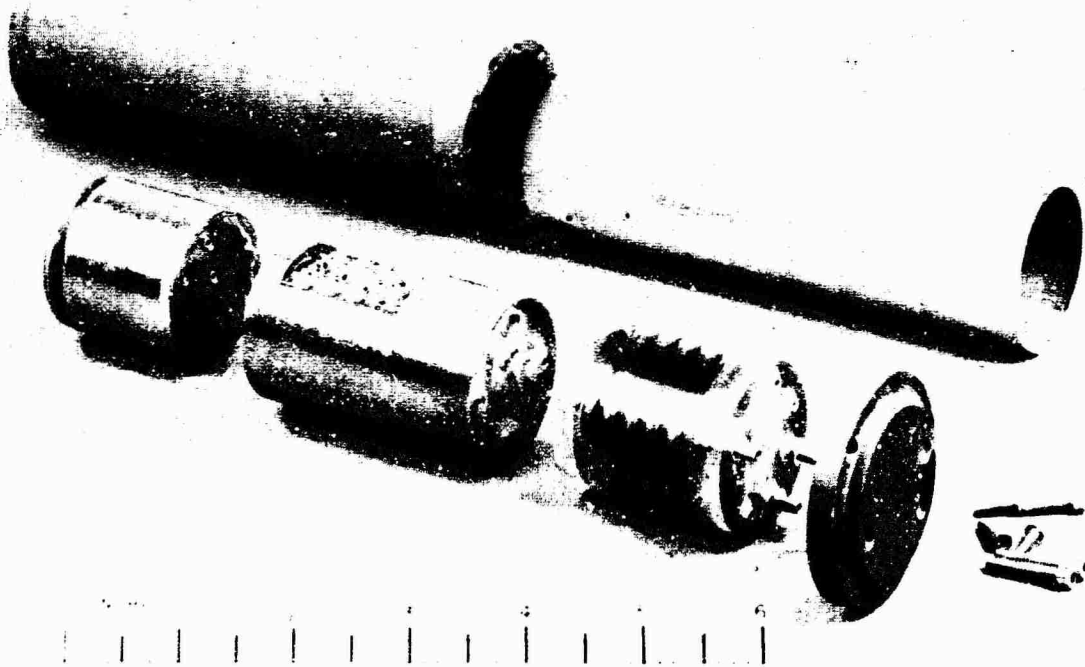


Fig. 7. Telemetry projectile.

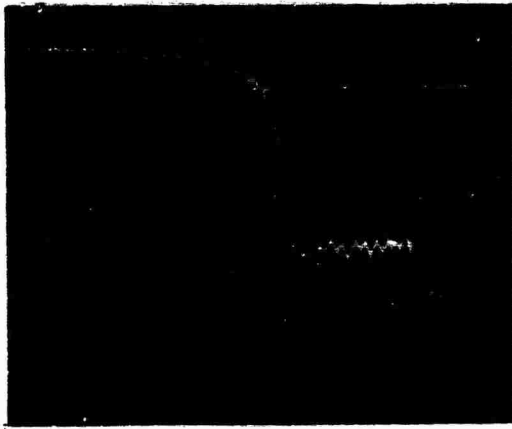


Fig. 8. Accelerometer signal. Note marked zero shift although overload is not indicated. (250 G/cm., 2500-G full scale, 4 khz Gaussian low-pass filter, 1-msec./cm.)

amplitude spikes that did not appear in the output signal. Although one manufacturer's literature discusses this, their overloading does drive the signal out of range. One way, to prevent the zero shift is to operate the shock amplifier on a much less sensitive range where there is no danger of overloading. If the system accuracy is 1% of full scale, operating on a scale that is 10 times larger than the signal to be measured immediately degrades 1% performance to 10%.

A second difficulty is that if we believe the acceleration calibration (as checked against a standard accelerometer) the integral of the acceleration pulse consistently produced velocity changes greater than actually measured [20]. However, if we assume that we should recalibrate our accelerometers based on velocity change [21], we are not able to reconcile it with shaker table calibrations. Matters are even more at odds if we compare the second integral of the acceleration pulse with the bird travel distance during impact. In this case, the discrepancy is even greater. However, whereas signal processing, i.e. electronic low pass filtering will not change the first integral of a pulse, it may change the second integral.

Therefore to eliminate electronic filtering, possible effects of transverse shock excitation, and other sources of spikes, we have recently undertaken an investigation of piezoelectric accelerometers encapsulated in putty as suggested by NOL [22]. Preliminary results have shown reduced noise, but whether we have really im-

proved our measurements is yet to be determined.

Photographic Measurements

A photographic technique using a high-speed framing camera has been devised to measure linear and angular displacements with time. From these data, velocity and acceleration can be computed. In this technique, a bird (Fig. 9) specially designed so that its tail extends out of the spinner during impact, was photographed. A high speed stroboscopic unit was slaved to the camera to freeze the projectile motion during each frame, to eliminate blur due to projectile motion. The resulting film was read on commercial digitizing equipment, and the punch card output, processed by computer. Typical results are shown in Figures 10-14. While the linear and angular displacement profiles appear very smooth (Fig. 10,11), first difference computations yielding velocities are noisy (Fig. 12,13). The linear acceleration data (Fig. 14) is noisier yet, and the angular acceleration data is too noisy to plot. The main difficulty is the inability to locate the lines in the frame accurately and precisely because of film graininess and reading-machine inaccuracies [23].

These data were obtained at about 6000 pps, actually 0.177 msec between frames. At this film speed, a 0.001-in. position error equals about 100 G. If the framing rate is slowed, the data is smoothed appreciably because the fractional displacement errors are decreased and the time interval which appears in the denominator in the differencing equations is increased. However, this is done at the expense of time resolution.

We are still attempting to develop this technique to reduce the noise, and we are getting data from it. One noteworthy item concerns the angular velocity. The acceleration pulse takes place between 1 and 4 milliseconds (Fig. 14). If you examine the angular velocity curve (Fig. 13), the bird goes from 0 to 16 rps in this time and continues to increase, but at a much lower rate for the duration of the data. The actual spinner speed on this shot was 50 rps. Since angular momentum must be conserved during impact, any increase of bird angular velocity will cause some decrease of mean angular velocity. But this does not account for this great difference in velocities. Actually the torque generated in the mitigator (about 100 ft-lb) is suffi-

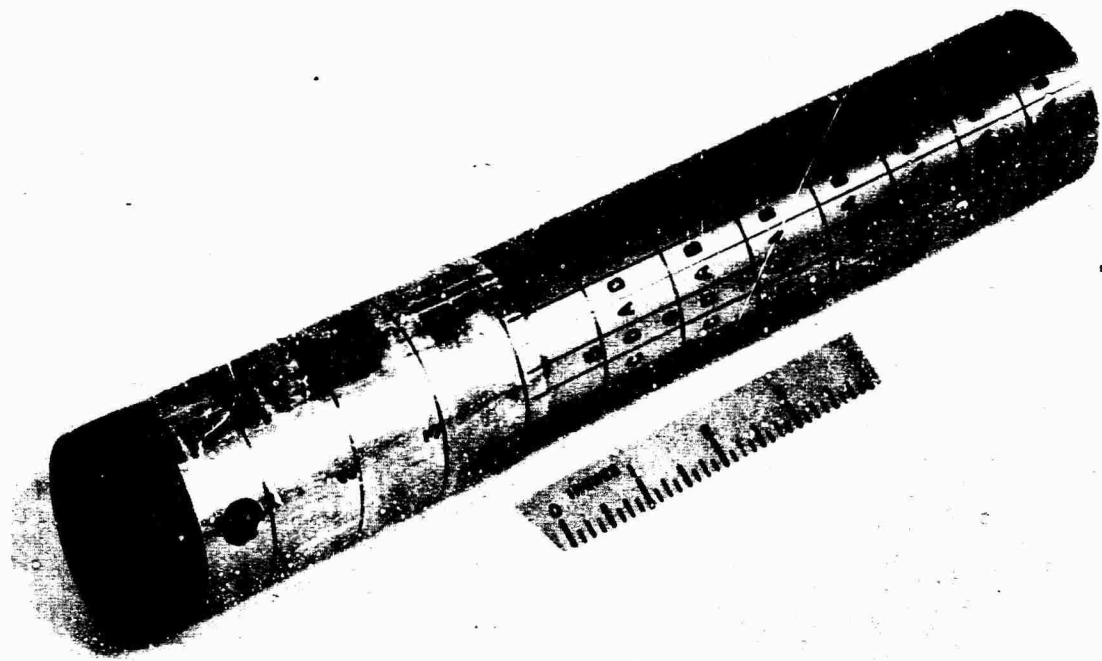


Fig. 9. Projectile for photographic measurements.

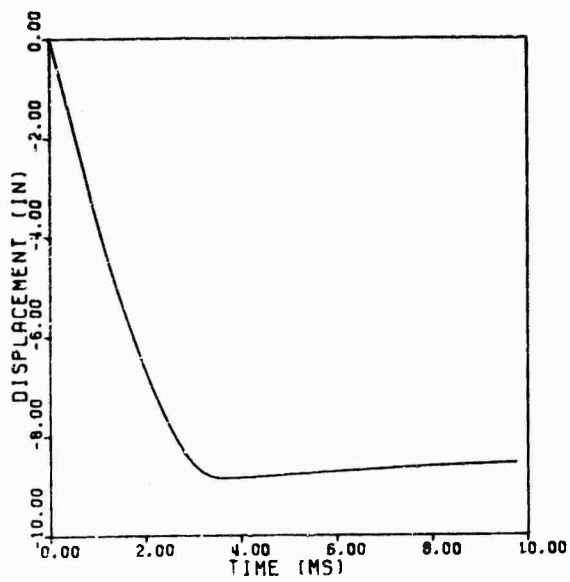


Fig. 10. Linear displacement profile.

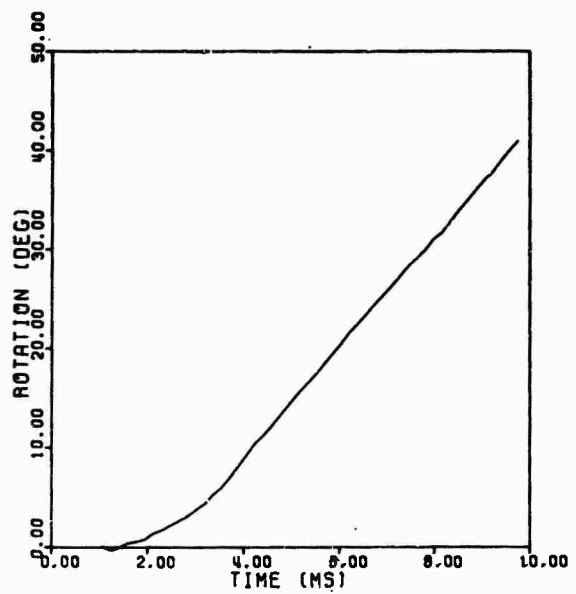


Fig. 11. Angular displacement profile.

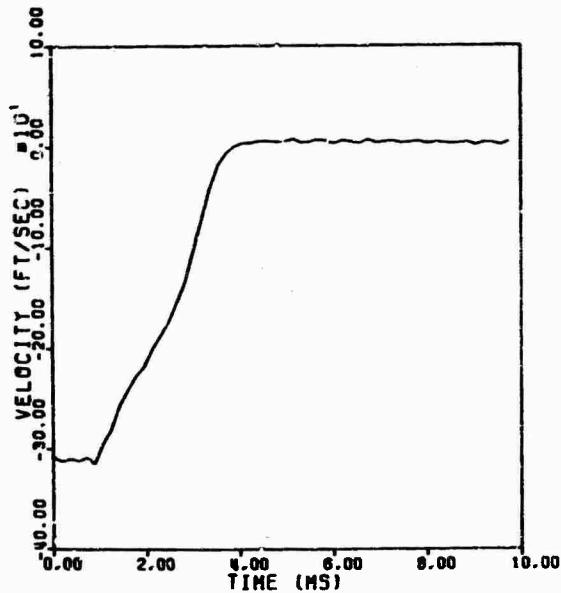


Fig. 12. Linear velocity profile.

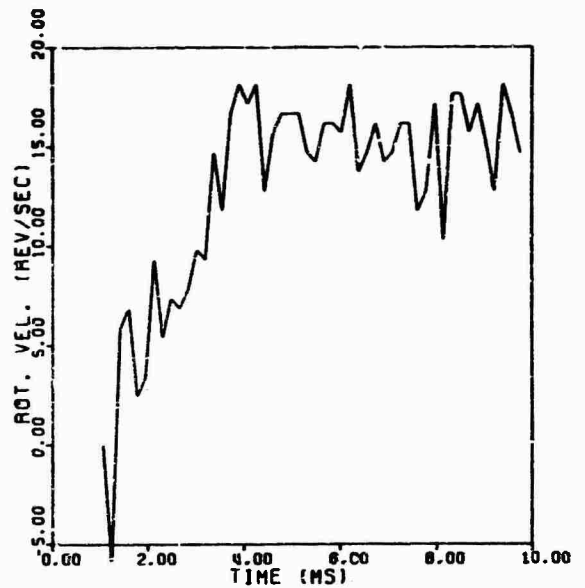


Fig. 13. Angular velocity profile.

cient to cause it to twist. Note the twist in the crushed honeycomb in Fig. 5. Therefore those mitigators with the highest shear strength will not only produce the greatest angular accelerations but will also produce a higher angular velocity during impact. The rate at which the bird achieves the velocity of the spinner after impact depends on friction and clearance. Generally (although not on this shot), steel pins are attached to the bird nose. These pins dig into the mitigator which then remains attached to the bird. Since the crushed mitigator is a tight fit in the spinner this secondary spin acceleration is increased.

Optical Angular Displacement Transducer

A new optical device being developed for angular displacement (velocity, acceleration) measurements operates as follows (Fig. 15): A small retroreflector is fitted to the rear of the projectile. The retroreflector contains two lenses and a reticle. The reticle pattern consists of 24 alternate transparent and reflecting sectors. When collimated light enters the retroreflector, a focused spot of light is formed on the reticle. Light is returned only when the focused spot falls on a reflecting sector. Thus, the return beam is amplitude-

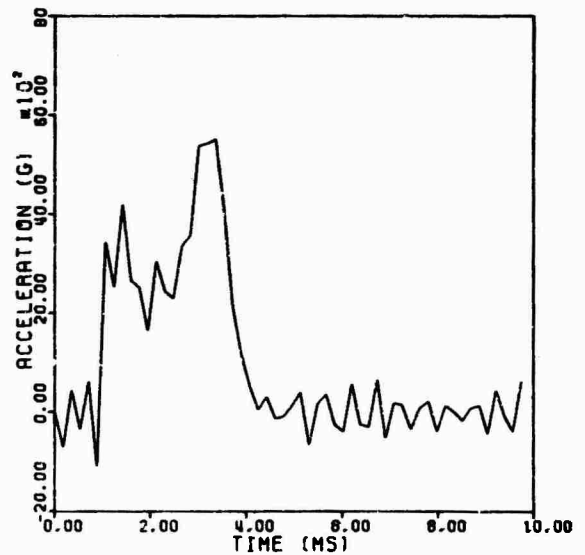


Fig. 14. Linear acceleration profile.

SENSOR BOX

RETROREFLECTOR

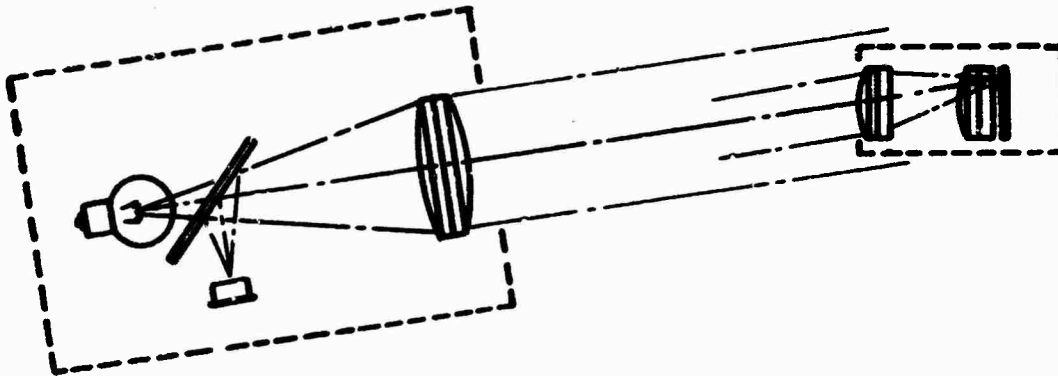


Fig. 15. Optical angular-deflection measuring system.

modulated at a frequency directly proportional to the spin rate of the projectile.

The collimated light is formed by a small incandescent lamp and a lens. These components are mounted in the sensor box along with a beam splitter, photodiode, and a transistor amplifier. The sensor box is mounted to one side of the gun muzzle, and the collimated beam illuminates the projectile as it enters the spin-catcher. The modulated return beam is collected by the sensor box lens. A portion of this light is diverted to the photodiode by the beamsplitter.

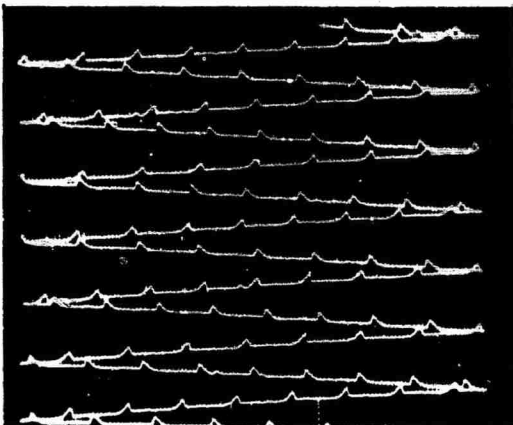


Fig. 16. Raster output from angular-deflection system.

The amplified output is displayed on a raster-type oscilloscope together with appropriate timing marks to obtain accurate time measurements (Fig. 16). The timing marks are 100- μ sec apart with every tenth timing mark accentuated. During this test the retroreflector was mounted on the shaft of a 30-rps motor. One revolution of the motor shaft corresponds to 24 signal pulses.

If this technique should prove useful, its use can be extended to the field. If the retroreflector (Fig. 17) (1-cm diameter by 2.3-cm long) is mounted on the nose of a projectile, readout of angular position data can be directly related to linear position data (if there is no rifling slip). Therefore, the device can be used as an accelerometer for artillery weapons.

TABLE-TOP TESTERS

One method of increasing the safety of a fuze component is to have it activate only when influenced by multiple environments. The three predictable environments which produce the greatest force in artillery field fuzes are linear, angular, and centrifugal accelerations. New fuze components which require two or three of these environments were sometimes difficult to test and often required artificial modification to determine if a production run was acceptable. For this reason, the Artillery Simulator techniques

were applied to "miniature" testers to determine if a table top tester (Fig. 18) capable of velocities of 100 ft/sec could reproduce that portion of the environment necessary for determining activation levels and/or performance of fuze components.

Two fully automated testers were developed for use with components for a particular fuze [3,4]; however, their utility extends to other components as well. One of the testers is for testing safety-and-arming mechanisms and requires acceleration, impact velocity, and spin rate control to determine sensitivity. The mitigator used is aluminum honeycomb, which we have found to be very uniform, and it lends itself to a simple acceleration calibration procedure [20]. In operation this device takes about 20 seconds for a shot, and up to four temperature-conditioned units can be tested per shot. Test rates in excess of 400 per hour are readily achievable. The operating cost of the unit outside of operator cost is mainly the cost of the honeycomb. All the operator is required to do is remove the used honeycomb and bird, insert new honeycomb, change the diaphragm, insert a new bird, and press a button.

The second class of tester is

for power supply performance. It was desired to provide sufficient signature to activate the device. Absolute control was not necessary since the main concern was with the electrical characteristics of the power supply after activation. This tester required hard-wire readout and the running time is determined by the life of the power supply, which often exceeds two minutes. Therefore test rates are about 25 units per hour. However, the cost of the honeycomb as well as the inconvenience of having to use a new piece each shot has been eliminated by the development of a hydraulic reusable mitigator mem combination (Fig. 19). The device which is akin to a dashpot or shock absorber is unique in that by varying the density of the oil used or the contour of one piece, acceleration amplitude and profile can be controlled [24]. Aside from the operator, who no longer has to worry about honeycomb, the main cost of the operation of the power supply tester is for diaphragm material. Both types of testers have automatic pumpdown, spinner control, firing, mem reloading, and projectile ejection.

ADVANTAGES OF THE ARTILLERY SIMULATOR TECHNIQUE

We realize that we cannot hope

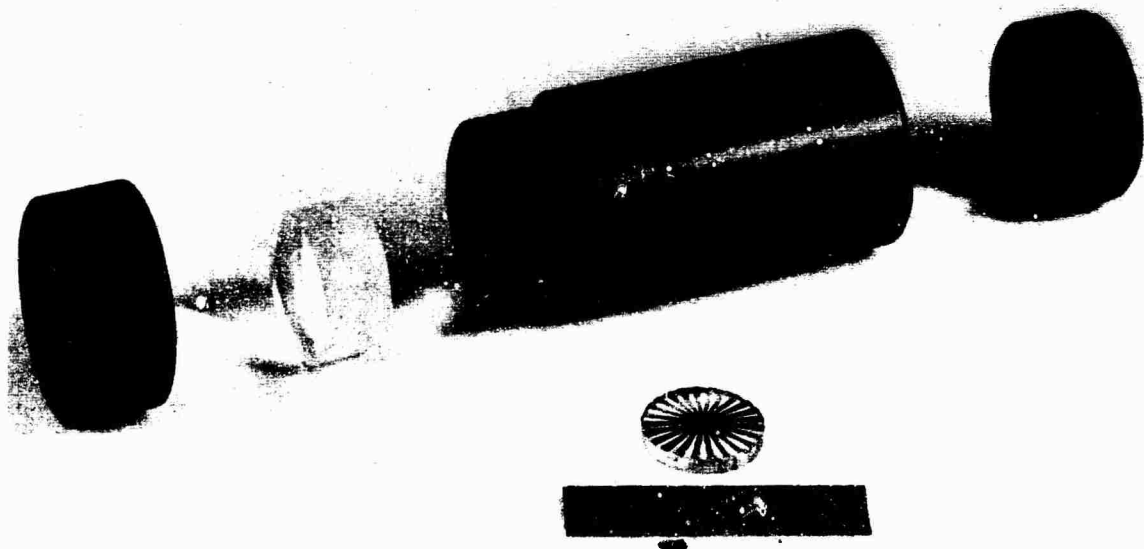


Fig. 17. Retroreflector for angular displacement measurement.

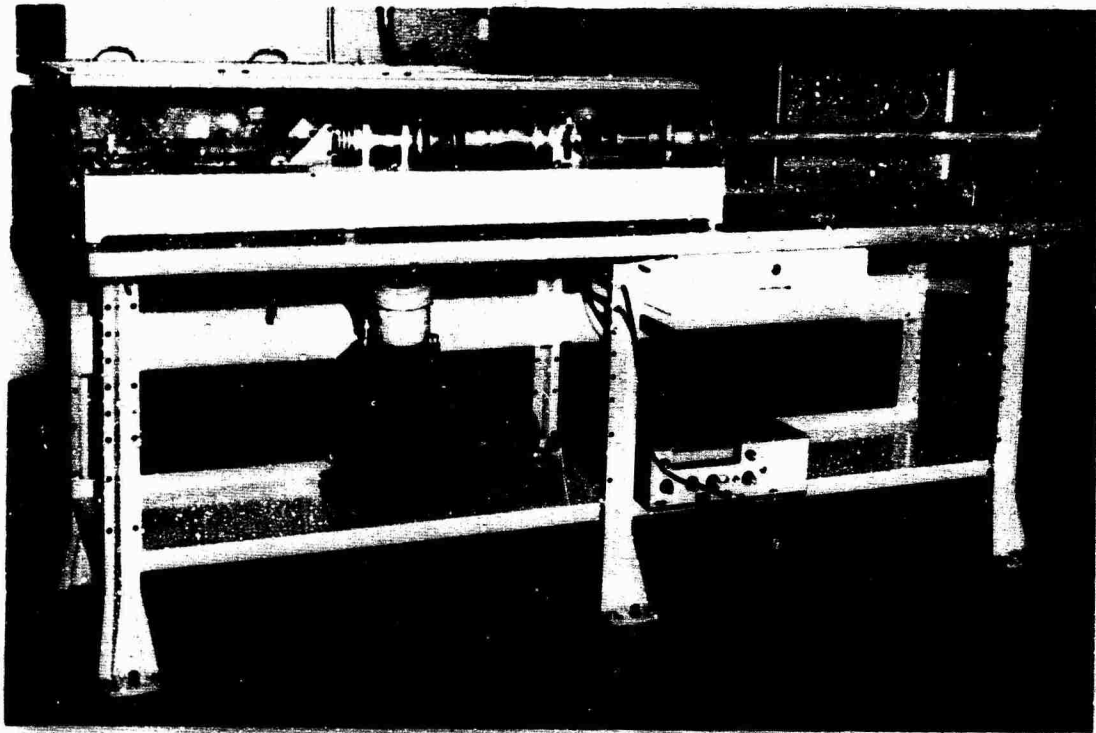


Fig. 18. Table-top tester for power supplies.

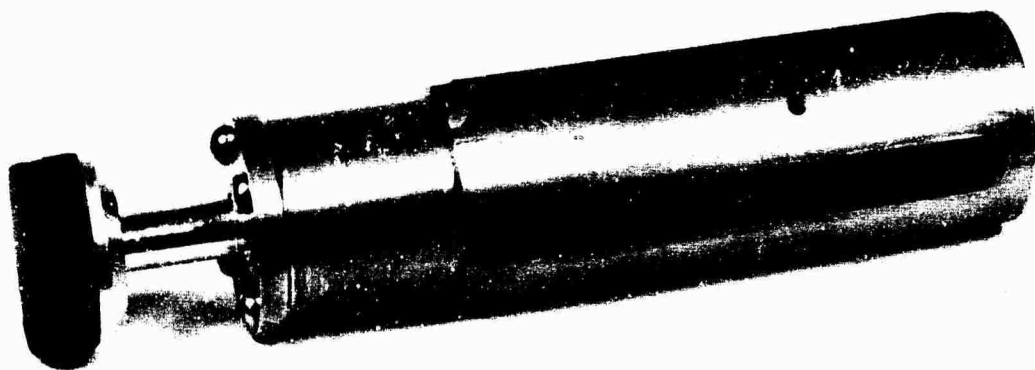


Fig. 19. Hydraulic mitigator-mem for use in table-top tester.

to reproduce artillery weapon firing. We can do things for the fuze designer, however, which in some cases are equivalent or superior.

As evidenced by correlation with field tests, we can control our acceleration amplitude up to 5000 G quite well. Our duration is limited so that its product with the acceleration yields a velocity of less than 600 ft/sec. This coupled with spin up to 130 rps allows excellent simulation of the 4.2 spin mortar and some of the howitzers when fired at low charge. Most of our testing concerns fuzes that must perform under these "minimum" conditions, which we can effectively reproduce.

We can monitor (when required) three separate channels of information via hard wire within 30 millisecond after impact or via telemetry before, during, and after impact. We can reuse our telemetry unit over and over again.

We can test components within minutes after they are removed from their temperature bath.

Recovery is 100% and immediate. This is especially important when devices malfunction. For example if a power supply gives reduced output, the test is terminated, and an immediate post mortem is performed. The cause of the failure which is usually chemical in nature can be observed. By the time the shell is recovered in a field test the chemistry will have gone to completion, i.e., all possible reactions would have taken place and the reason for failure would be obscured.

We have only one high acceleration pulse. To examine fuzes after firing in a field test, some recovery method must be utilized to recover the fuze for inspection. The two most common methods, vertical recovery and parachute recovery, both involve second acceleration pulses. The round impacts the ground in vertical recovery and the fuze is blown out of the round in parachute recovery. These secondary accelerations may lead to damage or reactions which may mask the reason recovery was required. Since we have only one sizeable acceleration, no such confusion is possible in the simulator tests.

The simulator has a low operating cost, simplicity, and speed of operation. The cost associated with equipment use is from \$1 to \$15 per shot

depending upon the nature of the instrumentation required. Because the equipment is very simple and safe to operate, any fuze engineer who will be using the equipment, and so desires, is instructed in the operation so that he can run his own tests. This allows us more effective utilization of personnel since the fuze engineer usually is an observer anyway. Setup time is usually about 15 minutes but will be significantly less if many shots of the same type are made. Cost of field tests when recovery and telemetry are involved are many times as high.

We have no scheduling problems. Because of the rapidity at which tests can be performed we have never had waiting lines. We are not at the mercy of the weather, and we keep a large supply of mitigator materials to accommodate our users.

The table-top tester provides limited but often useful simulation. For a modest investment of funds, depending upon the instrumentation required, a table-top tester can be built that is very simple to operate and can be placed anywhere in a laboratory where 3 x 10 feet of space is available.

AREAS FOR FURTHER DEVELOPMENT

While we have had considerable success with our present facility, we are aware of several deficiencies. Some can be corrected by engineering redesign, and others require considerable investigation.

1. Larger Bore Gun

Most fuzes are somewhat over two inches in diameter, some as much as five inches, therefore a larger bore facility would add considerably to the utility of the device.

2. High Speed Spinner

The present spinner attains speeds over 120 rps but this is only one third the spin needed to test fuzes at the extreme artillery environment. Increased bore size complicates this problem since the bearings must be larger than the bore. Another problem is the effect of the mitigator, mem, and bird on the dynamic balance of the spinner. This entire problem is currently being investigated, and hopefully will result first in a table top tester capable of 360 rps, and, subsequently, in a larger version for the simulator.

3. Extension to Howitzer Environments

To extend the facility to larger weapon environments we must redesign our spin-catcher to a size that is somewhat larger than the barrel of the weapon we want to simulate and we must provide impact velocities comparable to the weapon muzzle velocity. Combined with the requirement that the gas gun acceleration must be small compared with impact deceleration leads to the conclusion that a much larger installation is required. Because in gas guns velocity efficiency decreases with velocity, we must increase the length even further. Therefore, for an ability to fire birds at 1500 ft/sec at moderately low accelerations (200 G max) a gun, 250 ft long, using a helium driver, will be required (From [1] Fig. 14). An air-driven gun would be 500 ft long. The ideal gun need only be 175 ft. Such an installation is impractical at our Washington, D. C. Laboratories and a suburban location would have to be used.

4. Better Simulation Profiles

As our instrumentation tech-

niques are perfected, we will be able to make more quantitative measurements of linear and angular acceleration profiles. This will provide us with mitigator performance data which we in turn will use to tailor the profile. However, actual acceleration time histories for many weapons do not appear in the literature. The best source of calculated data [25] must be our guide.

SUMMARY

The Artillery Simulator after four years of continued use and development has proven to be a very effective, reliable, and inexpensive simulator of the low end of the artillery environment. Table top simulators and this simulator are being used to test fuze components in production and in the laboratory. There is still much to be done on instrumentation and in extending the simulation to higher spin rates and longer acceleration durations. However, these problems are being attacked, and, hopefully, their solution will permit construction of a superior facility.

LITERATURE CITED

1. H. D. Curchack, "An Artillery Simulator for Fuze Evaluation," HDL Report TR1330, Nov. 1966.
2. H. Martin, "Construction Details of HDL Artillery Simulator (Prototype)," HDL Report TR1356, Aug. 1967.
3. "Dynamic Environment Test Position for M514A1E1 Fuze Power Supply Test Equipment Manual," HDL Manual TL-EM-89-8, Feb. 1970.
4. "Dynamic Environment Test Position for M514A1E1, Fuze Projectile Booster Assembly Test Equipment Manual" HDL Manual TL-EM-89-7, Nov. 1969.
5. H. J. Davis, "Impact Testing Using a Four Inch Air Gun and Lead Targets," HDL TR1383, 1968.
6. S. T. Marks, "High g Component Test," Ordnance, pp. 386-388. Jan-Feb, 1968.
7. V. F. DeVost, "NOL Copper-Ball Accelerometers," NavOrd Report 6925, Nov. 1960.
8. A. S. Zhmur et al "Single Action Accelerometers," Mechanical Measurements, 12, 997, 1963.
9. V. F. DeVost, "NOL Copper Ball Accelerometers," NOL TR63-279, Feb 1966.
10. "Energy Absorbing Characteristics of Several Materials," Report SCTM 284-57 (51) Sandia Corp., Livermore, Calif. 1960.
11. R. M. Morrison, "Momentum Transfer Method for High Shock and Acceleration Testing, Using Aluminum Honeycomb," SCTM 18-60-81, June 1961.
12. P. S. Brody, "Strong Shock Waves in "Polled" Barium Titanate Ceramic Elements," DOFL Report TR869, Oct. 1960.
13. A. H. Shapiro, "The Dynamics and Thermodynamics of Compressible Fluid Flow," Ronald Press, New York, 1953.
14. A. E. Seigel, "The Effect of the Optimum Chambrage on the Muzzle Velocity of Guns with a Qualitative Description of the Fundamental Phenomena Occuring During Gun Firing" NavOrd Report 2691, Oct. 1952.
15. A. E. Seigel, V. C. D. Dawson,

- "Results of Chambrage Experiments on Guns with Effectively Infinite Length Chambers," NavOrd Report 3636, April 1954.
16. A. E. Seigel, "The Theory of High Speed Guns," AGARDograph 91, NATO, May 1965.
 17. M. G. Otten, "Projectile Efficiency Investigation for Two-Inch Artillery Simulator Using an Air Driver," HDL Student Trainee Technical Symposium, In Publication, Aug. 1970.
 18. F. M. Carson, "Precision Telemeter for Use During High Shock," HDL. In preparation.
 19. Ira Smith, "Piezoelectric Accelerometer Instrumentation for Gas Guns," HDL TM-68-29, Oct 1968.
 20. D. Lanigan, "Correlation Between Measured and Computed Deceleration for a Honeycomb Energy Absorbing System," HDL TR1488 (Late 1970).
 21. R. R. Bouche, "The Absolute Calibration of Pickups on a Drop-Ball Shock Machine of the Ballistic Type," pp. 155-121, Proc. IES, 1961.
 22. V. F. DeVost, P. S. Hughes, "Piezoelectric Accelerometer Signal Error in Complex Shock Recordings," NOL TR 67-194, Dec. 1967.
 23. J. R. Woodside, Jr., "Artillery Simulator Kinematics: A High Speed Motion Picture Study," HDL Student Trainee Technical Symposium, In Publication, Aug. 1970.
 24. S. Katz, H. D. Curchack, "Hydraulic Shock Absorber for High Acceleration Testing," HDL Report in Preparation.
 25. L. D. Heppner, "Special Study of Setback and Spin for Artillery, Mortar, Recoilless Rifle and Tank Ammunition," Report No. DPS-2611, Jan 1968.

* * *

DISCUSSION

Mr. Herzing (Honeywell Ordnance): What was the amplitude scale factor for the acceleration time-history plots that you presented.

Mr. Curchack: It was t.n. Our computer plotter gives figures and then multiplies by ten.

Mr. Herzing: So it was 5600 g's?

Mr. Curchack: It was roughly 5600 g's peak at the end. We have tested as high as 15,000 g's with spin. Without spin we have gone up to 40,000 g's but we do not use a spin catcher, we use an open impact device.

GAS SPRING FIRING AND THE SOFT RECOVERY OF A HARD-WIRE INSTRUMENTED 155 MM PROJECTILE*

By

S. L. Fluent
Heat, Plasma, Climatic, Towers Division,
Sandia Laboratories, Albuquerque, New Mexico

This paper discusses a technique used in testing hard-wire instrumented 155 mm projectiles. An 18-inch pneumatic actuator was used as the energy source while a gas spring was used to transmit the energy to the projectile and shape the longitudinal acceleration pulse. The projectile was accelerated through a short section of rifled gun barrel to produce angular acceleration simultaneously with the longitudinal acceleration. The projectile was stopped in a tapered recovery tube which was free to slide on a set of rails. This soft recovery system prevented further damage from occurring to the components inside the projectile after the initial acceleration pulse. A discussion on field testing versus gas spring testing is also presented.

INTRODUCTION

In the past there has generally been but one way to test 155 mm shell components in an environment of combined longitudinal and angular acceleration. This method has been to actually fire a projectile containing the components in a 155 mm gun. The actual firing has given the best test to the components as far as the environment is concerned, but there have been some drawbacks. First, full-scale field testing has generally been quite expensive. Second, until the recent development of the parachute recovery system, it has always been questionable whether or not the projectile would be recovered to permit inspection of any damage that might have occurred. If it was recovered, it was difficult to determine whether firing or impact caused the damage. Another drawback has been projectile instrumentation. Although there have been attempts to use hard-wire instrumentation of a projectile during firing most attempts failed while others were only partially successful. P. S. Hughes and L. A. Vagnoni [1] at the Naval Ordnance Laboratory at Silver Spring, Maryland,

developed a method to monitor the leading edge of the acceleration pulse associated with a 5-inch projectile. Telemetry also has offered a possible way of obtaining instrumentation data from the projectile. In spite of formidable difficulties, data has been successfully transmitted out the gun barrel during firing. Most of the data gathered in this manner has had the problems of high frequency response limitations.

Because of the foregoing problems, Sandia Laboratories built a facility that would simulate the effects of a portion of the acceleration conditions associated with a 155 mm gun firing; namely, the setback acceleration which included both the longitudinal and angular acceleration but not the radial acceleration. No attempt was made to simulate the effects of radial acceleration with the setback conditions because in an actual gun firing the maximum longitudinal acceleration and the maximum radial acceleration do not occur simultaneously. Hard-wire instrumentation with high frequency response and a soft recovery of the projectile were two capabilities that were designed into the facility.

* This work was supported by the United States Atomic Energy Commission.

FACILITY DESIGN

It was determined at the outset that simulation of the setback acceleration would require a large amount of energy. To bypass the expense, time, and effort of building a completely new facility, it was decided to modify an existing one. The one chosen was an 18-inch pneumatic actuator which would deliver approximately a half million foot-pounds of energy.

The 18-inch actuator was capable of generating velocity changes up to 300 feet per second, but the corresponding accelerations were low in comparison to the setback acceleration of the 155 mm projectile. Previous work [2], however, showed that with the addition of a gas spring to the actuator higher velocity changes with very high accelerations could be achieved. A diagram of the gas spring assembly is shown in Fig. 1. To provide a column of gas to be used as the spring,

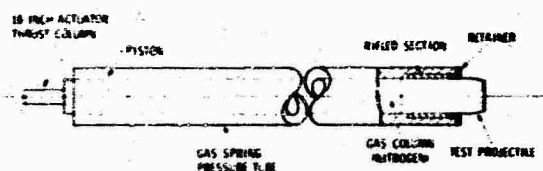


Fig. 1 - Gas Spring

a high-strength steel pressure tube was fitted with a piston at one end and a short section of rifled gun barrel with a projectile pressed into it at the other end. This left a column of gas in the middle which could be initially pressurized to provide various spring characteristics. The rifled section served two purposes. The main purpose was to provide the projectile with the angular acceleration associated with the longitudinal acceleration in an actual gun firing. The second purpose was to lock the projectile in place until the high pressure was built up in the gas behind it. A hydraulic press was used to pre-engage the projectile so that friction alone was enough to hold the projectile in place.

In this application the thrust column of the 18-inch actuator was used to accelerate the piston in the gas spring to a predetermined velocity. As the piston left the thrust column and moved down the tube, it compressed the column of gas ahead of it until the pressure was built up sufficiently to overcome the friction and to accelerate the projectile through the rifled section. Upon leaving the

rifled section, the projectile entered a free moving, tapered recovery tube and, by means of a momentum exchange using a wedging action, slowly came to rest. Because of the selected mass ratio between the piston and the projectile, the piston continued out of the gas spring tube with a low velocity and either fell to the floor or entered the recovery tube and stopped some distance from the projectile.

GAS SPRING DESCRIPTION

The tube used for the gas spring was 6-feet long with an outside diameter of 10 inches and an inside diameter of 6 inches. The high-strength steel tube was machined on one end to accept an 8-inch length of 155 mm gun barrel that had been machined to an outside diameter of 8 inches. A retainer, bolted to the end of the gas spring tube, was used to hold the rifled section in place.

Fig. 2 shows the rifled section and its retainer. A series of steel pistons of different weights, shown also in Fig. 2, was used in conjunction with various piston velocities

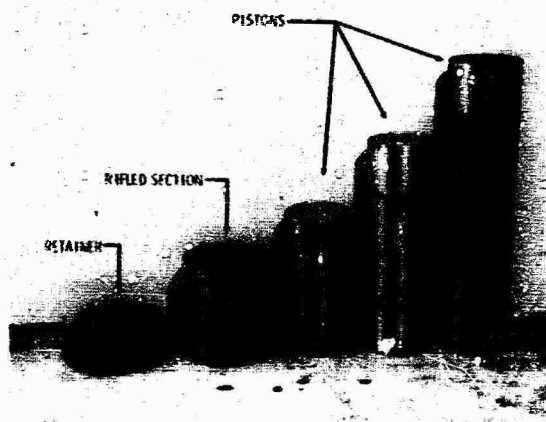


Fig. 2 - Gas Spring Hardware

and initial gas spring pressures to vary the shock pulse characteristics. The mathematical expressions relating the different setup and control parameters have been developed in the Appendix. The three pistons shown weighed 100 pounds, 150 pounds, and 200 pounds. Each piston was fitted with O-ring seals to contain the pressure built up ahead of it in the gas spring as the piston moved down the tube. A set of four runners was also fastened to the gas spring tube so that it could be positioned on the existing rail system in front of the thrust column of the 18-

inch actuator and still be moved easily. An overall view of the test setup is shown in Fig. 3.

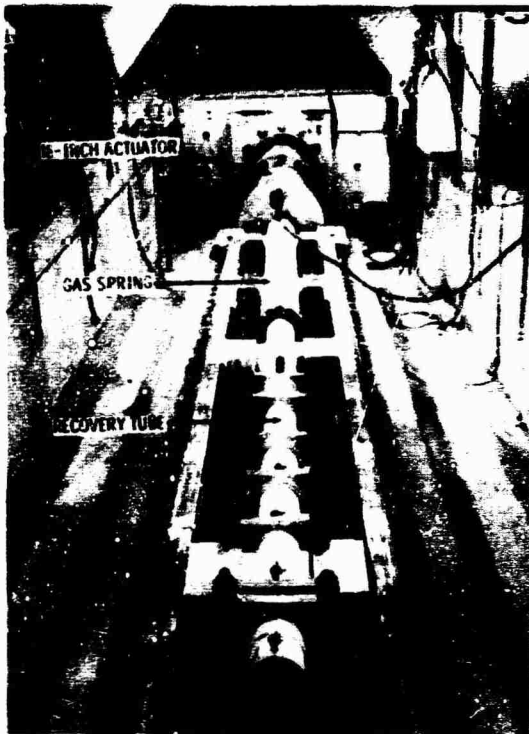


Fig. 3 - Overall View of Test Setup

PROJECTILE DESCRIPTION

The projectile used for each test was an empty 155 mm illuminating round as shown in Fig. 4. The base plate was machined so that it could be fastened to the wall of the projectile with bolts, and the ogive portion of the shell was cut off to allow for hard-wire instrumentation. The rotating band of the projectile was also prescored by pressing the shell into the short rifled section until the band was fully engaged. The inside cavity of the projectile was used for mounting the components to be tested. The components could be mounted in one of three ways--to the base of the projectile, to the wall of the projectile, or encased in some type of potting material that filled the entire cavity of the projectile. It was found that some types of potting materials generated a voltage when exposed to the acceleration shock which could cause zero shift to occur in the recording electronics. (This phenomenon is known as the triboelectric effect.) As a result, this method received minimal use.

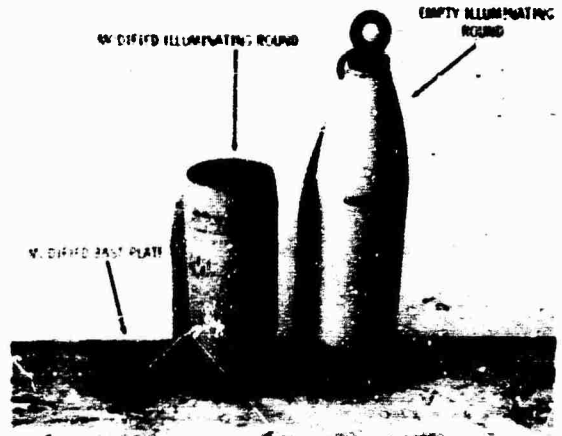


Fig. 4 - 155 mm Projectiles

Fig. 5 shows a typical projectile ready to be tested. The weights of the projectiles varied considerably, but most weighed between 50 and 75 pounds.

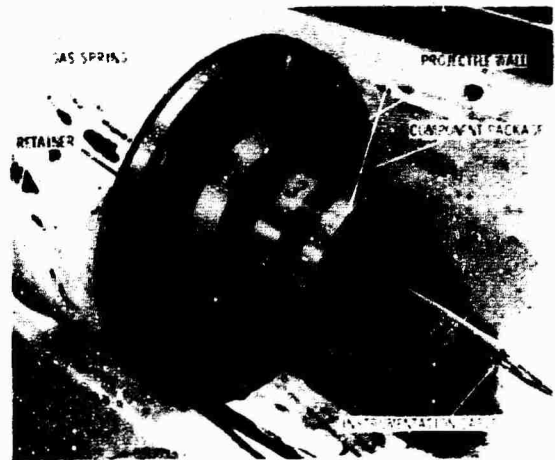


Fig. 5 - Test Projectile

RECOVERY TUBE DESCRIPTION

A method of recovery was designed such that when the projectile was fired from the gas spring, it was decelerated and recovered with no further damage to the components being tested. The method used was a momentum exchange technique. The tube shown in Fig. 6 was used to slow the projectile down. It was

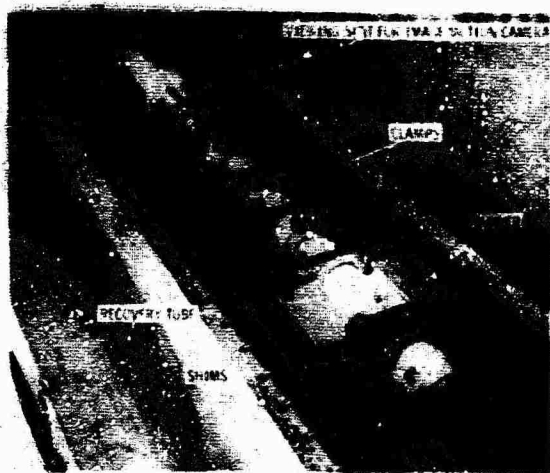


Fig. 6 - Recovery Tube

made from a 10-foot length of stock steel tubing with an inside diameter of 6.25 inches and an outside diameter of 7.50 inches. A half-inch slot was cut in the tube for a distance of 8 feet so that when it was clamped together again it formed a tapered tube. A set of runners was also fastened to this tube to allow it to slide freely on the rail system when the projectile was fired into it. The momentum of the projectile was transferred to the recovery tube through the wedging action in the tapered portion of the tube. Various combinations of lead and steel shims under the clamps provided a gradually increasing stopping force to the projectile as it moved farther into the tapered portion of the recovery tube. Because of the selected mass ratio between the recovery tube and the projectile, the tube acquired only a low velocity from the momentum of the projectile and was allowed to slide along the rails until it was finally stopped by the friction force between the runners and the rails. The maximum faired deceleration experienced by the projectile while stopping was measured at less than 5 percent of the maximum faired acceleration during the initial part of the test.

HARD-WIRE INSTRUMENTATION

One of the capabilities designed into the facility was to provide hard-wire instrumentation on the test projectile. The instrumentation cables were brought out the nose of the projectile and suspended so that the projectile would gather the wires as it was accelerated.

Data has been obtained for times from 4 milliseconds to as long as 500 milliseconds, depending on the requirements of the test and

the distance in which the instrumentation cables had been suspended in front of the projectile. Types of data recorded included acceleration input and response signatures from various points within the projectile and the pressure in the gas spring behind the projectile. The foregoing data was in addition to anything required by the components being tested. Image motion photography was used as one means of determining the velocity of the projectile, which provided a check on the velocity change under the input acceleration-time signature.

A quartz accelerometer, rated to 100,000 g (checked to 50,000 g) was used to monitor the acceleration level of the projectiles. The mounted resonant frequency of the accelerometer was 60 kHz. A high frequency fidelity check was performed on the rest of the electronic system to show that it was capable of accurately recording frequencies to 140 kHz with amplitudes as high as those present during a test.

Data from the projectile has been obtained using hard-wire instrumentation, making possible 1 MHz data recording for 15 milliseconds and 80 kHz data recording for as long as needed. The number of channels of information has been limited only by the size of the bundle of wires extending from the projectile and the channels of recording electronics available.

CAPABILITIES

From the energy available from the 18-inch actuator, velocity changes on the 155 mm projectile of up to 375 feet/second have been generated. The longitudinal acceleration experienced by the projectiles has ranged from a pulse of 5,500 g maximum faired peak (MFP) with a duration of 3.6 milliseconds (at the 10 percent level) to a pulse of 47,000 g MFP with a duration of .17 millisecond (10 percent level). A typical pulse for component testing might be from 10,000 g MFP with a duration of 1.65 milliseconds (10 percent level) to 16,000 g MFP with a duration of 1.05 milliseconds (10 percent level).

Figure 7 shows an 80 kHz data playback record of a typical test pulse. The theory developed for the ideal situation was found to predict the rise time of pulses adequately (within ± 10 percent). However, since the gas spring is a highly nonlinear spring and the magnitude of the acceleration pulse is very sensitive to small changes in the piston velocity, calibration shots with repeatable setup

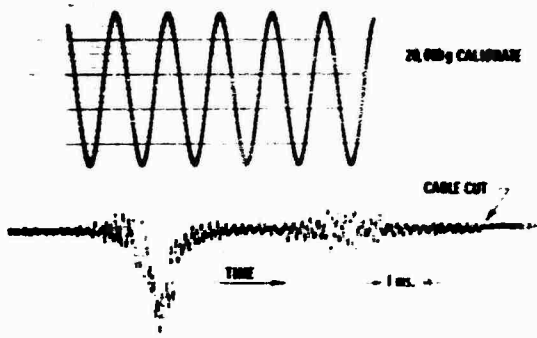


Fig. 7 - Typical Acceleration-Time Signature

conditions were also required to produce accurate, specified test pulses. For a given test requirement, the amplitudes of the pulses were repeatable within an error of ± 10 percent.

FIELD TESTING COMPARED TO LABORATORY TESTING

The question that arises in any laboratory test is: How well does it simulate the environmental conditions of the field? Not only that, but what criteria is used to determine the validity of the laboratory test? It was decided that shock spectra should be used to compare longitudinal and angular acceleration of the gas spring firing of a 155 mm projectile to that of an actual gun firing. To do this, a longitudinal acceleration pulse was obtained from an actual field test so that a shock spectrum could be made of the pulse. Likewise, a typical faired shock pulse from the gas spring testing technique with a similar amplitude was analyzed and compared to the field test data. The shock signatures compared are shown in Fig. 8 while their respective shock spectra appear in Fig. 9. It can be seen that even though there was nearly an order of magnitude difference in the pulse durations, the effect of the two shocks to any single, undamped, linear spring mass component within the projectile with a natural frequency above 3 kHz was very nearly the same. In fact, had the amplitude of the gas spring pulse been the same as the field pulse, the results of the comparison would have been even closer.

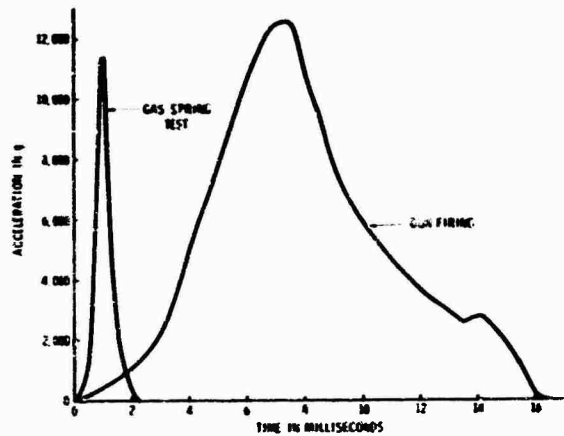


Fig. 8 - Acceleration Shock Signatures

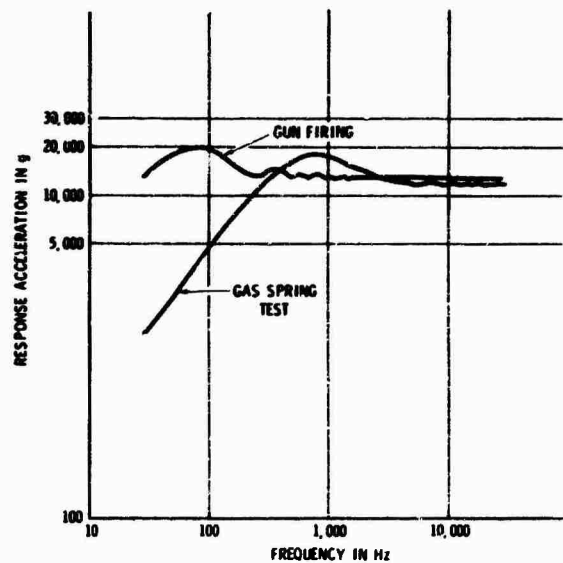


Fig. 9 - Shock Spectra

Another interpretation of Fig. 8 and Fig. 9 is that any component having a natural frequency greater than 4.5 kHz is only sensitive to the amplitude of the applied shock, provided the base line duration of the pulse is at least 2.2 milliseconds. Fig. 9 also indicates that for components having a natural frequency between 300 Hz and 4.5 kHz the gas spring pulse with the same amplitude as the field pulse would be an overttest. Likewise, the gas spring pulse would be an undertest for components with natural frequencies below 300 Hz. However, the peak-to-peak

deflection involved with a component having a natural frequency of 300 Hz is 2.4 inches for an acceleration level of 11,000 g, which implies that such a natural frequency is unlikely to occur in the 155 mm projectile. On the other hand, the peak-to-peak deflection of a component with a natural frequency of 4.5 kHz with the same acceleration level is 0.011 inches. Therefore it can be concluded that the gas spring test is valid for faired longitudinal and angular acceleration environmental tests involving components with natural frequencies of 4.5 kHz or higher.

It should be noted that both shock signatures in the above comparison had no high frequency vibration superimposed on the main pulse. The reason for this was briefly mentioned earlier. There was no high frequency data available from an actual gun firing since hard-wire instrumentation has not been used successfully for the total duration of the pulse. Consequently, the vibration superimposed on the gas spring pulse was faired so that two similarly smooth pulses could be compared. The pulse from the field test was filtered to 300 Hz. From the results of the gas spring tests, it is believed that there is a significant amount of vibration present in the components of a 155 mm projectile during a gun firing which can only be recorded by high frequency response instrumentation.

Component testing in the past has in general used nothing but clean input pulses, which may be adequate only if a similar environment exists in an actual gun firing. However, from what has been learned from the gas spring tests, there is reason to believe that much of the vibration recorded is due to inherent natural frequencies within the projectile itself. Therefore, the frequencies and amplitudes recorded during a gas spring firing may be similar to those of an actual gun firing. Since there is so little known about the high frequency vibration and its effect on the components, future work is planned to study this area.

REMARKS

The general testing technique outlined has the capability of being extended to other projectiles besides the 155 mm projectile. The gas spring and the rifled section could be designed for any number of other projectiles. The main consideration would be the amount of energy available to shape the acceleration pulse by the momentum exchange between the piston and the projectile. A wide latitude in selecting the characteristics of the pulse demands a large amount of energy. For this reason, future work has been planned on the existing test setup in the area of energy generation. One system to be investigated will be a piston that carries a very high pressure reservoir that will be released at a point where the piston would normally attain its maximum velocity. Other energy generation systems to be investigated would include modifications to the 18-inch actuator.

Future work has also been planned in the area of theoretical prediction of the results. Specific points to be investigated include gas and heat losses from the system, compressibility of a real gas, and the disassociation of the diatomic gas at high temperatures and pressures. A refinement of the theory would allow for a more optimum use of the available energy in shaping the acceleration pulse.

References

1. P. S. Hughes and L. A. Vagnoni, "Direct Measurement of 5"/54 Gun Setback Acceleration," Shock and Vibration Bulletin, 36, Part 2, January 1967.
2. F. H. Mathews, "Test Techniques for Increasing the Acceleration and Velocity Capabilities of an 18-Inch Pneumatic Actuator," Shock and Vibration Bulletin, 34, Part 3, December 1964.

APPENDIX

MATHEMATICAL ANALYSIS OF THE GAS SPRING TEST SETUP

Since there are so many variables involved in this testing technique and their interaction of such a complex nature, there is a need for an analytical expression which will facilitate the selection of setup parameters. The acceleration-time data of the projectile is the main concern of the test; therefore, the following analysis will concentrate on this point.

To mathematically analyze the gas spring, it is necessary to make some simplifying assumptions. For a first approximation it is assumed that an ideal gas is used and that the process is a reversible adiabatic process with a constant specific heat ratio. It is also assumed that there are no losses in the gas spring.

There are three distinct regions of piston travel that are of interest. The first region is from the point where the piston starts from rest to the point where its velocity is measured (some distance after the piston has left the thrust column). This is shown in Fig. 10.

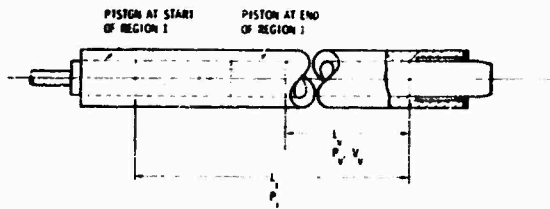


Fig. 10 - Region 1 of Piston Movement

Region Two, shown in Fig. 11, is defined from the point where the velocity of the piston is measured to the point where motion of the projectile is impending. Region Three of

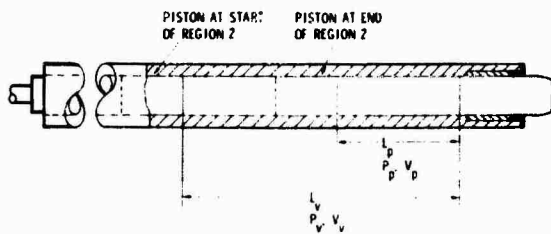


Fig. 11 - Region 2 of Piston Movement

piston travel is shown in Fig. 12 and is defined from the end of Region Two to the point where the distance between the piston and the projectile reaches a minimum.

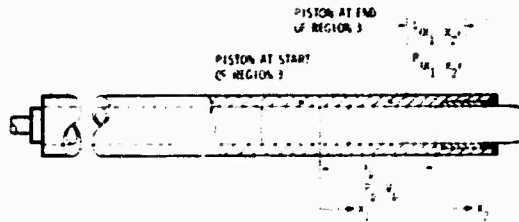


Fig. 12 - Region 3 of Piston Movement

The following nomenclature is used in the development of the analysis:

- A - Cross-sectional area of gas column
- d - Diameter of projectile
- F - Maximum axial force on projectile due to friction in rifled section
- I - Mass moment of inertia of projectile
- k - Constant of proportionality between linear and angular acceleration for a given gun barrel
- L_i - Initial length of gas column
- L_p - Length of gas column when motion of projectile is impending
- L_v - Length of gas column when velocity of piston is measured
- $L(X_1, X_2)$ - Distance between piston and projectile when they are respectively at X_1 and X_2
- M_1 - Mass of piston
- M_2 - Mass of projectile
- M_{2e} - Effective mass of projectile
- N - Force exerted on the circumference of the projectile by the rifled section normal to the grooves
- P_a - Atmospheric pressure

- P_i - Initial pressure of gas column
- P_p - Pressure of gas column when motion of projectile is impending
- P_v - Pressure of gas column when velocity of piston is measured
- $P_p(X_1, X_2)$ - Pressure of the gas column when the piston and projectile are respectively at X_1 and X_2
- γ - Specific heat ratio
- U - Variable defined to be $X_1 - X_p$
- \dot{U} - Variable defined to be $\dot{X}_1 - \dot{X}_2$
- \ddot{U} - Variable defined to be $\ddot{X}_1 - \ddot{X}_2$
- V_p - Velocity of the piston when projectile motion is impending
- V_v - Measured velocity of piston at the end of Region One
- X_1 - Distance piston moves as measured from position of piston when motion of projectile is impending
- X_2 - Distance projectile moves as measured from the initial position of the projectile
- \dot{X}_1 - Velocity of piston
- \dot{X}_2 - Velocity of projectile
- \ddot{X}_1 - Acceleration of piston
- \ddot{X}_2 - Acceleration of projectile
- μ - Coefficient of friction between projectile and rifled section
- ϕ - Angle of twist which grooves in rifled section make with longitudinal axis
- $\ddot{\theta}$ - Angular acceleration of projectile

Region One (Fig. 10)

From thermodynamics and the assumptions stated previously, it is known that

$$P_v (AL_v)^\gamma = P_i (AL_i)^\gamma ,$$

or

$$P_v = P_i \left(\frac{L_i}{L_v} \right)^\gamma . \quad (1)$$

From Eq. (1) the pressure in the gas spring can be determined at the selected point where the velocity of the piston is measured. There is no need to analyze the exact motion of the piston within this region as the actuator setup can be varied to produce a desired velocity with a known piston mass, M_1 , and a given initial gas spring pressure, P_i .

Region Two (Fig. 11)

It should be noted that the position of the piston when projectile motion is impending is not fixed but varies with the initial gas spring pressure, P_i , and volume, and the projectile friction, F . Impending motion of the projectile is defined as the point where the force on the projectile from the pressure in the gas spring is equal to the sum of all other forces acting on the projectile in the opposite direction.

$$P_p A = F + P_a A ,$$

or

$$P_p = \left(\frac{F}{A} \right) + P_a . \quad (2)$$

Since P_p is essentially constant and F is measured and nearly constant from one projectile to the next, then P_p becomes a known constant. Eq. (2) says that, although the piston is not always in the same position when projectile motion is impending, the pressure ahead of the piston at that point is always the same.

Two other equations are also known:

$$P_p (AL_p)^\gamma = P_i (AL_i)^\gamma \quad (3)$$

and

$$\frac{M_1 (v_p^2 - v_v^2)}{2} = \frac{(P_p AL_p - P_v AL_v)}{1 - \gamma} + P_a A (L_v - L_p) . \quad (4)$$

Rearranging Eq (3) and Eq. (4) gives

$$L_p = L_i \left(\frac{P_i}{P_p} \right)^{\frac{1}{\gamma}} \quad (5)$$

and

$$V_p = \sqrt{\left[\frac{(P_p L_p - P_v L_v) A}{1 - \gamma} + P_a A (L_v - L_p) + \frac{M_1 V_v^2}{2} \right] \frac{2}{M_1}} \quad (6)$$

where P_p , L_p , and P_v are given by Eqs. (2), (5), and (1), respectively.

Region Three (Fig. 12)

Looking now at Region Three, it is seen that

$$\begin{aligned} L(X_1, X_2) &= L_p - X_1 + X_2 \\ &= L_p - (X_1 - X_2) \quad (7) \end{aligned}$$

and

$$P(X_1, X_2) \left[AL(X_1, X_2) \right]^{\gamma} = P_p (AL_p)^{\gamma} \quad (8)$$

Substituting Eq. (7) into Eq. (8) and rearranging gives

$$P(X_1, X_2) = P_p \left(\frac{L_p}{L_p - (X_1 - X_2)} \right)^{\gamma} \quad (9)$$

Applying Newton's Second Law of Motion to the piston, results in

$$M_1 \ddot{X}_1 = -P(X_1, X_2) A + P_a A; \quad (10)$$

likewise for the projectile as shown in Fig. 13,



Fig. 13 - Forces Acting on the Projectile

$$\begin{aligned} M_2 \ddot{X}_2 &= P(X_1, X_2) A - F - P_a A \\ &\quad - 2\mu N \cos \phi \\ &\quad - 2N \sin \phi \quad (11) \end{aligned}$$

Now consider the angular motion of the projectile:

$$\frac{1}{d} \ddot{\theta} = N \cos \phi - \mu N \sin \phi$$

or

$$N = \frac{1}{d} \ddot{\theta} \left(\frac{1}{\cos \phi - \mu \sin \phi} \right),$$

but

$$\ddot{\theta} = k \ddot{X}_2.$$

Therefore

$$N = \frac{k \ddot{X}_2}{d} \left(\frac{1}{\cos \phi - \mu \sin \phi} \right) \quad (12)$$

Now substitute Eq. (12) into Eq. (11) and rearrange

$$\begin{aligned} \ddot{X}_2 \left[M_2 + \frac{2Ik}{d} \left(\frac{\mu \cos \phi + \sin \phi}{\cos \phi - \mu \sin \phi} \right) \right] &= P(X_1, X_2) A - F \\ &\quad - P_a A \quad (13) \end{aligned}$$

The form of Eq. (13) indicates that an effective mass, M_{2e} , for the projectile can be defined to account for the angular motion.

$$\begin{aligned} M_{2e} &= M_2 + \frac{2Ik}{d} \\ &\quad \left(\frac{\mu \cos \phi + \sin \phi}{\cos \phi - \mu \sin \phi} \right) \quad (14) \end{aligned}$$

Then Eq. (13) becomes

$$\ddot{X}_2 M_{2e} = P (X_1, X_2) A - F - P_a A. \quad (15)$$

Now substitute Eq. (7) into Eqs. (10) and (15) and divide by the appropriate mass

$$\ddot{X}_1 = -\frac{P_a A}{M_1} \left[\frac{L_p}{L_p - (X_1 - X_2)} \right]^\gamma + \frac{P_a A}{M_1} \quad (16)$$

$$\ddot{X}_2 = \frac{P_a A}{M_{2e}} \left[\frac{L_p}{L_p - (X_1 - X_2)} \right]^\gamma - \frac{F}{M_{2e}} - \frac{P_a A}{M_{2e}} \quad (17)$$

Eq. (17) will give the acceleration of the projectile, but there is no way of knowing from this equation where the maximum acceleration occurs. Maximum acceleration point will occur when the relative velocity between the piston and the projectile is zero. Therefore an expression involving both the relative velocity and the relative displacement must be found. Subtracting Eq. (17) from Eq. (16) gives

$$\ddot{X}_1 - \ddot{X}_2 = -P_a A \left(\frac{1}{M_1} + \frac{1}{M_{2e}} \right) \left[\frac{L_p}{L_p - (X_1 - X_2)} \right]^\gamma + \frac{P_a A}{M_1} + \frac{F}{M_{2e}} + \frac{P_a A}{M_{2e}} \quad (18)$$

Now define two constants and simplify. Let

$$K_1 = P_a A \left(\frac{1}{M_1} + \frac{1}{M_{2e}} \right) \quad (19)$$

and

$$K_2 = P_a A \left(\frac{1}{M_1} + \frac{1}{M_{2e}} \right) + \frac{F}{M_{2e}} \quad (20)$$

Then Eq. (18) becomes

$$\ddot{X}_1 - \ddot{X}_2 = -K_1 \left[\frac{L_p}{L_p - (X_1 - X_2)} \right]^\gamma + K_2 \quad (21)$$

For the purpose of solving Eq. (21), introduce the change of variables

$$U = X_1 - X_2$$

$$\dot{U} = \dot{X}_1 - \dot{X}_2$$

$$\ddot{U} = \ddot{X}_1 - \ddot{X}_2$$

Therefore

$$\ddot{U} = -K_1 \left(\frac{L_p}{L_p - U} \right)^\gamma + K_2 \quad (22)$$

Now let

$$\dot{U} = z ;$$

then

$$U = \frac{dz}{dt} = \frac{dz}{du} \frac{du}{dt} = z \frac{dz}{du} .$$

Substituting into Eq. (22) gives

$$z \frac{dz}{du} = -K_1 \left(\frac{L_p}{L_p - U} \right)^\gamma + K_2$$

or, after integrating, becomes

$$\frac{z^2}{2} = K_2 U + \frac{K_1 L_p^\gamma (L_p - U)^{1-\gamma}}{1-\gamma} + C_1$$

or

$$\frac{\dot{U}^2}{2} = K_2 U + \frac{K_1 L_p^\gamma (L_p - U)^{1-\gamma}}{1-\gamma} + C_1 \quad (23)$$

where C_1 is the constant of integration.

The initial conditions used to evaluate C_1 are:

$$U = X_1 - X_2 = 0 \text{ at } X_1 = 0, X_2 = 0$$

$$\dot{U} = \dot{X}_1 - \dot{X}_2 = V_p \text{ at } X_1 = 0, X_2 = 0.$$

By substituting the above values into Eq. (23) and solving for C_1 , it is found that

$$C_1 = \frac{V_p^2}{2} - \frac{K_1 L_p}{1-\gamma}.$$

Therefore Eq (23) becomes

$$\frac{\dot{U}^2}{2} = K_2 U + \frac{K_1 L_p^\gamma (L_p - U)^{1-\gamma}}{1-\gamma} + \frac{V_p^2}{2} - \frac{K_1 L_p}{1-\gamma} \quad (24)$$

or

$$\dot{U}^2 = 2K_2 U + \frac{2K_1(L_p - U)}{1-\gamma} \left(\frac{L_p}{L_p - U} \right)^\gamma + V_p^2 - \frac{2K_1 L_p}{1-\gamma} \quad (25)$$

where K_1 , K_2 , and V_p are given by Eqs. (19), (20), and (6), respectively.

Eq. (17) can also be written as

$$\ddot{X}_2 = \frac{P A}{M_{2e}} \left(\frac{L_p}{L_p - U} \right)^\gamma - \frac{F}{M_{2e}} - \frac{P_a A}{M_{2e}} \quad (26)$$

Now the relative velocity, \dot{U} , between the piston and the projectile and the acceleration of the projectile are both expressed in terms of a common parameter, the relative displacement, U . It is then possible to calculate the acceleration at that value of relative displacement for which the relative velocity is zero. This point gives the maximum acceleration of the projectile but not the time at which it occurs. In general, acceleration-time data is needed rather than acceleration-displacement data; so to express time as an explicit variable, a numerical technique can be used with the plot obtained from Eq. (25). A relative displacement-time curve can then be drawn. The time, t , can then be substituted for U in Eq. (26) to get an acceleration-time signature of the projectile.

DISCUSSION

Mr. Hughes (Naval Weapons Evaluation Facility, Albuquerque): I would like clarification of the duration at which you can record 80 KHz signals. I believe you said forever, but it appeared on one slide that you had a cable cut.

Mr. Fluent: Yes, the cable was cut after several milliseconds in that particular test. I said that we had obtained data for as long as needed. The reason that we tried getting extended data was that somebody required that we have data for 15 milliseconds. So on a calibration shot we tried to see

how long we could get it, and as it turned out, the first cable that cut was after 500 milliseconds. Some of the cables never did cut--they ran the full 70 feet and we could still record data.

Mr. Hughes: So which one gets cut first appears to be sort of a chance type of thing.

Mr. Fluent: Yes, we have not really gone into the feasibility of trying to see if we can record data all the way through, even full stopping.

**FULL-SCALE RECOIL MECHANISM SIMULATOR
(FORCED FLUID FLOW THROUGH A CONCENTRIC ORIFICE)**

W. J. Courtney
IIT Research Institute
Chicago, Illinois

and

R. Rossmiller and R. Reade
U.S. Army Weapons Command
Rock Island, Illinois

A full-scale recoil mechanism simulator weighing 14,000 lbs, was designed, fabricated and operated. This simulator was designed as a tool to investigate high pressure high velocity hydraulic fluid flow through a concentric orifice. The non-linear mathematical model, used as a design aid, is presented. The computer prediction of piston velocities and oil velocities will be compared with the experimental data. Finally, a discussion of the orifice flow together with accumulated data, which includes high speed photography of the oil flow through a viewing part, will be presented.

INTRODUCTION

This full-scale simulator, HYFLOS for hydraulic flow simulator was developed to measure the various parameters needed to define the coefficient of discharge (C_D) of a recoil mechanism. Of immediate interest is the discharge coefficient of the recoil control orifice of the M140 tank recoil mechanism which is used in the M60-A1 tank. The definition of the C_D , particularly for high speeds and pressures, will be of general interest. A typical recoil mechanism is shown in Fig. 1.

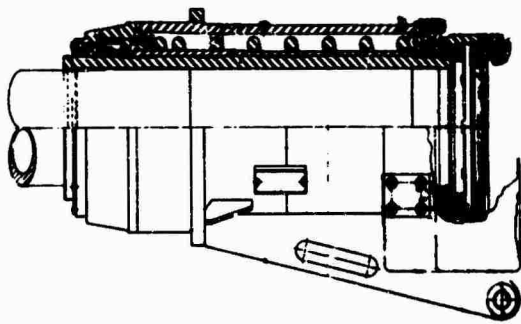


Fig. 1 Sectional View Recoil Mechanism

It is historically interesting that the French 75mm Field Gun of WWI was the first gun manufactured by the United States of America that contained a modern recoil mechanism. Until recent years, and the advent of computers, all recoil mechanism design was by trial and error. Most of the necessary design parameters are adequately understood and defined. The most elusive parameter is the coefficient of discharge because it changes rapidly during a cycle. Experience factors are now used to make the necessary approximations for design changes.

The trend of modern experimental tank guns is to fire projectiles at higher and higher muzzle velocities resulting in recoil times from 25 to 65 milliseconds. Breech forces can be measured in millions of pounds and trunnion reactions in excess of 1/4 million pounds. As muzzle velocities become higher, the parameters which the designer has to juggle become more critical. In one mechanism the oil flow was so violent that the stainless steel locking wires were "washed" off the screw heads (see Fig. 2). The damage could have been due to cavitation induced erosion since stainless steel powder was recovered from the bottom of the mechanism.



Fig. 2 End View Recoil Orifice
(Note: Loss of Locking Wire)

The HYFLOS was installed in WECOM's Gas Dynamics Laboratory (Fig. 3), the Fastex cameras which were used to record the motion of the piston extension rod and the flow of oil through the orifice are not shown. A 5000 psi nitrogen gas compressor is shown in the right rear. An oil sealed vacuum pump was used to remove dissolved gases from the hydraulic fluid. The horizontal dynamic cradle was used because of a Corps of Engineers restriction on bedrock reaction forces loading.

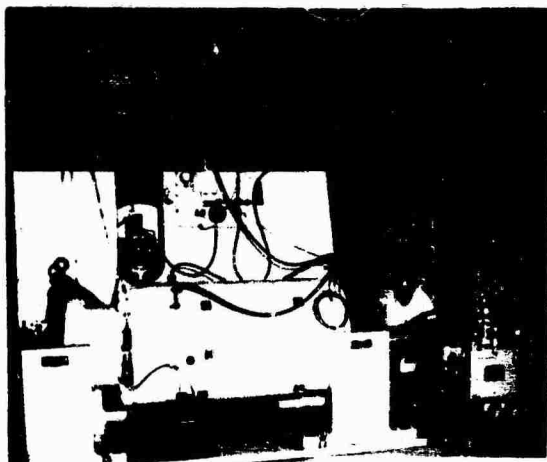


Fig. 3 HYFLOS Installed in WECOM Laboratory

The preparation of the HYFLOS for an experimental velocity excursion is straight forward. The buffer and drive zone pressures are reduced to atmospheric. The metal to metal seal of the piston is made by raising the buffer pressure to 100-150 psig. Then the buffer pressure is reduced to the desired level determined by the maximum

excursion desired, i.e., the p_1/p_2 ratio. Subsequently, the drive zone pressure is set at the required level (maximum velocity desired) and the trigger valve is actuated to release the piston.

TECHNICAL DISCUSSION

This discussion is concerned with the main problems encountered in designing and using the HYFLOS. The following equation of motion was used as a tool in the design and testing of the device,

$$m\ddot{x} + (c_1 \dot{x}^2 + c_2) \frac{\dot{x}}{|x|} + (p_2 - p_1) A = 0 \quad (1)$$

where

m = piston mass, (lb ft⁻¹-sec²)

x, \dot{x}, \ddot{x} = piston motion (ft) and its time derivatives

c_1 = damping constant due to oil flow through orifice (lb ft⁻² sec²)

c_2 = damping constant, friction of bearings and seals, (lb)

p_1 = absolute drive pressure (lb ft⁻²)

p_2 = absolute buffer pressure (lb ft⁻²)

A = piston end area (ft²)

Nitrogen is used as the drive gas (p_1) and as the buffer gas (p_2); the expansion and compression processes were assumed to be adiabatic and specific heat ratio was assumed to remain constant ($k = 1.4$). Thus the dynamic pressures, p_1 and p_2 , can be determined as a function of piston motion from,

$$p_1 v_1^k = C_1 = p_{1-in.} v_D^k \quad (2)$$

and

$$p_2 v_2^k = C_2 = p_{2-in.} v_B^k \quad (3)$$

where

$$v_1 = v_D + x A$$

$$v_2 = (l-x) A$$

as

$$p_1 = \frac{C_1}{(v_D + xA)^{1.4}} \quad (4)$$

$$p_2 = \frac{C_2}{[(l-x)A]^{1.4}} \quad (5)$$

where

- v_D = drive volume before motion is initiated (ft³)
- v_B = buffer volume before motion is initiated (ft³)
- l = buffer zone length (1.25 ft)

The drive volume (v_D) can be changed by installing inserts, the drive volume can be 550, 300 or 150 in.³.

The values of the damping coefficients were estimated in the following manner. The dynamic coefficient of friction was assumed to be 0.2 and since the piston weighs 580 lb there is constant drag, opposing motion, of 116 lb (c_2). The force required for flow of oil through the orifice is a function of the orifice geometry, the oil velocity and quite significantly the main reason that the HYFLOS was developed. However, the maximum oil pressure response of an M140 recoil mechanism was known from test firings. Thus the value of coefficient discharge (C_D) could be determined at a point of maximum pressure from

$$\Delta p = C_D \frac{\rho}{2} V_o^2 \quad (6)$$

where

- Δp = pressure drop across the orifice (lb ft⁻²)
- ρ = oil density (lb ft⁻⁴ sec²) (1.66 for oil used)
- V_o = oil velocity through orifice (ft sec⁻¹)

Since the downstream oil pressure is approximately zero the change in pressure across the orifice (Eq. 6) can be assumed to be the total pressure that resists piston motion thus,

$$F_p = c_1 \dot{x}^2 = \Delta p A_M \quad (7)$$

or

$$c_1 \dot{x}^2 = \frac{\rho C_D}{2} \left(\frac{A_M}{A_o} \right)^2 \dot{x}^2 A_M \quad (8)$$

where

$$\frac{A_M}{A_o} \dot{x} = V_o$$

and

- A_M = annular area between piston and chamber (ft²)
- A_o = annular area of orifice (ft²)

The damping coefficient (c_1) is 32.1 (Eq. 1) for the straight piston shown in Fig. 4 and for a pressure of 4000 psi - experimentally measured on the M140 - at a piston speed (\dot{x}) of 50 ft/sec from Eq. 7. The value of c_1 varies when the tapered piston (Fig. 5) is used.

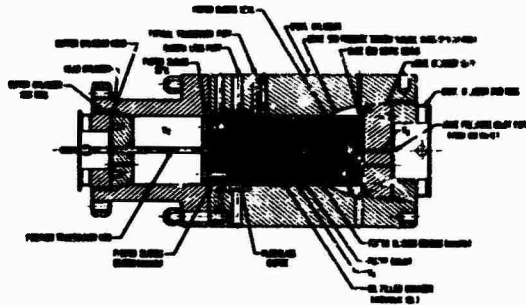


Fig. 4 Experimental Recoil Mechanism

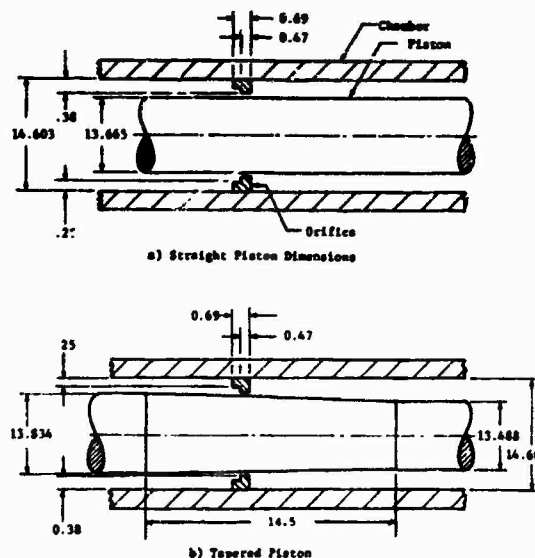


Fig. 5 Piston and Orifice Dimensions

The coefficient of discharge was assumed to be constant during computer simulation of piston motion. This constancy was assumed because it would yield realistic pressures at high piston velocities where high oil pressures would be expected. The importance of the high piston velocity and acceleration with resultant high oil pressures

will be discussed in a later section when the plexiglass orifice is discussed. The effect of assuming a constant C_D will be discussed in the final section.

Equations 4, 5, 8 and the value of c_2 were inserted into Eq. 1 and it was evaluated on a digital computer. Fig. 6 shows the piston velocity and displacement versus time for a few computer simulations of recoil mechanism operations.

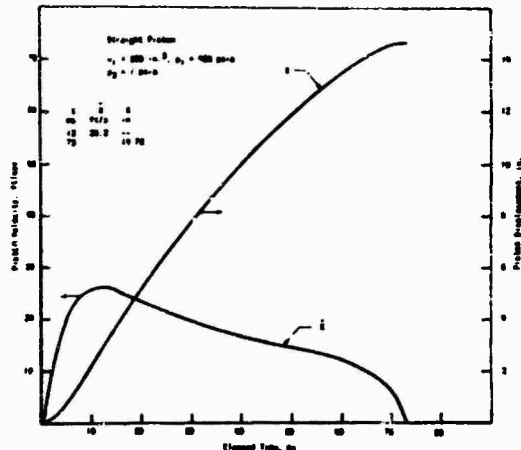


Fig. 6 Computer Simulation of Motion (Straight Piston)

ORIFICE

The orifice (Figs. 4 and 5) was fabricated from plexiglass so that the flow of hydraulic fluid could be observed through the viewports. The use of plexiglass imposed restrictions on the operation of the simulator. Due to the relatively low strength of the plexiglass and its low Young's modulus the oil pressure level must be carefully controlled and the dynamic expansion of the orifice must be monitored.

Since the orifice is enclosed on three sides by the relatively unyielding steel an approximate solution for the expansion of the orifice can be made by assuming hydrostatic compression of the plexiglass due to a pressure equal to the dynamic oil pressure. The value of Young's modulus for steel is 29.5×10^6 psi; and, for plexiglass it is 0.45×10^6 psi. Poisson's ratio for plexiglass is 0.35. The change in volume per unit volume is,

$$\epsilon_v = \frac{1-2\nu}{E} (\sigma_1 + \sigma_2 + \sigma_3) = \frac{3(1-2\nu)}{E} p_0 \quad (9)$$

where

$\nu = 0.35$ Poisson's ratio

$E = 0.45 \times 10^6$ Young's modulus, psi

$\sigma_1, \sigma_2, \sigma_3 =$ principal stresses and $\sigma_1 = \sigma_2 = \sigma_3 = p_0$ for the hydrostatic case

If the dynamic oil (p_0) pressure equals 1000 psi then $\epsilon_v = 2 \times 10^{-3}$ in.³/in.³. Since the plexiglass orifice is approximately 14 in. in diameter and can only yield in the radial direction a volume strain of 2×10^{-3} amounts to a gap increase of 3×10^{-3} in. A 4000 psi oil pressure, equal to the maximum M140 recoil mechanism pressure, would cause the orifice gap to increase by 12×10^{-3} in., Fig. 7 shows the effect of oil pressure on the orifice gap.

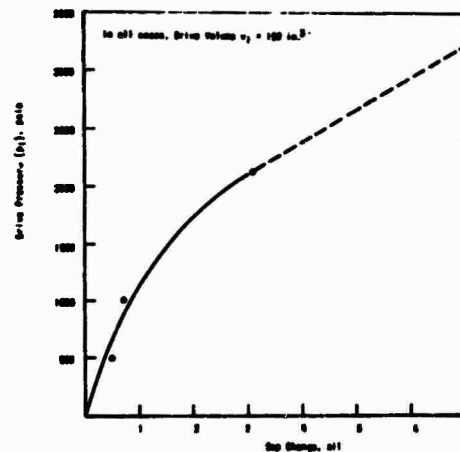


Fig. 7 Change in Gap Dimensions, Tests 4, 5 and 6

INSTRUMENTATION

Because of the predicted change in the orifice gap a capacitive probe was specifically designed to monitor the orifice gap. Four piezo-electric pressure transducers were used to monitor the gas and oil pressures, i.e., buffer zone, drive zone, and upstream and downstream of the orifice. The pressure transducers were Kistler #601H in conjunction with charge amplifiers type #503. The oil temperature was monitored on both sides of the orifice with thermocouples, American Standard ARI #T22-M-1.5-8-L-8-F-24. All of the electrical signals were conditioned and recorded on tape, from which they were played back as oscillograph traces for analysis.

A Fastex-Model W16269-camera was used to record the piston motion and a Fastex-Model WF3T-camera was used to record the orifice oil flow. Both cameras were operated at a nominal speed of 4000 frames per second; both also had 50mm focal length Wollensack lenses. Timing marks at a rate of 120 flashes/sec were put on the film during a test run. A Gerber-Model GADSR-4PPS Data Reduction System was used to determine the piston displacement as a function of time.

EXPERIMENTAL RESULTS

Prior to the acceptance tests a number of computer simulations of test firings were made to assist in the selection of drive and buffer pressures and the drive zone volume. Only the 150 in.³ drive zone volume was used during the acceptance tests.

Figs. 8 and 9 show the displacement versus time and the velocity versus time for the tests made during acceptance testing. The displacement and velocity curves for an M140 recoil mechanism are also shown in the figures. The acceptance tests were not designed to be a complete synthesis of the M140 recoil but rather to show that the curves could be synthesized. Particularly the first 15 to 20 ms of the M140 synthesis was avoided as a synthesis of this portion with the very high accelerations required would have prematurely overstrained the plexiglass orifice. Figs. 10 and 11 show additional computer simulations.

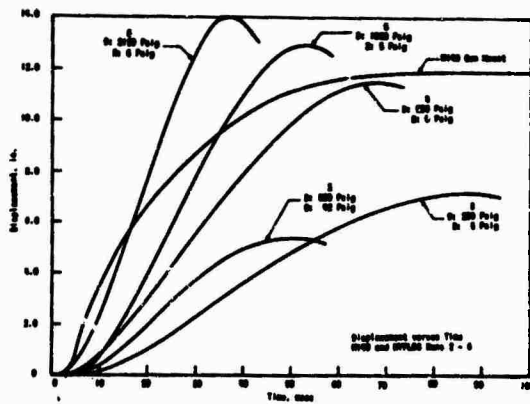


Fig. 8 Piston Displacement versus Time for 5 Pressure Ratio Experiments

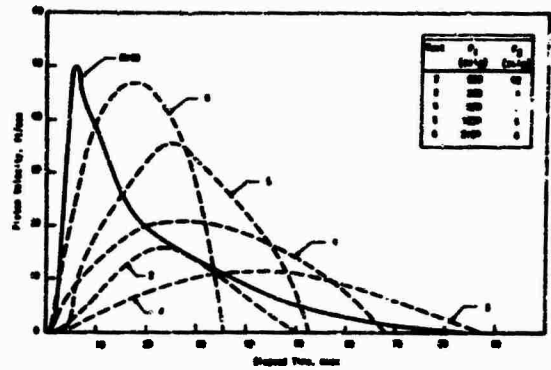


Fig. 9 Acceptance Testing Piston Velocity (Tapered Piston)

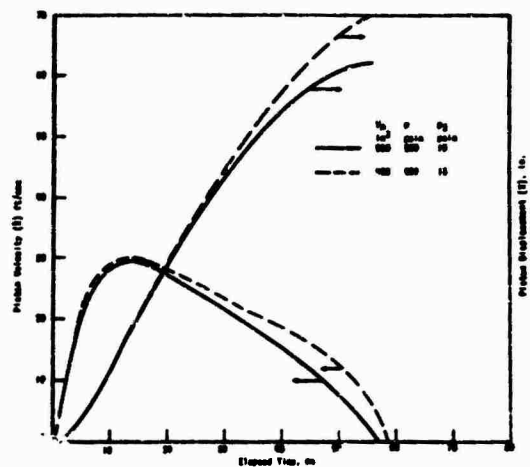


Fig. 10 Computer Simulation (Tapered Piston)

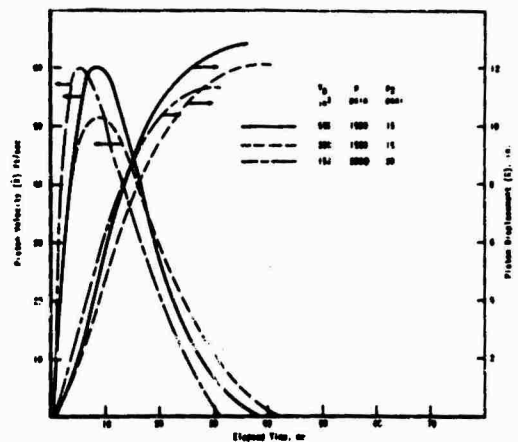


Fig. 11 Computer Simulation (Straight Piston)

The maximum displacement of the piston was predicted using the equilibrium position of the vibrating piston as a guide. Fig. 12 shows the calculated equilibrium position as solid lines for each of the drive volumes as a function of the pressure ratio p_1/p_2 . The experimental points show the maximum displacement for each of the tests made during acceptance testing with the 150 in.³ drive zone volume. For test #6 the maximum displacement was predicted to be 13-3/4 in. and experimentally it was 14 in.

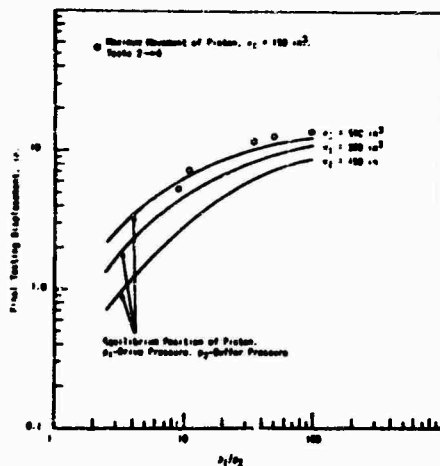


Fig. 12 Piston Movement as a Function of Pressure Ratios

Fig. 13 (a, b and c) as still reproductions, cannot convey the intuitive grasp of the effect of piston speed on the oil flow through the orifice, that is observed in the 16mm motion pictures. The onset of cavitation can be seen quite clearly. As the piston velocity was increased from Test #2 through Test #6 the extent of the cavitation zone monotonically increased.



(a) Piston View Prior to Motion



(b) Piston Velocity 19 ft/s



(c) Piston Velocity 46 ft/s

Fig. 13 Oil Flow through Orifice

Fig. 14 shows the dynamic change in the orifice gap during tests #4, 5 and 6. Obviously a change of 4×10^{-3} in. in a gap 89×10^{-3} in. requires that the effect be accounted for during analysis.

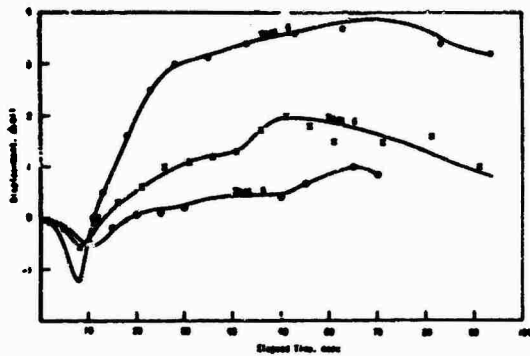


Fig. 14 Transient Orifice Gap Displacement

CONCLUSIONS

The most important result is that for which the HYFLOS was developed, the investigation of oil flow effects due to the orifice.

Figs. 15 and 16 show the oil pressure determined by computer simulation and the experimental results. The computer simulation predicted much higher oil pressures particularly for the lower piston velocities.

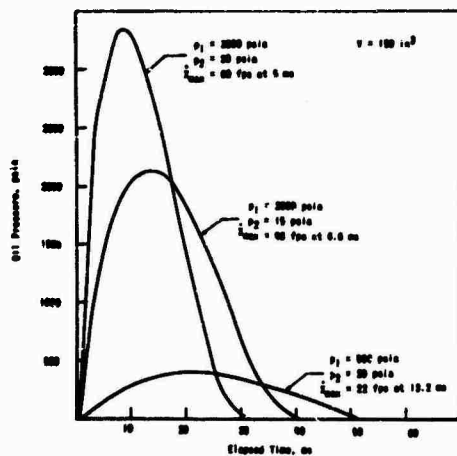


Fig. 15 Computer Predicted Oil Pressure Response

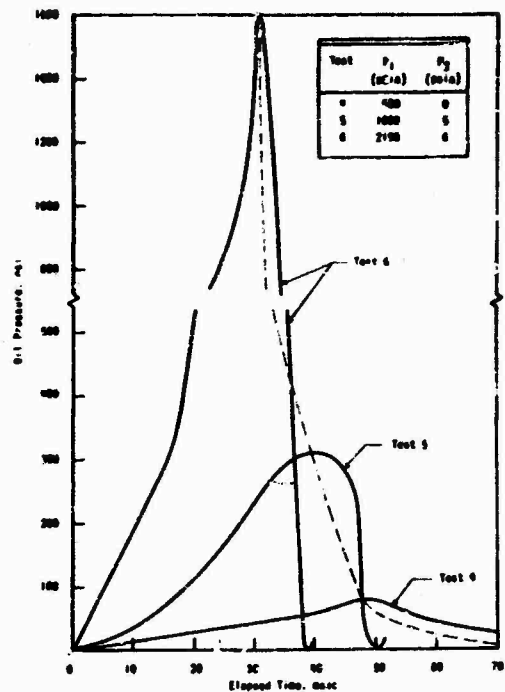


Fig. 16 Pressure Response of Hydraulic Fluid (Upstream Oil Pressure Transducer)

It is of considerable interest to compare the ratios of measure and predicted oil pressures. Recall that the coefficient of discharge was evaluated from M140 data for a piston velocity of ≈ 50 ft/sec. The ratios of the experimentally measured oil pressure to the computer predicted oil pressure was for Test #4 (19 ft/sec) $P_{ex}/P_{comp} = 0.2$ and for Test #6 (48 ft/sec) $P_{ex}/P_{comp} = 0.74$. Note that as the piston velocity approaches that at which the discharge coefficient was evaluated that the computer predictions more closely approach the experimental values. The computer predictions were adequate for the selection of drive and buffer pressures. The HYFLOS will be adequate to investigate the discharge coefficient at the required piston velocities.

ACKNOWLEDGEMENTS

The authors are pleased to acknowledge the help that was made by technical personnel at the IIT Research Institute and at the Army Weapons Command Rock Island Arsenal. Particularly, it is appropriate to mention Mr. G. Farrell who developed the original concept, Mr. R. Joyce who designed the orifice gap monitor and the instrumentation circuits, Mr. W. F. Ridenour who was a Design Engineer with exceptional talent

and Mr. R. Coberly and Mr. J. Mayer of AMSWE-RET. The HYFLOS development was initiated and supported by the U.S. Army Weapons Command under Contract DAAF01-68-C-0174. Further details can be obtained from AMSWE-RET, Rock Island Arsenal.

ISOTOPE FUEL IMPACT FACILITY

Larry O. Seamons
Sandia Laboratories
Albuquerque, New Mexico

The use of radioisotope thermoelectric generators as electrical power supplies for space applications has led to a need to characterize the impact sensitivity of the radioactive materials used in these generators. The knowledge is required to more realistically appraise the safety of potential uses. A facility is being developed at Sandia Laboratories for safely conducting impact tests of this class of potentially dangerous materials.

INTRODUCTION

Radioisotope thermoelectric generators (RTG's) are being used to provide electrical power for many space missions. These power supplies consist of subcritical amounts of radioisotope material from which the heat byproduct of radioactive decay in conjunction with a thermoelectric process is used to generate electricity. The radioisotope fuels involved are exposed to all the environments associated with accident situations or mission aborts. One category of these accident environments is impact. Such impact could result, for example, from a launch pad explosion, an early abort leading to subsequent aerodynamic heating and impact, or an orbital abort resulting in re-entry and impact.

All radioisotope fuels are health hazards to some degree and in most instances the degree can be altered by impact. In particular, a new fuel under consideration is a solid solution of thorium dioxide and plutonium 238 dioxide with the ThO_2 playing the role of dilutant. Sintered solid solution particles, a ceramic, are coated with molybdenum to produce the basic cermet fuel particles, approximately 150 microns in diameter, which in turn are hot pressed together to form a large shape. From the health hazard standpoint, this material is primarily an alpha radiation emitter. In turn, alpha emitters are of most

concern when the material particle size is a few microns diameter and thus easily inhaled or ingested. Just a few of these small particles represents enough inhalation material to be extremely hazardous. Therefore, large pieces of this material can become very dangerous if only a small amount is sufficiently pulverized by impact.

The preceding remarks imply a need to know the impact characteristics of radioisotope fuels so that the safety of any space application can be realistically appraised. Eventually an experimental verification or determination of fuel break-up vs. impact conditions becomes necessary. Because of the potential extreme toxicity of the $\text{PuO}_2/\text{ThO}_2$ solid solution cermet (SSC) fuel material, facilities for impact testing at other than mild impact conditions are virtually nonexistent. A facility for safely performing this type impact is being developed at Sandia Laboratories and has been named the Isotope Fuel Impact Facility (IFIF). The target date for having the facility qualified for impacting materials containing Pu 238 is December, 1970.

The IFIF is intended to be used to characterize fuel form break-up and to characterize fuel simulant break-up. If a less hazardous simulant can be found that will reasonably represent actual fuel

This work was supported by the United States Atomic Energy Commission.

behavior under impact, impact testing can be performed on simulants at facilities not equipped to safely handle actual fuel. Other simulant advantages would be availability, low cost and less stringent material accountability requirements.

The initial impact test specifications which determined the facility design were:

1. Impact the fuel forms at a maximum velocity of 600 ft/sec. and pre-heat the fuel forms to a maximum temperature of 1,000 °F. These two constraints were initially considered reasonable maximums for earth surface terminal velocities and operating and/or aerodynamic heating induced temperatures. More recently the temperature requirement has increased to 2,000 °F with 2,500 °F as an ultimate goal.
2. Prevent postimpact fuel residue from contamination by or entrapment in foreign materials. This is necessary because fuel break-up is determined by sorting and counting all the fuel remaining after impact. The residue is mechanically sieved through a series of screens with a 10-micron sieve mesh opening being the finest screen used. Particles which pass the 10-micron sieve are further sorted and counted by other means down to 0.1 micron "size" particles. Particles below 0.1 micron are a separate category and only the mass fraction of this category is determined. This fines analysis process is impaired by foreign materials because additional separation procedures must be used throughout the process.
3. Establish fuel form orientation relative to the impact surface without mechanical connections to the fuel forms. This constraint eliminates any false contribution to or restriction of fuel break-up that might be created by spring clamps, positioning wires, bond joints, etc., and also eliminates one source of possible fuel residue contamination or entrapment.

4. Guarantee safety of the personnel and environment surrounding the test area by sufficient multiple or concentric containment of the toxic material. The IFIF uses triple concentric containment to satisfy this requirement. The primary and tertiary containment are established before a test is conducted and the secondary containment is formed during a test.

VERTICAL AIR GUN SEQUENTIAL DETAIL

The resultant IFIF uses a vertical air gun and auxiliary hardware as shown in Fig. 1 to conduct the fuel impacts. The air gun launches a piston which in turn carries a fuel container assembly shown in position atop the piston in Fig. 1 and shown in detail in Fig. 2.

The best way to explain the vertical air gun and associated hardware is to first run through the sequence of events which takes place during a typical test and then individually discuss the hardware components. Bear in mind that the object of the test is to impact the fuel specimen against the fuel impact surface shown in Fig. 2.

Primary container hardware is shipped to another laboratory where the fuel specimen is placed inside and the primary container is sealed by welding. The container and fuel specimen are returned and a fuel container assembly is built up and positioned atop a piston. The piston and assembly are placed in launch position and electrical power is applied to the blanket heater to bring the primary container and fuel specimen up to temperature. When test temperature has been reached and the necessary soak time has elapsed, the compressed air reservoir is remotely pressurized to the desired level. High pressure air is dumped into the trigger air line thus forcing the piston off the piston seat and allowing the fire air access to the bottom of the piston. The fire air accelerates the piston and fuel container assembly up the air gun barrel to achieve test velocity. The piston and fuel container assembly exit the gun barrel and fire air begins venting through vent holes in the spacer and guide can as shown in Fig. 3. Shortly after the base of the piston clears the air gun barrel muzzle, the piston intercepts the internally tapered catch tube and the fuel container

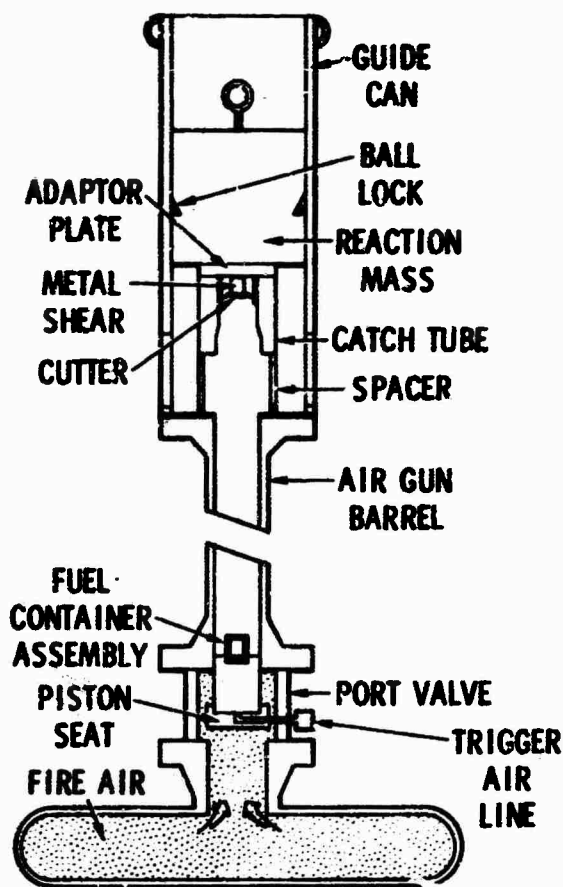


Fig. 1 - Vertical Air Gun Schematic

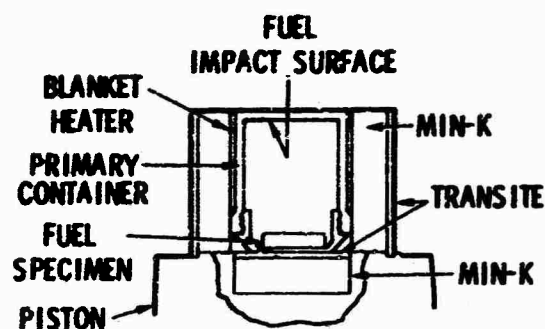


Fig. 2 - Fuel Container Assembly Schematic

assembly continues on trajectory. The piston swages into the catch tube and in the process forms a metal-to-metal seal which completes and slightly pressurizes the secondary containment of the fuel specimen. The secondary container consists of the piston, catch tube and adaptor plate (Fig. 1) and can be removed from the reaction mass and handled as a unit. The piston/catch tube impact approximates a perfectly inelastic impact and initiates the upward reaction mass displacement inside the guide can as shown in Fig. 4. The fuel container assembly meanwhile has been in free flight inside the secondary container and now impacts the cutter and drives the cutter through eight metal shear bars. The fuel specimen separates from the bottom of the primary container and begins displacing upward relative to the container as soon as the container contacts the cutter. The metal

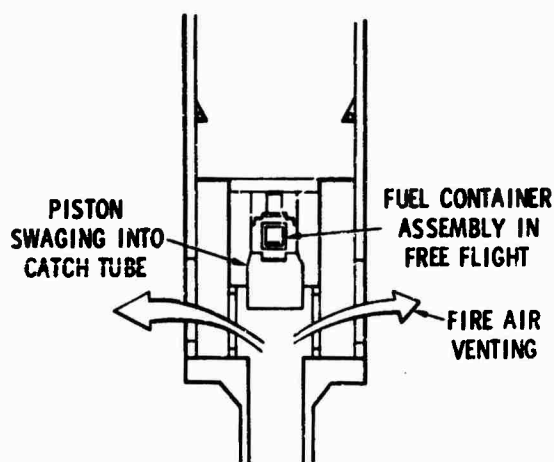


Fig. 3 - Piston Impact and Release of Fuel Container Assembly

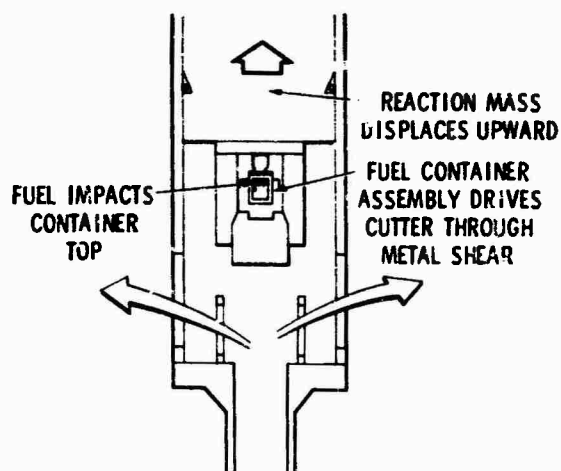


Fig. 4 - Impact of Fuel Container Assembly and Fuel Specimen

shear bars decelerate the primary container in a controlled manner such that the container is at zero velocity relative to the reaction mass or rebounding from the reaction mass when the fuel specimen impacts the top inside container surface.

The relative impact velocity between the fuel specimen and primary container is essentially the maximum piston velocity vector relative to ground minus the primary container velocity vector relative to ground at the time of impact. The container velocity direction relative to ground can be vertically upward or downward depending on how the container rebounds off the reaction mass. In any event, the rebound and reaction mass velocities are so small compared to maximum piston velocity that they are in practice neglected.

After all the various force inputs to the reaction mass are over, the reaction mass continues displacing upwards converting all the energy it has acquired to potential energy. The reaction mass acquires energy from the piston and fuel container assembly impacts and from the fire air which is expanding up the air gun barrel and out onto the bottom of the reaction mass for many milliseconds after all the various impacts occur. When the reaction mass reaches zero velocity and tries to start back down, the ball lock mechanism (Fig. 1) engages the guide can and retains the reaction mass. The ball lock mechanism is a mechanical diode in that it restricts relative displacement between the reaction mass and guide can to one direction.

After the test is over, environmental health personnel make the necessary radioactivity checks and facility disassembly proceeds accordingly until the primary container is reached. The primary container and fuel residue are sent to a laboratory equipped to handle the fuel, and the container is machined open and a fines analysis is performed. In the event of primary container failure, the secondary container would be sent to the same laboratory for disassembly and fuel recovery. A fines analysis would not be possible.

VERTICAL AIR GUN COMPONENT DETAIL

The air gun was designed to fire vertically upward so that the third basic test specification, as mentioned in the introduction, could be met. That is, establish the fuel specimen orientation relative to the impact surface without using mechanical connections to the fuel forms. The primary container internal

geometry and gravity are used to determine the initial fuel specimen orientation. Internal geometry plus piston acceleration are used to maintain fuel specimen orientation following piston launch.

The basic air gun consists of a compressed air reservoir, a port valve and a barrel. The air reservoir is T-shaped in the horizontal plane and is a welded assembly made up of 10-inch steel pipe and fittings. The T-shape provides a stable structural foundation for the gun and is clamped to a large foundation plate. A vertical riser takes off from the leg of the T and terminates with an 8-inch pipe flange fitting. The port valve sits on top of the air reservoir flange and is nothing more than a housing and structural support for the piston seat and a structure which provides air flow passages around the piston seat into the gun barrel. The fire air occupies a volume of eight cubic feet within the air reservoir and port valve and is limited to a maximum working pressure of 1,500 psi. The gun barrel sits atop the port valve and is terminated at each end with an 8-inch steel pipe flange. The bottom barrel flange and the air reservoir flange are tied together by eight 1 5/8-inch stud bolts and the port valve is compressed between the two flanges as the stud bolts are tensioned.

Two port valve options are available. Mod I is nominally 12 inches high by 12 inches outside diameter and is not accessible when assembled between the barrel and reservoir except through the barrel muzzle. Mod II is approximately 30 inches high and equipped with a concentric sleeve around the outside of the valve which will displace vertically and provide access to the fuel container assembly and top of the piston. This access can be used for final adjustment of the fuel container assembly, for in-place X-ray of the fuel specimen to verify pre-launch orientation, and for routing of thermocouple and heater power cables through the port valve wall, but the piston and fuel container assembly must still be muzzle loaded. Both port valves are mild steel weldments with a 1,500 psi internal working pressure rating that is compatible with the air reservoir rating. Mod I can be seen between pipe flanges and among stud bolts in Fig. 5 and Mod II is shown in Fig. 6.

The gun barrel is 8-1/2 feet long overall and consists of a length of 8-inch schedule 80 steel pipe and two 8-inch steel pipe flanges all welded together. The weldment is smooth bored to a 7.72-inch diameter.

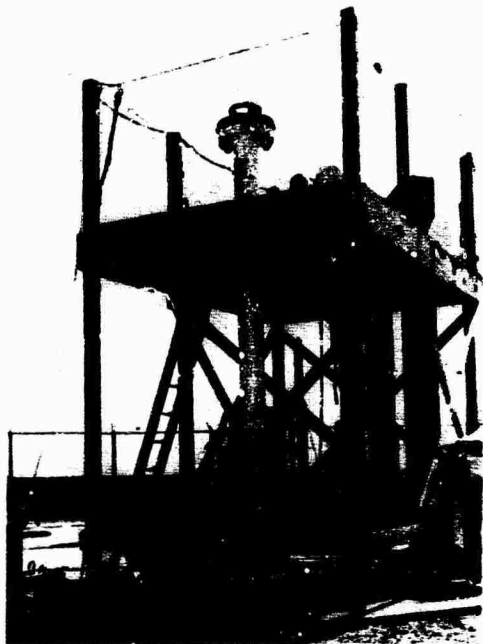


Fig. 5 - Ground Level Checkout Installation of Vertical Air Gun



Fig. 6 - Mod II Port Valve

The piston serves three functions which all affect the piston design. It is used as a support for the fuel container assembly, as the only moving part in the valving of the compressed air, and as a structural member of the secondary containment. The piston is shown in Fig. 7. It is nominally 7.70 inches outside diameter by 8 inches long. The top of the piston is counterbored to accept thermal insulation to protect it from the hot primary container and the bottom is counterbored for weight reduction. Two O-ring grooves are machined in the piston such that with the piston in launch position one O-ring seals at the piston seat and the other seals against the port valve interior just above the air flow passages. As mentioned previously, the piston is muzzle loaded and forced down the length of the barrel until it bottoms out in the port valve piston seat. The piston seals are checked by pulling a vacuum first on the trigger air line and then on the air reservoir. The 22 pound piston is condition "O" aluminum alloy (2024) because of weight considerations and because this material flows nicely and forms a good metal-to-metal seal under dynamic loading into the catch tube. Vertical air gun proof tests over the 125 to 600 ft/sec velocity range have shown that the seal formed between the piston and catch tube has a leak



Fig. 7 - Piston and Thermal Insulation Which Fits in Top Piston Counterbore

rate less than 10^{-4} cc of helium per second at standard temperature and 1 atmosphere pressure differential. At all but the lowest velocities a 600,000 pound hydraulic press is not capable of removing the piston from the catch tube unless the piston stress is first relieved by drilling a large hole through the piston. Even after being drilled out, several hundred thousand pounds of force are required to press out the piston.

The fuel container assembly shown in Fig. 8 consists of the primary container (A in Fig. 8) with the fuel specimen inside, a blanket heater (B in Fig. 8), annular rings of Johns-Manville Min-K 2,000°F thermal insulation (C in Fig. 8), a transite shell (D in Fig. 8), and fiberfrax thermal insulation (E in Fig. 8).

The primary container shown weighs about 3-1/2 pounds and is built of 15-5 precipitation hardened stainless steel because of its good strength at temperature and oxidation resistance up to 1,000°F. Since the fuel specimen is placed inside the primary container and the container is welded shut at a location other than the test facility, the container internal geometry must be such that the fuel specimen can be oriented properly within the container without having visual access to the operation. This same geometry must maintain fuel orientation throughout the test. The present test program calls for orienting a 2.12-inch diameter by 0.22-inch thick fuel disk at every 22-1/2-degree interval between edge on and flat on. At present, test temperatures have not exceeded 1,000°F and the 15-5 PH containers have survived the test environment. Preliminary results indicate that similar containers of Haynes-25 alloy will be usable to 1,500°F. Container materials for 2,000°F have not been tested in the facility but a T-111 alloy is under consideration. Low strength and high oxidation rates at temperature will be serious material constraints at the high temperatures. The oxidation problem can be limited by providing an inert atmosphere inside the air gun barrel and inside the primary container. The low strength problem is more difficult as the primary container stopping acceleration runs as high as 50,000 g's. The solution will probably require designs relying on a relatively fragile looking structure aft of the impact end and massive primary container deformation.

The blanket heater is a 400-watt, 220-volt electric resistance heater capable of 1,600°F and sized to fit the cylindrical surface of the primary container. Similar heaters can be purchased with temperature capabilities to 2,000°F. The electrical leads from the heater exit the top of the fuel container assembly (Fig. 9) and are routed either out the port valve wall or up the gun barrel and out the muzzle.

Thermal insulation is positioned all around the primary container and blanket heater to reduce heat loss and protect nearby aluminum, rubber O-rings and low carbon steel parts from the high temperatures. The

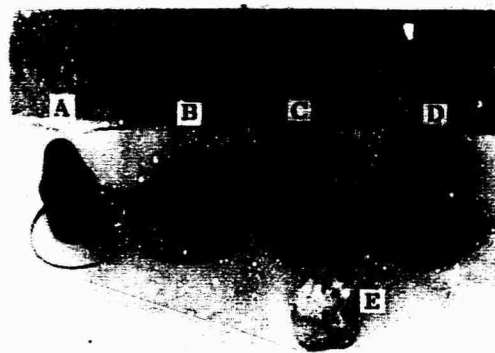


Fig. 8 - Typical Components for a Fuel Container Assembly:
A. Primary Container
B. Blanket Heater; C. Min-K
D. Transite; E. Fiberfrax



Fig. 9 - Typical Fuel Container Assembly in Position on a Piston

Fiberfrax thermal insulation is a cotton like substance good to 2,000°F used to fill irregularly shaped volumes around the primary container. The transite is a pressed asbestos-fiber based material with fair strength and thermal insulation characteristics to a temperature of 750°F or so. The transite cylindrical shell is used to house the remainder of the fuel container assembly as shown in Fig. 9.

The spacer is shown in Fig. 10 and provides a stand off between the catch tube and upper barrel flange as well as concentric alignment between all three parts. The stand off is required to allow fire air venting to begin before the piston impacts the catch tube. Otherwise the fire air imparts too much energy to the reaction mass to be able to maintain a reasonable guide can length. The spacer is a mild steel tubular weldment generously vented for passage of fire air and for optical access by photographic equipment to the piston and fuel container assembly prior to piston/catch tube impact.

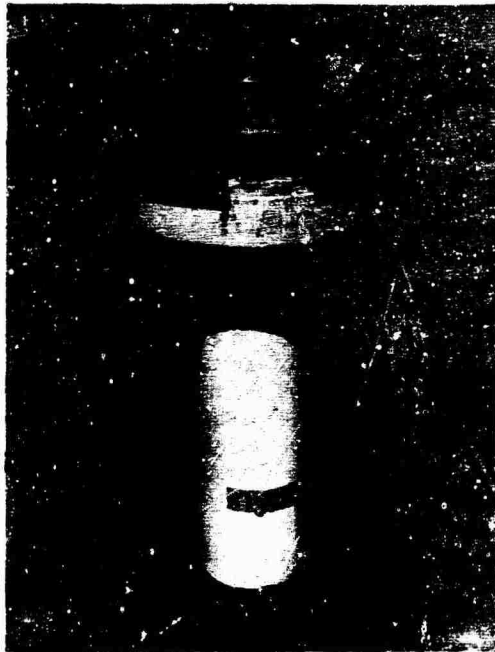


Fig. 10 - Muzzle End of Air Gun Barrel in Ground Level Checkout Installation

The catch tube, shown in Fig. 11, is a 300-pound hollow cylinder 18-inches long by 12-inches outside diameter. The tube has a 5° internal taper at the end which receives the piston. The tube material is D6A-C alloy heat treated to Rc 35. This heat treat results in a tough material with a tensile yield strength around 120,000 psi and the capability of withstanding the piston impact without suffering permanent strain. Experience has shown that the piston/catch tube seal can be verified remotely by monitoring the hoop strain at the bottom of the catch tube and ascertaining that it attains and maintains an expected strain level. The upper end of the tube



Fig. 11 - Catch Tube and Adaptor Plate with Piston Swaged into Tube

receives the metal shear and adaptor plate, and an O-ring seal exists between the metal shear and catch tube. An access hole has been machined through the wall of the catch tube so that an air valve and small HEPA filter can be attached as shown in Fig. 11. This feature is provided so that after a test the secondary container overpressure may be vented through the filter and the filter checked for radioactivity indicating a primary container failure.

The metal shear is a piece of hardware for stopping the primary container in the requisite time without unduly loading the container. It is shown in Fig. 12 with three of the metal shear bars and bar holders removed for clarity. The metal shear is used in conjunction with a cutter which is a disk shaped piece of hardened 4340 steel alloy with a cutting edge on the outer periphery. The cutter is bonded to the metal shear with the cutting edge in contact with the leading edges of the metal shear bars shown in Fig. 12. When the primary container impacts the cutter, it drives the cutter through the eight shear bars thus stopping the container. The fuel specimen must traverse two inches or more inside the primary container to reach its impact surface, and the shear bar thickness is adjusted to stop the container in less than an inch. As much as 2-1/2 inches

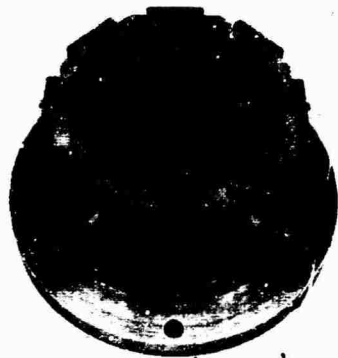


Fig. 12 - Metal Shear Shown with Three Metal Shear Bars and Holders Removed

thickness of the 1018 mild steel shear bar metal is sheared to stop a 3-1/2-pound container from 600 ft/sec. The original attempt to use this technique was to have the cutter moving with the container, but it was found that the cutter would not maintain proper orientation and penetrate all the shear bars equally. This type of difficulty disappeared when the cutter was mounted to the shear bars. The cutter mass was minimized to reduce the primary container/cutter impact severity. The metal shear fits inside the top end of the catch tube and is attached to the catch tube by eight 1/2-inch bolts which pick up the bolt circle in the metal shear flange and sandwich the flange between the adaptor plate and the catch tube.

The adapter plate is shown bolted to the top of the catch tube in Fig. 11 and is a one-inch thick mild steel plate which picks up a bolt pattern on the bottom of the reaction mass and the bolt pattern on the top of the catch tube. It can be unbolted from the reaction mass without being unbolted from the catch tube but the reverse is not true.

The reaction mass is a solid steel cylinder approximately 19-inches in diameter by 34-inches long and weighs 2,700 pounds. It displaces upwards inside the guide can and is retained at apogee by the row of spring loaded balls that run on a 5° taper machined into the reaction mass as shown in Fig. 13. The guide can is a mild steel tube 20 inches outside diameter by 1/2-inch wall thickness which is well vented for air flow and photography. The guide can is also shown in Fig. 13. Approximately 700 psi fire pressure is required to achieve 600 ft/sec with a 28-pound total launch



Fig. 13 - Reaction Mass and Guide Can

weight. These conditions result in a reaction mass displacement of 34 inches which is about as far as you can comfortably go with existing hardware. A quick calculation shows that the launch mass momentum alone would result in a reaction mass displacement of only 5-1/2 inches. The rest of the displacement is caused by fire air expansion. To accommodate higher fire pressures, test velocities, or launch weights, the reaction mass could be significantly increased by using a more dense material, the guide can could be lengthened, or the spacer stand off distance could be increased.

MISCELLANEOUS FACILITY DETAILS

One critical facility performance characteristic is to stop the primary container prior to fuel specimen impact. The hardware configuration will not allow direct observation of this phenomena. It is possible to calculate at what time the fuel impact occurs if you are willing to make assumptions of the force-time input to the container, but such calculations need verification. The best verification is provided by measurements of the metal shear bar compressive strain during container deceleration and the length of metal which is sheared. The container stop time is the same as the compressive stress duration in the metal shear bar. The time of flight of the fuel specimen inside the container is the fuel specimen free flight distance inside the container plus the shear distance required to

stop the container divided by maximum piston velocity. A comparison of these two times produces the desired verification.

Another question of interest is: Did the fuel specimen impact at the proper orientation? This question is answered by observation of the impact surface after the container has been opened and the fuel removed. The indentation left in the target surface by the fuel specimen impact can be measured to verify orientation.

It appears that the primary limitation of this whole general test technique is the maximum temperature environment that can be provided. At some high temperature the structural integrity of the primary container is nil and any breach of the primary containment voids any chance of performing the desired fines analysis. One way of eliminating this constraint would be to devise a facility where only the fuel specimen is heated and material strength at temperature thus would not be as great a concern. Also, the impact variable of target temperature would be eliminated from test data. The IFIF could be used in this manner after some modification except that it is not located where the handling of bare fuel specimens is permissible. Such an impact scheme is possible by using quick heat source removal and fuel specimen multiple containment that is generated at the time of the test in a manner similar to the IFIF secondary containment.

The present test program and related hardware requires accelerating approximately 28 pounds to a maximum of 600 ft/sec. The air gun is capable of accelerating 60 to 70 pounds to 600 ft/sec and the air flow characteristics out of the reservoir and through the port valve are probably good enough to accelerate lighter weight projectiles to somewhere in the 800 to 1000 ft/sec range. This general capability could be used to conduct higher velocity impacts or turn-around impacts where the impact target is fired into a stationary test item.

CHAMBER DETAILS

Considering only the hardware that has been described so far, a simultaneous failure of the primary and secondary containment is possible and such an event could create a dangerous environment. For this reason, it was decided to operate the vertical air gun inside an underground sealed chamber which would provide tertiary safety containment of

the toxic material. Then if both the primary and secondary containment fail, environmental health personnel would assume control of the facility and a lengthy decontamination procedure would begin.

The resultant overall facility is shown schematically in Figure 14. All the fire air is dumped into the chamber whenever a test is conducted and the chamber is capable of accepting this gas expansion. Referring to Fig. 14, the chamber usage during a test is nominally as follows:

1. Prepare the vertical air gun for testing, begin heating the fuel specimen, and close up the chamber.
2. Close the two positive seal butterfly valves and open the bypass valve.
3. Start the blower and verify chamber seals.
4. Finish temperature conditioning, pressurize the air gun reservoir and fire the air gun thus pressurizing the chamber to a maximum of 4.8 psi above the initial chamber pressure.
5. Wait for the air to pass through the bypass valve, filter system and blower. The function of the bypass valve is to regulate the pressure applied to the filter system.
6. Check the filter system to verify no radioactivity and open the butterfly valves to continue chamber purge and radioactivity check.
7. Open chamber and begin vertical air gun disassembly when tertiary container has been verified as being free of toxic material.

The chamber is a 25,000-pound cylindrical vessel with a 12-foot internal diameter and 22-foot depth yielding a chamber volume of approximately 2,500 cubic feet. The chamber walls are 3/16-thick rolled steel sheet backed up by a 4-inch thickness of reinforced concrete and dirt fill. The chamber lid and bottom are basically one inch steel plate with generous stiffening structure added. The chamber is shown in Fig. 15 just prior to implantation. The lid has two access hatches, as seen in Fig. 16. One hatch is located near the periphery and is used by personnel while the other hatch is located in the center of the

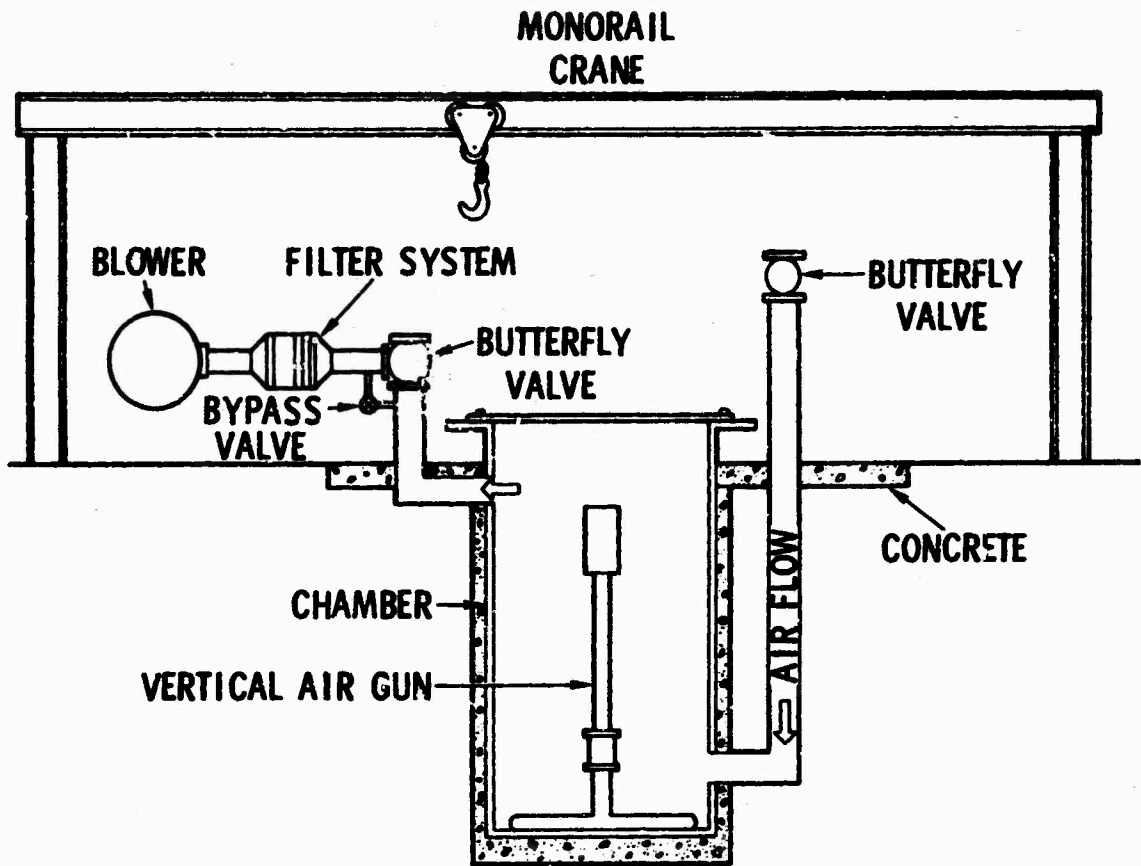


Fig. 14 - Isotope Fuel Impact Facility Schematic



Fig. 15 - Facility Chamber Prior to Underground Installation



Fig. 16 - Chamber Lid Prior to Underground Installation

lid and used for air gun hardware assembly. The chamber sits atop a twelve-inch thick reinforced concrete pad. All of the chamber welds, ducting and ducting welds were helium leak checked and X-rayed before being installed underground. The 8-inch chamber inlet and outlet ducts feed a filter system consisting of a 24" x 24" x 2" FARR J-12 course filter which is backed up by a 24" x 24" x 12" high-efficiency particulate air (HEPA) filter. The system will remove all particles larger than 0.3 microns. The filters are housed in a metal structure which provides a test hole for radiation detection equipment. A 1,000 cfm squirrel cage blower is used for air

circulation. The chamber interior is equipped with a full diameter work platform at mid-depth and spiral staircases leading to the work platform and chamber bottom. The hemichambers partitioned off by the work platform are individually lighted. The chamber walls are penetrated by compressed air lines, electrical power lines, instrumentation cables, and electrical control cables. An overhead 4-ton monorail crane is provided to support routine test assembly and to install and remove all hardware inside the chamber whenever necessary.

A REVERBERATION CHAMBER FOR USE AT REDUCED PRESSURES

M.H. Hieken, J.N. Olson, and G.W. Olmsted
McDonnell Aircraft Company
St. Louis, Missouri

A reverberation chamber with an internal volume of 283 cubic feet has been designed, fabricated and evaluated. This chamber has the unique property that it can be used at absolute pressures below 5 psi, in addition to normal operation at ambient pressure.

Design and fabrication of the chamber are described. The requirement to operate with low internal pressures resulted in heavy external structural reinforcement. Steel plates form the walls, and provide both rigidity and low acoustic absorption properties. A conventional mechanical vacuum pump is used to evacuate the chamber to the required internal pressures.

The results of evaluation tests of the chamber are presented and applications for the chamber are described.

INTRODUCTION

Long duration space missions planned for this decade will demand greatly improved levels of crew comfort. An important aspect of crew comfort is ambient noise level. Noise generated by electromechanical equipment such as fans and blowers may be perfectly acceptable in our earth environment, but this same noise might be unacceptable in a spacecraft where there is an absence of the usual background noises. A logical step toward reducing noise levels is the measurement of acoustic power radiated by such potentially noisy equipment. After an acoustic source has been characterized, experiments can be performed to evaluate proposed sound reduction materials and techniques.

The General Engineering Division Laboratories of the McDonnell Aircraft Company (MCAIR) recently designed and placed in operation a 283-cubic-foot reverberation chamber in which to measure sound power levels and to evaluate sound attenuating systems. A unique property of the chamber is that it can be used at pressures from below 5 psia to 14.7 psia (ambient pressure).

DESIGN AND FABRICATION

The basic design of the reverberation chamber took into consideration a number of factors:

- Acoustic performance
- Operation at reduced pressures
- Size
- Cost

Satisfactory acoustic performance of a reverberation chamber [1] depends upon the chamber having low absorption throughout the frequency range of interest. The term "absorption" is used here in the usual sense,

$$a = \alpha S \quad (1)$$

where a is the absorption of the chamber, in sq ft, S is the exposed area in the chamber, and α is the absorption coefficient of the exposed area.

The use of Equation (1) in the form shown implies that the entire internal surface has the same absorption coefficient. The absorption coefficient α is the fraction of acoustic power that is lost to a surface as a result of sound impinging on that surface. Low values of α are associated with surfaces that combine high rigidity with low porosity. Accordingly, reverberation chamber walls are commonly made from smoothly finished concrete or steel plate. Steel was selected for the chamber because it combines a hard, non-porous surface with ease of fabrication and relatively low cost.

A reverberation chamber must also provide a diffuse sound field. Such a field is characterized by uniform sound energy density, and by all directions of propagation being equally probable. To achieve the diffuse field, an irregularly shaped chamber was chosen. The chamber is pentagonal in shape, with a door at one end and a pentagonal pyramid at the other end. This irregular shape provides a more uniform distribution of modal density throughout the frequency band than is possible in a chamber with more regular walls. An overall view of the chamber is shown in Figure 1.

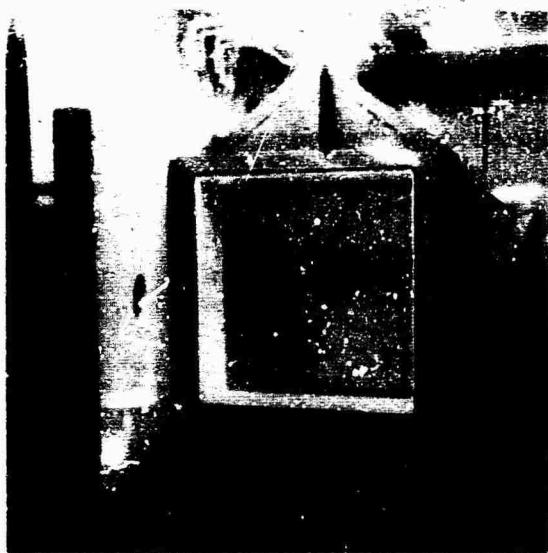


Fig. 1 283 cu ft Reverberation Chamber

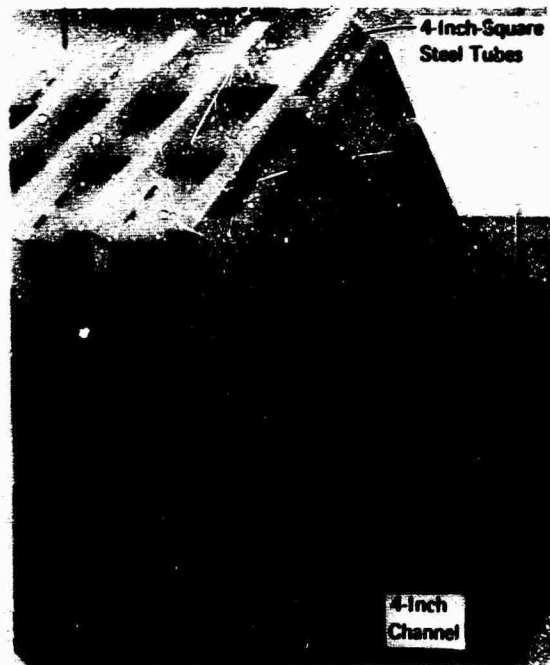
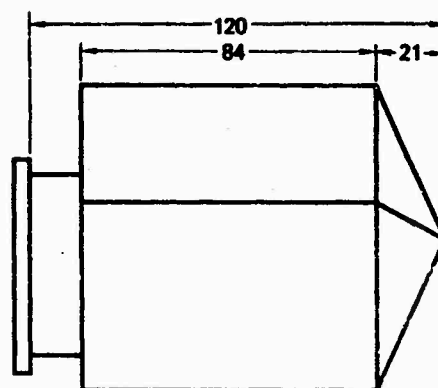


Fig. 2 Structural Details of the Chamber

The requirement to operate the chamber at internal pressures below 5 psia was the critical structural design factor. Since the ultimate pressure which the chamber may have to be operated was not known, the structural design was based on a total vacuum inside the chamber, or a differential pressure (external minus internal), of 14.7 psi. The $\frac{1}{2}$ -inch-thick steel plates forming the sides of the pentagonal section were therefore reinforced by a series of external pentagonal frames, each made from $\frac{1}{2}$ -inch wall, 4-inch-square steel tubing. One frame is located at each end of the chamber, and four frames are equally spaced between the ends. The pentagonal pyramid end is similarly reinforced with a frame near the vertex. In addition, 4-inch channels are welded along the edges of the pyramid, and square tubing is located on the center of each side of this section. Details of the chamber structure are shown in Figure 2.

The overall chamber size was determined from several considerations [2]. First, the anticipated sound pressure levels that would be produced in the chamber by relatively quiet equipment should be sufficient to permit measurement with conventional microphones. However, the low frequency performance of the chamber depends on the total internal volume of the chamber, with larger volumes providing extended low frequency range. Another factor was a structural constraint resulting from the low-pressure operation requirement: the decision to use flat sides for the chamber implied that the chamber size should be kept to a minimum. Finally, the cost factor was important. A substantial saving was effected by designing into the chamber an existing 4-foot-square door assembly from an obsolete vacuum chamber. The final chamber design provided an internal volume of 283 cubic feet, with an internal surface area of 252 square feet. The chamber dimensions are shown in Figure 3.



Reverberation Chamber Volume - 283 cu ft
 Internal Surface Area - 252 cu ft
 All Other Dimensions in Inches

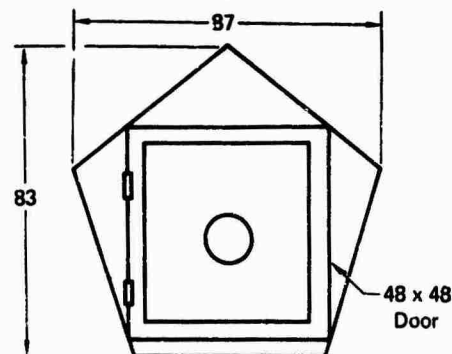


Fig. 3 Chamber Internal Dimensions

Fabrication costs of the chamber were minimized by using loose dimensional tolerances wherever possible. The inner pentagonal section was assembled from five identical rectangular plates, with virtually no tooling required. The pentagonal pyramid end was made separately, using five triangular-shaped sections. The end section required only minimal tooling, that being a pentagonal outline to insure that the end would properly mate with the five-sided center section. The door-end of the chamber was then built up on the main chamber section and the existing door frame was welded into place. All joints that formed part of the inner chamber were made with full penetration welds and were dye-penetrant inspected to insure that there were no cracks or voids in the welds.

After the chamber was fabricated, the inner surfaces were cleaned with disc grinders. Zinc chromate primer was applied to the inner walls, and finish coats of white epoxy enamel were applied.

A 10-inch viewing port existed in the 4-foot door used on the chamber. This port was retained, but the frame for the port was modified by making it hinged to swing outward. Light springs are normally used to keep the port closed, and, when the chamber is evacuated, external pressure keeps the port tightly sealed. However, if the chamber were accidentally pressurized, the port would open, acting as a pressure relief valve.

EVALUATION OF THE CHAMBER

After the chamber fabrication was completed, the chamber was moved to its present location in the MCAIR Acoustics Laboratory Control Room for evaluation tests. This area has an acceptably low ambient noise level, and the acoustic instrumentation needed for operation of the chamber was already located there.

Ambient Noise Level — A check of the ambient sound pressure level (SPL) in the reverberation chamber was made. A low ambient SPL is essential if an adequate signal-to-noise ratio is to be achieved when measuring sound radiated from test specimens. The overall ambient SPL at 14.7 psi was measured and found to be 43.8 dB, with a frequency distribution as shown in Figure 4.

Vacuum Operation — A 50 CFM mechanical vacuum pump has proven adequate to evacuate the chamber. The vacuum pumping arrangement is shown in Figure 5. The chamber can be evacuated to 5 psia in slightly over 6 minutes, as plotted in Figure 6. Because of the noise generated by the vacuum pump, the pump is turned off and the chamber sealed when noise measurements are made. Chamber pressure can be maintained at 5 psia for long periods, as indicated by Figure 7. Ample time is available, with the pump off, to conduct tests. The absolute minimum pressure to which the chamber can be evacuated has not been established experimentally, since no test requirements below 5 psia have yet been encountered. However, the door seals and the integrity of the welds indicate that the chamber could be evacuated to less than 1 psia using only the presently installed mechanical pump.

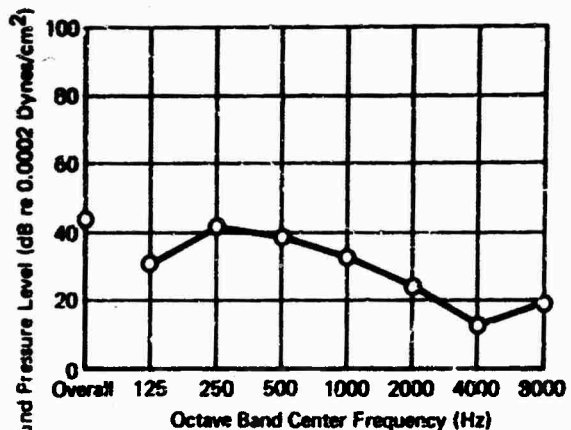


Fig. 4 Ambient Noise Level Inside Chamber

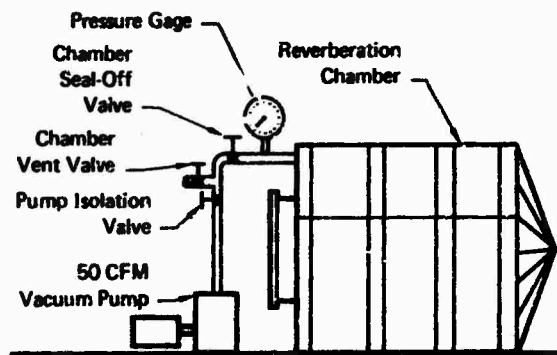


Fig. 5 Vacuum Pumping System

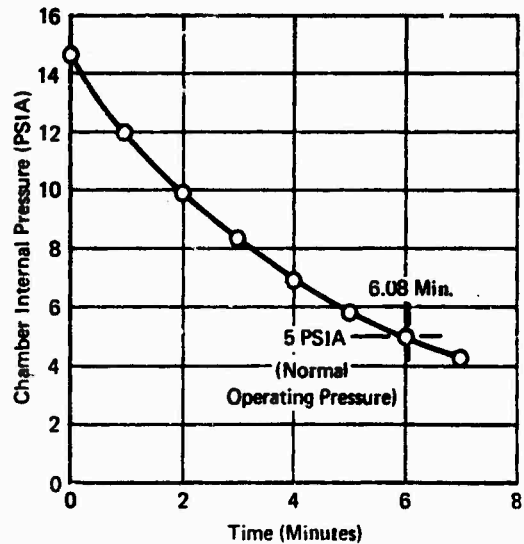


Fig. 6 Chamber Pump-Down Characteristics

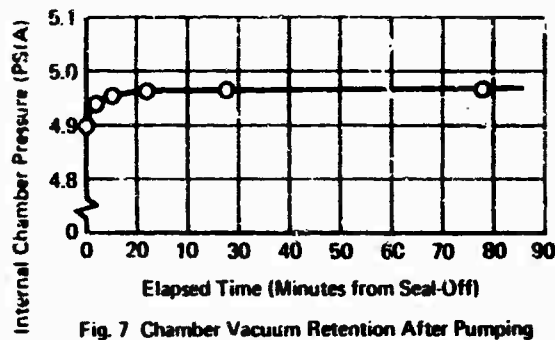


Fig. 7 Chamber Vacuum Retention After Pumping

Acoustic Calibration of Chamber – Measurement of the absorption coefficient of the chamber at ambient pressure was made by conventional methods [3]. A warble tone, centered on each of the preferred octave band center frequencies, was introduced into the chamber and then abruptly stopped. Decay of the sound pressure level in the octave band was recorded, and the reverberation time was determined by observing the time required for the level to decay 60 dB. The absorption coefficient α was calculated from the Sabine equation.

$$\alpha = \frac{0.049V}{ST} \quad (2)$$

where V is the chamber volume in cu ft,
 S is the chamber internal area in sq ft,
 and T is the measured reverberation time, in seconds.

This procedure was repeated at each octave band within the frequency range of interest.

The derivation of Equation (2) depends only on the geometric properties of the chamber and the velocity of sound in the chamber. Therefore, in order to apply Equation (2) for the case in which internal pressure is reduced, only the change in the velocity of sound was considered. The velocity of sound can be determined from the solution to the wave equation and the expression for the density of a gas in terms of absolute temperature and pressure. The resulting expression for air [4] is

$$c = 1087 \sqrt{1 + t/273} \quad (3)$$

where c is the velocity of sound in feet per second, and t is the temperature in degrees Centigrade.

The temperature of the air in the reverberation chamber stabilizes at approximately ambient temperature (20°C) for all pressure conditions. Even if the temperature changed as much as $\pm 10^\circ\text{C}$, the change in sound velocity would be on the order of 1 percent. Therefore, Equation (2) was used without modification to evaluate the absorption coefficients at reduced pressure. Figure 8 shows the values of absorption coefficient for each octave band, based on measured reverberation times.

Uniformity of Sound Field – The uniformity of the sound field in the chamber was also measured. For this purpose, a microphone was mounted on a rail inside the cham-

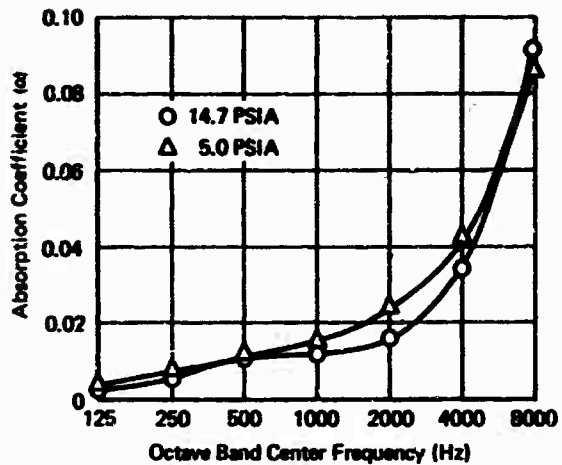


Fig. 8 Absorption Coefficients of Chamber

ber, three feet above the floor. The chamber was driven with a random noise source at a sound pressure level of 120 dB. An octave band analysis of the signal is plotted in Figure 9. With the chamber closed, the microphone was slowly moved across an 18-inch span of the rail, and the SPL variations were recorded as shown in Figure 10. The variation in overall SPL is small, and well within the tolerances of a typical test specification such as MIL-STD-810B, Method 515.1 [5].

The field uniformity was briefly checked with other types of chamber excitation, ranging from pure sinusoidal tones to narrow-band random signals. As expected, the spatial variation of SPL was very pronounced for pure tones, and present to a lesser degree for narrow band random signals. Several investigators have recently reported on the problem of measuring the sound energy in chambers of this type [6,7,8]. A closely related difficulty is that of establishing criteria for the sound fields in reverberation chambers. Evaluation tests conducted in the present chamber were not addressed to these basic problems, but they point out the need for additional analytical and experimental work.

APPLICATIONS

The reverberation chamber has proved its value in the measurement of acoustic power radiated from electromechanical devices. Evaluation tests of sound absorbing materials have also been conducted in the chamber. Potential uses of the facility include conducting psychological and physiological tests, and using the chamber for high intensity acoustic environment tests.

Noise Measurements – For measuring the acoustic power radiated from electromechanical equipment, the test specimen is suspended within the chamber. Power is supplied to it through an electrical pass-through built into the chamber. A microphone placed in the chamber detects the acoustic radiation from the specimen. The output of the microphone is filtered with either 1/3 octave or full octave filters and the filtered outputs are recorded for each frequency band of interest. The radiated acoustic power in each frequency band

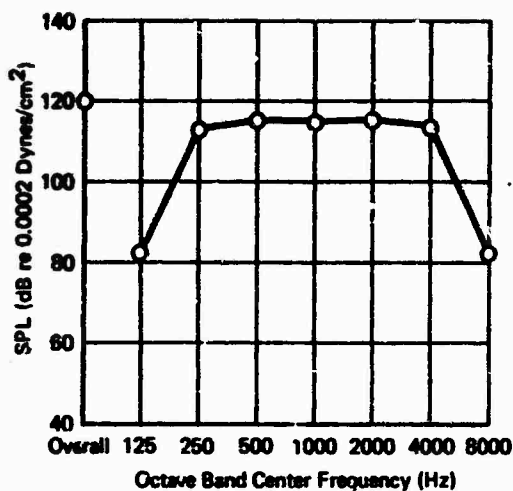


Fig. 9 Analysis of Noise Signal

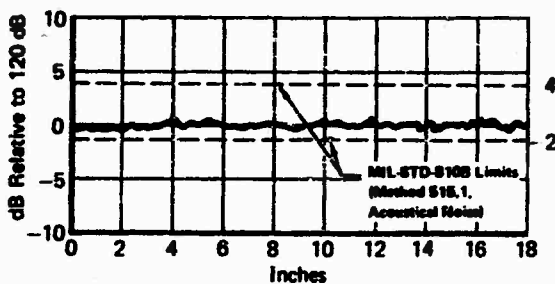


Fig. 10 Variation in SPL Over 18-Inch Distance in Chamber

is then calculated [9] from

$$W = \frac{p^2 \alpha S}{4 \rho_0 c} \quad (4)$$

where W is the radiated acoustic power, in watts
 p^2 is the measured mean-square pressure
 S is the surface area of the chamber
 α is the sound absorption coefficient
 and $\rho_0 c$ is the characteristic impedance of the air in the chamber.

The sound power level (PWL) in dB is obtained from

$$PWL = 10 \log \left(\frac{W}{W_0} \right) \quad (5)$$

where W_0 may be either of the generally accepted reference power levels, 10^{-12} or 10^{-13} watts [10].

The same experimental procedure is used at reduced chamber pressures. In computing the power levels, however, Equation (4) is corrected for the value of characteristic impedance at the absolute pressure in the chamber. Typical measurements of sound power levels at ambient pressure and at 5 psia are shown in Figure 11.

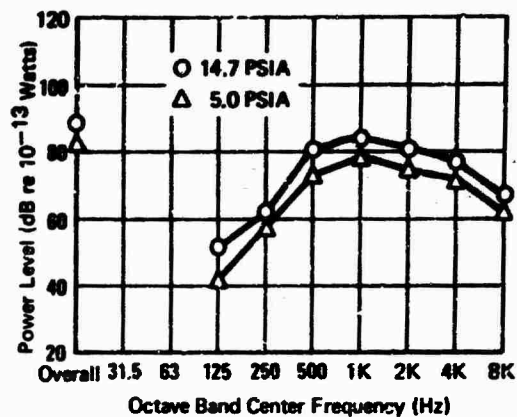


Fig. 11 Sound Power Levels of a Typical Small Fan

Measurement of Absorption Coefficients – The MCAIR Acoustics Laboratory includes a conventional standing wave apparatus that is used to measure the normal acoustic absorption coefficient of sound-absorbing materials. This device is designed to be used at ambient pressures. If sound absorbing materials are proposed for use at lower pressures, it is of interest to determine the change in absorption coefficients at those reduced pressures. The reverberation chamber has been found to be satisfactory for this purpose. The absorption of the chamber walls is sufficiently low that a specimen of relatively small area can be used in the chamber. A small specimen will not destroy the diffuse field in the chamber, yet it will provide a readily measurable change in the reverberation time, compared with the empty chamber.

In studying the variations of absorption coefficients with pressure, the material sample is introduced into the chamber and the reverberation times are measured as described above. Values of α can be calculated by several methods [11]. An example of the variation of α with pressure is shown in Figure 12. This data was obtained for a pair of 16-inch by 25-inch samples of a compacted woven-wire mesh material, backed by a 2-inch layer of spun fiberglass. The normalized absorption coefficients were obtained by selecting the maximum calculated value of α , and dividing all other values by this maximum value.

Psychological and Physiological Tests – The chamber has not yet been used for tests with human subjects, although it is considered to be suitable for such tests. Conventional loudspeakers have been used to produce sound pressure levels in excess of 125 dB in the chamber, with full control over the frequency spectrum. The ease with which the sound field in the chamber can be controlled suggests that the chamber could be used for speech intelligibility tests in the presence of high ambient noise backgrounds. Again, the low pressure capability would permit such tests to be conducted at pressures simulating those in an aircraft or spacecraft cabin.

High Intensity Acoustic Environment Tests – It is anticipated that the reverberation chamber will eventually be used for conducting high intensity noise tests. For this purpose, it is planned to install an outer shell on top of the 4-inch

square tubes, and to pack sand in the space between the chamber wall and the outer shell. The packed sand would add mass, provide additional damping for the chamber walls, and increase the transmission loss from inside the chamber

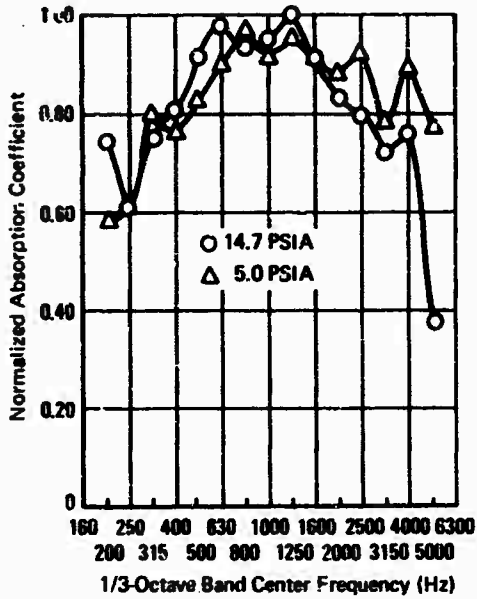


Fig. 12 Absorption Coefficient Variations

to the room in which the chamber is located. Acoustic power could be provided by air stream modulators. For this purpose, the existing four-foot-square door could be replaced by a special adapter to hold the horn from the acoustic source. Anticipated sound pressure levels in the chamber for available sound power in each octave band are plotted in Figure 13. These curves are based on the measured absorption coefficient for each frequency band, but do not take into account the losses that would result from replacement of the door section with the acoustic source, or additional losses through the walls at high sound pressure levels.

SUMMARY AND CONCLUSIONS

The 283-cubic-foot reverberation chamber has satisfactory acoustical characteristics. In addition, the chamber has the unique property that it can be used at pressures from below 5 psia to atmospheric pressure.

The chamber has been used for measuring noise radiated from electromechanical equipment, and for studying the acoustic absorption properties of materials.

The design, fabrication, and evaluation of this chamber have indicated the need for further study in predicting the behavior of irregularly-shaped chambers of this type. In addition, more work should be done on experimental evaluation of reverberation chambers.

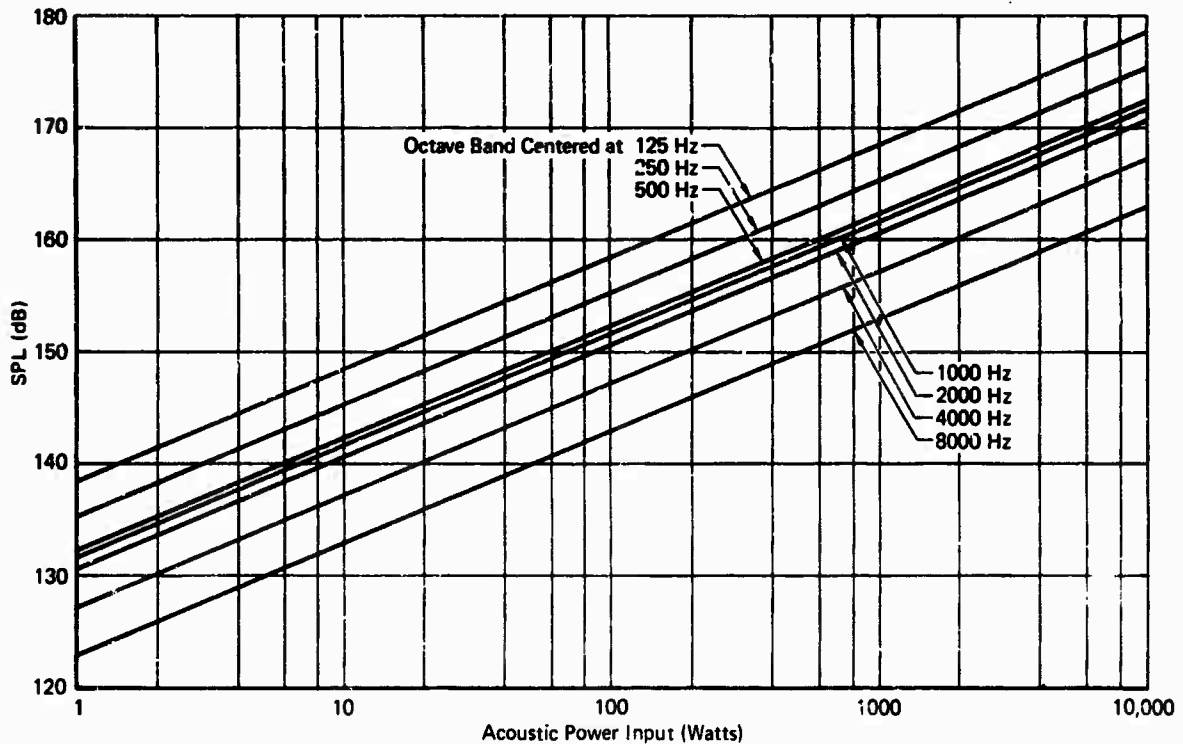


Fig. 13 Predicted Chamber SPL for Various Acoustic Powers

REFERENCES

1. L.E. Kinsler and A.R. Frey, *Fundamentals of Acoustics*, pp. 420-434. John Wiley and Sons, Inc., New York, 1962
2. American Standard Method for the Physical Measurement of Sound, Standard S 1.2 - 1962, pp. 13-22, American Standards Association, New York, 1962.
3. L.E. Kinsler and A.R. Frey, *op. cit.*, p. 431
4. L.L. Beranek, *Acoustics*, p. 10. McGraw-Hill Book Company, Inc., New York, 1954
5. Environmental Test Methods, Military Standard MIL-STD-810B, June, 1967 (Method 515.1, Acoustic Noise)
6. J.F. Mills, "A Study of Reverberation Chamber Characteristics," *Proceedings of the Institute of Environmental Sciences*, 1967
7. D. Lubman, "Spatial Averaging in a Diffuse Sound Field," *Journal of the Acoustical Society of America*, Volume 46, Number 3, September 1969
8. M.R. Schroeder, "Spatial Averaging in a Diffuse Sound Field and the Equivalent Number of Independent Measurements," *Journal of the Acoustical Society of America*, Volume 46, Number 3, September 1969
9. L.E. Kinsler and A.R. Frey, *op. cit.*, p. 423
10. American Standard Method for the Physical Measurement of Sound, *op. cit.*, p. 15
11. L.L. Beranek, *Acoustic Measurements*, pp. 862-864. John Wiley and Sons, Inc., New York, 1954

DESIGN OF AN OFF-ROAD VEHICLE MOTION SIMULATOR

Nelson M. Isada
Cornell Aeronautical Laboratory, Inc. and
State University of New York at Buffalo
Buffalo, New York

and

Robert C. Sugarman, and E. Donald Sussman
Cornell Aeronautical Laboratory, Inc.
Buffalo, New York

An off-road vehicle motion simulator was designed which is suitable for man-in-the-loop off-road mobility research. One result of this study is the establishment of design specifications for two motion simulator concepts with three degrees of freedom (roll, pitch, and throw). One concept has a short throw (± 6 inches) and the other a long throw (± 24 inches). The feasibility of the short-throw concept was demonstrated by the construction and testing of a working model.

INTRODUCTION

In developing techniques for analyzing off-road mobility problems related to driver-vehicle systems, it has been found desirable and necessary to use an off-road driving simulation facility, such as shown in Fig. 1, to conduct man-in-the-loop human factors research. Because of the unusual characteristics of an off-road environment, no commercial equipment is available to meet this need. Therefore, a study* was initiated consisting of two parallel programs, namely, (1) definition and development of a visual simulator, and (2) design and development of a motion simulator. This paper discusses the progress of the motion simulator program. This program consisted of: (1) conceptual design and development of technical specifications of a short-throw (± 6 inches) motion simulator; (2) conceptual design and development of technical specifications of a long-throw (± 24 inches) motion simulator; and, (3) selection of a concept and fabrication of a working scale model. Both of the foregoing concepts provide for a maximum roll amplitude of $\pm 30^\circ$ and a maximum pitch amplitude of $\pm 45^\circ$. Each of the concepts is electro-hydraulically powered and controlled.

* "Off-Road Driving Simulation: Design for a Moving-Base Simulator," by R. C. Sugarman, N. M. Isada, and E. D. Sussman, CAL No. VJ-2330-G-57, Cornell Aeronautical Laboratory, Inc., Buffalo, N. Y., 1969.

More detailed descriptions of the two motion simulator concepts and the results of tests on the small-scale model of the short-throw concept will now be given.

SHORT-THROW DESIGN DETAILS

In this design, the crew station is placed on top of a movable platform, as shown in Fig. 2. The platform has freedom to move in the pitch and roll modes. The crew station moves in the throw direction relative to the platform in order to reduce the payload. In this concept, one should note that throw, or z-axis motion, is perpendicular to the platform and has a maximum amplitude of ± 6 inches.

The selection of the motion specifications were dictated by human tolerance limits and vehicle motions. Hydraulic power requirements and specifications for the mechanical driving components (cylinders) were determined based on the motion requirements. The results of these calculations are shown in Table 1. It may be noted that the motion specifications consist of a long-duration sinusoidal motion and a transient (short-duration) motion such as caused by a bump, boulder, or chuck hole. These two motions are assumed to peak at the same time, hence, are added to yield the total motion. Note further that the total design weight is 2,000 lbs. (1,000 lbs. for the crew station and 1,000 lbs. for the platform). This design weight will require a hydraulic flow rate of 150 gpm (gallons per

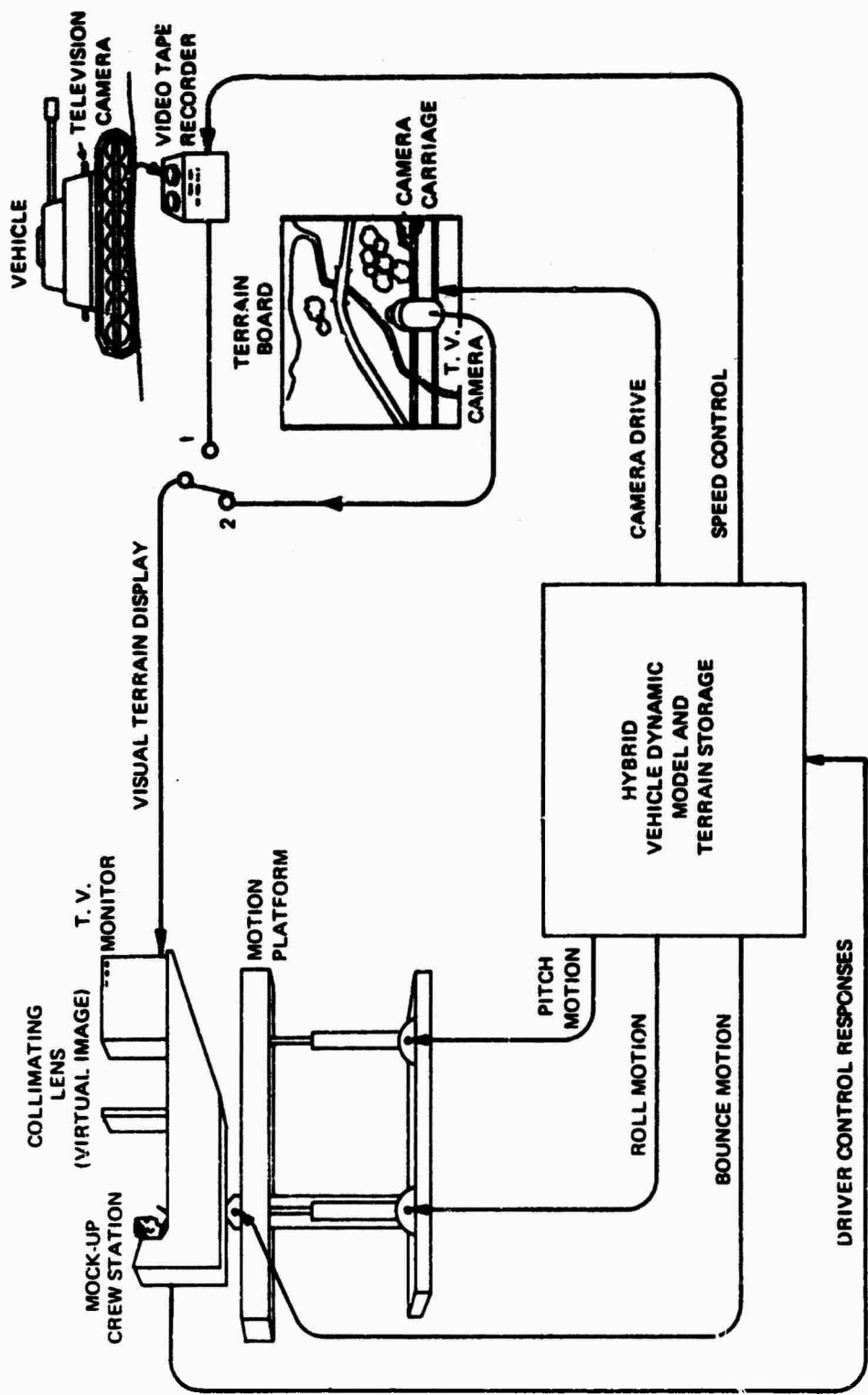


Figure 1 ADVANCED OFF-ROAD DRIVING SIMULATOR. CONCEPTUAL SKETCH FOR A MOVING-BASE SIMULATOR WITH PROGRAMMED (1) AND UNPROGRAMMED (2) VISUAL DISPLAY CAPABILITIES

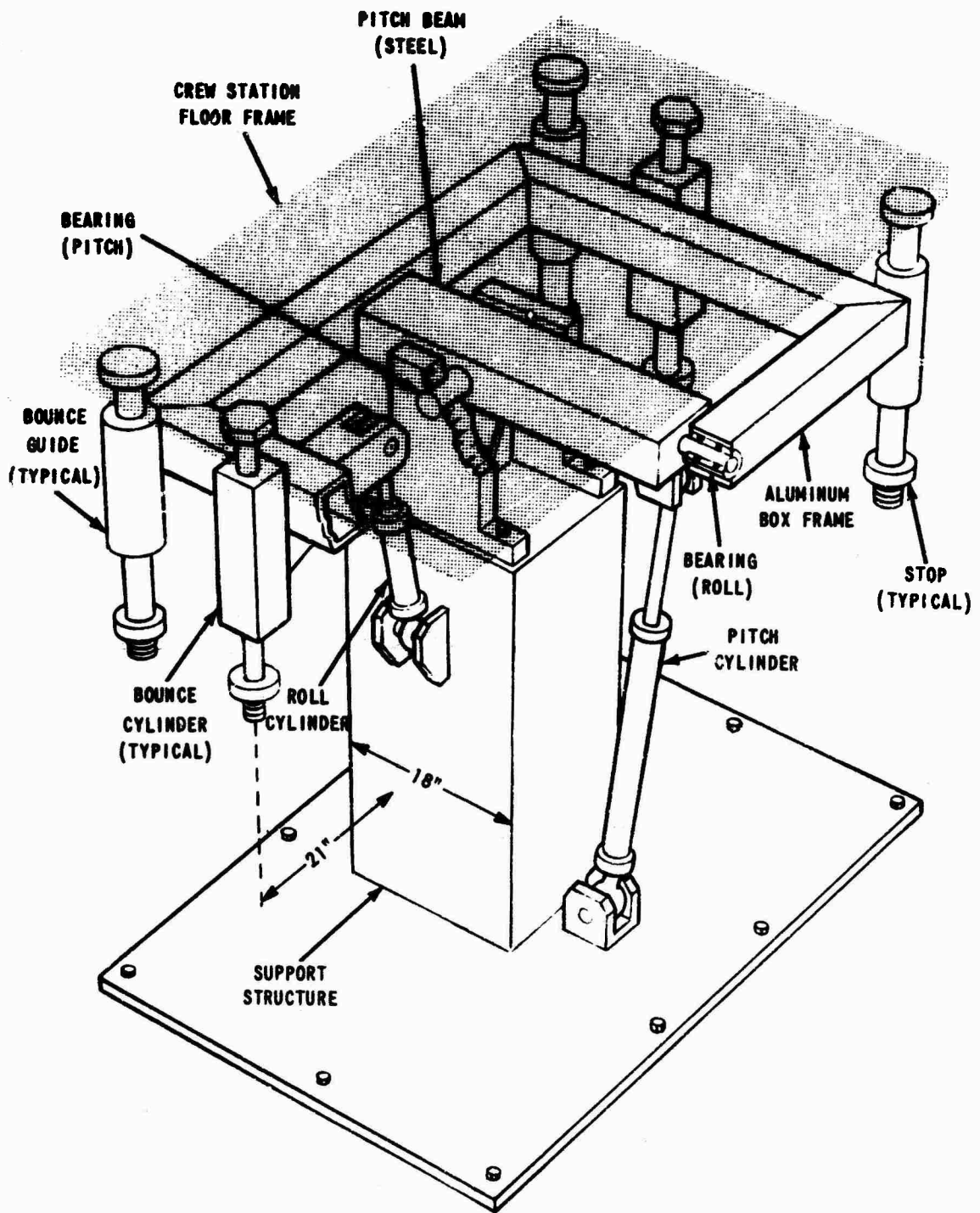


Figure 2 "SHORT-THROW" MOTION SIMULATOR.
CONCEPTUAL SKETCH OF MECHANICAL COMPONENTS.

Table 1
MOTION SPECIFICATIONS, HYDRAULIC POWER REQUIREMENTS, AND
MECHANICAL SPECIFICATIONS FOR A "SHORT THROW" (± 6 IN.)
MOTION SIMULATOR

PARAMETERS	SLOW SINUSOIDAL MOTION	TRANSIENT MOTION	TOTAL
1. BOUNCE (WEIGHT = 1000 lbs)			
MAXIMUM DISPLACEMENT, ft	± 0.5		± 0.5
MAXIMUM VELOCITY, ft/sec	3.2	5.2	8.4
MAXIMUM ACCELERATION, g's	0.6	4.0	4.6
FREQUENCY, Hz	1.0		
SUPPLY PRESSURE, psi			3,000
NET PRESSURE, psi			2,000
NET AREA, sq. in.			2.3
FLOW RATE, gpm			60.2
CYLINDER STROKE, ft			1.0
2. PITCH (WEIGHT = 2000 lbs, LENGTH = 8 ft, INERTIA = 332 lb-ft-sec²)			
MAXIMUM DISPLACEMENT, deg	± 45		± 45
MAXIMUM VELOCITY, deg/sec	141	100	241
MAXIMUM ACCELERATION, deg/sec ²	443	1,200	1,643
FREQUENCY, Hz	0.5		
SUPPLY PRESSURE, psi			3,000
NET PRESSURE, psi			2,000
TORQUE ARM, ft			1.0
CYLINDER NET AREA, sq. in.			4.76
FLOW RATE, gpm			62.5
CYLINDER STROKE, ft			2.0
3. ROLL (WEIGHT = 2000 lbs, LENGTH = 5 ft, INERTIA = 130 lb-ft-sec²)			
MAXIMUM DISPLACEMENT, deg	± 30		± 30
MAXIMUM VELOCITY, deg/sec	92	100	192
MAXIMUM ACCELERATION, deg/sec ²	300	1,800	2,100
FREQUENCY, Hz	0.5		
SUPPLY PRESSURE, psi			3,000
NET PRESSURE, psi			2,000
TORQUE ARM, ft			1.0
CYLINDER NET AREA, sq. in.			2.38
FLOW RATE, gpm			25.0
CYLINDER STROKE, ft			2.0

minute) at a supply pressure of 3000 psi.

The following description refers to Fig. 2. The motion platform is driven in roll by a single cylinder and in pitch by a single cylinder. Two bounce cylinders are connected to the pitch-roll frame to drive the floating crew station in the x direction. The pitch beam is supported by two bearings, two bearing blocks and a support structure. It should be noted that the bounce guides and bounce cylinder supports are made as low as possible so as to lower the center of mass of the system. This will provide better stability than has been achieved in a working scale model of this design, which tended to be top heavy.

The pitch-roll frame is designed to be made of six-inch aluminum box sections with overall dimensions of 42" x 56". The two pitch bearings and the two roll bearings are each three inches in diameter.

LONG-THROW DESIGN DETAILS

The design for the long-throw platform was pursued in order to determine if we could simulate the motions of the center of gravity of a vehicle going over a large bump, as well as the bounce introduced by the suspension system. It is unlikely that the throw of the short-throw design could be extended beyond ± 9 inches. The design in Fig. 3 provides a bounce amplitude of ± 2.0 feet at 0° pitch and ± 1.0 feet at $\pm 45^\circ$ pitch.

As compared to the long-throw design, the short-throw bounce movements are better suited to simulating the suspension system, since the motion is always perpendicular to the floor of the crew station. The throw motions of the long-throw design are always in the direction of the true vertical and have a lower frequency response.

The mechanical concepts employed here were to: (1) drive a platform differentially by means of two hydraulic cylinders to provide vertical (bounce) and pitch motions simultaneously, and (2) use a rotary hydraulic actuator to drive a frame in the roll mode. In this design the crew station would be attached directly to the roll frame. Table 2 lists the design specifications for the long-throw simulator.

As previously mentioned, the linear z-axis motion is always vertical in this design, whereas the analogous motion in the short-throw concept is always perpendicular to the roll-pitch frame. Other differences between the long-throw and short-throw designs are as follows:

1. For the long-throw design, the maximum throw varies with the pitch; i. e., at 0° pitch the maximum throw is two feet, while at 45° pitch, the throw is restricted to one foot. Maximum throw is independent of roll and pitch in the short-throw design.

2. Because twice the mass (2,000 lbs.) must be moved in the bounce mode for the long-throw design, the flow rate for this mode is increased to 120.7 gpm, as compared to 60.2 gpm for the short-throw design in which the mass was only 1,000 lbs.
3. The cylinder stroke is four feet for the long-throw design, demanding more stringent structural requirements.
4. The long-throw design uses a rotary actuator for the roll mode.

The following descriptions refer to Fig. 3. Two cylinders are used to drive the pitch-bounce frame differentially to achieve pitch and bounce movements. The pitch-bounce platform is made stable by a center support structure and a movable (but unpowered) guide. A rotary actuator mounted on top of the pitch-bounce platform drives the roll frame which is constructed of eight-inch aluminum pipe or box. The rotary actuator is attached to the roll frame by means of a 2-1/4 in. steel shaft supported by four pillow block bearings.

CONCEPT CHOICE AND WORKING SCALE MODEL

After comparing the two motion platform alternatives, the short-throw design was selected as the primary candidate for the motion platform. This selection was made for two reasons. First, the power requirements and structural demands are more severe for the long-throw design than they are for the short-throw. Second, what little evidence is available indicates that the lower amplitude, higher frequencies of the short-throw design are more efficacious in combination with pitch, roll, and visual cues in achieving a satisfactory vehicle "ride" simulation.

A one-third scale model of the selected design was constructed with the following objectives:

1. to determine the feasibility of the design concept;
2. to identify additional factors that must be considered in the full-scale version; and,
3. to experiment with safety concepts.

The successful operation of the model, with and without a human rider, supports the choice of the design concepts in this program. Preliminary studies with a motion picture camera mounted in the driver's position lends further support to the efficacy of the design.

The initial calculations for the model were based on a somewhat simplified design concept in order to make the equations of motion more manageable. It was anticipated, therefore, that certain factors requiring design modifications would not become apparent until the working

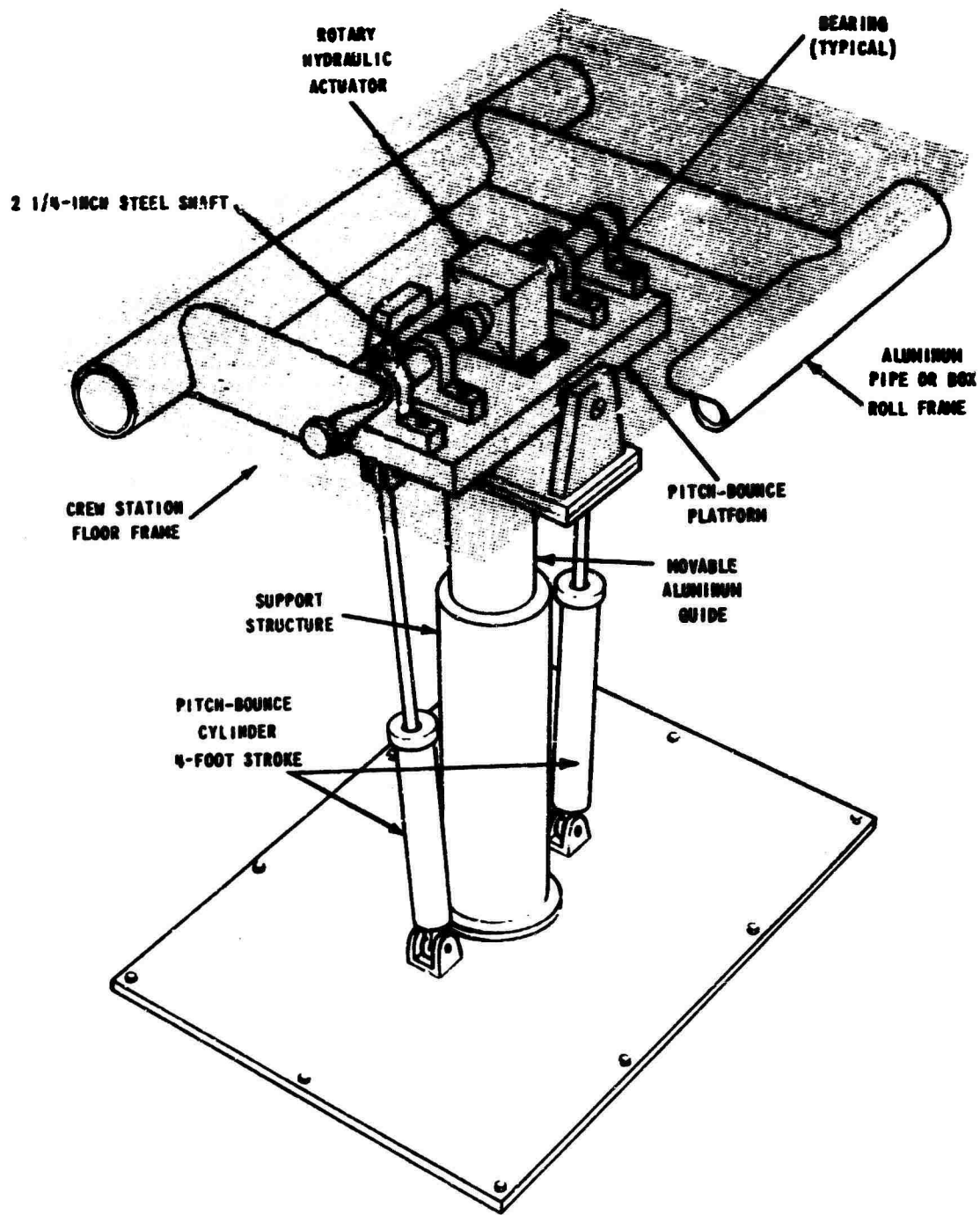


Figure 3 "LONG-THROW" MOTION SIMULATOR, CONCEPTUAL SKETCH OF MECHANICAL COMPONENTS.

Table 2
SPECIFICATIONS AND POWER REQUIREMENTS FOR A
"LONG THROW" (± 24 IN.) MOTION SIMULATOR

PARAMETERS	SLOW SINUSOIDAL MOTION	TRANSIENT MOTION	TOTAL
1. BOUNCE (WEIGHT = 1,200 lbs., ACCESSORIES = 800 lbs) MAXIMUM DISPLACEMENT, ft MAXIMUM VELOCITY, ft/sec MAXIMUM ACCELERATION, g's FREQUENCY, Hz MAXIMUM FORCE, lb SUPPLY PRESSURE, psi NET PRESSURE, psi NET CYLINDER AREA, sq. in. FLOW RATE, gpm CYLINDER STROKE, ft	± 2.0 3.2 0.6 0.25 (TWO CYLINDERS)	5.2 3.0	± 2.0 8.4 3.6 9,200 3,000 2,000 4.60 120.7 4.0
2. PITCH (WEIGHT = 1,200 lbs., LENGTH = 8 ft, INERTIA = 200 lb-ft-sec²) MAXIMUM DISPLACEMENT, deg MAXIMUM VELOCITY, deg/sec MAXIMUM ACCELERATION, deg/sec ² FREQUENCY, Hz MAXIMUM TORQUE, lb/ft TORQUE ARM, ft MAXIMUM FORCE, lb SUPPLY PRESSURE, psi NET PRESSURE, psi CYLINDER NET AREA, sq. in. FLOW RATE, gpm CYLINDER STROKE, ft	± 45 141 443 0.5 (TWO CYLINDERS)	100 1,200	± 45 24 1,643 5,720 1.0 5,720 3,000 2,000 2.86 75.0 4.0
3. ROLL (WEIGHT = 1,200 lbs., LENGTH = 5 ft, INERTIA = 78 lb-ft-sec²) MAXIMUM DISPLACEMENT, deg MAXIMUM VELOCITY, deg/sec MAXIMUM ACCELERATION, deg/sec ² FREQUENCY, Hz MAXIMUM TORQUE, lb/ft SUPPLY PRESSURE, psi NET PRESSURE TORQUE FACTOR, in. ³ /rad FLOW RATE, gpm	± 30 92 300 0.5	100 1,900	± 30 192 2,100 3,000 3,000 2,000 24.9 21.7

model was studied. One such factor, top heaviness in the model when the hydraulic power was off, indicated that changes in the full-scale design were required to lower the center of mass of the simulator. These changes can be effected by lowering the crew station, through the use of stepped floor frame, lower guides, and lower cylinder supports and brackets. A second factor requiring design modification, as determined from studying the model, was shaft stress. The stresses in the model shafts were greater than those calculated from the simplified equations of motion. In light of this experience with the model, larger shafts have been recommended.

Springs were added to the mechanical stops of the model in order to cushion the shock of sudden failure of the electrical control. One set of springs was installed for each of the three modes of motion. An over-travel limit switch for each mode, similar to the ones used in electro-dynamic shakers, is deemed necessary in a full-scale version on the basis of experience with the model.

Although the scale model motion platform was not built to meet the specifications for the

dynamics of the full-scale design, the model could be upgraded with some simple modifications for safe use by humans. A useful tool would then be available to carry out the previously mentioned studies which would define the vision-motion cue combinations required for realistic simulation. It is not until such studies are carried out that simulator design can become systematic.

CONCLUSIONS

Because of the successful tests made on the one-third scale model of the short-throw motion simulator concept, it can be concluded that a full-scale version when constructed would have a high probability of success. However, it is not recommended that a full-scale version of the long-throw concept be built until a small-scale version is fabricated and tested.

ACKNOWLEDGMENT

The authors would like to thank the Advanced Research Projects Agency (ARPA Order No. 841 Under Contract DAHC0467C005), U. S. Department of Defense for partially supporting this study.

AN AERIAL CABLE TEST FACILITY USING ROCKET POWER*

C. G. Coalson
Sandia Laboratories
Albuquerque, New Mexico

Sandia Laboratories, Albuquerque, New Mexico has recently developed an Aerial Cable Test Facility which is being used to duplicate many types of air drops. The two basic components of the facility are: an aerial cable stretched between two mountain peaks, and a rocket powered sled track on the valley floor. A test vehicle, attached to a carriage on the aerial cable, is cut loose and accelerated downward via two wire rope towlines (affixed to the test vehicle) which pass through two underground wire rope tunnels and hence to the rocket sled. Impact velocities approaching 1000 ft/sec (with 200 lb test vehicle) can be achieved. The test facility is in a remote area and tests involving large quantities of high explosives can be conducted in complete safety.

Sandia Laboratories has recently developed an Aerial Cable Test Facility using a novel--and perhaps heretofore never used--application of rocket power. Rockets are used to pull a test vehicle (via two wire rope towing lines) into its target with impact velocities approaching 1000 ft/sec. Typically this system duplicates an air drop. The wire rope towing lines can be separated from the test vehicle at a suitable time or position above the target leaving the test vehicle free of extraneous hardware when it strikes target. A pictorial description of the Test Facility is presented in Figure 1.

The aerial cable incorporates suitable apparatus for hoisting, translating, and positioning the test vehicle for the desired flight trajectory and velocity. Test vehicles are accelerated in the 25g to 40g range via the towing lines attached to the rocket sled assembly. Target media typically have been concrete, dirt, or water. The test facility is in a remote mountain/canyon area and tests involving large amounts of explosives can be conducted in complete safety.

*This work was supported by the United States Atomic Energy Commission.

Test vehicles can be delivered to within inches of a pre-selected target. With such accuracy it is now possible, with standard photometrics instrumentation, to record with unsurpassed clarity and great detail the impact and/or detonation of the test vehicle on target. An overhead camera station (on a separate aerial cable) provides an aerial view of impact/detonation events that is really superb. In addition to photometrics instrumentation the target zone can be instrumented with impact sensors, pressure transducers, etc.

One of the greatest difficulties associated with air drops perhaps has been the difficulty of delivering the test vehicle sufficiently close to the instrumented target zone and consequently data acquisition has been somewhat difficult and costly. Tests conducted at the Aerial Cable can in many applications almost duplicate--rather than simulate--an air drop and do so at about one-tenth the cost while data acquisition can be assured.

The foregoing has been a brief and simple description of the Cable Facility. The objective of this paper is not to delve into details of the facility but more importantly

to illustrate the capability, potential, and general mode of operation. It is believed the Engineering Community--knowing the basic physical and operating parameters of the facility--can determine if the facility could meet their testing requirements even though such testing might be a significant departure from the 'standard' pulldown test described herein.

Presented in Figure 2 is a Velocity vs Weight performance curve and shown in Table I are basic specifications of the Aerial Cable Facility as currently applicable.

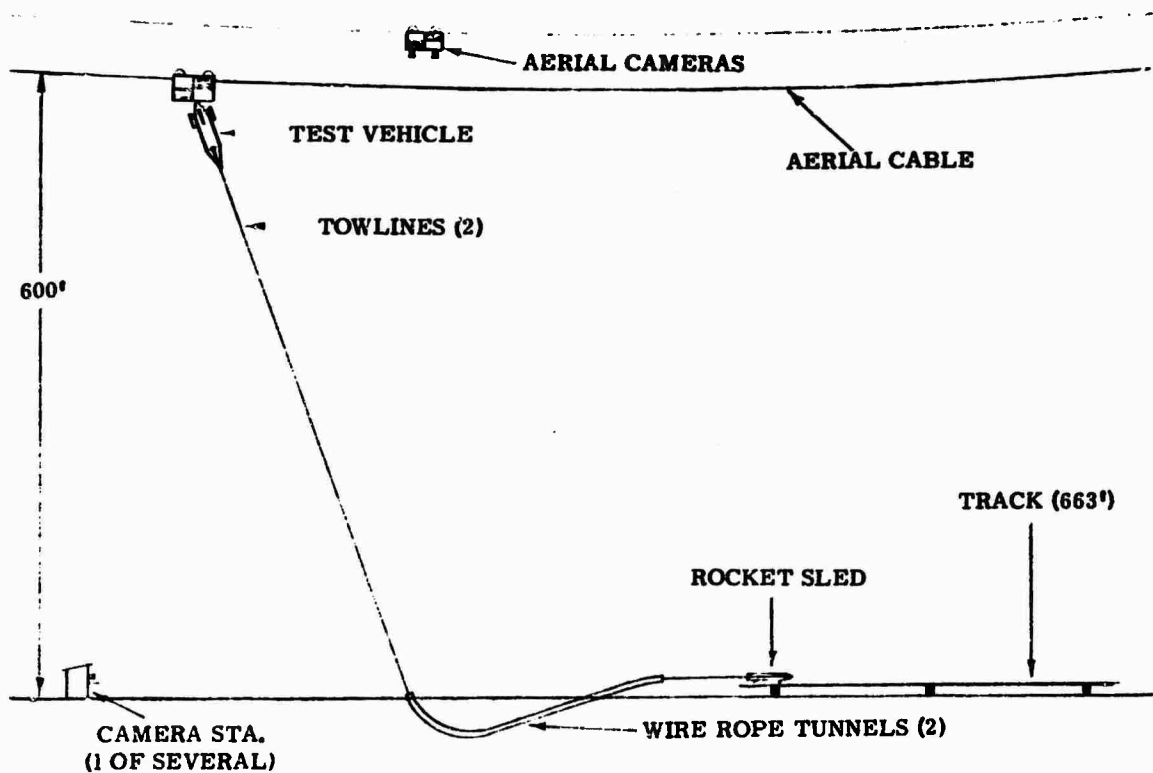


Fig. 1 - Basic test arrangement

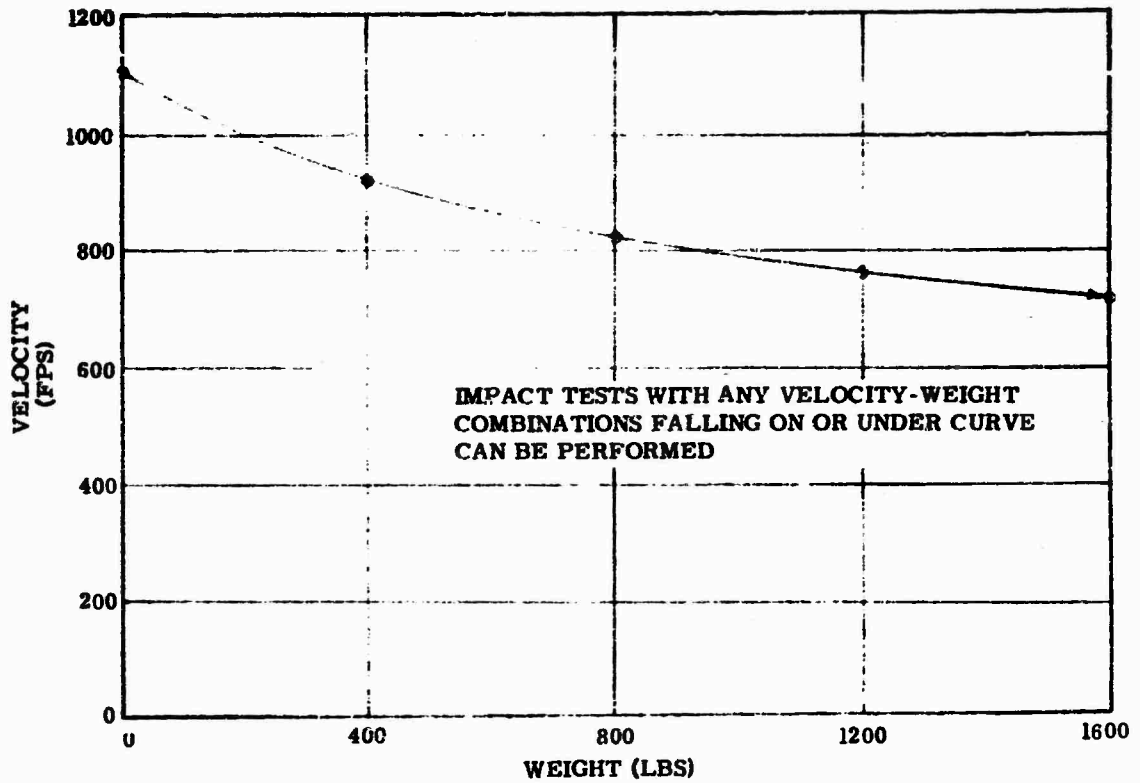


Fig. 2 - Impact velocity vs weight of test vehicle

TABLE I
Basic Specifications of Aerial Cable Facility

Main span, unsupported length	5, 000 ft
Main span, wire size, dia.	1-3/8 in.
Maximum height above test pad	600 ft
Maximum live load supported at 600 ft height	3, 000 lb
Maximum live load supported at 300 ft height	12, 000 lb
Maximum live load supported at 100 ft height	20, 000 lb
Elevation of test pad	6, 350 ft
Elevation of east support	7, 400 ft
Elevation of west support	7, 000 ft
Rocket sled track, length	663 ft
Track, twin rail, std. railway	115 lb/yd
Track gauge (center-to-center)	26-5/16 in.
Track, grade, from horizontal	+ 10 deg.

DISCUSSION

Mr. Schell (Shock and Vibration Information Center): Is the bomb free at the impact point, or are the towing lines still attached?

Mr. Coalson: We can do either. We can sever the wire rope just prior to impact or if the wire

ropes are still attached—and that is no detriment—we leave them on because it simplifies the setup. In that case as the bomb approaches the nozzles the wire ropes begin to make a divergent spread and then they are cut right outside the nozzles, just by the sharp bend that they have to make. So that is a satisfactory means of severing the wire rope.